UNIVERSIDAD DE OVIEDO

Departamento de Ingeniería Eléctrica, Electrónica, de Computadores y Sistemas

Programa de Doctorado

Control de Procesos, Electrónica Industrial e Ingeniería Eléctrica

Tesis Doctoral

BATERÍAS DE Li-IÓN DE ALTA POTENCIA: ANÁLISIS DE PRESTACIONES Y ESTUDIO MECANÍSTICO DE LOS FENÓMENOS DE DEGRADACIÓN

Doctoral Thesis

HIGH POWER Li-ION BATTERY PERFORMANCE: A MECHANISTIC ANALYSIS OF AGING

David Anseán González

Mayo, 2015

Directores de tesis: Manuela González Vega

Víctor M. García Fernández

RESUMEN DEL CONTENIDO DE TESIS DOCTORAL

1.- Título de la Tesis	
Español/Otro Idioma: Baterías de Li-ión de alta potencia: análisis de prestaciones y estudio mecanístico de los fenómenos de degradación	Inglés: High Power Li-ion Battery Performance: a Mechanistic Analysis of Aging

2.- Autor	
Nombre: David Anseán González	DNI/Pasaporte/NIE:
Programa de Doctorado: Control de Procesos, Electrónica Industrial e Ingeniería Eléctrica	
Órgano responsable: Centro Internacional de Postgrado (C.I.P.)	

RESUMEN (en español)

En la actualidad, las baterías de litio-ión *(lithium ion battery, LIB)* están omnipresentes en nuestra sociedad. Como resultado de su elevada densidad de energía y potencia, y de una vida cíclica cada vez más larga, las LIB son las baterías más empleadas en los dispositivos electrónicos portátiles, y están extendiéndose rápidamente en el campo de los vehículos eléctricos *(electric vehicle, EV)* y de los sistemas de almacenamiento de energía eléctrica *(electrical energy storage, EES)*. De ahí que esta tecnología juegue en la actualidad un rol fundamental en aplicaciones tanto comerciales como industriales. En este contexto, el interés creciente en las baterías de litio-ión está generando numerosas oportunidades en el área de investigación. Además, las aplicaciones de los sistemas LIB de alta potencia demandan carga rápida, lo que supone un reto científico-técnico ya que los procedimientos y técnicas desarrollados hasta el momento no aseguran una carga rápida eficiente y fiable, adaptada a las características específicas de cada batería.

La carga rápida y/o el ciclado de alta potencia pueden afectar negativamente al comportamiento de las LIB, reduciendo sus prestaciones y acortando la vida de servicio esperada. Esta degradación prematura incide negativamente en el rendimiento general del sistema que incluye a las baterías y genera problemas de seguridad. Por tanto, el fenómeno de envejecimiento en las LIB es una cuestión clave en aplicaciones de larga durabilidad como los EV y los EES, donde se requiere una vida cíclica y de servicio prolongadas. De ahí que resulte esencial analizar y evaluar el fenómeno del envejecimiento y los mecanismos de degradación en estas nuevas tecnologías de baterías.

Por todo lo expuesto, la presente tesis doctoral se centra en el estudio de las baterías de litio-ión comerciales para aplicaciones de alta potencia, en la evaluación de sus prestaciones y en la identificación de los mecanismos de envejecimiento a través de técnicas *in situ*. Más en concreto, este trabajo presenta un detallado análisis del funcionamiento y de los mecanismos de degradación en baterías comerciales de litio hierro fosfato (LFP), sometidas a diferentes condiciones de servicio (ciclado estándar, ciclado con carga rápida y ciclado con estrés dinámico). Además, en el presente trabajo se propone una metodología para diseñar métodos de carga rápida eficientes y fiables, y se evalúa el protocolo multietapa diseñado específicamente para la tecnología de baterías seleccionada. En cuanto a la identificación de los mecanismos de degradación en las baterías ensayadas, para su análisis cualitativo y cuantitativo se han empleado técnicas *in situ*, incluyendo análisis de capacidad incremental *(incremental capacity, IC)* y de área de pico *(peak area, PA)*, y simulaciones mecanísticas con la *toolbox 'Alawa*. Asimismo, con el objetivo de obtener resultados fidedignos en las simulaciones, se ha desarrollado una estrategia innovadora que consiste en desensamblar baterías del mismo tipo de las ensayadas, extraer y analizar los materiales electródicos, y alimentar con la información obtenida la *toolbox* de simulación.

Respecto a los resultados obtenidos, se demuestra que el protocolo de carga rápida desarrollado es eficiente y fiable, completando la carga en aproximadamente un tercio del tiempo requerido por una carga estándar, y sin causar degradación adicional. Esto queda demostrado por el hecho de que la vida útil de las baterías ensayadas bajo carga estándar y bajo carga rápida supera en ambos casos los 4500 ciclos. Además, se identificaron los mismos modos de degradación en ambos tipos de ciclado: pérdida de inventariado de litio *(loss of lithium inventory, LLI)* y, en menor medida, pérdida de material activo *(loss of active material, LAM)* en el electrodo negativo. Sin embargo, el ciclado de estrés dinámico causa una degradación más acelerada de la batería, que reduce a 1100 ciclos su vida útil. En este caso, la degradación se debe a una gran pérdida de material activo en el electrodo negativo (LAM_{NE}), acompañada en menor grado por la pérdida de inventariado de litio. Asimismo, esta batería manifiesta electrodepósito, que se identificó y midió empleando técnicas *in situ.* Para finalizar el trabajo, se pronosticó/simuló la evolución esperada, más allá de su vida útil medida, de la batería ensayada con carga rápida. El resultado mostró que el protocolo de carga rápida diseñado no produce riesgo de electrodepósito en ningún momento, si se mantienen los mismos mecanismos de envejecimiento.

A modo de recapitulación, la presente tesis investiga el funcionamiento y los mecanismos de envejecimiento en baterías comerciales de alta potencia de tecnología LFP. Se desea destacar que las técnicas *in situ* propuestas proporcionan una metodología sistemática para identificar la degradación en baterías de litio-ión, de forma cualitativa y cuantitativa. Además, la metodología desarrollada resulta idónea para el diseño de modelos de diagnóstico y pronóstico en sistemas de gestión de baterías *(battery management system, BMS)*. Por último, se ha demostrado que la combinación de una tecnología de batería apropiada, junto con el empleo de un protocolo de carga rápida eficiente y fiable, permite la aplicación de carga rápida a LIB en aplicaciones de alta potencia.

RESUMEN (en Inglés)

Nowadays, lithium ion batteries (LIBs) are omnipresent on a worldwide level. As a result of their high energy density, high power density and increasing cycling life, LIBs are a well-founded technology for its use on portable electronic devices, electric vehicles (EVs) and electrical energy storage (EES) systems. The extensive use of LIBs accentuates the fact that LIBs are currently playing a crucial role in the commercial and industrial applications. As a result of the rapid growth and substantial interest devoted to LIBs, an increasing number of opportunities in the industrial and research LIB fields are emerging.

Fast charging is gaining momentum in order to meet the demands of high power LIB systems. The ability of a LIB to perform fast charging depends on various factors, including cell active materials, and the design of a reliable fast charging protocol. To date, efficient fast charging protocol and procedures to achieve rapid charges still remains lacking. In addition, fast charging/high power duty cycling may affect the battery's performance due to accelerated aging. The effects of battery aging are detrimental to LIB systems, reducing its performance and even causing safety issues. In fact, the aging phenomenon is a key issue in durable applications such as EVs and EES, where long-term cycling and long service life are demanded. Hence, it becomes essential to evaluate the performance and the aging mechanisms ongoing on battery systems.

This thesis is focused towards the key field of high power applications of commercial LIBs, and the study of the performance and identification of battery aging mechanisms through *in situ* techniques. A broad analysis of the performance and the degradation mechanisms that various cycling schemes (i.e. standard, fast charging and dynamic stress) cause on commercial high power $LiFePO_4$ batteries is reported in this work. In addition, an efficient, multistage fast charging protocol is developed and analyzed. In order to identify both qualitatively and quantitatively the aging mechanisms ongoing on the tested batteries, we use *in situ* analyses, including incremental capacity (IC), peak area (PA), and mechanistic model simulations using the *'Alawa* toolbox. An innovative approach to attain accurate simulation results is carried out by feeding the toolbox with harvested half-cell data from the actual cells.

The results show that the developed fast-charge protocol is efficient, completes full charges within ~22 min. and does not cause additional degradation in comparison with standard cycling. The end-of-life both for standard and fast charge cycling schemes surpassed 4500 cycles. The quantitative degradation measured for both cycling schemes is equal, caused by a linear loss of lithium inventory (LLI), coupled with a less degree of linear loss of active material (LAM) on the negative electrode (NE). The dynamic stress cycling caused more rapid degradation, reaching 1100 cycles at end-of-life. The degradation is caused by large LAM on the NE, and in less degree, LLI. Moreover, the cell exhibited Li plating, which was identified and quantitatively measured using the *in situ* techniques. To finish the study, prognosis analyses on the fast charging scheme are carried out and we found that the use of fast charging protocol does not risk Li plating after all.

In total, this thesis investigates the performance and aging mechanisms in commercial high power $LiFePO_4$ batteries. The *in situ*, online techniques used in this work provide a systematic methodology to attain battery degradation identification, both qualitatively and quantitatively. The use of these techniques could be quite enlightening for the development of diagnosis and prognosis models for battery management system (BMS) applications to effectively manage and control LIB systems. Finally, the combination of proper cell chemistry and architecture, coupled with the use of an efficient fast charging protocol is key to achieving optimal fast charging in high power LIB applications.

SR. DIRECTOR DE DEPARTAMENTO DE_____/
SR. PRESIDENTE DE LA COMISIÓN ACADÉMICA DEL PROGRAMA DE DOCTORADO EN _____

RESUMEN DEL CONTENIDO DE TESIS DOCTORAL

1.- Título de la Tesis	
Español/Otro Idioma: Baterías de Li-ión de alta potencia: análisis de prestaciones y estudio mecanístico de los fenómenos de degradación	Inglés: High Power Li-ion Battery Performance: a Mechanistic Analysis of Aging

2.- Autor	
Nombre: David Anseán González	DNI/Pasaporte/NIE: 10901896-B
Programa de Doctorado: Control de Procesos, Electrónica Industrial e Ingeniería Eléctrica	
Órgano responsable: Centro Internacional de Postgrado (C.I.P.)	

RESUMEN (en español)

En la actualidad, las baterías de litio-ión *(lithium ion battery, LIB)* están omnipresentes en nuestra sociedad. Como resultado de su elevada densidad de energía y potencia, y de una vida cíclica cada vez más larga, las LIB son las baterías más empleadas en los dispositivos electrónicos portátiles, y están extendiéndose rápidamente en el campo de los vehículos eléctricos *(electric vehicle, EV)* y de los sistemas de almacenamiento de energía eléctrica *(electrical energy storage, EES)*. De ahí que esta tecnología juegue en la actualidad un rol fundamental en aplicaciones tanto comerciales como industriales. En este contexto, el interés creciente en las baterías de litio-ión está generando numerosas oportunidades en el área de investigación. Además, las aplicaciones de los sistemas LIB de alta potencia demandan carga rápida, lo que supone un reto científico-técnico ya que los procedimientos y técnicas desarrollados hasta el momento no aseguran una carga rápida eficiente y fiable, adaptada a las características específicas de cada batería.

La carga rápida y/o el ciclado de alta potencia pueden afectar negativamente al comportamiento de las LIB, reduciendo sus prestaciones y acortando la vida de servicio esperada. Esta degradación prematura incide negativamente en el rendimiento general del sistema que incluye a las baterías y genera problemas de seguridad. Por tanto, el fenómeno de envejecimiento en las LIB es una cuestión clave en aplicaciones de larga durabilidad como los EV y los EES, donde se requiere una vida cíclica y de servicio prolongadas. De ahí que resulte esencial analizar y evaluar el fenómeno del envejecimiento y los mecanismos de degradación en estas nuevas tecnologías de baterías.

Por todo lo expuesto, la presente tesis doctoral se centra en el estudio de las baterías de litio-ión comerciales para aplicaciones de alta potencia, en la evaluación de sus prestaciones y en la identificación de los mecanismos de envejecimiento a través de técnicas *in situ*. Más en concreto, este trabajo presenta un detallado análisis del funcionamiento y de los mecanismos de degradación en baterías comerciales de litio hierro fosfato (LFP), sometidas a diferentes condiciones de servicio (ciclado estándar, ciclado con carga rápida y ciclado con estrés dinámico). Además, en el presente trabajo se propone una metodología para diseñar métodos de carga rápida eficientes y fiables, y se evalúa el protocolo multietapa diseñado específicamente para la tecnología de baterías seleccionada. En cuanto a la identificación de los mecanismos de degradación en las baterías ensayadas, para su análisis cualitativo y cuantitativo se han empleado técnicas *in situ*, incluyendo análisis de capacidad incremental *(incremental capacity, IC)* y de área de pico *(peak area, PA)*, y simulaciones mecanísticas con la *toolbox 'Alawa*. Asimismo, con el objetivo de obtener resultados fidedignos en las simulaciones, se ha desarrollado una estrategia innovadora que consiste en desensamblar baterías del mismo tipo de las ensayadas, extraer y analizar los materiales electródicos, y alimentar con la información obtenida la *toolbox* de simulación.

Respecto a los resultados obtenidos, se demuestra que el protocolo de carga rápida desarrollado es eficiente y fiable, completando la carga en aproximadamente un tercio del tiempo requerido por una carga estándar, y sin causar degradación adicional. Esto queda demostrado por el hecho de que la vida útil de las baterías ensayadas bajo carga estándar y bajo carga rápida supera en ambos casos los 4500 ciclos. Además, se identificaron los mismos modos de degradación en ambos tipos de ciclado: pérdida de inventariado de litio *(loss of lithium inventory, LLI)* y, en menor medida, pérdida de material activo *(loss of active material, LAM)* en el electrodo negativo. Sin embargo, el ciclado de estrés dinámico causa una degradación más acelerada de la batería, que reduce a 1100 ciclos su vida útil. En este caso, la degradación se debe a una gran pérdida de material activo en el electrodo negativo (LAM_{NE}), acompañada en menor grado por la pérdida de inventariado de litio. Asimismo, esta batería manifiesta electrodepósito, que se identificó y midió empleando técnicas *in situ.* Para finalizar el trabajo, se pronosticó/simuló la evolución esperada, más allá de su vida útil medida, de la batería ensayada con carga rápida. El resultado mostró que el protocolo de carga rápida diseñado no produce riesgo de electrodepósito en ningún momento, si se mantienen los mismos mecanismos de envejecimiento.

A modo de recapitulación, la presente tesis investiga el funcionamiento y los mecanismos de envejecimiento en baterías comerciales de alta potencia de tecnología LFP. Se desea destacar que las técnicas *in situ* propuestas proporcionan una metodología sistemática para identificar la degradación en baterías de litio-ión, de forma cualitativa y cuantitativa. Además, la metodología desarrollada resulta idónea para el diseño de modelos de diagnóstico y pronóstico en sistemas de gestión de baterías *(battery management system, BMS)*. Por último, se ha demostrado que la combinación de una tecnología de batería apropiada, junto con el empleo de un protocolo de carga rápida eficiente y fiable, permite la aplicación de carga rápida a LIB en aplicaciones de alta potencia.

RESUMEN (en Inglés)

Nowadays, lithium ion batteries (LIBs) are omnipresent on a worldwide level. As a result of their high energy density, high power density and increasing cycling life, LIBs are a well-founded technology for its use on portable electronic devices, electric vehicles (EVs) and electrical energy storage (EES) systems. The extensive use of LIBs accentuates the fact that LIBs are currently playing a crucial role in the commercial and industrial applications. As a result of the rapid growth and substantial interest devoted to LIBs, an increasing number of opportunities in the industrial and research LIB fields are emerging.

Fast charging is gaining momentum in order to meet the demands of high power LIB systems. The ability of a LIB to perform fast charging depends on various factors, including cell active materials, and the design of a reliable fast charging protocol. To date, efficient fast charging protocol and procedures to achieve rapid charges still remains lacking. In addition, fast charging/high power duty cycling may affect the battery's performance due to accelerated aging. The effects of battery aging are detrimental to LIB systems, reducing its performance and even causing safety issues. In fact, the aging phenomenon is a key issue in durable applications such as EVs and EES, where long-term cycling and long service life are demanded. Hence, it becomes essential to evaluate the performance and the aging mechanisms ongoing on battery systems.

This thesis is focused towards the key field of high power applications of commercial LIBs, and the study of the performance and identification of battery aging mechanisms through *in situ* techniques. A broad analysis of the performance and the degradation mechanisms that various cycling schemes (i.e. standard, fast charging and dynamic stress) cause on commercial high power $LiFePO_4$ batteries is reported in this work. In addition, an efficient, multistage fast charging protocol is developed and analyzed. In order to identify both qualitatively and quantitatively the aging mechanisms ongoing on the tested batteries, we use *in situ* analyses, including incremental capacity (IC), peak area (PA), and mechanistic model simulations using the *'Alawa* toolbox. An innovative approach to attain accurate simulation results is carried out by feeding the toolbox with harvested half-cell data from the actual cells.

The results show that the developed fast-charge protocol is efficient, completes full charges within ~22 min. and does not cause additional degradation in comparison with standard cycling. The end-of-life both for standard and fast charge cycling schemes surpassed 4500 cycles. The quantitative degradation measured for both cycling schemes is equal, caused by a linear loss of lithium inventory (LLI), coupled with a less degree of linear loss of active material (LAM) on the negative electrode (NE). The dynamic stress cycling caused more rapid degradation, reaching 1100 cycles at end-of-life. The degradation is caused by large LAM on the NE, and in less degree, LLI. Moreover, the cell exhibited Li plating, which was identified and quantitatively measured using the *in situ* techniques. To finish the study, prognosis analyses on the fast charging scheme are carried out and we found that the use of fast charging protocol does not risk Li plating after all.

In total, this thesis investigates the performance and aging mechanisms in commercial high power $LiFePO_4$ batteries. The *in situ*, online techniques used in this work provide a systematic methodology to attain battery degradation identification, both qualitatively and quantitatively. The use of these techniques could be quite enlightening for the development of diagnosis and prognosis models for battery management system (BMS) applications to effectively manage and control LIB systems. Finally, the combination of proper cell chemistry and architecture, coupled with the use of an efficient fast charging protocol is key to achieving optimal fast charging in high power LIB applications.

SR. DIRECTOR DE DEPARTAMENTO DE_____ ____ _____/
SR. PRESIDENTE DE LA COMISIÓN ACADÉMICA DEL PROGRAMA DE DOCTORADO EN _____

Abstract

Nowadays, lithium ion batteries (LIBs) are omnipresent on a worldwide level. As a result of their high energy density, high power density and increasing cycling life, LIBs are a well-founded technology for its use on portable electronic devices, electric vehicles (EVs) and electrical energy storage (EES) systems. The extensive use of LIBs accentuates the fact that LIBs are currently playing a crucial role in the commercial and industrial applications. As a result of the rapid growth and substantial interest devoted to LIBs, an increasing number of opportunities in the industrial and research LIB fields are emerging.

Fast charging is gaining momentum in order to meet the demands of high power LIB systems. The ability of a LIB to perform fast charging depends on various factors, including cell active materials, and the design of a reliable fast charging protocol. To date, efficient fast charging protocol and procedures to achieve rapid charges still remains lacking. In addition, fast charging/high power duty cycling may affect the battery's performance due to accelerated aging. The effects of battery aging are detrimental to LIB systems, reducing its performance and even causing safety issues. In fact, the aging phenomenon is a key issue in durable applications such as EVs and EES, where long-term cycling and long service life are demanded. Hence, it becomes essential to evaluate the performance and the aging mechanisms ongoing on battery systems.

This thesis is focused towards the key field of high power applications of commercial LIBs, and the study of the performance and identification of battery aging mechanisms through *in situ* techniques. A broad analysis of the performance and the degradation mechanisms that various cycling schemes (i.e. standard, fast charging and dynamic stress) cause on commercial high power $LiFePO_4$ batteries is reported in this work. In addition, an efficient, multistage fast charging protocol is developed and analyzed. In order to identify both qualitatively and quantitatively the aging mechanisms ongoing on the tested batteries, we use *in situ* analyses, including incremental capacity (IC), peak area (PA), and mechanistic model simulations using the *'Alawa* toolbox. An innovative approach to attain accurate simulation results is carried out by feeding the toolbox with harvested half-cell data from the actual cells.

The results show that the developed fast-charge protocol is efficient, completes full charges within ~22 min. and does not cause additional degradation in comparison with standard cycling. The end-of-life both for standard and fast charge cycling schemes surpassed 4500 cycles. The quantitative degradation measured for both cycling schemes is equal, caused by a linear loss of lithium inventory (LLI), coupled with a less degree of linear loss of active material (LAM) on the negative electrode (NE). The dynamic stress cycling caused rapid cell degradation, reaching 1100 cycles at end-of-life. The degradation is caused by large LAM on the NE, and in less degree, LLI. Moreover, the cell exhibited Li plating, which was identified and quantitatively measured using the *in situ* techniques. To finish the study, prognosis analyses on the fast charging scheme are carried out and we found that the use of fast charging protocol does not risk Li plating after all.

In total, this thesis investigates the performance and aging mechanisms in commercial high power $LiFePO_4$ batteries. The *in situ*, online techniques used in this work provide a systematic methodology to attain battery degradation identification, both qualitatively and quantitatively. The use of these techniques could be quite enlightening for the development of diagnosis and prognosis models for battery management system (BMS) applications to effectively manage and control LIB systems. Finally, the combination of proper cell chemistry and architecture, coupled with the use of an efficient fast charging protocol is key to achieving optimal fast charging in high power LIB applications.

Resumen

En la actualidad, las baterías de litio-ión *(lithium ion battery, LIB)* están omnipresentes en nuestra sociedad. Como resultado de su elevada densidad de energía y potencia, y de una vida cíclica cada vez más larga, las LIB son las baterías más empleadas en los dispositivos electrónicos portátiles, y están extendiéndose rápidamente en el campo de los vehículos eléctricos *(electric vehicle, EV)* y de los sistemas de almacenamiento de energía eléctrica *(electrical energy storage, EES)*. De ahí que esta tecnología juegue en la actualidad un rol fundamental en aplicaciones tanto comerciales como industriales. En este contexto, el interés creciente en las baterías de litio-ión está generando numerosas oportunidades en el área de investigación. Además, las aplicaciones de los sistemas LIB de alta potencia demandan carga rápida, lo que supone un reto científico-técnico ya que los procedimientos y técnicas desarrollados hasta el momento no aseguran una carga rápida eficiente y fiable, adaptada a las características específicas de cada batería.

La carga rápida y/o el ciclado de alta potencia pueden afectar negativamente al comportamiento de las LIB, reduciendo sus prestaciones y acortando la vida de servicio esperada. Esta degradación prematura incide negativamente en el rendimiento general del sistema que incluye a las baterías y genera problemas de seguridad. Por tanto, el fenómeno de envejecimiento en las LIB es una cuestión clave en aplicaciones de larga durabilidad como los EV y los EES, donde se requiere una vida cíclica y de servicio prolongadas. De ahí que resulte esencial analizar y evaluar el fenómeno del envejecimiento y los mecanismos de degradación en estas nuevas tecnologías de baterías.

Por todo lo expuesto, la presente tesis doctoral se centra en el estudio de las baterías de litio-ión comerciales para aplicaciones de alta potencia, en la evaluación de sus prestaciones y en la identificación de los mecanismos de envejecimiento a través de técnicas *in situ*. Más en concreto, este trabajo presenta un detallado análisis del funcionamiento y de los mecanismos de degradación en baterías comerciales de litio hierro fosfato (LFP), sometidas a diferentes condiciones de servicio (ciclado estándar, ciclado con carga rápida y ciclado con estrés dinámico). Además, en el presente trabajo se propone una metodología para diseñar métodos de carga rápida eficientes y fiables, y se evalúa el protocolo multietapa diseñado específicamente para la tecnología de baterías seleccionada. En cuanto a la identificación de los mecanismos de degradación en las baterías ensayadas, para su análisis cualitativo y cuantitativo se han empleado técnicas *in situ*, incluyendo análisis de capacidad incremental *(incremental capacity, IC)* y de área de pico *(peak area, PA)*, y simulaciones mecanísticas con la *toolbox 'Alawa*. Asimismo, con el objetivo de obtener resultados fidedignos en las simulaciones, se ha desarrollado una estrategia innovadora que consiste en desensamblar baterías del mismo tipo de las ensayadas, extraer y analizar los materiales electródicos, y alimentar con la información obtenida la *toolbox* de simulación.

Respecto a los resultados obtenidos, se demuestra que el protocolo de carga rápida desarrollado es eficiente y fiable, completando la carga en aproximadamente un tercio del tiempo requerido por una carga estándar, y sin causar degradación adicional. Esto queda demostrado por el hecho de que la vida útil de las baterías ensayadas bajo carga estándar y bajo carga rápida supera en ambos casos los 4500 ciclos. Además, se identificaron los mismos modos de degradación en ambos tipos de ciclado: pérdida de inventariado de litio *(loss of lithium inventory, LLI)* y, en menor medida, pérdida de material activo *(loss of active material, LAM)* en el electrodo negativo. Sin embargo, el ciclado de estrés dinámico causa una degradación más acelerada de la batería, que reduce a 1100 ciclos su vida útil. En este caso, la degradación se debe a una gran pérdida de material activo en el electrodo negativo (LAM_{NE}), acompañada en menor grado por la pérdida de inventariado de litio. Asimismo, esta batería manifiesta electrodepósito, que se identificó y midió empleando técnicas *in situ.* Para finalizar el trabajo, se pronosticó/simuló la evolución esperada, más allá de su vida útil medida, de la batería ensayada con

carga rápida. El resultado mostró que el protocolo de carga rápida diseñado no produce riesgo de electrodepósito en ningún momento, si se mantienen los mismos mecanismos de envejecimiento.

A modo de recapitulación, la presente tesis investiga el funcionamiento y los mecanismos de envejecimiento en baterías comerciales de alta potencia de tecnología LFP. Se desea destacar que las técnicas *in situ* propuestas proporcionan una metodología sistemática para identificar la degradación en baterías de litio-ión, de forma cualitativa y cuantitativa. Además, la metodología desarrollada resulta idónea para el diseño de modelos de diagnóstico y pronóstico en sistemas de gestión de baterías *(battery management system, BMS)*. Por último, se ha demostrado que la combinación de una tecnología de batería apropiada, junto con el empleo de un protocolo de carga rápida eficiente y fiable, permite la aplicación de carga rápida a LIB en aplicaciones de alta potencia.

Acknowledgments

First and foremost, I would like to begin by expressing my gratitude to my advisors, Dr. Manuela González Vega and Dr. Víctor M. García Fernández who made this research project possible. Their excellent mentorship, guidance and support throughout this thesis are deeply appreciated. I would also like to thank my colleagues at the Battery Research Laboratory, Dr. Juan C. Viera Pérez, Dr. Cecilio Blanco Viejo, Dr. Juan C. Álvarez Antón and Dr. Luciano Sánchez Ramos for their support and collaboration. I am also especially thankful to Constantina Álvarez Peña at the University of Oviedo, for her welcoming recommendation to my "future" thesis advisors.

I am also greatly thankful to the research team at the Electrochemical Power Systems Laboratory, University of Hawaii at Manoa, Dr. Bor Yann Liaw, Dr. Matthieu Dubarry and Dr. Arnaud Devie for their kind support and highly valuable guidance during my stay at their laboratory. Mahalo!

Several lab mates at the Battery Research Laboratory deserve special recognition for their comradeship during my doctoral studies, including José L. Antuña Albuerne, Héctor Corte León, Gustavo Grillo, and also to Yuvini Echevarría Cartaya and Yoana Fernández Pulido, who recently joined us at the lab. I would also like to thank all my friends outside academia, for all the good times we have had, and the great moments to come. Salud!

Most specially, I would like to thank my family for being always there, and to my wife Maite and our cat Misha for their love and unconditional support.

And finally, I am also greatly thankful to the Spanish Ministry of Science and Innovation (MICINN) for providing the funding (TEC2009-12552) of this work.

David Anseán González

Gijón, Spain

May, 2015

A Thesis Dedicated to the Memory of my Late Father

TABLE OF CONTENTS

List of Acronyms

BMS: battery management system

BOC: beginning of cycling

BOL: beginning of life

CC-CV: constant current, constant voltage

DST: dynamic stress test

EES: electrical energy storage

EOCV: end of charge voltage

EODV: end of discharge voltage

EOC: end of cycling

EOL: end of life

EV: electric vehicle

FPP: formation of parasitic phase

FRD: faradic rate degradation

FSCC: four stage constant current

GIC: graphite intercalation compounds

HE: high energy (batteries)

HEV: hybrid electric vehicle

HP: high power (batteries)

HRC: high rate charge

IC: incremental capacity

IP: inflection point

IR: internal resistance

LAM: loss of active material

LAM_{NE}: loss of active material on the negative electrode

LAM_{PE}: loss of active material on the positive electrode

LAM_{deNE}: loss of active material on the negative electrode when delithiating

LAM_{liNE}: loss of active material on the negative electrode when lithiating

LAM_{dePE}: loss of active material on the positive electrode when delithiating

LAM_{liPE}: loss of active material on the positive electrode when lithiating

LCD: linear current decay

LCO: lithium oxide cobalt

LIB: lithium-ion battery

LFP: lithium iron phosphate

LLI: loss of lithium inventory

LMO: lithium manganese oxide

LR: loading ratio

LTO: lithium titanium oxides

MCM: multistage charging method

MLCD: modified linear current decay

NCA: lithium nickel cobalt aluminum oxide

NE: negative electrode

NMC: lithium nickel manganese cobalt oxide

OCV: open circuit voltage

OFS: offset

ORI: ohmic resistance increase

PA: peak area

PE: positive electrode

PHEV: plug in hybrid electric vehicle

RPT: reference performance test

SEI: solid electrolyte interface

SEM: scanning electron microscopy

SOC: state of charge

SOH: state of health

TEM: transmission electron microscopy

TMS: thermal management system

UPS: uninterruptible power supply

USABC: United States Advanced Battery Consortium

VCM: varying current method

XRD: X-Ray diffraction

This page intentionally left blank

1. Introduction

In the modern society, lithium ion batteries (LIBs) have become ubiquitous. Indeed, it is difficult to ignore the presence of LIBs, as more than 3000 millions of units are produced per year worldwide, yielding annual profits within ~$12 billion. Furthermore, market research foresees a steady growth of LIBs over the next decade. The large majority of the LIBs produced are used to power portable electronic devices such as cell phones, laptops and tablets. More recently, on account of the continuous improvements in battery science and technology, LIBs have also become the power sources of choice for sustainable transport, such as electric vehicles (EVs) and hybrid electric vehicles (HEVs). Similarly, LIBs are also gaining considerable attention towards electrical energy storage (EES) applications, where have been successfully introduced to the structure of the electricity sector and renewable energy integration. Furthermore, LIBs have a niche market in military, aerospace and medical applications. In view of these facts, it is clearly observed that LIBs are currently playing a key role in the industrial and commercial applications.

Compared to other types of batteries and portable electrochemical power sources, LIBs are characterized by a high specific energy (~200 Wh/kg), high energy density (~600 Wh/L), high energy efficiency (>90%), long cycle-life (>1000 cycles) and relative low cost (~$400 per kWh). Depending on the selected battery technology and architecture, these figures can be even improved. In addition, other advantages of LIBs such as high rate charge/discharge capabilities or broad temperature range operation have been demonstrated. The combination of these qualities, with a cost effective and hermetic package has been the key of success of LIB technologies. Most importantly, as a result of substantial funding in active research and development, battery performance continues to improve, with innovations generally focused towards increasing the energy and power density, cycle life, safety, temperature operational range and reduce the final costs.

Despite continuous improvements, LIBs still face issues to be addressed related to battery aging, performance decrease and safety concerns caused by battery deterioration. Battery degradation is a major concern for durable applications such as EVs, EES or aerospace applications, where long-term cycling and services of over 10 years with very demanding duty schedules are required. The effects of battery aging are detrimental to the LIB system, reducing its performance and even causing safety issues. Thus, it becomes essential to understand and to identify the aging phenomenon, a complex process originated from multiple mechanisms that can act simultaneously.

Another issue that LIBs face today is the ability to perform fast charging. In fact, one of the major issues hampering the acceptance of EVs is the anxiety associated with long charging time. Similarly, fast charging is demanded in portable electronics to enhance mobility, and is also required in battery powered renewable EES systems. Unfortunately, fast charging may also affect the battery's performance and cause accelerated aging. This is because fast charging typically involves high rates and high temperatures, which are known as the main factors in battery degradation. Therefore fast charging is also an important area of study in LIBs, and it becomes necessary to analyze the technical factors to achieve fast charging without adding further aging to the battery. Hence, it becomes again essential to identify battery aging and quantify the effects that fast charging may introduce to the LIBs.

Regardless of the recent achievements in understanding the aging mechanisms in LIBs, online diagnosis of the aging effects in a battery system remains lacking. Respecting fast charging, although several efforts have been carried out in this field, to date, there has been little agreement on what strategies should be applied to achieve efficient and reliable fast charges. Most fast charging protocols do not address in detail the importance of the battery technology of choice, or safety issues related with fast

charging. Furthermore, a detailed study using online diagnosis tools to identify the degradation effects that fast charge/discharge may cause on high power LIBs under demanding schedule duties, over long-term cycle aging have not been studied. Consequently, the identification and further analyses of the aging mechanisms ongoing in real life LIB systems through *in situ* techniques could be quite enlightening for the development of prognostic models to predict the performance and useful service life of LIB systems.

In this thesis, we seek to address the aforementioned questions: the identification and further analyses of the aging modes through *in situ* techniques of commercial high power LIBs, the study and design of fast charging protocols that do not add further aging to the battery, and to evaluate high power LIBs under demanding duty schedules. These findings would allow efficient, reliable and safe operation on demanding long-term, high power LIB systems.

1.1. Thesis objectives

The main thesis objectives are summarized below:

- To provide a detailed quantitative and qualitative analysis of the degradation modes on LIBs, using *in situ,* online techniques. The identification of the aging modes is carried out on high power LIBs, tested under demanding and realistic duty cycles which cause complex degradation patterns.

- To propose, design, analyze and validate an efficient and reliable fast charging protocol for high power LIBs. Within this objective, we also aim to provide an optimized design strategy to develop safe, efficient, fast charging protocols for LIBs applications.

- To evaluate high power LIBs under long-term, diverse and demanding duty cycling schemes. The study of the performance is compared versus the United States Advanced Battery Consortium (USABC) goals, to evaluate the feasibility of the tested LIBs for EV applications.

- To provide a description of valuable tools to facilitate the identification of the aging mechanisms in commercial LIBs. These tools comprise *in situ* electrochemical techniques, computerized mechanistic simulation models and *ex situ* strategies (i.e. harvesting half-cell data) to optimize battery diagnosis and prognosis.

- To demonstrate the potential of combining different methodologies and analysis techniques to attain adequate battery quantitative and qualitative aging modes identification. The approaches should aim to offer an effective method with sufficient accuracy yet simplicity to study complex LIB behavior.

To attain the thesis objectives, we first provide a broad and updated overview on the main topics related to the aforementioned objectives. We highlight the overview provided in Chapter **2** where the LIB fundamentals, materials, aging mechanisms and main characteristics of commercial LIBs are reported. In addition, Chapter **3** addresses the important subject of fast charging, where an evaluation of current battery architectures and charging methods for their application in fast charging LIBs is provided.

Lastly, a general goal that this thesis aims to address is to establish a connection between fundamental science (i.e. material science, electrochemistry, physics and chemistry) and engineering (i.e. electrical, power electronics, systems and computer science engineering). These two disciplines are often studied separately. However, our understanding is that improvements on battery performance and management shall be using approaches and knowledge from both disciplines altogether.

To sum up, this thesis aims to make contributions in the LIB field to enhance the current understanding of LIB degradation and identification, and to improve management, performance and control of LIB systems.

1.2. Thesis scope

To date, from a technical perspective, battery design follows a straightforward approach starting from the initial active research to the final product launch. The active research is generally carried out at atomic, particle and electrode level system, where disciplines such as material science, electrochemistry and physical-chemistry play a fundamental role. As the battery product is completed, the next step is generally to embed the battery product in the final application. In this final stage, disciplines related to electrical, power electronics, systems and computer science engineering are essential to deliver a reliable final product.

Unfortunately, the two main disciplines that technically contribute to a successful completion of a battery system do not often interact. For example, engineers who design the battery management system (BMS) to control in a reliable way the final battery system, may have little knowledge on the electrochemical principles related to battery degradation. Vice versa, scientists at the particle-level design are not required to understand advanced power electronics topologies for the energy conversion. From a background perspective, it seems understandable that neither material scientists nor electrical engineers must have an extensive domain of both disciplines. However, we understand that a fair level of knowledge of both disciplines is required to improve management, performance and control of the final LIB application. With this perspective in mind, the scope of this thesis is the intersection of the fundamental research and the engineering disciplines. A schematic representation of the scope of this thesis is shown in Fig. **1.1**.

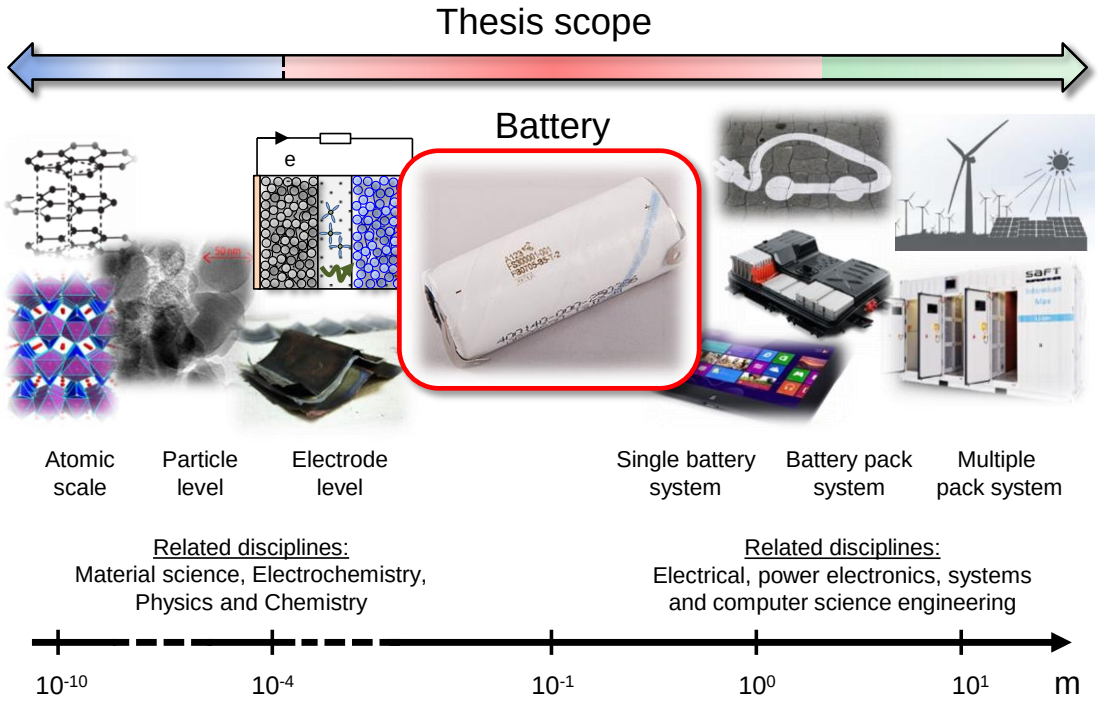

Fig. 1.1. This thesis seeks to contribute knowledge in the battery level, which shares the background of fundamental battery science and several engineering disciplines.

This thesis covers the intersection of the fundamental battery research approach and the engineering disciplines related to LIB applications. We shall point out that, even if multidisciplinary topics are addressed in this work, the final goal is oriented towards the improvement of LIBs final applications. That is, we understand that to improve management, performance and control of LIB systems (i.e. engineering approach) it is necessary to acquire a certain degree of knowledge of the main battery principles (i.e. fundamental battery research approach).

1.3. Thesis organization

This thesis is organized as follows:

Chapter **2** provides an updated and broad review on LIB fundamentals, materials, aging mechanisms and battery performance. First, the fundamentals and basic battery materials are presented. Next, the aging mechanisms are examined and described, to finish the chapter describing the commercial LIB products and its main performance characteristics.

Chapter **3** addresses the subject of fast charging. It starts analyzing LIBs optimized for fast charging applications. Thereafter, a review on fast charging methods is presented. Next, a new step-by-step guideline to implement fast charging is presented, to finish with the design of a fast charging protocol for high power lithium iron phosphate (LFP) batteries.

Chapter **4** presents the techniques for LIB aging analysis to be used in the thesis. This chapter also includes a descriptive set of tools and degradation patterns to facilitate the aging analyses on commercial LIBs.

Chapter **5** presents the general procedures and materials used in this thesis. This includes the details of the testing procedures, cell disassembling process, testing equipment characteristics and the mechanistic computer simulation toolbox, *'Alawa.*

Chapter **6** investigates the performance and degradation of the tested batteries using *in-situ* degradation and performance analyses techniques. Here is provided a general, first evaluation and discussion of the performance and degradation of the tested batteries.

Chapter **7** complements the investigations previously carried out in Chapter 6, by deciphering the degradation mechanisms, both from a qualitative and quantitative perspective, via mechanistic simulations. The chapter concludes with a prognosis approach.

Chapter **8** presents the conclusion of this thesis, its main contributions and possible future research directions.

Every chapter ends with a summary, where the main topics addressed are recapitulated and set into context as concluding remarks.

2. Li-ion batteries

Currently, lithium ion batteries (LIBs) are the power sources of choice for portable electronic devices and modern sustainable vehicles such as the electric (EV) and plug in hybrid (PHEV) vehicles. In addition, LIBs have been recently introduced in electrical energy storage (EES) systems, mostly in renewable energy plants. As a result of the rapid growth and substantial interest in LIBs, several LIB technologies have been commercialized, using enhanced material chemistry approaches and cell architectures. Despite the continuous improvements, LIBs still face issues to be addressed such as; battery aging, performance decrease, safety concerns and cost reduction.

One of the main limitations of LIBs resides in the battery aging. This is particularly important for durable applications such as EVs and EES, where long-term cycling and services of over 10 years are required. The effects of battery aging are detrimental to the LIB system, reducing its performance and even causing safety issues. Thus, it is necessary to understand and identify the aging phenomenon, a complex process originated from multiple mechanisms that can act simultaneously. Respecting LIB technologies, in recent years new battery materials have been developed, providing new characteristics and performance. Consequently, to understand LIB aging mechanisms, and the characteristics of new battery technologies, the battery fundamentals and electrochemical principles shall be provided first.

To date, there have been excellent discussions on battery fundamentals, materials, aging mechanisms and battery performance. However, these topics have been usually addressed separately. Due to their relevance in this thesis, in this chapter we aim to provide an updated review of this topics altogether. We highlight the aspects of battery aging, providing a broad analysis of the main degradation modes found on LIBs. The topics described in this chapter are widely used throughout this thesis work.

This review can be divided in three main parts, following a bottom-up approach. The first part deals with LIB fundamentals and elementary battery materials. As the LIB foundations are established, the aging mechanisms in commercial LIBs are presented. The chapter ends describing the commercial LIB products, its main characteristics and performance merits. Due to the mixed nature of this thesis work, including material science, electrochemistry and electrical engineering concepts, the three main parts of this chapter are closely related.

2.1. Li-ion battery fundamentals

The first electrochemical cell or battery[1], named the voltaic pile, was first described by Alessandro Volta in 1800. Over the course of the next 200 years, developments in science and technology have increased remarkably. Hence, it seems obvious that today's commercial LIB abruptly outperform the one that Alessandro described. Still, the first developments on LIBs (dated from the early 1970s) were plagued with multiple problems, mostly caused by the materials of choice used in those first prototypes. Thanks to further R&D development investments, several breakthroughs were achieved in the 1980s [1]. As a result, in 1991 Sony Co. commercialized the first rechargeable LIB, based on intercalation materials. This new battery technology had a great success because of its higher specific energy and energy density, when compared to existing battery technologies (see **Fig. 2.1**a). Indeed, due to its advantages, LIBs rapidly substituted the old existing technologies in most applications, particularly in the consumer electronic market. Nowadays LIBs are omnipresent in the modern world, with an overall production that exceeds 3000 million of cells per year for several applications (see **Fig. 2.1**b) [2]. Similarly, market research has projected the global LIB revenue to expand up to $53.7 billion in 2020 from ~$11.8 billion in 2010 [3]. Hence, the LIB industry foresees a steady growth over the next years, playing a crucial role in the industrial and market domains.

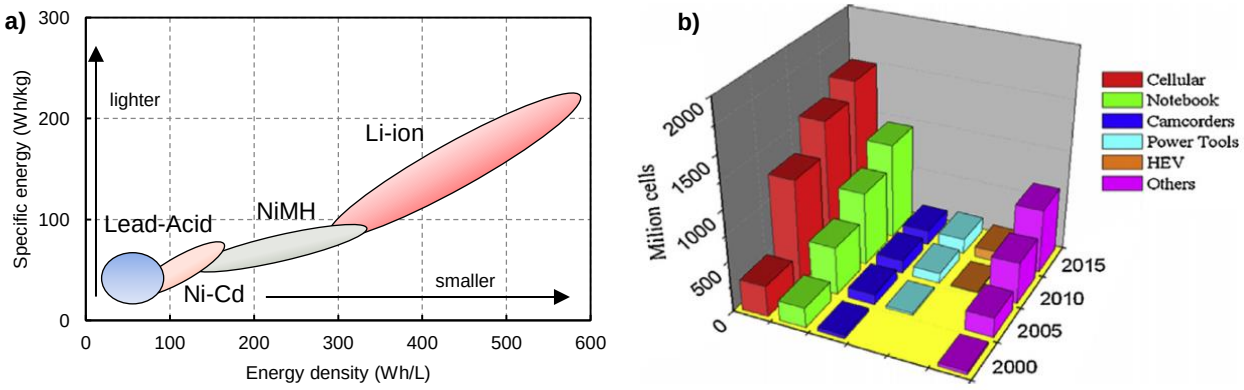

Fig. 2.1. a) Comparison of the energy storage capability of various battery systems b) evolution of the Li-ion battery sale in the consumer electronic and HEV market [2].

Technology improvements in LIBs are continuous, and novel materials, constructive techniques and new approaches are constantly in progress. However, the LIB fundamentals, including principles of operation and the electrochemical background remain unchanged. Hence, the aim of this section is to provide the essential knowledge to understand how a LIB operates, based on the electrochemical principles.

2.1.1. Principles of operation

As defined in Linden's Handbook of Batteries [4], a rechargeable battery is an electrochemical system that converts the chemical energy contained in its active materials into electrical energy by means of an electrochemical oxidation-reduction (redox) reversible reaction. Hence, a battery provides two functions: during discharge delivers energy to the external load, while on charge an external power supply provides the energy that is stored in the battery.

[1] Cell vs. Battery: A cell is the basic electrochemical unit, whereas a battery consists of one or more assembled cells. In this thesis, cell and battery is always referred as a secondary or rechargeable unit. Readers shall refer to Section **2.1.3** for further details on definitions

As shown schematically in **Fig. 2.2** (not scaled), the basic elements of a LIB are the anode or negative electrode (NE)[2], the cathode or the positive electrode (PE), the electrolyte, a separator and the current collectors. Each electrode is a composite made from particles (grey and blue balls, ~80% by mass) with which Li^+ ions react and into which the lithium inserts. On a typical commercial LIB, both the anode and cathode materials are layered (or tunneled) compounds. As a result Li atoms can reside between the layers (see **Fig. 2.2**, graphite layered structure) and can be easily intercalated or deintercalated from the electrodes. The electrolyte is a chemical solution that provides a medium of ion transport between the electrodes, but is electronically nonconductive. Physically, the NE and PE are electronically isolated to prevent short circuit. This function is mechanically attained by the separator, which is permeable to the electrolyte to maintain ionic conductivity. The current collectors (i.e. aluminum and copper foil) are metals that receive the electrons from the external circuit to allow oxidation-reduction on the electrodes. The electrodes of modern LIBs consist of porous composites, which provide high particle/electrolyte contact area. To hold the active material particles together and in contact with the current collectors, binders are used, typically 10% by weight. Similarly, to enhance the conductivity of the PE materials, electronic conductive filler additives are used, typically by 5-10% wt (see **Fig. 2.2**, black and blue squiggles) [5].

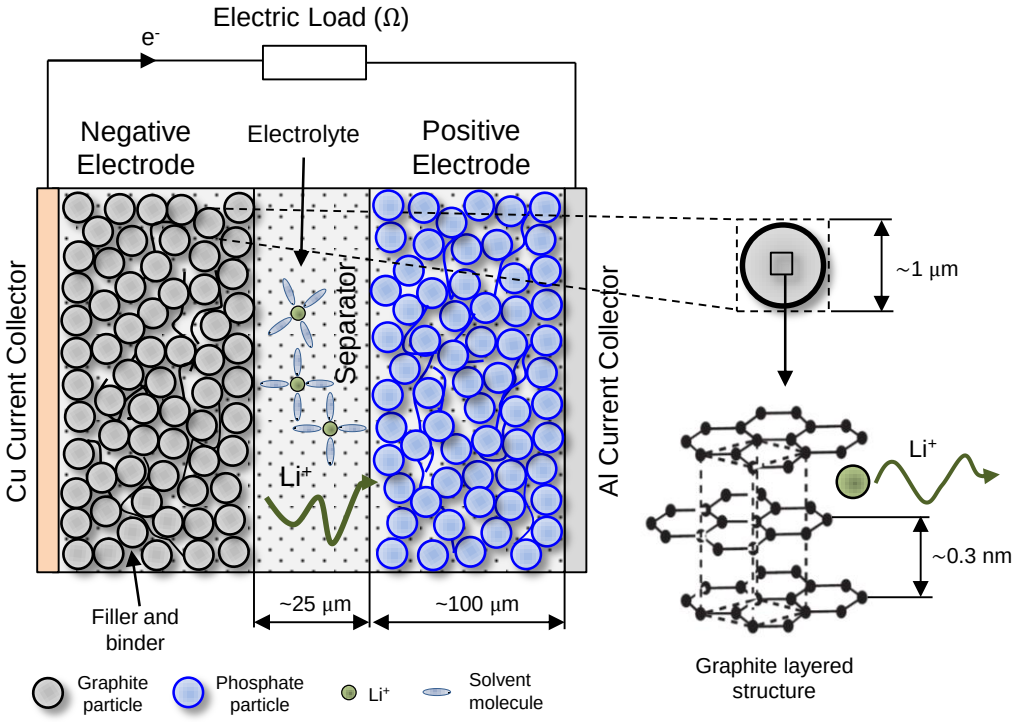

Fig. 2.2. Schematic representation of a typical LIB being discharged, showing the different components in different microscopic scales.

The operation of a cell during discharge is shown in **Fig. 2.2**. During discharge, electrons flow through the external load from the anode, which is oxidized, to the cathode, where the electrons are accepted and the cathode material is reduced. Li^+ ions are moved through the electrolyte from the anode to the cathode. During charge, a reversible process occurs. The electrochemical reactions that occur on both electrodes during discharge, particularized for a graphite anode material and a lithium iron phosphate ($LiFePO_4$) cathode material in stoiquiometric or balanced proportion can be written as follows:

[2] By definition, anode is the electrodes where oxidation takes place. However, during discharge the negative electrode (NE) of the cell is the anode, and during charge the positive electrode (PE) of the cell is the anode. To avoid confusion, the discharge process is used as the reference to name the electrodes: the anode NE and cathode as PE. The positive or negative polarity of each electrode is physically maintained for both charge and discharge.

Negative electrode: anodic reaction

$$LiC_6 \longrightarrow Li_{1-\xi}C_6 + \xi Li^+ + \xi e^-$$

Positive electrode: cathodic reaction

$$FePO_4 + \xi Li^+ + \xi e^- \longrightarrow Li_\xi FePO_4$$

Overall reaction (discharge)

$$LiC_6 + FePO_4 \rightarrow Li_{1-\xi}C_6 + Li_\xi FePO_4$$

These reactions result in a theoretical voltage, capacity and energy that determine the basic functioning of the battery. The next subsections cover the nature of these phenomena.

2.1.2. Electrochemical background

The theoretical maximum voltage and capacity (Coulombic) on a LIB are a direct function of the active materials. Both parameters can be derived theoretically or experimentally at equilibrium conditions, and are described by thermodynamic principles. However, the equilibrium conditions are not maintained during the operation of a LIB; as soon as current flows through the electrodes, electrochemical reactions take place inside the cell, which are influenced by the kinetic parameters. Hence, it is necessary to consider both thermodynamics and kinetics to understand the practical characteristics of a LIB.

Thermodynamic principles

Thermodynamics apply under equilibrium conditions, i.e. when no reactions occur within the LIB. Under these conditions, the maximum electric energy that can be delivered by the materials contained in the LIB depends on the change in Gibbs energy ΔG of the electrochemical couple:

$$-W_{max} = \Delta G = -nFE \tag{2.1}$$

where $-W_{max}$ represents the maximum electric energy delivered by the chemicals, ΔG is the change of free energy per mol when the reaction progresses, n is the number of electrons transferred during the reaction, F is the Faraday constant (96,487 coulombs mol^{-1}) and $E_{Cell} = \Phi_{PE} - \Phi_{NE} > 0$ is the potential difference between the battery terminal or just the cell voltage. The cell voltage is also defined by the electrode potential difference ($E_{Cell} = E_{PE} - E_{NE}$), expressed relative to a reference electrode (Lithium metal in LIB). Therefore, maximizing the *electrode potential* difference of the electrodes results in a high voltage cell, this increases the energy delivered by the LIB system.

The thermodynamic parameters describe the fundamental values of the theoretical maximum voltages and capacities of practical battery materials. An example of the electrode potentials (measured vs. Li/Li^+) for the most commonly used electrode materials on LIBs is shown in **Fig. 2.3**. Interested readers may refer to [4], appendix B and C for a complete list of electrochemical equivalents of battery materials. Materials such as Li_xCO_2 or Li_xFPO_4 exhibit a high voltage relative to lithium metal, making them ideal as positive electrodes. On the other hand, graphite and Li metal have low voltages, making them suitable for negative electrodes.

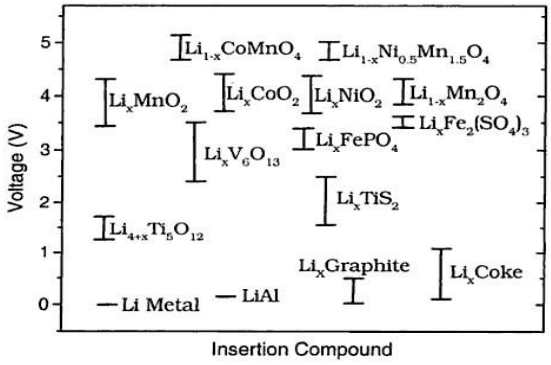

Fig. 2.3. Standard reduction potential at 25°C of common LIB electrode materials [6].

Thermodynamic properties of commercial LIBs are of crucial importance to study several internal parameters of a battery, including aging mechanisms. From a practical perspective, we can measure the voltage of a LIB under pseudo-thermodynamic conditions by allowing the battery to rest at open circuit (i.e. no load connected to the terminals) for at least 2 h. This margin of time is considered sufficient to balance the reactions and achieve equilibrium conditions [7], [8]. The voltage measured at open circuit (E_{0CV}) represents the approximation of the theoretical potential of the electrodes at a particular capacity of the battery (E_{Cell}= E_{0CV}). Similarly, to measure the thermodynamic voltage of a LIB as a continuous function of the capacity, one can perform a very slow full charge/discharge test, at least within 25 hours. This low current cycling scheme reduces the kinetic effects [7], [8].

Hence, in this thesis we assume thermodynamic conditions on a LIB (at room temperature 23°C) when:

- The battery has been resting at open circuit for at least 2 h
- A very slow full charge/discharge cycle of at least 25 h of duration is carried out

Electrode kinetics

Electrode kinetics apply under non equilibrium conditions, i.e., reactions occur within the LIB. From a practical perspective, kinetic reactions occur when a load current passes through the electrodes. To achieve this current flow, additional energy is required. The additional energy is consumed by the kinetic effects, which is given off as waste heat. Hence, not all the theoretically available energy within a battery – defined by thermodynamics –, is fully converted into useful electrical energy. As a result, the theoretical battery voltage (E_{Cell}= E_{0CV}) when current flow is reduced during discharge or increased during charge.

The energy losses occur due to the polarization effects caused when current flows within a battery. The polarization losses include [4], [9], [10]:

(1) ohmic polarization (η_{ohmic}), resulting both from electronic and ionic resistance of the battery, such as electrolyte conductivity, the electrical connections (terminals, current collectors, weld joints and contacts in electrodes) and the separators and contact resistances.
(2) charge transfer or activation polarization ($\eta_{Ch.Tr}$), which is the energy associated with chemical reactions that takes place during the electrode reactions
(3) diffusion polarization (η_{diff}), due to mass transport limitations in the electrolyte and electrode materials

The expression that relates the actual cell voltage (V_{Cell}) under kinetics with the polarization losses and the theoretical battery voltage, particularized for discharge is expressed as:

$$V_{\text{Cell}} = E_{\text{OCV}} - \eta_{\text{ohmic}} - \eta_{\text{Ch.Tr}} - \eta_{\text{diff}} \tag{2.2}$$

Notice that Eq. (2.2) contains both thermodynamic (E_{OCV}) and kinetic effects (polarization). Since the sources of polarization are current dependent, Eq. (2.2) can be rewritten from an electrical engineering perspective as:

$$V_{\text{Cell}} = E_{\text{OCV}} - IR_{\text{Cell}} \tag{2.3}$$

where R_{Cell} is the internal resistance (in Ohms) of the battery including all the sources of polarization, and I is the electric current (in ampere) that flows through the battery. At high currents, the polarization effects become predominant; hence the cell voltage (V_{Cell}) is reduced. Vice versa, very low currents reduce the kinetic effects. As a result, the cell voltage gets closer to its theoretical thermodynamic value.

Kinetic effects are also related with the time domain of a LIB system, since current flows through the battery for a certain period of time. This is observed in **Fig. 2.4**, where the electrochemical details of the polarization sources are shown as a function of time, on the battery voltage waveform after applying discharge current pulse. In terms of time scale, as the current is injected, the ohmic effects occurs within microseconds range, followed by charge transfer effects which occur in the ms range, and by the diffusional polarization effects for multiples of seconds [11].

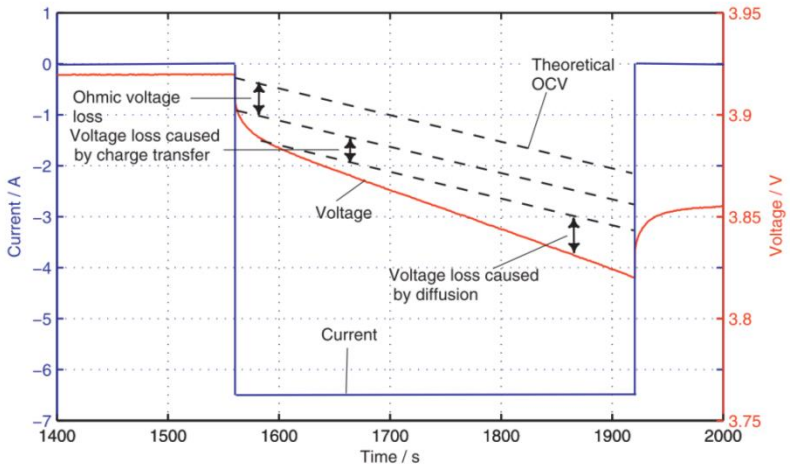

Fig. 2.4. Voltage response of a LIB after a current pulse, identifying the polarization effects [12].

In principle, the polarization effects can be calculated from theoretical equations [13]. However, due to the complex structure of the electrodes and electrolytes in commercial LIBs, the calculation through analytical methods is problematic. To decipher the polarization sources, a practical solution includes experimental measurements of the voltage evolution after a current pulse. As carried out by Ratnakumar *et al.* [9], taking into consideration the battery dynamics coupled with less complicated approximations of the electrode reaction equations, the polarization sources can be measured. Similarly, from electrochemical impedance spectroscopy measurements one can obtain the equivalent electric circuits of a battery, such as the Randles model [14]. The model can represent the electrode processes behavior, and can be used to obtain the polarization components of a battery [12], [15].

2.1.3. Definitions and figures of merit

As the electrochemical background has been established, we shall consider here including a summary of the main definitions and figure of merit that are directly related to LIBs. This ensures that

the following chapters of the thesis are consistent and well defined. For a complete list of definitions, readers may refer to [4], [16].

- **Cell, battery**: a cell is the basic electrochemical unit providing a source of electrical energy by direct conversion of chemical energy. A battery consists of one or more assembled electrochemical cells electrically connected. In this thesis, the term "cell" will be generally used when describing the cell component of the battery and its chemistry. The term "battery" will be generally used when presenting general performance characteristics, etc. of the commercial product. Popular usage considers the "battery" and not the "cell" to be the product that is sold or provided to the user.
- **Thermodynamics:** cell characteristics under equilibrium conditions, i.e. when no reactions occur within the cell
- **Kinetics:** cell characteristics under non-equilibrium conditions, i.e. current flows through the cell
- **Cell voltage (V_{cell}):** the measured voltage across the cell terminals. This voltage results from voltage difference of the cell electrodes and is dependent on the thermodynamic and kinetic conditions
- **Open circuit voltage (OCV) [*%*]:** the difference in voltage between the terminals of a cell when the circuit is open (no-load condition)
- **End of charge voltage (EOCV), [*V*]:** the prescribed voltage at which the charge of a cell or battery may be considered complete (also cutoff voltage)
- **End of discharge voltage (EODV), [*V*]:** as described above, on discharge
- **Capacity [*Ah*]:** the total number of Ampere-hours (Ah) that can be withdrawn from a fully charged cell or battery under specified conditions of discharge
- **Maximum cell capacity [*Ah*]:** the maximum capacity of a cell or battery, which is determined by cycling the cell between EOCV and EODV using a very slow C-rate (i.e. at least C/25) to minimize any polarization loss
- **Rated capacity:** the number of ampere-hours a battery can deliver under specific conditions (rate of discharge, end voltage, temperature); usually the manufacturer's rating
- **C-rate (C):** in describing cells or batteries, charge/discharge currents are often expressed as a C-rate, in order to normalize against battery capacity. A C-rate is the battery charge/discharge current, in Amperes, expressed as a multiple of the rated capacity in ampere-hours. For example, the 0.5C or C/2 discharge current for a battery rated at 10 Ah is 5 A. Conversely, a battery rated at 2 Ah is discharged at a current of 500 mA the discharge rate is 0.25C or C/4
- **Energy density [Wh/L]:** the ratio of the energy available from a battery to its volume
- **Specific energy [Wh/kg]:** the ratio of the energy output of a battery to its weight
- **Power density [W/L]:** the ratio of the power available from a battery to its volume
- **Specific power [W/kg]:** the ratio of the power delivered by a battery to its weight
- **State of charge (SOC) [*%*]:** the available capacity in a battery or cell expressed as a percentage of its maximum cell capacity
- **Cycle life:** the number of cycles under specified conditions which are available from a battery before it fails to meet specified criteria as to performance
- **End-of-life:** the stage at which the battery meets specific failure criteria (e.g., capacity and/or power degradation)
- **Battery Internal Resistance [*Ω*]:** the opposition or resistance to the flow of an electric current through a battery. It comprises the ohmic, charge transfer and diffusional polarization effects
- **Energy throughput [Wh]:** cumulative, net energy output provided by a battery over its service life. It is the sum of all energy delivered over all the discharges that the battery has provided

2.2. Li-ion battery materials

Since the commercialization of LIBs in 1991, a broad array of new chemistry materials and synthesize approaches have been developed. The purposes of these innovations are generally focused towards increasing the energy and power density, cycle life, safety, temperature operational range and reduce the final costs [2], [17]. Although worldwide research and development efforts are offering new exciting advances on LIBs [18], [19], today, many of these advances are only demonstrated under laboratory scale. Hence, due to the practical objectives of this thesis, this section provides a description of the LIB materials that are currently found on commercial LIBs. Still, when appropriate we shall provide comments on new battery trends and progresses in the field.

2.2.1. Anode

In a practical LIB, the ideal anode electrode should have high efficiency as a reducing agent, high coulombic output (Ah/g), good conductivity, stability, ease of fabrication and low cost [4], [5]. Since lithium is the most electropositive element, reacts with the majority of materials and holds one of the highest specific capacities among anode materials (3860 mAh/g), the first anode electrodes for LIBs were based on lithium. However, this type of battery did not commercially succeed because it was unsafe, as lithium dendrite growth eventually short circuited the NE and the PE, which led to explosion hazards. The first commercialized LIB utilized intercalation/deintercalation materials, such as petroleum coke as the NE. Coke offers a low potential profile and has good stability and a specific capacity of 180 mAh/g. Improvements led to the use of graphite (372 mA/g), which nowadays is the NE material of choice of practically every commercial LIB. Due to its importance, graphite is described in the next subsection.

Nowadays, efforts are carried out to substitute graphite NE to materials with higher capacity, energy, power density and lower cost. Lithium titanate (LTO) is an alternative that is already being commercialized [20], being its main advantage the extremely long cycle life, high power capability and excellent safety properties. This is because of its high potential of 1.55 V versus Li, which reduces the reactivity of LTO with electrolyte. However, because its high potential, full cells based on LTO anodes have low voltages (2.8 V) which lead to low specific energies (70 Wh/kg).

In terms of next generation NE materials, insertion materials such as graphene (960 mAh/g) are being studied [21]. However, its complex fabrication and high theoretical surface area (2630 m^2/g) are the main impediments for its commercialization on LIBs. Similarly, alloy/de-alloy materials such as Silicon (4212 mAh/g), Germanium (1624 mAh/g) among others [19], are being studied due to their attractive specific capacities, energy densities and safety. However, the major burden of allow/de-allow materials is the huge capacity fade per cycle caused by the high volume expansions of over 400% [19]. Conversion materials such as metal oxides exhibit similar advantages and problems. However, improvements in nanotechnology are a formidable approach to solve the fore mentioned issues on new NE materials. A summary of commercial and next generation anode materials is shown in **Fig. 2.5**. An excellent review by Goriparti *et al.* [19] discusses the state of the art of anode materials for next generation LIBs.

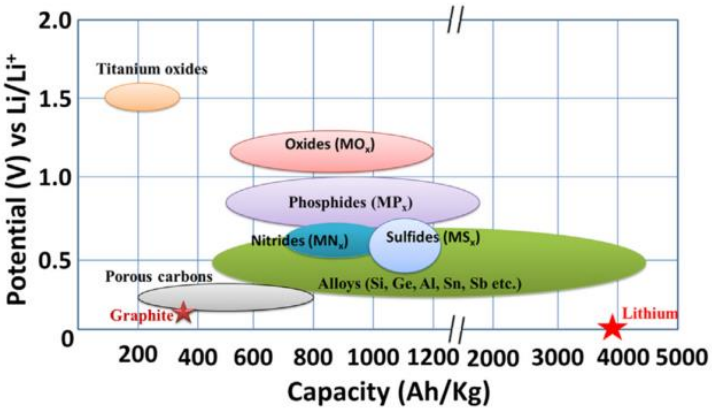

Fig. 2.5. Schematic illustration of active anode materials for commercial and next generation LIBs [19].

Graphite and its intercalation compounds

Graphite and its intercalation compounds (GIC) is the most used anode material in commercial LIBs. The main advantages are a relatively flat and low working potential vs. lithium, low cost, good cycle life and a relatively high specific capacity (372 mAh/g). Due to its advantages, and because of the fact that carbon is the most versatile element on the periodic table [22], many types of carbon materials are commercially available. The performance of these materials varies depending on the morphology, electrochemical properties, precursor phase and temperature treatments [22], [23].

To describe the intercalation/deintercalation phenomena on GIC, here the graphite is presented as pure crystalline. As shown in **Fig. 2.6**a-b, crystalline graphite has hexagonal crystal structure and is formed by graphene layers stacked in a registered fashion. **Fig. 2.6**b shows schematically the intercalation/deintercalation process, in which Li ions can be inserted between the layers of graphite. This process is highly reversible and produces a relatively low volume expansion of about 9%–10%, mostly observed during the first 20% of lithium insertion [24].

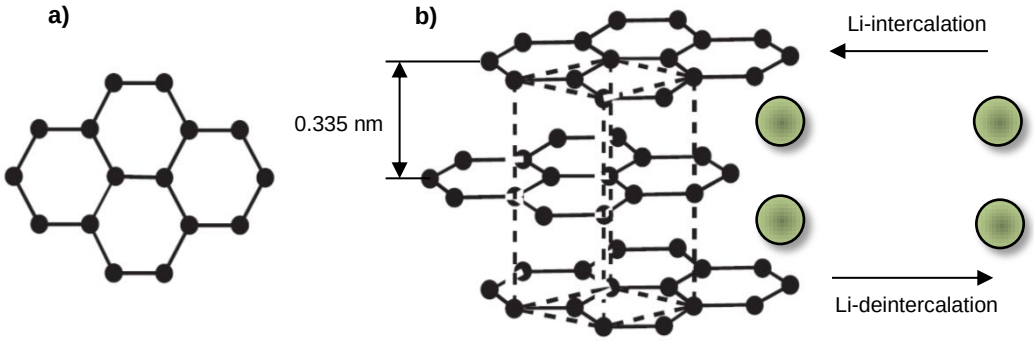

Fig. 2.6. a) The hexagonal structure of a carbon layer; b) structures of hexagonal graphite schematically showing the intercalation and deintercalation of Li ions between the graphite layers (adapted from [4]).

A significant feature of the GIC is the staging phenomena, characterized by a periodic sequence of Li intercalation/deintercalation between layers in a determined fashion. This is schematically described in **Table 2-1**, adapted from Groot [25], based on the classical model defined by J.R. Dahn [26].

Table 2-1. Graphite intercalation phenomena [25], [26].

x in Li_xC_6 (0<x<1)	**Graphite stage**	**Identification number**	**Voltage Characteristic (under slow delithiation ≤C/25)**
0 – 0.04	Stage – 1 (dilute)	❺	Curved
0.04 – 0.12	Stage – 1 (dilute) & Stage 4	❹	Curved
0.12 – 0.20	Stage – 4 & Stage 3	❸	Plateau 210 mV
0.20 – 0.25	Stage – 3 & Stage – 2 (liquid)	❷	Plateau 120 mV
0.25 – 0.50	Stage – 2 (liquid) and Stage – 2	❷	Plateau 120 mV
0.5 – 1	Stage – 2 and Stage – 1	❶	Plateau 85 mV
1	Stage – 1	-	Curved

The staging phenomena of the GIC cycled under thermodynamic condition (i.e. C/25) are shown in **Fig. 2.7**. The different staging compounds on the GIC are labeled with ❶ to ❺ to facilitate the analysis. When GIC is completely empty (C) and no Li ion is positioned between the graphene layers, the GIC is at its higher voltage potential. When Li ions are subsequently intercalated between the GIC layers, a series of reactions and distinct stages (phases) are formed. This Li intercalation process causes voltage plateaus and curves on the GIC, which are associated with two–phase coexistence and solid solutions, respectively. The final state corresponds to the fully lithiated graphite of one Li per six carbons, or LiC_6. The deintercalation process follows the same (inverse) graphite phase sequence with a small hysteresis caused by the natural behavior of GIC.

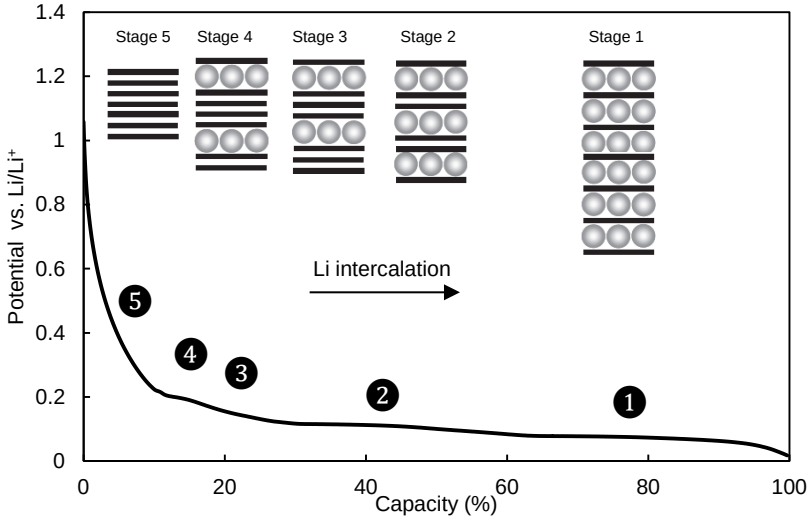

Fig. 2.7. Li intercalation/deintercalation process of a GIC cycled at C/25. The numbers (❶–❺) identify the different staging stages. The corresponding graphite stage are schematically represented on top.

We shall point out that current GIC materials used in LIBs may contain structural disorder as well as random stacking and may slightly differ from the crystalline model presented here. Indeed, the staging phenomenon and phase coexistence is rather complex and not yet fully understood in detail [27]–[29]. However, for the purpose of this thesis, and in agreement with the LIB related works [30]–[32], this model has been validated and is therefore adequate.

To sum up, due to its advantages, the anode material of choice for the large majority of commercial LIBs is GIC. A significant feature is the periodic sequence of Li intercalation/deintercalation processes, which results in voltage plateaus. Similarly, numbering the five GIC staging compounds (❶ - ❺) allow an easy interpretation of the staging phenomena. The staging numbering is extensively used throughout this thesis, particularly as "sensors" to facilitate the identification of the degradation mechanism and other characteristics that affect the NE on a LIB.

2.2.2. Cathode

The optimal characteristics of a cathode on a LIB system include high efficiency as an oxidizing agent, stability (safety), high working voltage, among others. A summary of requirements for cathodes are given in **Table 2-2.** These characteristics are often met by oxides of transition metals, such as lithium oxide cobalt ($LiCoO_2$ or LCO), lithium manganese oxides ($LiMn_2O_4$ or LMO) or lithium iron phosphate ($LiFePO_4$ or LFP), to name a few examples.

Table 2-2. Summary of requirements for LIB cathode materials [4].

Requirements for LIB cathode materials
High free energy of reaction with lithium
Can incorporate large quantities of lithium
Reversibly incorporates lithium without structural change
High lithium ion diffusivity
Good electronic conductivity
Insoluble in the electrolyte
Prepared from inexpensive reagents
Low cost synthesis

Lithium oxide cobalt (LCO) has been the material of choice for the majority of LIBs, especially for consumer electronics applications [2], [4] due to its high voltage (4.0 V vs. Li/Li^+) capacity (151 mAh/g) and energy density (602 Wh/kg) [33]. However, LCO has relative low cycle life due to side reactions with the electrolyte [34]. Most importantly, LCO has safety concerns due to instability when overcharged, which produces a highly exothermic reaction [35]. Eventually, this process may lead to thermal runaway and potential fire hazard [36], [37]. Still, LCO is today the cathode of choice used in consumer electronics, with productions of +3000 million units per year [2].

Despite the advantages of LCO, several alternatives are being developed to substitute LCO for less expensive, safer and higher potential cathodes. These materials are classified based on their chemical structure, i.e. layered lithium transition metal oxides, lithium manganese oxides spinels and lithium transition-metal phosphates. As with anode materials, every cathode has many variations and configurations, optimized for several applications [33], [38]. Here is covered the fundamental specifications of commercially available cathodes.

In the last decade, high performance layered transition systems such as nickel cobalt manganese (NMC = $LiNi_{0.5}Mn_{0.3}Co_{0.2}O_2$-$LiNi_{1/3}Mn_{1/3}Co_{1/3}O_2$, etc.) have been studied. Substituting Cobalt for lower cost materials (i.e., Mn/Ni) provides a cheaper electrode. Similarly, NMC has specific capacities of ~220 mAh/g and a voltage of 4.0 V [33]. In addition Mn/Ni adds stability to the system, therefore safer LIBs. Similarly, adding Al (NCA = $LiNiCoAlO_2$, etc.) also shows high capacity and potential (~200 mAh/g, 3.80 V) and improved stability [33], [39]. These materials (i.e. NMC, NCA) are already commercially available in LIBs, and in constant research to increase their power performance and cycle life.

Lithium manganese oxides (LMO = $LiMn_2O_4$-$LiNi_{0.5}Mn_{1.5}0_4$, etc.) are of considerable interest because of their high capacity and voltage (280 mA/g, 4 V) [33], low cost, abundant supply, environmental friendliness, good safety characteristics and high power capability [40]. A disadvantage is the severe capacity fade at elevated temperatures, caused by corrosion of the manganese oxides with the electrolyte.

Another promising cathode materials are phosphates (LFP = $LiFePO_4$-$LiMnFePO_4$-$LiNiPO_4$). The main advantage of these materials is their inherent safety properties and the constant voltage profile, caused by the two-phase coexistence of the material (FP-LFP) [41]. This material was initially not suited for high-rate applications due to its low electronic conductivity and poor lithium diffusion. However, approaches such as the use of nano-structured materials have been used to overcome these issues [42]. Similarly, to improve the actual energy density and voltage (170 mAh/g, 3.43 V) of LFP materials, transition metals such as Mn, Co and Ni are being used [33] (see **Fig. 2.8**).

To sum up, nowadays several commercially available transition metal based cathode materials can provide good performance characteristics for LIBs. Although LCO continues to be the material of choice for the majority of commercial LIBs (especially for consumer electronics), other promising materials are also commercialized. Among them, LFP is a promising cathode material, due to its advantages. **Fig. 2.8** compares the voltage vs. capacity curves of commonly used cathode materials in commercial LIB systems. Further readings on recent developments on cathode materials can be found elsewhere [33], [38], [40].

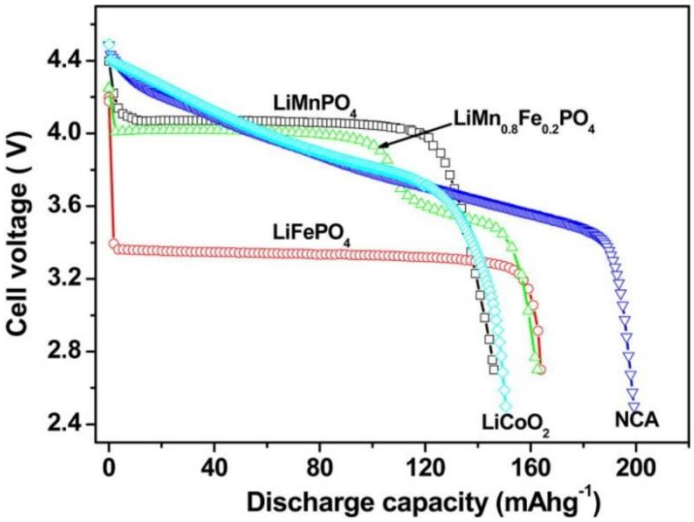

Fig. 2.8. Voltage vs. discharged capacity of commonly used cathode materials in commercial LIB systems [43].

2.2.3. Electrolyte

The role of the electrolyte is to act as an ionic conductor to transport ions back and forth between the electrodes as the cells are charged and discharged, without allowing the flow of electrons through the electrodes. Similarly, the aim of the electrolyte is also to improve the performance of LIBs. Main properties of electrolytes include high ionic conductivity, electronic isolating, non-reactivity with the electrodes (i.e. large stability voltage window), temperature stability, safety and low cost [4]. A good electrolyte must be absorbed in the electrode and separator materials to provide a complete path of ions to the electrodes where the reactions take place.

Same as with electrode materials, many types of electrolytes with various chemical species are used in commercial LIBs. Most of the electrolytes are liquid, based on nonaqueous solutions. The solution is mainly formed by 1 mol dm^{-3} of lithium hexafluorophosphate ($LiPF_6$) salt dissolved in the mixture of carbonate solvents selected from cyclic carbonates – ethylene carbonate (EC), and propylene carbonate

(PC) –, and linear carbonates, such as dimethyl carbonate (DMC), ethyl methyl carbonate (EMC), and diethyl carbonate (DEC) [1]. This electrolyte ($LiPF_6$) offers high ionic conductivity (10^{-2} S/cm), high lithium-ion transference number (~0.35), and provides acceptable safety properties [4]. Similarly, gel electrolytes (often termed as gel-polymer or simply polymer electrolytes) are employed in commercial LIBs. However, this type of electrolyte usually has low ionic conductivity at room temperature, and its application is generally limited to high-energy lithium batteries [40].

The electrolyte is a key component regarding battery safety and degradation phenomena. Electrolyte participates in all reactions within the cell and may cause unwanted side reactions. High temperatures, short circuits, overcharging, physical damage or stressful cycling conditions are actors that may lead to self-accelerating reactions, as well as fire and explosion. To overcome these issues, additives are used in the electrolyte.

Additives

The role of additives is to enhance the performance of a LIB. Adding organic molecules, salts, inorganic compounds, or gases to the electrolyte can significantly improve safety characteristics, reduce internal resistance, reduce reactions with electrolyte, or dramatically increase cycle life [44]–[46]. Usually, additives are present at less than about 10% by weight in the electrolyte [4]. Similarly, additives are combined to enhance LIB properties. A commercial LIB may contain from 1 to 5 additives. Studies shown that adding four additives on the electrolyte can increase ten times the battery lifetime when compared to the same battery with no additives [47]. Since additives can increase LIB performance, its composition and combination is highly secret. Still, common additives such as vinylene carbonate (VC), vinyl ethylene carbonate (VEC) or propylene carbonate (PC) can be found on different studies [4], [47], [48]. To sum up, additives play a major role in LIB performance and safety improvements, although little information is known on additive formulations on commercial LIBs [4].

2.2.4. Solid Electrolyte Interface (SEI) film formation

The solid electrolyte interface (SEI) is one of the most important phenomena that occur within a LIB. The SEI is a film that is naturally formed when the graphite becomes intercalated with lithium and is exposed to the electrolyte. This process occurs mainly (but not exclusively) at the beginning of cycling, especially during the first cycle [36], [48]–[50]. The reason is because graphite operates at voltages that are outside the electrochemical stability of the electrolyte. No electrolyte has been found that withstands the low electrochemical potential of highly lithiated carbons [22], therefore the anode reacts with the electrolyte solution. This reaction causes electrolyte decomposition, accompanied with lithium ion consumption. The reaction products and species formed, quickly precipitate and grow on the anode surface, resulting in the SEI layer. Hence, the formation of the SEI causes irreversible capacity loss due to the reactions on the electrode-electrolyte interface, which directly reduce the available energy of the LIBs [36], [48]–[50].

Even if the SEI is directly linked with LIB degradation, paradoxically, the SEI also acts as a protective element. When the SEI is formed, a thin passive layer (usually from 1 to 10 nm) [51], [52] is deposited over the graphite surface and prevents further reactions to occur. If fewer reactions occur, less lithium ion from the LIB is consumed in subsequent SEI formation. This is because the properties of the reaction products deposited on the graphite. Although the actual morphology of the SEI is very complex and varies with electrolyte (and additives) composition, it is best described as a thin heterogeneous film of organic and inorganic components [50], [53].

The schematic sketch of a lithiated graphite composite electrode, surface-covered by the SEI is shown in **Fig. 2.9**. The SEI components shown in darker shades of grey are mainly inorganic, while those shown in lighter shades of grey are organic [50]. These components that form the SEI are permeable for lithium cations but rather impermeable for other electrolyte components and electrons [36], [48], [49]. Thus, an

effective SEI protects the electrolyte compounds from further reactions and the charged electrode from corrosion [36].

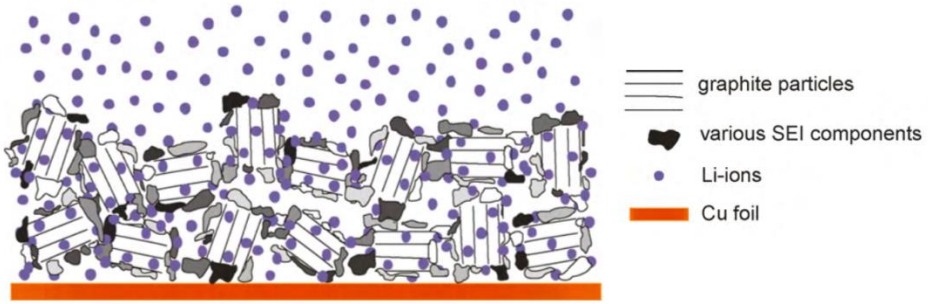

Fig. 2.9. Schematic representation of the of a lithiated graphite surface-covered by inhomogeneous SEI [50].

The SEI formation and its properties play a significant role in performance of LIBs. A poorly formed SEI would consume large quantities of lithium, as further reactions in the electrode-electrolyte interface would keep occurring. This causes further irreversible lithium consumption and SEI growth, which reduces the LIB capacity. Similarly, thickness of the SEI reduces ionic mobility and increases polarization effects, therefore reducing the performance of LIBs.

To improve the formation and SEI structure, battery manufacturers use additives that modify the properties of the electrolyte and change the surface properties on the carbonaceous anode [46], [48]. The use of additives inhibits further solvent decomposition. As a result, both capacity fade and impedance growth of the LIB can be reduced. The impact of using different additives on SEI stability and growth can be found elsewhere [4], [38], [40], [47], [48]. Vinylen carbonate (VC) is confirmed as outstanding additive in this respect [24]. The first cycling conditions also play a significant role in the SEI formation. Indeed, commercial LIBs are sold with the SEI layer formed in factory. To form the SEI, battery manufacturers typically perform the first cycles at low discharging rates, floating regimes and sometimes elevated temperatures. This formation step can take several weeks to complete, consuming both time and resources [4], [54]. Therefore, an effective and robust SEI layer formation is fundamental to enhance the performance of LIBs.

A technique to study the effects of the SEI formation process consist in cycling graphite versus lithium (i.e. GIC vs. Li/Li^+). For this particular case (contrary to full LIB configurations) the graphite acts as the PE (has higher electrode potential), whereas the lithium acts as the NE and reference electrode at 0 V. **Fig. 2.10** schematically shows this cell configuration. The black curve represents the first lithiation of the graphite, the solid red curve represents the first delithiation, whereas dotted red curves represent subsequent delithiation cycles by 20 cycle-steps. As previously described, when the graphite is first lithiated, reactions occur in the electrode-electrolyte interface and the SEI is formed. This causes an irreversible capacity loss Q_{irr}, which is the difference of the first lithiation and delithiation of the graphite (black and red solid lines respectively). A robust formed SEI layer prevents further reactions and less capacity losses. This is shown by the dotted lines, where even if many lithiation/delithiation processes take place, only a small fraction of capacity is lost. Usually, the first irreversible capacity (Q_{irr}) in well-designed commercial LIB is within 10-15% of the total graphite capacity [22], [30], [55], although this data cannot be directly measured in commercial LIB systems. Similarly, the irreversible capacity loss derived from subsequent cycling cannot be generalized, as it is dependent on electrolyte materials and cycling conditions.

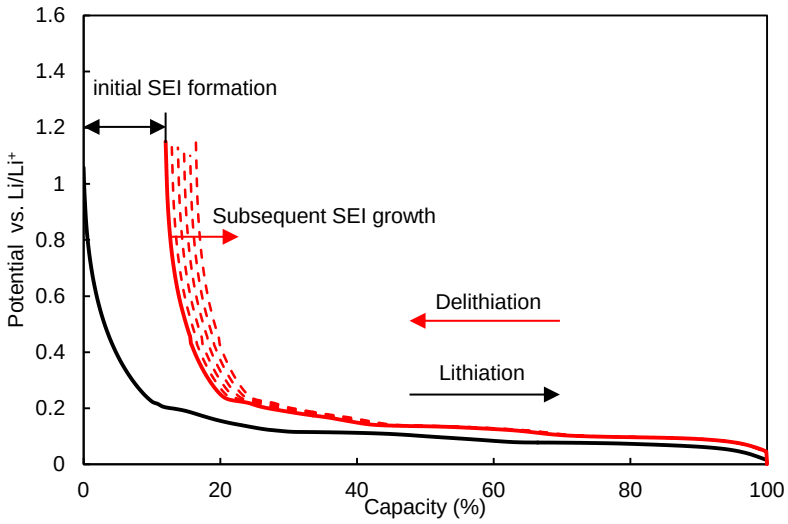

Fig. 2.10. Schematic representation of the SEI formation during the first lithiation (black) and delithiation (red) at C/25 of a GIC vs. Li/Li^+ half-cell. Subsequent delithiation cycles are represented by dotted lines in red.

To summarize, the solid electrolyte interphase (SEI) is a protecting layer formed in the electrode-electrolyte interface of LIBs as a result of electrolyte decomposition. This process occurs mainly during the first cycle. The initial formation of the SEI causes capacity loss in a LIB, usually estimated in 10-15%. Similarly, in subsequent cycling side reactions keep occurring in the NE interface, resulting in more SEI growth. This affects the battery performance, usually producing capacity loss and impedance growth. To minimize the negative effects of the SEI, an effective and robust SEI layer is a prerequisite for optimal performance of a LIB.

2.2.5. Cell constructive parameters

The cell constructive parameters are used to identify the main characteristics and behavior of a LIB. The parameter configuration is based on half-cell mechanistic models defined by Dubarry *et al.* [30], [31]. Furthermore, this type of representation and identification of cell constructive parameters facilitates further analysis on cell performance and aging evolution, and is extensively used in this thesis work.

Fig. 2.11 presents an example of the cell constructive parameters. The cell is formed by graphite and its intercalation compounds (GIC) as the NE (black line), vs. $LiFePO_4$ as the PE (blue line). This type of cell is abbreviated as GIC||LFP. Both the NE and PE have distinctive potential voltages and capacities, defined by the material properties and mass of active material. The capacities are represented in percentage (or capacity in Ah), as Q_{NE} and Q_{PE} respectively. The full-cell voltage signature (red line) is the subtraction of PE and NE, which represents the actual output characteristics of the GIC||LFP cell, with a total capacity Q_{FC}. The initial SEI formation here is adopted as the offset (OFS), and represents the total capacity loss caused from the first lithiation of the NE. Because of the uncertainty of the initial capacity loss at the NE, it is more convenient and reliable to use the SOC scale at the PE (SOC_{PE}) as the basis for the calculation of cell SOC [31]. Similarly, adopting capacity instead of SOC for the horizontal axis can be also convenient for more realistic comparisons. Either way, the PE is the reference electrode. Similarly, the staging phenomena on the NE are identified by the numbers (❶-❺).

The electrodes are linked by another cell constructive parameter, the loading ration (LR), defined as:

$$LR = \frac{Q_{NE}}{Q_{PE}} \tag{2.4}$$

where Q_{NE} and Q_{PE} are measured in percentage or capacity (Ah), and LR is therefore dimensionless. The LR is related to the optimization of the mass of active material in the two electrodes to achieve the maximum capacity (or energy) from the cell under conditions of steady cycling [49].

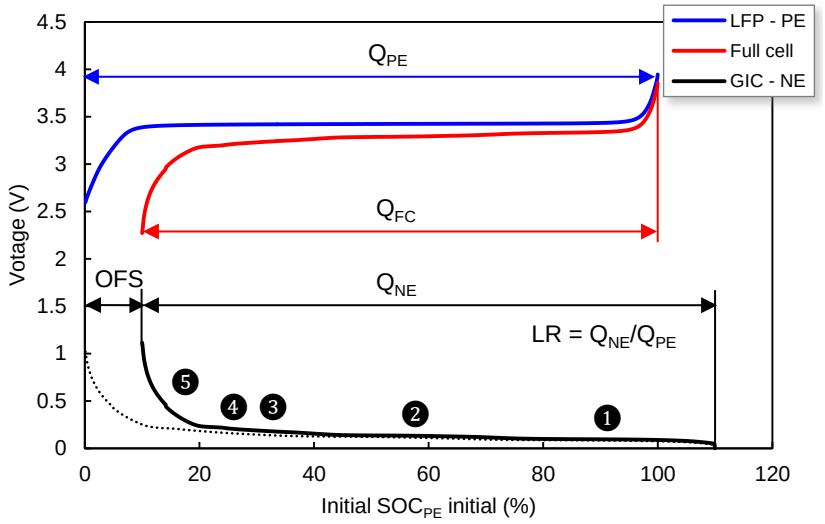

Fig. 2.11. Schematic representation of a GIC||LFP cell identifying the cell constructive parameters and GIC staging stages.

An example of cell constructive parameters is shown in **Fig. 2.11**: the OFS is 10%, whereas the mass of electrode capacities after the SEI formation is identical, hence LR = 1. Notice however that before SEI formation (see **Fig. 2.11**, thin dotted line) the initial loading ratio was $LR_{ini} = Q_{NEini}/Q_{PE} = 110/100 = 1.1$. The capacity ratio before SEI is established by the battery manufacturer's to be larger than one, to prevent the formation of lithium metal on the anode surface [56]–[58]. Because of the initial capacity loss due to SEI formation and the LR value, the full-cell capacity (Q_{FC}) is 90% when referred to the PE. Notice that the parameters can be converted in terms of capacity.

2.3. Aging mechanisms in Li-ion batteries

Currently, one of the most significant discussions in LIBs is the study of the aging mechanisms [7], [24], [30], [36], [49], [59]–[64]. The main reason is because some of today's LIB systems are complex, expensive and may require long service life. For instance, in EVs or PHEVs a lifetime up to 15 years or a cycle life of +1000 cycles are demanded [65]. Similarly, energy storage systems may require investments of millions of dollars, and lifetime expectancies of more than 15 years [66], [67]. Therefore, the identification and understanding of the aging mechanisms is of crucial importance, in order to provide safer and more effective functioning of LIB systems.

LIBs are complex systems, composed of several chemical materials where different reactions take place. Unfortunately, the processes of LIB aging are even more complicated. Still, the main ideas of LIB aging are simple enough: in an ideal cell, all of the lithium should be intercalated/deintercalated in a 100% efficient reversible process. However, this process is not ideal, since side reactions between electrodes and electrolyte occur. This side reactions cause LIBs to loss capacity and power through its use. As a result, the cell ages. Unfortunately, capacity loss and power fading do not originate from a single cause, as several processes may interact simultaneously. Moreover, these processes may be difficult to separate, which complicates the study of aging mechanisms.

This section aims to provide an analysis on aging mechanisms that occur in LIBs, based on the current understanding of this topic. The description of the aging modes is based on several methodologies and techniques carried out in the literature, which helped to identify morphological and structural

changes in the electrodes. Similarly, even though aging mechanisms are often interrelated, here are presented individually, exposing its causes, effects and influences. Each aging mechanism is described from a mechanistic perspective, based on the model described in [31]. The model graphically shows how the different aging modes affect individual electrodes and full-cell signature. The descriptions of aging mechanisms presented in this section set the basis for the aging analysis and identification, covered in subsequent chapters of this thesis.

2.3.1. Loss of lithium inventory (LLI)

The majority of the reports agree that the loss of lithium inventory (LLI) is the main cause of degradation in LIBs [7], [24], [36], [49], [59]–[63], [68]. The LLI causes the loss of usable Li ions due to parasitic reactions, leading to byproducts in the electrolyte solution and/or on the electrode surface [30]. This process causes capacity loss in LIB systems. However, LLI does not change the content of the active materials in the electrodes and their properties. To avoid confusion, notice that LLI is equally named in the literature as cyclable lithium loss or consumption of cyclable lithium. In addition, it is important to point out that the SEI formation results in a loss of cyclable lithium, due to the reactions on the electrode-electrolyte interface. In fact, LLI is mainly attributed to two phenomena: the principal cause is SEI formation, growth and destabilization [30], [31] and secondly, due to side reactions of the lithium ion with decomposed electrolyte compounds and water in the electrolyte [60]. Hence, previous concepts covered on SEI (see Section **2.2.4**) directly cause LLI.

The study of LLI is commonly particularized to the electrode/electrolyte interface, as is where the phenomenon takes place. The main changes and degradation occur in the negative electrode/electrolyte interface; few studies showed SEI creation on the positive electrode [69], [70]. The SEI on the PE is more difficult to detect due to the high voltage of the PE, is highly dependent on the material of choice and the degradation effects on the battery are usually much lower than that found on the NE. Hence, because GIC is the material of choice of the vast majority of commercial LIBs and is where LLI is more predominant, this section focuses on the LLI caused on graphitic materials.

The SEI layer plays a major role in the LLI. Even a strongly formed, protective SEI is not stable, and would eventually consume lithium inventory that irreversibly reduces the LIB capacity. This usually occurs due to (1) SEI formation, (2) SEI growth, (3) SEI dissolution and (4) lithium plating [24], [36], [71]. When the SEI is formed (1), a thin passive layer is deposited over the graphite surface. However, side reactions may occur that create charged species and impurities that react with the SEI. As a consequence, electrolyte decomposition, graphite exfoliation, gas formation and/or cracking of the graphene layers occur. These effects cause “gaps” in the SEI layer that expose pristine graphite which is subsequently covered with new SEI layer by consuming lithium inventory. SEI growth (2) naturally occurs within the electrolyte/electrode interface, due to side reactions. The new deposited species on the SEI are formed by reactions formulated by the consumption of lithium inventory. Hence, the protective layer grows with cycling. SEI dissolution (3) and destabilization may occur due to a small amount of impurities dissolved from the PE [72] and NE and their interaction may dissolve the SEI layer. Hence, further SEI reconstruction consumes lithium inventory. Lastly, lithium plating (4) is a major aging mechanism that also consumes lithium inventory. Due to the importance of this aging mode, its study is covered alone in Section **2.2.4**. Finally, the effects of LLI described in (1) – (4), may trigger other aging mechanisms which may interact and generate additional aging mechanisms [36]. **Fig. 2.12** shows a schematic summary of the main changes at the anode surface due to several parasitic reactions.

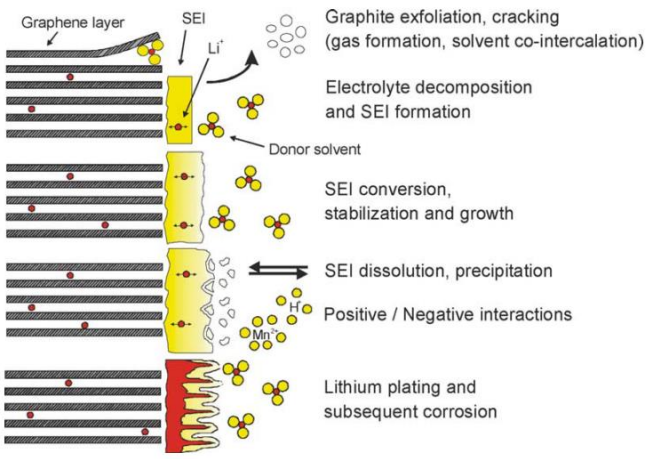

Fig. 2.12. Changes at the anode/electrolyte interface that lead to loss of lithium inventory (LLI) [36].

The effects of LLI on a LIB mainly affects to the loss of capacity, which leads to a loss of energy delivered by the cell. In addition, LLI caused by subsequent growth of the SEI may also increase the impedance of the cell. As a consequence, the power capabilities of the cell would be reduced. However, some LIB systems may not show impedance increase even if LLI takes place [59], [73]. SEI growth and subsequent LLI is highly dependent on temperatures. At high temperatures, the SEI either grows in thickness and/or becomes non-protective, which leads to performance degradation [48]. On the contrary, low temperatures result in different challenges which can cause rapid cell degradation. The main effects of low temperature operation are the risk of lithium plating and dendrite growth [36], [57], [74].

The LLI can be represented using the mechanistic model based on [31] and [55], as shown in **Fig. 2.13**, for a GIC||LFP cell. After initial SEI formation, subsequent cycling induces LLI. The effect of LLI results in an overall slippage of the NE over higher relatives SOC_{PE}, causing cell imbalance. As a consequence, the full-cell capacity (Q_{FC}) is reduced accordingly to the slippage effect of the NE, causing that less lithium on the PE is utilized on the full-cell. Contrary to the initial SEI formation where actual capacity on the NE is lost [22], on subsequent cycling LLI neither causes capacity reduction on the NE nor the PE, i.e. $Q_{NEinitial} = Q_{NEfinal}$ and $Q_{PEinitial} = Q_{PEfinal}$. That is, LLI does not cause degradation on the structure of either electrode materials [30], [31], [75]. Finally, in terms of cell constructive parameter, LLI increases the OFS values, although does not affect the loading ratio (LR).

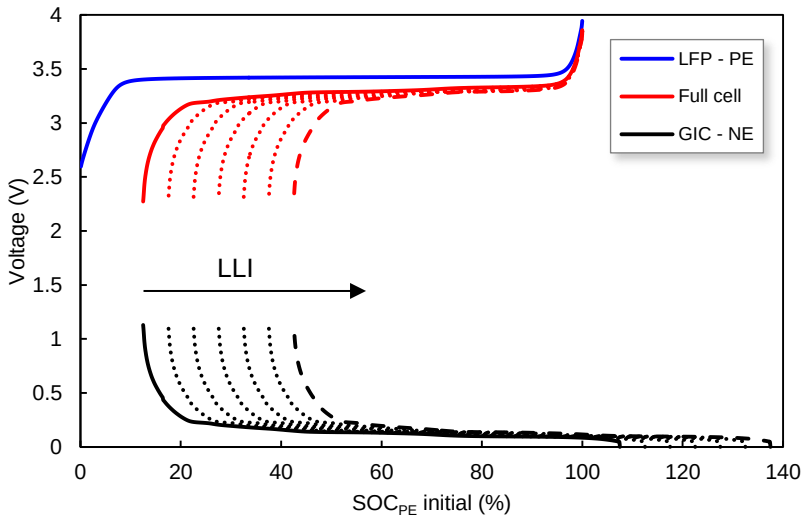

Fig. 2.13. Schematic representation of loss of lithium inventory (LLI) degradation mode in a GIC||LFP cell, cycled at C/25.

To summarize, LLI is one of the main degradation mechanisms that affect LIBs, causing loss of capacity, sometimes coupled with an increase of impedance. The stability of the SEI plays a major role in this degradation. Similarly, LLI as an aging mode does not cause direct degradation on the structure of the electrodes. However, the effects of LLI may trigger other aging mechanisms, as aging modes often interact and generate different aging effects. Another common aging mode which is commonly shown as LIBs age is the loss of active material (LAM).

2.3.2. Loss of active material (LAM)

The loss of active material (LAM) is a degradation mechanism that can cause capacity loss and power fade on a LIB. The LAM directly affects the structure of the electrodes, reducing the volume of active material that can be used in a LIB. Although LAM can affect both electrodes, the aging effects are more prominent in graphite based NEs than in PEs [30], [36], [56], [61], [68], [76]–[78]. Due to the internal intercalation/deintercalation processes that occur within a LIB, the LAM can emerge from regular LIB use and subsequent cycling. However, LAM can be also enhanced by external factors (e.g., high current rates, high SOC, high temperatures). In general, LAM is a complex aging mechanism caused by several effects that usually leads to the loss of capacity and power fade of the battery. The aim of this section is to cover the main causes of LAM from a graphite based NE and a standard commercial PE. Equally important, the effects that LAM causes on each individual electrode are presented using the cell mechanistic model.

Generally, the LAM can be caused by (1) particle isolation, (2) side reactions within the active materials of the electrodes and/or (3) physical degradation.

(1) LAM caused by particle isolation. The active material particles are hold together and in contact with the electrolyte and current collectors using binders. Due to binder degradation, contact loss between carbon particles, current collector and carbon, binder and carbon and between binder and current collector can occur [36]. Due to increased thickness in the SEI layer and/or due to volume changes, porosity reduction of the active materials may occur, which damages the percolation network for the ionic conduction in the electrode [79]. Also, due to volume changes, particle-particle contact reduction may occur, which damages the percolation network for the electronic conduction in the electrode [69]. In general, contact loss (mechanical or electronic) within the composite electrode results in loss of capacity (as the active material is isolated) and higher cell impedance [36].
(2) LAM caused by side reactions within the active materials of the electrodes. Chemical decomposition/dissolution reactions lead to loss of active material. In addition, metal transition ions released from the side reactions can move to the NE and can be incorporated in the SEI at the NE, which leads to accelerated aging [36]. Also, volume changes in the active materials lead to changes in the crystalline network which may cause further side reactions. The formation of parasitic phase (either Li reactive or non-reactive) is another type of LAM [31].
(3) Physical degradation. Due to volume changes and side reactions (mostly on the NE, at the electrode/electrolyte interface), solvent co-intercalation and electrolyte reduction inside graphite [80], gas evolution and subsequent cracking formation in the particles occurs. Changes in the crystal structure scale (few nm) are produced due to solvent co-intercalation, whereas the cracking formation and delamination from the current collector occurs microscopic scale, damaging the graphitic particles [59]. These degradations introduce irreversible damage to the SEI layer whose subsequent repair consumes more active lithium (LLI).

The LAM is induced by the external battery operating factors. The degradation rate is usually enhanced at high cycling currents, high DOD and SOC and high temperatures. High cycling currents usually enhance the active material losses due to volume changes and changes in porosity, high DOD and SOC enhances the decomposition of binder and contact loss of active materials whereas high

temperatures also enhances binder decomposition and decreases accessible surface area due to continuous SEI growth [36].

The effect of LAM on a LIB mainly causes capacity loss and impedance rise, which leads to a loss of energy and power. Similarly, LAM is often attributed to cause second stages of cell degradation [24], [31], where abrupt capacity losses suddenly appear, after a steady capacity fade during a first stage. This is because some LAMs may be masked, and remain "silent" in terms of capacity fade detection, through hundreds of cycles. Standard procedures for aging identification, such as measuring the capacity evolution with cycling cannot detect "silent" LAM effects. Similarly, since LAM is usually accompanied by LLI, the overall effects on a full-cell may be identical (i.e. capacity and power fade). Indeed, as LAM and LLI may interact simultaneously, it is important to recall that LAM affects the usable capacity of the electrodes, whereas LLI consumes lithium from the electrolyte but does not cause structural degradation in the electrodes. In conclusion, identifying LAM can be very challenging. To solve this issue, first is important to identify how LAM affects both the NE and PE individually. To do so, a mechanistic analysis on individual electrode signatures is carried out, based on [31].

The LAM can be subsequently categorized in four types, depending on the affected electrode (NE or PE) and the degree of lithiation (i.e. predominantly in a lithiated or a delithiated state) in which LAM occurs [31]. Hence, the four types of LAM are: LAM on the NE (LAM_{NE}) when lithiated (LAM_{liNE}) or delithiated (LAM_{deNE}) or LAM on the PE (LAM_{NE}) when lithiated (LAM_{liPE}) or delithiated (LAM_{dePE}). **Fig. 2.14-15** schematically presents the effects that the four types of LAM cause on the individual electrodes and full-cell signature when cycled at C/25 on a GIC||LFP cell.

Loss of active material on the negative electrode (LAM_{NE})

A schematic representation of LAM_{deNE} and LAM_{liNE} is shown in **Fig. 2.14**a-b. The LAM_{deNE} is affected by the charging process, since by the time the PE is fully delithiated, the NE has a lower charging state on the NE than that of the prior cycle, since less amount of NE accepts the same charge [31]. This is shown as an overall shrinking effect of the NE, starting from its lithiated state (LiC_6) or high SOC_{PE} and fixed at its delithiated state (C_6) or low SOC_{PE}. Vice versa, LAM_{liNE} is affected during the discharge process, at the end of the discharging regime. The shrinking of the NE begins from the delithiated and is fixed at its lithiated state, as shown in **Fig. 2.14**b. It has to be noted that LAM_{deNE} does not show up on the full-cell signature during the first degradation stages. That is, LAM_{deNE} can remain "silent" and suddenly appear as a second degradation stage. On the contrary, LAM_{liNE} causes direct capacity loss on the full-cell signature as soon as it appears. From a cell constructive parameter perspective, both LAM_{deNE} and LAM_{liNE} causes LR reduction, whereas only LAM_{liNE} increases the OFS.

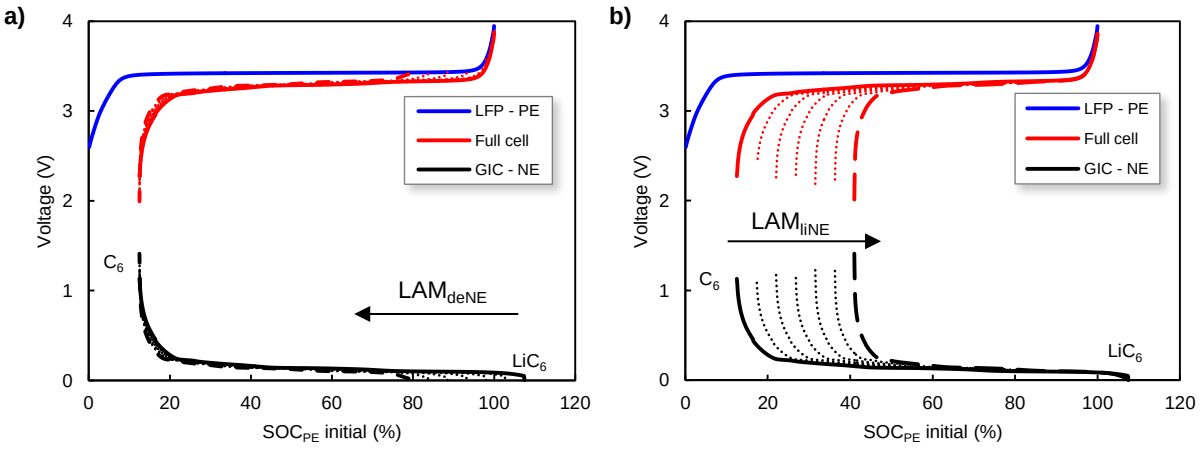

Fig. 2.14. Schematic representation of loss of active material on the negative electrode (LAM_{NE}) at C/25 when a) delithiated (LAM_{deNE}) and b) lithiated (LAM_{liNE}).

Loss of active material on the positive electrode (LAM_{PE})

A schematic representation of LAM_{dePE} and LAM_{liPE} is shown in **Fig. 2.15**a-b, respectively. The LAM_{dePE} is affected by the discharge process, since by the time the NE is fully delithiated, the PE has la lower SOC_{PE} than that of the prior cycle, since less amount of PE accepts the same discharge. This loss of active material is represented by an overall shrinking of the PE starting from its lithiated state (LFP) or low SOC_{PE} and fixed at the delithiated state (FP) or high SOC_{PE}. Vice versa, LAM_{liPE} reduces the total amount of active material starting from the delithiated state and fixed at the lithiated state. The LAM_{dePE} mode causes "silent" capacity loss, as the first cycling stages do not affect the full-cell signature. From a cell constructive parameter perspective, both LAM_{dePE} and LAM_{liPE} causes LR increase, whereas only LAM_{dePE} increases the OFS.

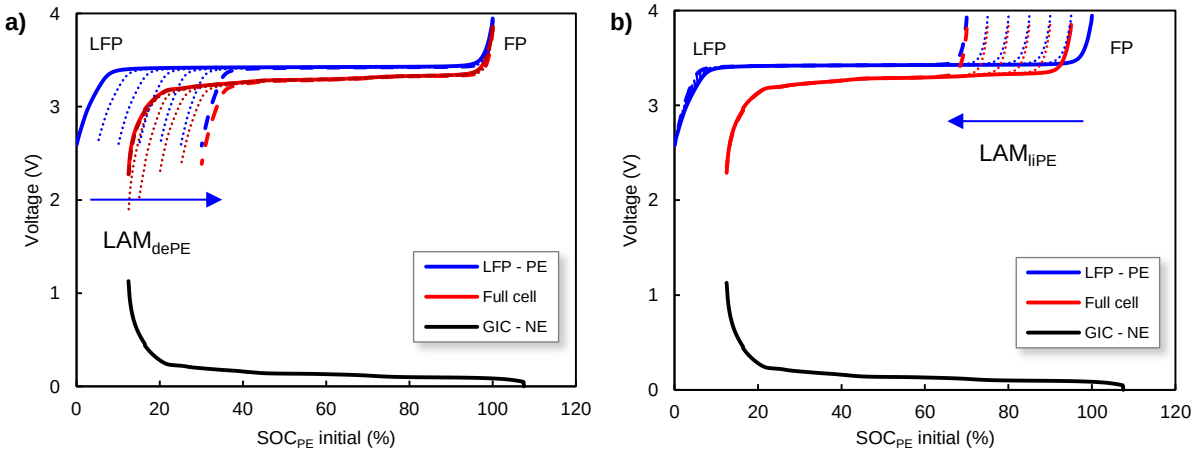

Fig. 2.15. Schematic representation of loss of active material on the positive electrode (LAM_{PE}) at C/25 when a) delithiated (LAM_{dePE}) and b) lithiated (LAM_{liPE}).

To sum up, LAM is caused by the structural degradation of the electrodes. As a result, capacity is loss and impedance can be increased. The origin of LAM can be caused by several causes, i.e., particle isolation, side reactions within the active materials of the electrodes and/or physical degradation. The LAM can be subsequently categorized into four types depending on the affected electrode (i.e. NE, PE) and the degree of lithiation in which LAM occurs. Also, LAM_{deNE} and LAM_{dePE} may cause "silent" capacity loss, which can lead to sudden appearances of capacity loss, known as second degradation stages. Additionally, LAM affects the cell constructive changes (i.e. LR and OFS). Moreover, the identification of LAM effects is very challenging with standard aging identification procedures, as some of its aging modes may remain "silent" (i.e. LAM_{deNE}, LAM_{dePE}). Finally, battery degradation can be very complicated, as it may be caused by LLI coupled with LAM on its four aging modes acting (or not) simultaneously.

2.3.3. Ohmic resistance increase (ORI)

The ohmic resistance increase (ORI) of a battery is referred as the degradation caused on the electrodes and electrolyte materials that directly result in an increase of the electronic and ionic resistance, respectively. The electronic resistance is composed by the electrical connections (terminals, current collectors, weld joints and contacts in electrodes) and particle-particle contact resistances. Similarly, LAM caused by particle isolation (i.e. either contact loss between carbon particles, current collector and carbon, binder and carbon and/or between binder and current collector) lead to ORI [36]. In addition, binder decomposition, current collector corrosion and volume changes in the active material also lead to ORI [36], [71]. The ionic resistance can be affected by electrolyte contamination, which results in a degradation of the electrolyte conduction. Similarly, SEI growth and destabilization also increases the ionic resistivity [47]. On a LIB, an increase of the ohmic resistance lowers the energy and

power that can be delivered by the battery, while increases the energy required to charge. As a result, the LIB is less energy efficient.

Fig. 2.16a-b shows a schematic representation of ORI, and their impacts on a charge (a) and discharge (b) on a GIC||LFP cell. When the cell is charged (a), the NE is lithiated and goes to lower potentials, whereas the PE is delithiated and goes to higher potentials. The overall result is an increase of the full-cell voltage. Vice versa, when the cell is discharged (b), the overall voltage of the full-cell is reduced. It is important to point out that large ORI on the NE, coupled with high charge rates can result in Li plating. Further details are unveiled in the next section.

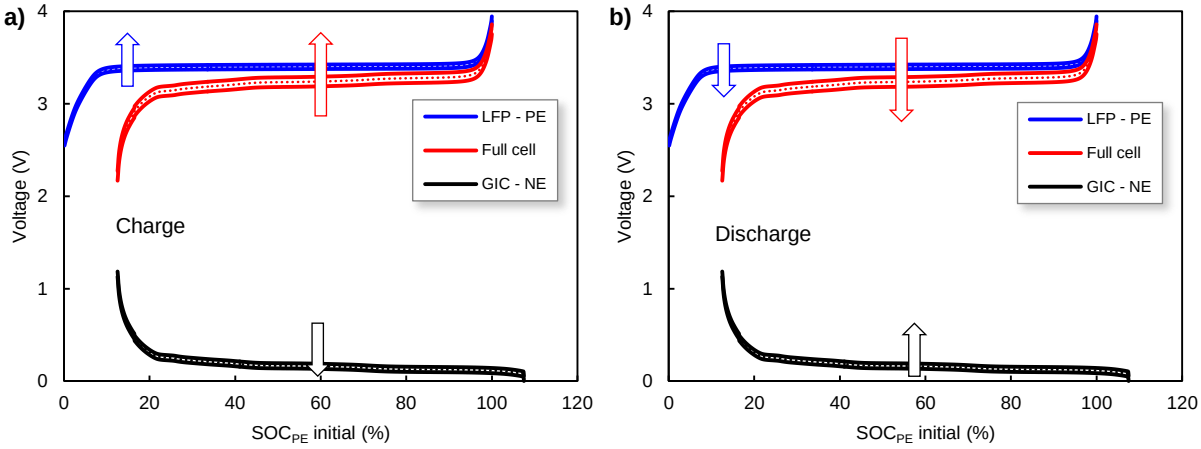

Fig. 2.16. Schematic representation of ohmic resistance increase (ORI) during, a) charge and b) discharge.

2.3.4. Lithium plating

Lithium plating (Li plating) is a phenomenon which occurs during charge, when the lithium ions deposit as metallic lithium on the NE surface instead of intercalating into graphite. Li plating can be considered as the most detrimental aging mechanism, as not only leads to further aging but also safety deterioration [24], [36], [50], [57], [60], [71], [74], [81], [82]. In addition, it is also one of the most complex phenomena to analyze in LIBs. There are several factors that initiate the formation of Li plating, ranging from constructive properties of the cell (e.g., poor cell balance, geometric misfits), to operating conditions (e.g., low operating temperatures, high current rates). Similarly, Li plating can be caused from thermodynamic and/or kinetic causes, and can be separated between reversible and irreversible.

When Li plating is formed, several detrimental effects are manifested within the cell. This is schematically presented in. **Fig. 2.17**a. The freshly deposited lithium covers the active surface area of the NE. Because metallic lithium is highly reactive with the electrolyte, it further reacts consuming more electrolyte, which leads to further LLI [36], [49]. The products formed from the reactions may block pores, isolating active particles on the NE, which leads to LAM [36], [47], [49], [71]. In addition, the formed metallic lithium deposits may result in the formation of moss-like deposits and dendrites [36], [81], [83], [84]. Dendrites can grow and pierce the separator, connecting the electrodes internally for the electronic transport. This produces internal short circuit in the cell, which may lead to thermal runaway [51], [60], [83], [85], [86]. In situ, measurements using SEM illustrate Li deposition, dendrite growth and cell short circuit (see **Fig. 2.17**b) [83]. In addition, dendritic growth may delaminate the copper current collector, leading to further LAM and impedance increase. To sum up, Li plating increases LLI and LAM, causing capacity loss and impedance rise and most importantly, Li plating may lead to safety concerns. Hence, the factors that initiate Li plating shall be established.

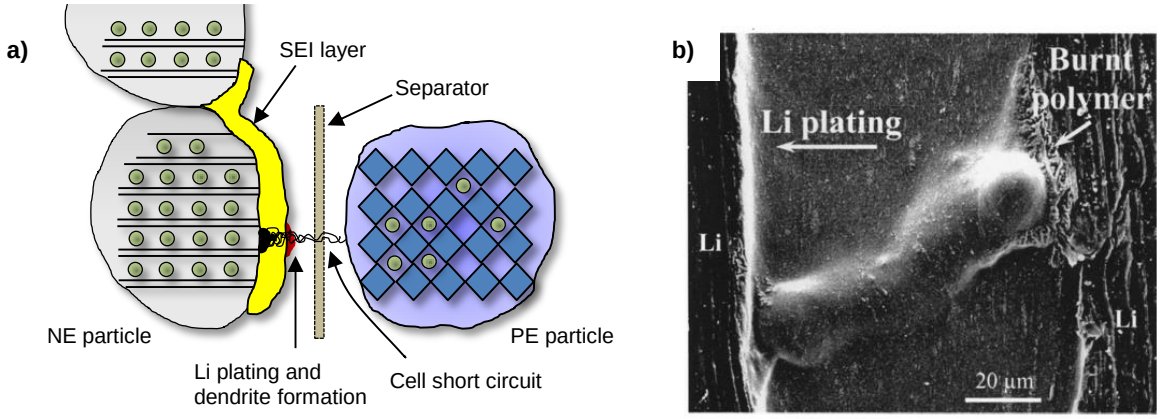

Fig. 2.17. a) Schematic representation of Li plating and dendrite formation, and b) *in situ* SEM image showing Li plating and dendrite growth causing short circuit across the separator on a cell [83].

Li plating can be originated by (1) hazardous cell operating conditions (2) cell constructive defects and (3) conventional aging of the cell. In a well-constructed cell, Li plating may suddenly occur due to low temperature operation [74], [81], [87] and fast charging or high pulse rates [36], [57], [82]. Low temperature affects the anode kinetics and reduces the solid state ionic diffusion rate, which causes Li deposition rather than Li intercalation on the NE. Similarly, fast charges can cause negative potentials on the NE below 0 V vs. Li, due to kinetic limitations, causing Li deposition on the NE. Cell constructive defects (2) include poor cell balance (e.g. excess of cathode material), geometric misfits (e.g. large cathodes overlapping anodes at the edges) and poor electrolyte formulation. The amount of active material on the electrodes, and therefore the loading ratio (LR) are directly related with the constructive parameters that cause Li deposition. Finally, Li plating can occur due to gradual degradation of the cell, as large capacity fade and impedance increase can lead to Li plating even under standard cell operating conditions. Further details on Li plating can distinguish between thermodynamic and kinetic causes.

Thermodynamic Li plating

Li plating can be originated under thermodynamic conditions by (1) large LAM_{deNE} degradation [30], [31], and (2) poor cell balance (e.g., an excess of cathode material) and/or geometric misfits (e.g., large cathodes overlapping anodes at the edges) [36], [58]. **Fig. 2.18**a-b presents these Li plating origins respectively, for a GIC||LFP cell cycled under thermodynamic conditions (i.e. C/25). Under severe LAM_{deNE} (1) caused by subsequent cycling, the NE would not be fully lithiated before the PE completely releases all its Li ions. This causes Li plating. From half-cell perspective, this is shown in **Fig. 2.18**a: Li plating occurs when the NE is reduced below 100% SOC_{PE}. Similarly, when a cell is not correctly constructed (2), Li plating may take place. **Fig. 2.18**b illustrates this event on a fresh cell: when the NE after SEI formation is fully lithiated before the PE completely releases all its Li ions (i.e. 100% SOC_{PE}), Li plating is induced. This can be avoided in the manufacturing process if LR is increased. As an illustrative example, **Fig. 2.18**b compares two cells which only differ in the LR: Cell 1 has LR = 1.2 and does not show Li plating, whereas Cell 2, with LR = 0.7 shows Li plating. Both cells have the same OFS (15%) after SEI formation.

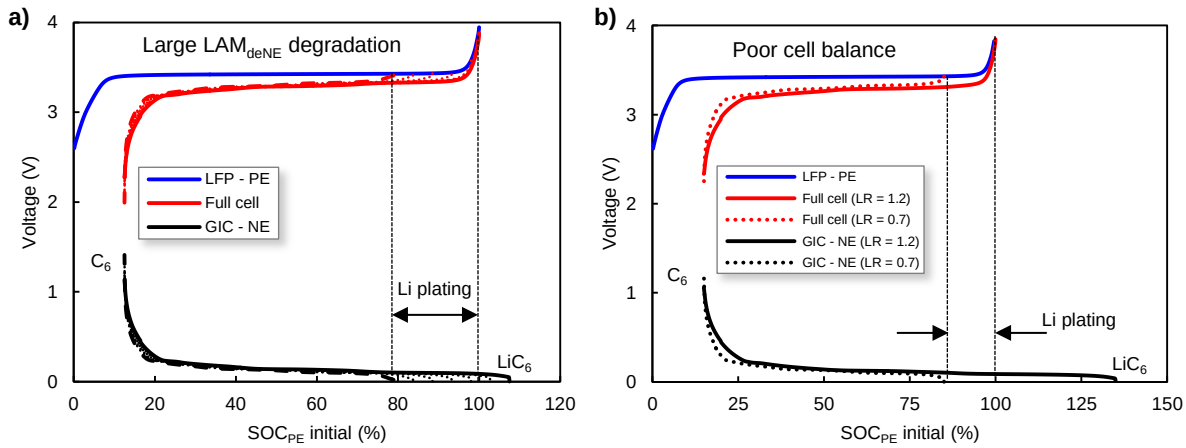

Fig. 2.18. Schematic representation of thermodynamic Li plating caused by a) large LAM_{deNE} degradation and b) poor cell balance and/or geometric misfits, showing Cell 1, LR = 1.2 (no Li plating) and Cell 2, LR = 0.7 (Li plating).

Kinetic Li plating

Kinetic Li plating occurs as soon as the NE potential becomes lower than or equal to the equilibrium potential of the Li^+ reference, i.e. $E_{NE} \leq 0$ V. The range of Li plating occurrence is schematically shown by the grey dotted area in **Fig. 2.19**. Generally, Li plating occurs under kinetic charging when (1) fast charging or high current pulses, (2) subzero temperatures and (3) ORI on the NE. For such conditions, there is an ongoing competition between intercalation of Li ions and Li plating on the NE. Under strenuous charging (1), caused commonly by a bad designed fast charging protocol or due to large regenerative charging pulses, the kinetic effects on the NE would be so large that overpotentials occur. If the overpotentials cause $E_{NE} \leq 0$ V, Li plating is formed. Still, graphite can tolerate for a brief periods of time (within the few seconds) [82] moderately negative potentials of -200 mV without Li plating occurrence, as demonstrated by Verbrugge and Koch [88]. Under subzero temperatures (2) the solid state diffusion of Li ions is reduced, which leads to low intercalation rates and thus favors Li plating [74], [89]. ORI (3) caused by cell aging produces overpotentials on the NE, which may also lead to Li plating. This effect may even occur under standard charging rates, if large ORIs are found.

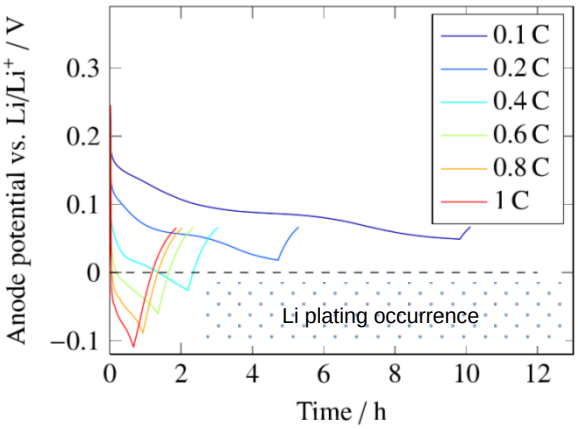

Fig. 2.19. Schematic representation of kinetic Li plating caused charging at low temperatures (0°C). The grey dotted area indicates Li plating occurrence, i.e. $E_{NE} \leq 0$ V [89].

Reversible and irreversible lithium plating

It is possible that part of the metallic lithium deposited on the anode during charge can be recovered as active lithium during the subsequent discharge [57], [90]. This process occurs because oxidation

(stripping) of lithium is a more facile reaction than Li deintercalation [57]. As a result, a reversible gain of lithium inventory takes place. In other words, reversible Li plating does not cause direct capacity loss because is another way of charging (delithiating) the NE electrode [74].

The stripping process has side effects, which may also cause part of the plated lithium to become electrically isolated from the NE [74], inducing LAM_{deNE}. Smart *et al.* [57], [90] showed an indirect evidence of reversible Li plating by investigating the subsequent discharge curves after Li plating occurred. This is shown in **Fig. 2.20**, where the voltage plateaus observed during discharge at high SOCs are attributed to the stripping of the metallic lithium deposited in the previous charge step. The study of the voltage plateau caused by the stripping process was recently used by Petzl and Danzer [74] to detect Li plating on a commercial LIB. Conversely, when Li plating occurs, not all of the deposited metallic lithium is recovered during subsequent discharge. That is, part of the plated lithium is irreversible. The irreversible plated lithium is the main responsible of the capacity losses and the subsequent detrimental effects. Nevertheless, irreversible Li plating can lead to sudden increases of SEI growth (i.e. LLI) [58]. Non-invasive identification of reversible and irreversible Li plating remains very challenging.

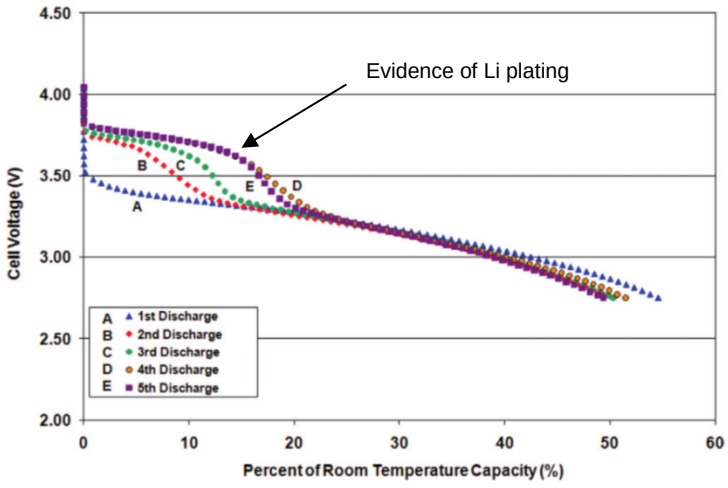

Fig. 2.20. Discharge curves of a LIB showing evidences of reversible Li plating [57].

There are some strategies to reduce the risk of Li plating and detect it. In terms of constructive parameters, the NE capacities shall be large enough to allow a total PE delithiation over the NE. This is directly related to the LR and the OFS of the cell after SEI formation. In addition, the effects of the electrolyte composition and the use of additives can reduce the risk of Li deposition, as shown by Smart *et al.* [57]. On a well-constructed commercial LIB, the simplest procedures to avoid Li deposition are avoiding low temperature operation and strenuous charging rates above what is recommended by the manufacturer. Similarly, even under standard operating conditions Li plating may be induced, especially if aging mechanisms i.e. LAM_{deNE}, and/or ORI appeared. Hence, keeping track of the degradation modes is of crucial importance to avoid Li plating. To detect Li plating, techniques using SEM, optical images, etc. [51], [68], [83] have been used. In addition, nondestructive methods based on the analysis of the high voltage plateau during discharge can be used to identify reversible/irreversible Li plating. Both approaches are useful to better understand Li plating and its effects on LIBs. However, its quantification remains very challenging.

To summarize, Li plating is an aging mechanism that occurs during charge, which is detrimental to LIB performance, reliability and safety. In addition, Li plating leads to further increase LLI and LAM. Most importantly, Li plating may lead to safety concerns. There are several factors that initiate the formation of Li plating, including strenuous charges, charging at low temperatures, cell constructive design or conventional aging of the cell. Similarly, Li plating can be formed from thermodynamic and/or

kinetic causes, and can be separated between reversible and irreversible. Although there are several approaches to detect Li plating (including destructive and nondestructive techniques), its detection and quantification through online, nondestructive techniques remains very challenging.

2.3.5. Other aging mechanisms

Subsequent categorization of the aging modes is not often given, as the main ones previously described (i.e., LLI, LAM, ORI and Li plating) cover the most common aging effects on LIBs. However, the degradation modes faradic rate degradation (FRD) and the formation of parasitic phase (FPP) have been reported in the literature [31], [91]. The FRD occurs when an electrode does not react with Li ions at the same kinetic rate in the aging [31]. As a result, the FRD induces changes in the electrochemical behavior of the cell. The main effects are shown in the voltage curves, where FRD shortens the voltage plateau, as a result of slower kinetics (see **Fig. 2.21**a, thin solid line). The FPP resembles a "composite" electrode, showing changes on its active phases in the electrode reactions, producing modifications on the voltage signature. Such signatures are shown on **Fig. 2.21**b, on the PE. Similar phenomena could also happen in the NE: Li plating may also induce FPP as a consequence of the deposited metal on the NE surface. As seen, both degradation modes affect the voltage signatures of the full cell. Hence, analyzing the voltage signature is useful to identify both FRD and FPP.

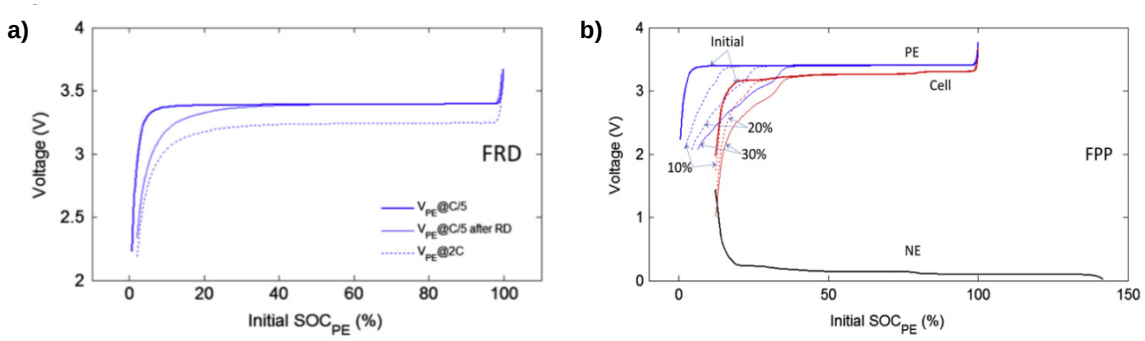

Fig. 2.21. a) Schematic representation of faradic rate degradation (FRD) and b) formation of parasitic phase (FPP) degradation [31].

2.4. Aging scenarios

The main purpose of a LIB is to deliver energy to a load or to be recharged when required, i.e., work under kinetic conditions. However, LIBs may also remain relatively long periods of time unused or "stored" under thermodynamic conditions (i.e. no current flowing). For instance, an EV usually spends 90 to 95% of its lifetime in storage mode when parked [92]. Applications such as Uninterruptible Power Supplies (UPS), second-life use of batteries or the time gaps between the end of the LIB manufacturing process and the final product usage are other examples of LIB storage conditions. Hence, it is important to distinguish the aging origins of LIBs under cycling and storage conditions. Notice that storage aging is usually referred in the literature as calendar aging.

Briefly, aging during cycling adds kinetically induced effects dependent on cycling conditions (e.g. operation temperature, cycling rates, voltage limits, etc.). On the contrary, calendar aging is due to side reactions resulting from thermodynamic instability of materials, and is dependent on the storage conditions such as temperature, and SOC of the cell. This section presents the aging effects that cycling and storage conditions cause on LIBs.

To provide a final overview on the causes and effects of aging from a general perspective, a summary of the aging mechanisms is presented in the last point of this section. The summary pretends to provide a general view of how the different aging modes exposed in Sections **2.3** and current Section **2.4** interact with each other.

2.4.1. Cycle aging

Aging on cycling occurs when the cell is under non-equilibrium conditions, i.e. current flowing through the system. In this case, aging is the result of the kinetic effects, and can lead to LLI, LAM, ORI, Li plating and/or other aging mechanisms (i.e. FRD and FPP), as described in Section **2.3**. Depending on the cycling conditions, different aging effects can be induced. The main external conditions that lead to cycle aging are temperature, charge/discharge rates and voltage utilization. Here is described how each external parameter causes aging on the cell, and its relation to the main aging modes.

As shown in the literature [36], [77], [93], [94], the operating temperature is considered the main factor that accelerates aging on LIBs. Slightly high temperatures (i.e. ~35ºC) may at first appear to be benign, because enhance the kinetics of the lithium intercalation/deintercalation process [36] reducing overpotentials, leading to an increase in delivered energy. However, in the long term, those slightly high temperatures can accelerate cell degradation. High temperatures (usually above 50ºC) have a rapid and direct impact on the battery, causing damage on the morphology of the SEI layer [36], [49], [50], decomposition of the electrolyte [36], [76] and in the worst case, high temperatures may cause thermal runaway and cause the cell to catch fire or to explode [36], [37]. In addition, the SEI reconstruction at elevated temperatures produces more stable inorganic products that result in lower ionic conductivity of the SEI for lithium [36]. Electrolyte decomposition may also produce solve co-intercalation which causes graphite exfoliation damaging the electrode. Another detrimental effect induced by high temperatures is binder decomposition, which causes particle isolation of active material. Hence, high temperatures induce (1) more LLI due to SEI consumption, (2) LAM due to particle isolation, exfoliation, SEI reconstruction and (3) ORI due to lower ionic conductivity as a result of SEI growth. Indirectly, if large LLI, LAM and ORI are presented, it could be possible that FRD and FPP were also induced. Low temperature (subzero) affects the anode kinetics and reduces the solid state ionic diffusion rate, which increases the risk of Li plating. The potential hazards and detrimental effects of Li plating have been widely covered in previous Section **2.3.4**.

High cycling rates also influence the degradation of LIBs [36], [77]. High charging rates are particularly hazardous because they can induce Li deposition and subsequent battery aging. Similarly, high cycling rates (both charge and discharge) tend to produce changes in the porosity of the NE due to volume changes, SEI formation and growth, causing LLI, LAM and ORI. The most detrimental effect is caused by the direct relation between high cycling rates and high temperatures. Indeed high current rates increase internal cell temperature, which lead to further acceleration of aging and even thermal runaway. Hence, high currents can cause, indirectly, all the temperature-related degradation effects exposed above.

Battery aging is also a function of the battery utilization mode, or DOD cycling interval [62], [77], [94]. Experiments shown that LIB working on a reduced DOD interval window in the mid SOC range is less prone to suffer from degradation. Indeed, many applications (including PHEV) usually work on a close DOD interval, which never fully charge or discharge the battery. The main reason of avoiding high or low SOC is because the electrodes are more prone to react. Low potentials can cause current collector corrosion, whereas high potentials tend to increase electrolyte and PE decomposition, binder decomposition and SEI formation [36]. Similarly, the charging protocol itself is a key factor on LIB aging. Due to its importance, charging techniques analyses are presented in Chapter **3**.

2.4.2. Calendar aging

Aging during storage occurs due to side reactions resulting from thermodynamic instability of the LIB materials [24]. As a result, the cell losses capacity irreversibly. It is important to point out that calendar aging differs from self-discharge. Although self-discharge also occurs during storage, it is referred as the loss of useful-recoverable capacity. As an example, a LIB may have 1% of self-discharge

per month, which means that if the cell was stored at 100% SOC with 10 Ah, after two months would have 9.8 Ah available. In contrast, calendar aging studies show how much of those 10 Ah would be irreversible lost (quantitatively) and what was the cause of the aging (qualitatively).

The degradation process is dependent on the storage conditions, namely the storage temperature and SOC of the cell [76], [95], [96]. Similarly, the degradation is strongly dependent on the electrolyte and the electrode active material [24], [36], [49]. There are several calendar aging studies in the literature. Indeed, Sarasketa-Zabala *et al.* [96] on their recent study on calendar aging cited 52 works exclusively dedicated to aging studies on several LIB technologies. Similarly, Kassem *et al.* [76], [95] provided a broad study on GIC||LFP cells at various storage temperatures and SOCs, performing several in situ and *post mortem* analysis (i.e. XRD, SEM). An example of the results is shown in **Fig. 2.22**, where 27 cells where aged at 3 initial SOCs (30%, 65% and 100%) and 3 different storage temperatures (30º, 45ºC and 60ºC). They concluded that the extent of capacity fade strongly increases with storage temperature, and to a less extent, with the SOC level (where high SOC is more detrimental). The LLI was identified as the main source of capacity fade, originated from side reactions taking place at the anode, i.e., solvent decomposition leading to the growth of the SEI. No evidences of LAM participated on the capacity fade, and internal resistance increase was negligible. These facts are widely accepted and are to be found in several relevant studies [24], [68], [94], [97], [98].

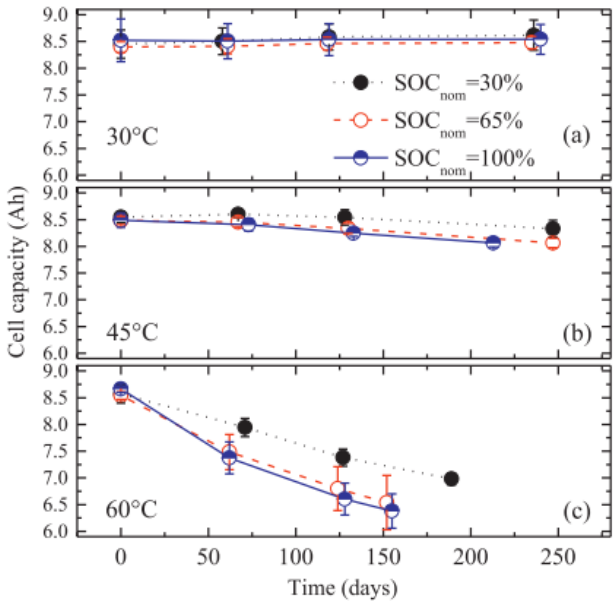

Fig. 2.22. Evolution of the discharged capacities of LIBs measured at nominal rates calendar-aged under different storage conditions of temperature and SOC [95].

Despite the large amount of studies on calendar aging, we found that the studied cells are set to calendar when fresh. Hence, a calendar study on aged cells is of significant interest, as it directly relates with the second-life use of batteries.

To sum up, calendar aging causes capacity loss, induced by LLI. Cell storage at high temperature and to a less degree, high SOCs are the main factors that cause capacity loss.

2.4.3. Summary of aging mechanisms

To summarize, cell aging results in capacity fade, generally accompanied by an impedance increase. As exposed, the aging degradation modes are multiple, complex, and often interrelated with each other. Moreover, some aging modes (i.e. $LAM_{deNE,}$ LAM_{dePE}) may remain "silent" or induce Li deposition (i.e.

LAM_{deNE}). To illustrate the complex interaction of the aging mechanisms that affect LIBs, **Fig. 2.23** schematically summarizes the main aging mechanisms covered in the previous section (Section **2.3**), and how they relate with each other. Battery aging is the result of several aging phenomena, associated in loss of lithium inventory (LLI), loss of active material (LAM) and change in polarization resistances. The degradation mechanisms lead to battery aging, which is mainly translated into cell capacity fade and increase of cell impedance, which leads to power fade. Li plating is detrimental to LIB performance, reliability and safety. Similarly, external factors such as high or subzero temperatures are detrimental, and may lead to safety issues. Cycling at high C-rates, and full charge/discharge cycles also increase cell degradation. Finally, even if a LIB is stored and not used (i.e. calendar aging), side reactions occur which cause cell deterioration, mainly attributed to LLI.

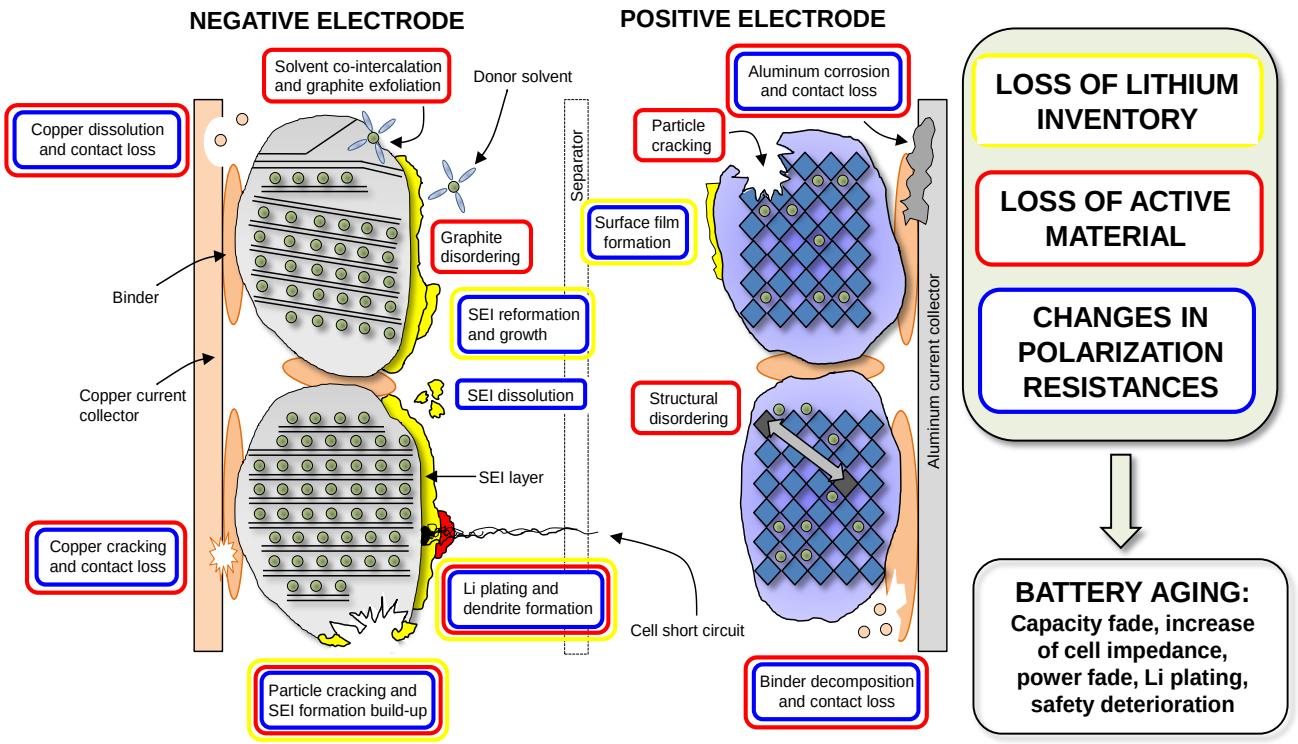

Fig. 2.23. Schematic representation of possible degradation processes in LIBs. Adapted from [25], [36], [99].

In conclusion, LIB degradation has significant consequences on battery performance, reliability and safety. Hence, the understanding and identification of the battery degradation mechanisms is of crucial importance to overcome such issues. Still, the identification of the aging modes (both qualitative and quantitative) through online, nondestructive methodologies remains very challenging today. In fact, aging mechanism diagnosis and prognosis is decisive in the LIB industry. The above issues originated the fundamental motivation, and main objectives of this thesis.

2.5. Commercial Li-ion batteries

Nowadays, there are several LIB systems available on the market, mainly named after its PE active material of choice (with the exception of LTO). Each of these systems is subsequently divided into high power (HP) or high energy (HE), and built on different constructive formats. The aim is to optimize the LIB characteristics to meet specific applications. From the different materials of choice, lithium iron phosphate (LFP) is gaining much interest both in the industrial and research community, because of its advantages. Hence, this section aims to provide further details and analysis of the current commercially available LIBs, with emphasis on LFP batteries.

2.5.1. Battery design architectures

In a LIB, the chemistry (i.e. active materials, electrolyte) is the main actor that makes a battery work. However, battery construction, mechanical, and structural properties of materials can make a battery more efficient, reliable or convenient for a given application. The battery design architecture includes the information of the design optimization (i.e. HP or HE) and the constructive formats. The constructive formats are built, mainly cylindrical, prismatic, pouch or bottom cells.

High power (HP) and high energy (HE) cell design

Batteries classified as HP can deliver high discharging powers both continuously (usually above 4C) or pulse (up to 50C) and can be rapidly charged (up to 6C). Its main applications are power tools, HEVs, power grid stabilization, and applications that require fast charging. The key to enhance power capabilities is to decrease the transport resistances so that energy can rapidly be extracted [100]. Using high power active materials, high rate chemistries or modifying the structure of the electrodes by engineering processes are some of the techniques to improve the power density [100]. The main disadvantage of HP batteries is their low energy density, which makes them heavier than HE cell designs. Usually, HP batteries are expected to work under harsh conditions, with very high current rates (even up to 30C), which may induce rapid cell degradation.

On the other hand, batteries classified as HE are optimized to deliver large amounts of energy during long periods of time. Generally, HE batteries cannot be charged above 1C rate or discharged above 2C. The main applications are consumer electronics where both lightweight and high capacity is desired. Since the energy density is the product of the voltage and the capacity, the major improvements are focused towards new high voltage materials and large specific capacities. The main drawbacks of this technology are their poor power capabilities and current abuse-tolerance.

It is important to point out the trade-offs between HE and HP batteries. For most applications, substantial sacrifices are produced when increasing one of the specifications. **Table 2-3** compares the estimated material content between HE and HP cell designs. As observed, cathode material and package mass account for the largest differences between both cell designs. Indeed, a larger proportion of cathode material produces a smaller LR, which is common in HE designs (LR_{HE} = 1.1 and LR_{HP} = 1.5 when derived from **Table 2-3**). Similarly, larger proportion of package mass directly reduces the specific energy of the battery.

Table 2-3. Estimated material content of typical Li-ion cells [42].

Material/component	High-energy cell (100 Ah)		High-power cell (10 Ah)	
	Quantity (g)	wt.%	Quantity (g)	wt.%
Anode (dry)	785	23	56	17
Cathode (dry)	1610	47	93	29
Active material	1408	41	74	23
Electrolyte	618	18	44	13
Separators	60	1.8	16	5
Package (other)	358	10	115	35

Cell constructive format

The most common battery constructive formats are shown in **Fig. 2.24**. These formats can be indifferently used with any type of battery chemistry (e.g. LCO, NCA, LFP, etc.). The cylindrical is the most common format, as the manufacturing process is the easiest [5]. The use of the prismatic cell design has become widespread, as it is commonly used in portable electronics. Pouch-type cells use a multilayer

foil enclosure, which optimizes weight and volume. Hence, this type of cell is usually cheaper and lighter, and is gaining acceptance in EVs, where thin designs are required. Frequently, cylindrical cells are used in HP designs, as this type of format optimizes power transmission by minimizing polarization losses caused by electrical conductivity. In contrast, prismatic and pouch-type formats are optimal for HE cell design as they maximize area. Coin cells are mostly used in primary, non-rechargeable cells where applications require ultra-low energy consumption (i.e. watches, or the CMOS memory in PCs).

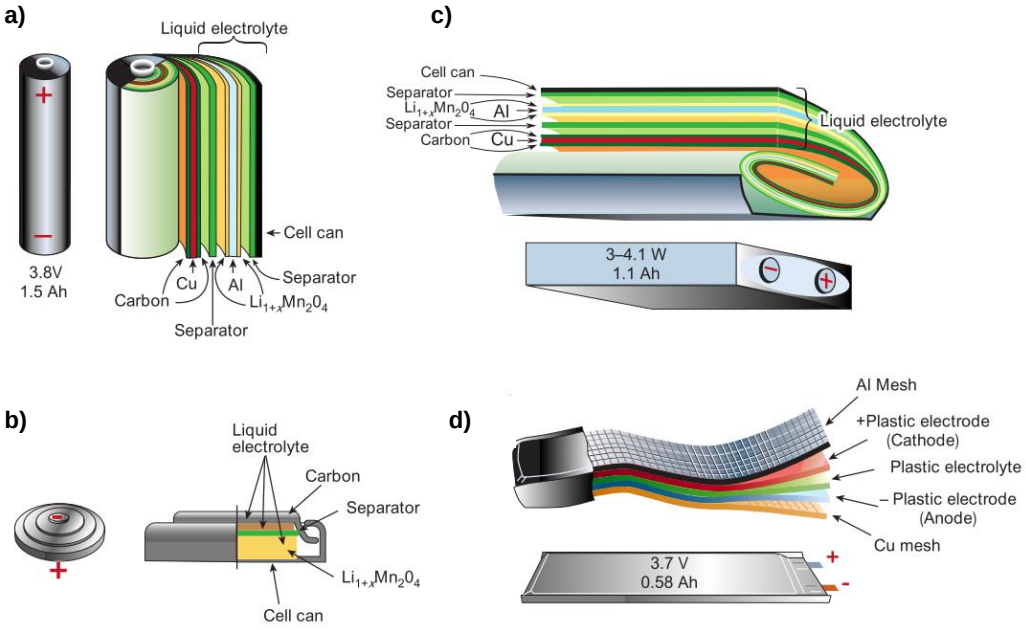

Fig. 2.24. Schematic drawing showing the shape and components of various LIB configurations a) cylindrical, b) coin, c) prismatic, and d) pouch type [17].

2.5.2. Commercial Li-ion batteries

The performance of LIBs is difficult to generalize, as LIBs are highly dependent on its active materials and cell design architecture. In fact, each battery manufacturer may provide a particular product, often specifically developed for a given application. For this reason, manufacturer's know-how on cell composition and additives is highly secret. Still, a general performance characteristic of commercial LIBs is outlined in **Table 2-4**. It is important to point out that for specific characteristics, one shall refer to the particular battery manufacturer's datasheet. Here the data is presented only as an illustrative approach.

Usually, LIBs can be classified in two main groups, i.e. high and low voltage cells. As indicated in the table, the cells which have high average voltage (LCO, NMC, NCA, and LMO) inherently have the highest values of specific energy and energy density, which are their main advantages. As expected, major drawback is their relatively low cycle life. In contrast, low-average voltage batteries (LFP, LTO) have lower specific energies, but have the longest cycle life. In particular, LTO has an unprecedented cycle life in commercial LIBs. Similarly, LFP stands out for its high rate capabilities, long cycle life, relatively good energy density and low cost.

Regarding LIB applications, in consumer electronics HE cells in chemistries such as LCO, NMC or NCA provide the best results. In particular, LCO has been the material of choice of the vast majority of consumer electronics [2], [4]. In high power applications, such as portable tools, LFP is the most used technology. In HEV and EV applications there is certain controversy on which technology is the optimal. When cell technologies are compared using the most significant parameters for EV or HEV applications (i.e. cost, specific energy, safety, performance and specific power), the studies conclude that each of these

technologies have its advantages and drawbacks, without any technology clearly standing out from the others [101]–[104]. Indeed, EV automakers use different LIB chemistry technologies. For example, BMW, or General Motors use LFP, whereas Tesla Motors uses Cobalt-based technologies and Nissan uses LMO on its Leaf model [105]. For grid energy applications, LFP and LTO have the best performance. The main disadvantage of LTO is its high cost, hence LFP is more common [106]. Hence, its applications are mostly oriented to grid-energy storage, where extremely long cycle life is required.

Table 2-4. General performance characteristics of commercial LIBs using most common cell chemistries (adapted from [4]).

Characteristics	LCO/graphite NMC/graphite NCA/graphite Energy cells	NMC/graphite LMO/graphite Power cells	LFP/graphite Power cells	LMO/LTO
Voltage range (V)	2.5–4.2 typ. 2.5–4.35 for some cells	2.5–4.2	2.5–4.2	2.8–1.5
Avg. Voltage (V)	3.7	3.7	3.3	2.3
Specific energy (Wh/kg)	175-240	100-150	60-110	70
Energy density (Wh/L)	400-640	250-350	125-250	120
Continuous rate capability (C)	2-3	Over 30	10-125	10
Pulse rate capability (C)	5	Over 100	Up to 250	20
Cycle life at 100% DOD (to 80% capacity)	500+	500+	1000+	4000+
Calendar life (yr)	>5	>5	>5	>5
Self-discharge rate (%/month)	2-10 %/mo	2-10 %/mo	2-10 %/mo	2-10 %/mo
Charge/Discharge temperatures (ºC)	0 to 45 / -20 to 60	0 to 45 / -30 to 60	0 to 45 / -30 to 60	-20 to 45 / -30 to 60
Power density (W/L) (pulse)	~2000	~10000	~10000	~2000
Specific power (W/kg) (pulse)	~1000	~4000	~4000	~1100

Battery manufacturers offer a wide variety of cell specifications, ranging from cell capacities, architecture design and performance, to name a few. The most important battery manufacturers are concentrated in the Asia region and North America. A few examples of the most important battery manufacturers are Sony, Panasonic, Sanyo or LG Chem (Asia region) and A123, Johnson Controls or Altairnano (North America).

2.5.3. Lithium iron phosphate (LFP) batteries

Since its discovery in 1997 by Goodenough's group [107] lithium iron phosphate (LFP or $LiFePO_4$) cathode materials have gained major attention in the literature and battery industry, due to its potential advantages. These can be summarized in: intrinsic safety and low toxicity, high cycle-lifetime, high-power capability, reliability, large availability of materials, flat voltage profile and low cost [42]. On the other hand, the main issues found with this technology are its relative low voltage resulting in low energy density, its poor lithium diffusion and a poor electronic conductivity [42]. However, approaches can be used to overcome the previous two issues, such as the use of nano-structured materials in its chemistry, among others [42]. Here are described the main characteristics and major advances of the LFP chemistry for its use in commercial LIB systems.

The crystal structure of $LiFePO_4$ (see **Fig. 2.25**a) belongs to the olivine family, and has a one-dimension tunneled structure, where the lithium insertion/extraction mechanism takes place. Similarly, the structure has a strong P-O covalent bond. These characteristics produce two of the main properties (drawbacks/advantages) of this material: one-dimensional tunnels can lead to poor rate capabilities because of the low diffusivity properties [108], whereas a strong P-O covalent bond rules out any risk of oxygen release, which makes this material very stable, even at 400ºC (LCO starts to decompose at 250ºC) [42]. Similarly, the high lattice stability, with volume changes upon Li insertion/extraction of only ~7%, results in excellent cyclic performance and operation safety. The two-phase transformation from $LiFePO_4$ to $FePO_4$ produces a long, flat plateau at 3.43 V vs. Li., which provides a theoretical specific capacity of 170 mAh/g, as observed in **Fig. 2.25**b.

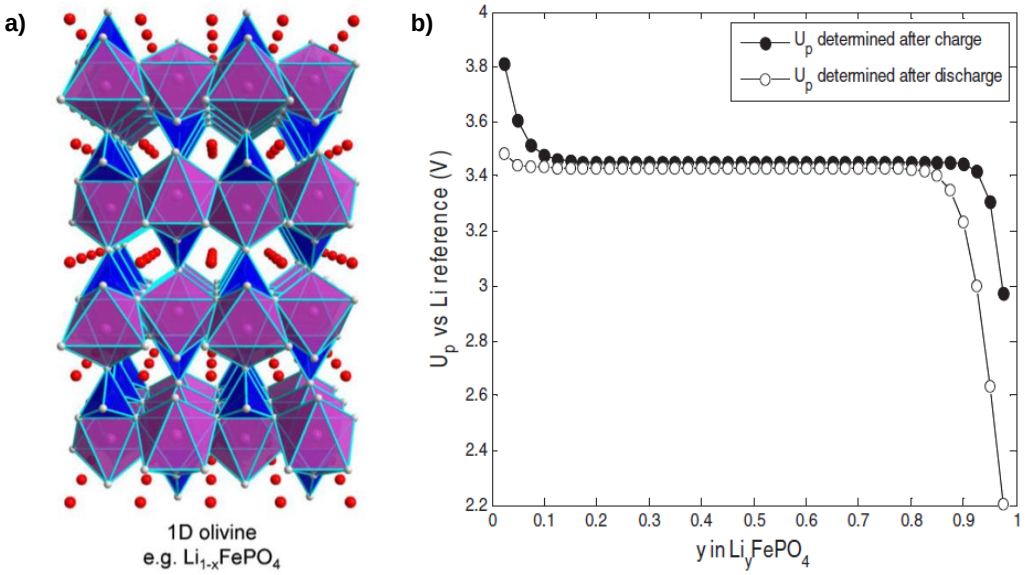

Fig. 2.25. a) Insertion compounds hosts with 1D interstitial space for Li ion transport [109], and b) thermodynamic charge/discharge process of LFP positive electrode material [110].

In recent years, major efforts have been made to overcome the drawbacks of LFP to reach successful commercialization. A key technology breakthrough was made by Chung *et al.* [111] in 2002, when they were capable of increase the electronic conductivity of $LiFePO_4$ by a factor of $\sim 10^8$, reaching values of $\sim 10^{-2}$ S/cm (compared to $\sim 10^{-3}$ S/cm found in $LiCoO_2$). In addition, high capacity rates (up to 40C) were also achieved, making this material ideal for high-power, safe applications. From that point, many contributions were made in the following aspects: particle size to improve rate capability and cycling stability, doping to increase the diffusion, carbon coating to improve specific capacity, and in synthesis method techniques to improve the manufacturing process. Readers can be referred to excellent review by Zhang [42] and Section **3.2.2** of this thesis to get insight details of these contributions.

As a result of the improvements, commercial GIC||LFP batteries have reached impressive power capabilities (4,000 W/kg) and long cycle (over 2,500 cycles). Indeed, post-mortem studies on commercial GIC||LFP batteries showed no signs of degradation on the LFP electrode when reaching end-of-life, and degradation was attributed to the NE [59], [61], [68], [78]. Still, cycle life evaluation under combined calendar, and/or dynamic cycling still needs to be carefully evaluated for HEVs, EVs and grid energy applications. In addition, improvements in energy density and reduce the energy cost of LFP batteries are required to both meet the technical requirements of EVs, and make this technology more competitive in portable electronics applications.

2.6. Summary

This chapter has given an account of the state of the art of commercial lithium ion batteries (LIBs). Here we provide a review of the battery fundamentals and materials, aging mechanisms on LIBs and the aging scenarios, to finish with an overview of the characteristics and performance of commercial LIBs. The descriptions provided here are used throughout this thesis work.

The operation principles of LIBs have been described first, focusing on the thermodynamics and kinetics aspects. In this thesis, the thermodynamics (i.e. equilibrium conditions) are assumed to be reached within 2h of cell rest or at C/25 cycling. In particular, C/25 cycling is widely used in this thesis to study several internal parameters of a battery, including its aging mechanisms. The kinetics (i.e. current flowing) include several sources of polarization that cause energy losses within a battery.

Although new chemistry materials and synthesize approaches are being developed, today, the majority of commercial LIBs use a graphite-based negative electrode (NE). Hence, its study has been covered here. For clarity, the staging phenomena on the NE are labeled with numbers (❶-❺); this numbering is widely used in this thesis work, particularly for aging analyses. A review of common commercial cathode materials, electrolytes and additives is also provided, highlighting the most commonly used materials and their main characteristics.

One of the most important phenomena that occur in a LIB is the solid electrolyte interface (SEI). The SEI is a protective layer formed during the first cycles in the electrode-electrolyte interface as a result of electrolyte decomposition, causing initial capacity losses of ~10-15%. Subsequent cycling also induces capacity losses, although in a much smaller quantity, due to its protective properties. An effective and robust SEI layer is a prerequisite for optimal performance of a LIB.

Currently, battery aging identification is one of the most significant (and challenging) fields of study in LIBs, and is a key subject in this thesis. In general, a LIB ages by capacity and power fade. However, the phenomena that cause aging are more complex, and can be originated from multiple mechanisms that can be acting simultaneously. The main aging mechanisms are: loss of lithium inventory (LLI), loss of active material (LAM), ohmic resistance increase (ORI) and lithium plating. In this chapter, each aging mechanism is presented schematically from an individual electrode perspective to provide a better understanding of the aging modes. This type of representation is used throughout this thesis.

Summarizing, the LLI is considered the main cause of degradation in LIBs. It causes loss of usable Li ions due to parasitic reactions originated in the NE electrode/electrolyte interface. The aging mode LAM is also common in LIBs, usually accompanied with LLI. The LAM is caused by the structural degradation of the electrodes, mostly affecting the NE. Also, LAM may cause "silent" degradation effects, which can lead to sudden appearances of capacity loss, known as second degradation stages. The ORI can result from several sources of aging, and causes a reduction of the energy efficiency of a LIB. Lastly, Li plating can be considered as the most detrimental aging mechanism; it leads to further aging, and also causes safety concerns due to dendrite growth that can short-circuit the cell. In total, battery degradation can be very complicated, as it may be caused by various aging modes acting (or not) simultaneously. With the analyses provided here we aim to enhance the understanding of the aging mechanisms and establish the fundamentals for the analyses covered in subsequent chapters of this thesis.

Battery aging can be separated into two parts: the calendar aging and the cycle one. In general, high temperatures coupled with high current rates and high SOCs are the most detrimental cycling conditions for LIBs. Under storage, high temperatures and, in less degree high SOCs, are the main factors that cause capacity loss. Hence, understanding the causes and effects of degradation is useful to minimize battery aging.

To complete the review, the characteristics of commercial battery design architectures and performance characteristic of various LIB chemistries are presented. This study provides a general overview to facilitate the battery of choice for a given application. Special consideration is given to lithium iron phosphate (LFP) batteries, due to its advantages and increasing interest in the industrial and research community.

This page intentionally left blank

3. Fast charging in Li-ion batteries

Fast charging is an important area of study in Li-ion batteries. The reduction of the charging time in battery operated systems such as electric vehicles (EVs), electrical energy storage (EES) or electronic devices is highly demanded. In the case of EVs, the reduction of the charging time is a crucial factor to increase its commercialization. Battery powered renewable EES systems also demand fast charging capabilities during peak intermissions. Similarly, the ability to perform charges in few minutes in portable electronic devices will boost its market value and improve mobility. Therefore, fast charging is a demanded capability, which improves the characteristics and value of battery systems.

Unfortunately, fast charging may affect the battery's performance by accelerating its aging. This is because fast charging typically involves high current rates which may lead to high cell temperatures. As presented in Chapter 2, high current and high temperatures are known to be some of the main factors to induce battery deterioration. Hence, it becomes necessary to analyze the technical factors to achieve fast charging without adding further aging to the battery.

Despite several efforts to achieve fast charging, to date, there has been little agreement on what strategies should be applied to achieve efficient and reliable fast charges. Most fast charging protocols do not address in detail the importance of the battery technology of choice, or safety issues related with fast charging. In particular, here we identify that fast charging can be enhanced by properly selecting a battery architecture optimized for fast charging (i.e. high power batteries) coupled with the use of an appropriate fast charging protocol. Indeed, the two technical subjects are interrelated, as different battery architectures lead to various voltage and current limitations.

This chapter addresses the important subject of fast charging. It starts analyzing the design factors that enhance LIB capabilities for fast charge. The analyses provide the required information to select the adequate battery architecture and technology for fast charging applications. Thereafter, an updated overview on fast charging methods is presented. The resulting conclusions enhance our understanding to improve fast charging protocols. Next, we present a new step-by-step guideline to implement fast charging, showing the most relevant factors to take into consideration for achieving an effective and reliable fast charge. As part of the main objectives of this thesis work, the chapter ends with the design of a fast charging protocol. The protocol is developed following the previous guidelines to implement fast charge, and is applied to a high power lithium iron phosphate (LFP) battery.

3.1. Battery fast charging: definitions and objectives

Nowadays, the specific goals to achieve fast charging are problematic to be established, as they depend on multiple parameters. This includes the charging time, energy efficiency, temperatures, the LIB technology of choice and the charging protocol complexity (which would lead to more expensive and complex electronic charger systems), to name some parameters. Similarly, external factors found in fast charging are the charging station power capability, the charging infrastructure, or the economical limitations. The latter factors are significant in high capacity systems, such as EVs [112] and EES systems.

The United States Advanced Battery Consortium (USABC) proposes a fast charging test for EVs. The USABC goal of fast charging (for batteries capable of such usage) is defined as when a battery is able to return 40% of the SOC within 15 min [16]. This is approximately a charging rate of ~2C hold during 15 min. However, low power systems such as mobile phones may require fast charging capabilities to fully recharge a battery within few minutes, using charging rates as high as up to 6C [113]. In general, in the battery engineering community fast charging is usually accepted when a battery system can be fully recharged in less than 1 h [81], [114].

The main objectives of fast charging can be summarized in five points: (1) shorter charging times than regular charging, (2) a reliable charging protocol that minimize fading-induced impacts on battery performance, (3) eliminate unwanted safety concerns, (4) efficient energy transfer, and (5) a simple charging protocol for ease implementation in electronic charger systems. In other words, a good fast charging process shall be quick and simple, adding the minimal detrimental effects to the battery.

As stated, the objectives of fast charging are related with the battery technology and the charging protocol. The following sections analyze both subjects.

3.2. Li-ion battery architecture design for fast charge

The LIB architecture design plays a significant role to achieve fast charging. To permit fast charge, battery architecture design include multiple factors to consider, namely the use of materials optimized for high rate operation, the use of nanomaterials in the electrodes, or the use of conductive additives, to name a few [100]. From the different battery configurations of choice, high power (HP) designed batteries accommodate best for fast charging.

This section aims to provide a description of HP cell design principles, studying the key factors to optimize fast rate capabilities. As this area of study is heavily based on material science and solid state fundamentals, and both fields are out of the main areas of this thesis, this section is therefore more oriented towards practical applications. The objective is to emphasize the importance of HP cell design, to properly select the right LIB to achieve fast charging. Readers interested in HP design considerations at the microstructural and materials science level shall be referred to excellent reviews in the field [3], [18], [100], [115].

3.2.1. Design rules for high power (HP) cells

High power density batteries primarily derives from kinetic effects associated with charge/discharge transport rates, ionic conductivity in the electrodes and electrolyte, and interfacial charge transfer resistance [115]. Hence, reducing the kinetic effects enhances the charge/discharge capabilities. This is observed from the expression of the voltage of a battery, as is dependent on both thermodynamic (E_{OCV}) and kinetic effects (R_{Cell}), i.e. $V_{\mathrm{Cell}}(I) = E_{\mathrm{OCV}} - IR_{\mathrm{Cell}}$. The larger the battery current *(I)* is, less energy is drawn from the battery during discharge, and vice versa during charge. Therefore, the optimization of HP batteries is oriented towards minimizing the kinetic effects and enhance rate capabilities.

As stated, the high power densities of HP batteries allow high charge/discharge rates. On the contrary, HE batteries maximize energy density in detrimental of power density. As a result, HP and HE batteries compete with each other. This is observed in **Fig. 3.1**, where HP LIB systems have low energy density, and vice versa. However, even if fast charging requires HP cell designs, energy density is still a critical parameter for many applications (e.g. EVs, laptop computers), as the LIB cannot be too heavy or bulky. The intrinsic question to optimize HP cells to reach both HP and HE key characteristics can be improved by using several techniques. These techniques reside within the engineering and basic science level, modifying constructive parameters and/or selecting active materials with higher power capabilities.

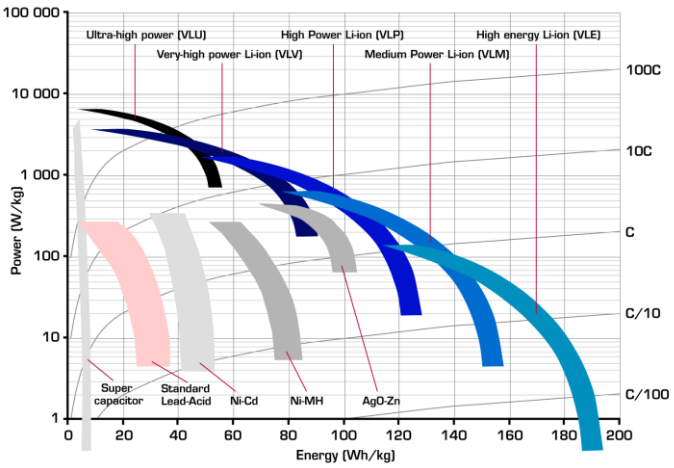

Fig. 3.1. Specific power vs. energy density plot, showing the relation of power and energy of commercial LIBs [116].

The optimization design of HP cells depends on both system chemistry and system design. The optimization approach can be divided into two levels, namely engineering and basic science level, as shown in **Fig. 3.2**. The engineering level deals with geometrical design and constructive parameters, to optimize cell weight and volume. Similarly, tabs distribution and current collectors design falls into this level. Respecting basic science level, active material properties, such as conductivity and porosity to enhance power capabilities can be enclosed in the category. The frontier here with the engineering level is slim, and both levels may coexist. Basic science level also includes the crystal structure, microstructure and surface coating which determines the lithium-ion and electron transport properties within the particles and the stability of the material. Particle size, particle architecture and the level of impurities of the material are also studied in this level.

Trade-offs often exists between different design factors, which impose practical limitations. For instance, requirements such as capacity, current rate capability, cycle life, processability, cost and safety, in most cases cannot be met simultaneously [5]. Still, several approaches can lead to optimal HP systems, where minimal energy density is sacrificed for power density.

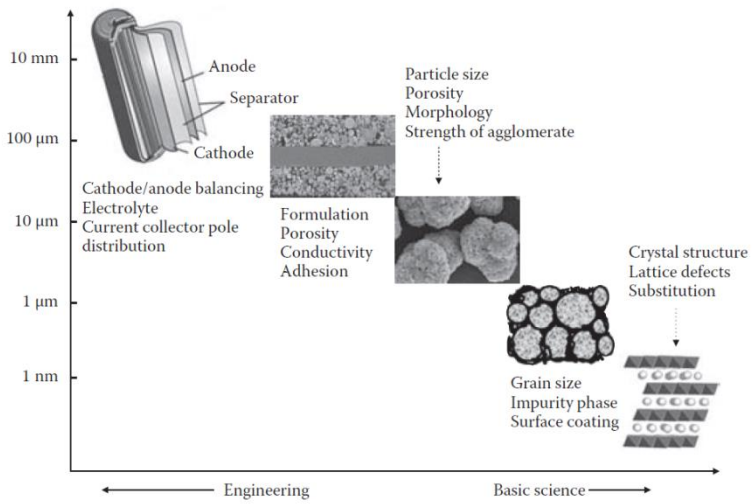

Fig. 3.2. Schematic diagram showing the main components affecting LIB performance [5].

Engineering level

HP cells are constructed in cylindrical or spiral wound cell design. This type of battery configuration optimizes power transmission by minimizing polarization losses caused by electrical resistance. For a spiral wound cell, the electrical resistance (R_{ohm}) of the electrode (if the cell is unwounded) can be expressed by the approximation:

$$R_{\text{Ohm}} = \frac{1}{k}\frac{t}{A_{\text{Cell}}}$$

where (k) is the conductivity of the electrode materials, (A_{Cell}) is the electrode area, and (t) is the thickness of the electrode. Hence, for a given electrode material, increasing the electrode area and reducing the electrode thickness minimizes the electrical resistance (R_{ohm}). Experiments carried out by Park *et al.* [117] studied the charging capabilities of a graphite||LCO based cell, and concluded that reducing electrode thickness (especially the PE) enhances the charging capabilities of the cell. They also found that cathode thickness is most important variable than anode in limiting the charging time. **Fig. 3.3**a-b shows the results of the experiments. Hence, maximizing the electrical conductance by adjusting cell geometry parameters leads to improve HP cell designs.

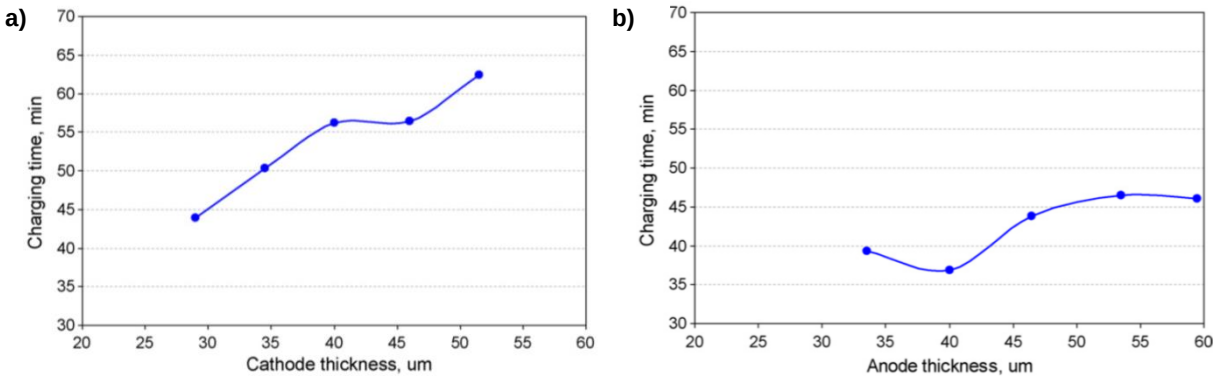

Fig. 3.3. Charge time based on electrode thickness a) cathode and b) anode [117].

Cylindrical LIBs ideally have a pair of long, wide continuous current collector wound, as shown in **Fig. 3.4**a-b. The electrical current of the cell is transported through the tabs of the current collectors. The cell design and tabs distribution affects the power capabilities of LIBs. Lee *et al.* [118] simulated

different tab distribution, and they concluded that very few tabs (see **Fig. 3.4**a) reduce the power capabilities of the cell, because non-uniform kinetics are produced. This results in an increase of cell impedance, and a reduction of its lifetime [118]. On the other hand, continuous tab design (see **Fig. 3.4**b) increases mass and cost, hence reducing the energy density of the cell. Therefore, a current collector shall have an optimized tab distribution.

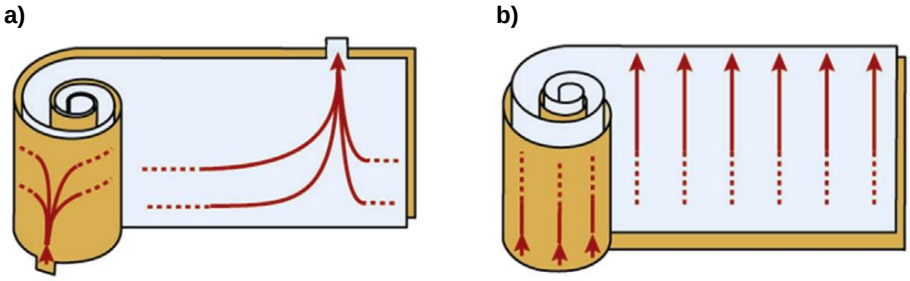

Fig. 3.4. Impacts of tab design on electric current in current collectors: a) cell with localized discrete tabs, b) cell with continuous tabs [118].

Other engineering parameters that enhance the charging capabilities are the separator and the loading ratio (LR). Experiments by Park *et al.* [117] showed that thin separators designed with high porosity enhances the charging capabilities of a LIB. The LR has to be sufficient to avoid Li plating, especially under fast rates. The PE has to completely release all its Li ions before the NE is fully lithiated, otherwise Li plating occurs. This is achieved by increasing the LR [58]. Similarly, the NE area has to be extended beyond the edges of the PE to avoid Li plating. Even 1 mm can significantly delay the occurrence of Li deposition [81].

Basic science level

At science level, the ionic conductivity of the electrolyte can be increased by modifying the ionic concentration and solvent composition of the electrolytes. Park *et al.* [117] showed that when the ionic conductivity of the electrolyte was increased, the charging time of the cell was reduced. Indeed, higher ionic conductivity of the electrolyte enhances the mobility of ionic species, which increases the charging rate of the cell [117]. The results of the experiment are shown in **Fig. 3.5**.

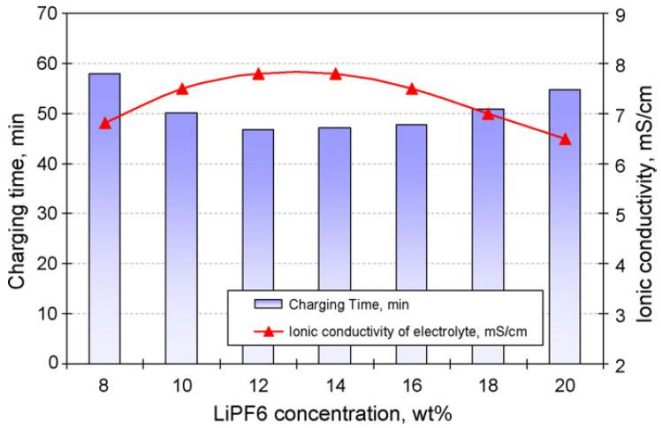

Fig. 3.5. Ionic conductivity of electrolyte and charge time of cells, based on $LiPF_6$ concentration [117].

The diffusivity of Li-ions in the electrode materials is the rate limiting component and the primary contributor to transport resistance [100]. The governing equation for ion transport is the Fick's law of diffusion. In general, the time constant for diffusion is proportional to the diffusion distance squared over the diffusivity. According to Fick's law, high discharge rates (or low diffusivity constant of materials) lead

to concentration and voltage gradients, as there is insufficient time for the ionic species to diffuse across the active material. In addition, slow diffusion kinetics leads to only partial lithiation and delithiation, as a result of which only a small fraction of the theoretical capacities are obtained, especially at higher cycling rates [3]. Hence, increasing the diffusivity of the active material improves the rate capability of LIBs.

The diffusivity of Li ions in the solid materials, the diffusivity of Li ions in the electrolyte, the conductivity of Li ions in the electrolyte and the electronic conductivity in solid materials are intrinsic properties (independent of the distances traveled by ions and electrons) of cell components and must have high values to reduce the transport ohmic or diffusive resistances [100]. Additionally, the transport ohmic and diffusive resistances can be also reduced if the electronic percolation network distances, the lithium ions through the tortuosity of the powers between particles, and the lithium ions inside the solid particles of the electrode are all minimized [100].

Charge transfer processes also affect the rate capability of LIBs. Charge transfer occurs at the surface of the active material particles, and its rate is dependent on the current and proportional to the superficial area. To reduce the charge transfer potentials, an increase in superficial areas is desired. This can be done by maximizing the active material surface area contacts. In this regard, the use of nanomaterials plays a significant role. Nanomaterials have a high surface/volume ratio to enhance surface area contacts, and are increasingly used in the design of HP batteries.

Summary of design rules for high power (HP) cells

Here is presented the design rules that battery manufacturers can control to optimize the performance for HP cells. As commented above, the key for high power is to decrease the polarization resistances, so energy can rapidly be extracted. This is done through various engineering and science level methods. The most important parameters, extracted from the excellent review on high power rechargeable batteries by Braun *et al.* [100] are:

(i) Active material solid-state ion diffusivity (maximize)
(ii) Electrical conductivity (maximize)
(iii) Solid-state path lengths for ion transport (minimize)
(iv) Path lengths for electron transport (minimize)
(v) Electrode/electrolyte contact area (maximize)

Unfortunately, for practical issues attaining the five points is extremely difficult, and sometimes even counterproductive. For instance, increasing the superficial area of active material particles indeed reduces charge transfer potentials, but also enhances side reactions inducing to the loss of active material (LLI). Another example is that while reducing particle size may enhance mass transport, it typically reduces packing efficiency in the electrode, decreasing the energy density. Despite the drawbacks, manufacturers have succeeded in producing HP batteries with decent energy density values.

3.2.2. High power chemistry designs

Active material chemistries with high power properties such as fast kinetics and low resistivity are ideal for its use in HP cell designs. In some cases, even active materials with low electronic conductivity (such as LFP) can take advantage of the use of nanomaterial and microstructure techniques to enhance its properties. Due to their relevance in current investigations, here is presented a quick summary of nanomaterial principles for LIB applications. This is followed by presenting high rate chemistries, paying special attention to nanomaterial based LFP cathodes.

Nanomaterial principles for Li ion battery applications

The formal definition of nanomaterials, adopted from the European Commission, stands that "a nanomaterial is a natural, incidental or manufactured material containing particles, in an unbound state or as an aggregate or as an agglomerate and where, for 50% or more of the particles in the number size distribution, one or more external dimensions is in the size range 1 nm – 100 nm." [119].

Nanomaterials for LIB applications can be used to make a significant impact on the performance of LIBs, as their reduced dimensions enable far higher intercalation/deintercalation rates, and hence power [18]. This is one of the several properties that may be enhanced by the use of nanomaterials. However, nanomaterials are certainly not a panacea, and have several drawbacks that need to be addressed. A summary of the main advantages and disadvantages of nanomaterials for LIB applications is presented in **Table 3-1**, extracted from [18].

Table 3-1. Summary of advantages and disadvantages of nanomaterials for Li-ion batteries [18].

Advantages	Disadvantages
Electron and ion transport within the particles is enhanced by reduced dimensions. Shorter distances increase the rate of charge/discharge process significantly	Nanomaterials may be more difficult and costly to synthesize, and dimensions may be more difficult to control on a large scale
The reduced dimensions increases significantly the rate of lithium intercalation/deintercalation, because of short distances for lithium-ion transport within the particles	A high electrolyte/electrode surface area may lead to more significant SEI side reactions with the electrolyte, and there could be more difficulty in maintaining interparticle contact
Electrode redox reactions that cannot take place in the micrometer-sized particles are enabled	The densities of nanomaterials are generally lower than that of micrometer-sized particles. The volume of the electrode increases for the same mass of material, thus reducing the volumetric energy density
A high surface area permits a high contact area with the electrolyte and hence increased ion fluxes across the interface	Nanomaterials with high surface energy tend to form agglomerates. This makes it difficult to disperse and mix them with carbon and binder
The chemical potentials for lithium ions and electrons are modified, resulting in a change of electrode potential	
The range of composition of solid solutions that exist is often more extensive for nanoparticles	
More strain associated with lithium-ion intercalation/deintercalation can be accommodated	

To sum up, reviews in this field [3], [18], [19], [100] agree that next generation LIBs will exhibit higher energy and higher power, and are expected to heavily rely on the use of nanostructured materials. However, investigations of the mechanism ruling the interaction between lithium and the nanosized materials, and electron transport properties need to be addressed. Similarly, challenges towards improving large-scale applicability and commercialization of LIBs using nanostructured materials are also a major liability.

High rate anodes

To increase the power capabilities of commercial LIB graphite anode materials, nanoparticle graphite could be used, as it would increase the Li intercalation/deintercalation rate. However, side reactions coupled with the formation of the SEI layer at the anode using nanoparticulate graphite would be vastly increased, because of the high-surface-area/volume ratio of nanoparticulate graphite. More importantly, the Li plating could be catastrophic for nanosized particles, leading to major safety

concerns. Hence, increasing the rate capability of LIBs by using nanoparticulate graphite presents formidable problems [18], hampering its commercialization.

A strategy to increase the power capabilities carbon materials is focused in the optimization of soft and hard carbons , porous carbon and carbon nanotubes (CNTs) [120]. Soft carbons represent the state of the art of anode materials in commercial LIBs, while hard carbons (are gaining attention, due to larger reversible capacity (more than 500 mAh/g). Lithium intercalates in layered carbons such as graphite and soft carbons, and it adsorbs on the surfaces of single carbon layers in nongraphitizable hard carbons [121]. However hard carbons have very poor rate capacity because the lithium diffusion is very slow [19]. Recently, J. Yang *et al.* [122] sythesyzed nano-porous hard carbons which exhibited high capacity (500 mAh/g), good cycling life and high rate capability. High rate capability was related to the high diffusion (D = 4.11 x 10^{-5} cm^2/s – graphite has 10^{-12} to 10^{-5} cm^2/s), associated for to the hierarchical nanoporous network.

The microstructure of graphitic anodes designs (i.e. HP and HE) were studied by Ender *et al.* [120], where, through X-ray nano-tomography techniques, parameters such as particle size, porosity or volume specific area (m^2/m^3), were set, according to produce HE or HP materials. They showed that HE and HP graphitic anode microstructures result in slightly different voltage profiles (see **Fig. 3.6**a), while maintaining the typical plateaus of the intercalation in GICs. Similarly, **Fig. 3.6**b shows the visualization of reconstructed volumes of HP and HE graphite anodes. The microstructure details show that active material volume fraction of the HP graphite is lower, whereas the porosity is higher, when compared to HE graphite anode. Also, particle size is smaller in HP than in HE anodes. These different design aspects enhance the high power capabilities of the HP graphite anode.

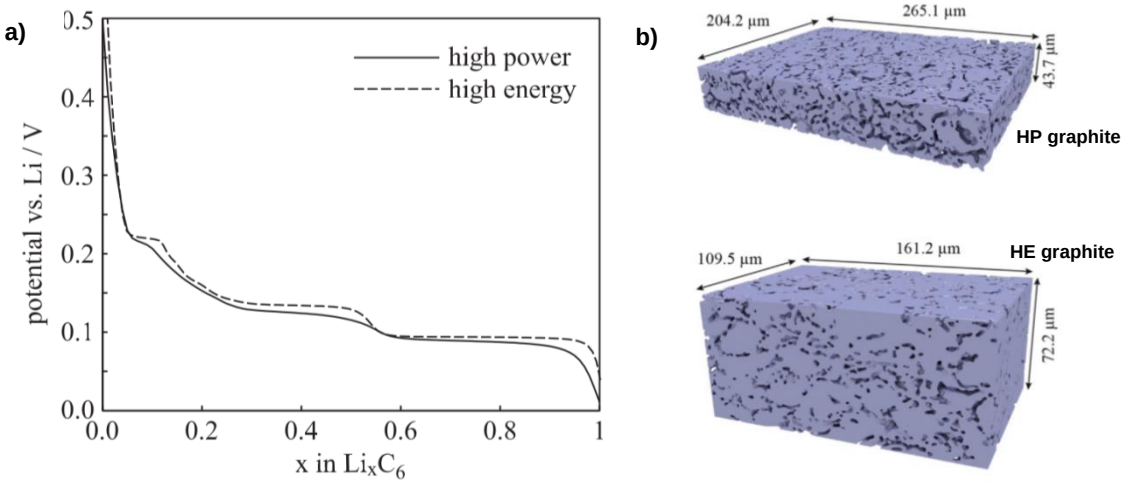

Fig. 3.6. a) Open circuit potential of the high power (solid line) and high energy (dashed lines) graphite anodes obtained from half-cell measurements against a lithium metal electrode and b) three-dimensional rendering of the reconstructed volumes of high power and high energy graphite anodes [120].

Research activity in CNTs is intense, due to superior electronic conductivity for HP applications, good mechanical and thermal stability, transport properties and large capacity (1116 mAh/g) [19]. However, CNT technology is not yet considered mature enough.

Other high rate anodes include titanium based oxides and alloy/de-alloy materials. Already commercially available, LTO has excellent charging capabilities (up to 6C) [123] and cycle life (over 5000 cycles). Downsizing titanium based oxides to nanoscale increases high charge/discharge rates, up to 10/100C respectively [124]. Research activity to overcome the main drawbacks of LTO (i.e. high operative potential and low capacity) is taking place at laboratory scale, using titanium dioxide and nanotube composites built on graphene layers [19]. Alloy/de-alloy materials (i.e. Lithium with Silicon, Germanium

or Tin oxide) are expected to fulfil the power demand for the next generation of LIBs. As shown in Section **2.2.1**, these materials have the largest specific capacities, high energy density and are safe. To overcome its drawbacks (i.e. large volume expansion and capacity loss over cycling), research is focused towards nanostructured materials with different morphologies like nanowires and nanotubes [19].

High rate cathodes

Olivine LFP materials for high power applications deserve special attention. As commented in Section **2.5.3**, the main issues found with intrinsic LFP materials are low potential (3.4 V), resulting in relatively low energy density, its poor lithium diffusion and a poor electronic conductivity. To improve its power capability, several approaches are applied. Nanoscaling LFP provides high rate capabilities due to shorter lithium ion diffusion distances. In addition, LFP powders are coated with a conductive carbon layer to increase electrical conductivity. For example, Wang *et al.* [125] synthesized nanosize carbon-coated particles to yield LFP particles of 20-40 nm electronically connected (see **Fig. 3.7**a). They demonstrated high power discharges at 60C discharge rate. The downside of this approach is that adding inactive materials such as carbon particles increase mass without contributing to capacity, thereby lowering energy density. Also, LFP nanoparticles coated with a thin fast ion-conducting layer increase power density. Kang and Ceder [126] demonstrated that discharge rates as high as 400C (see **Fig. 3.7**b) could be achieved using this approach. However, due to high carbon loading (up to 65 wt%), the capacity was reduced to 60 mAh/g. Other techniques to enhance LFP rate capabilities are the use of nanowires and hollow LFP cathodes, as described by [127].

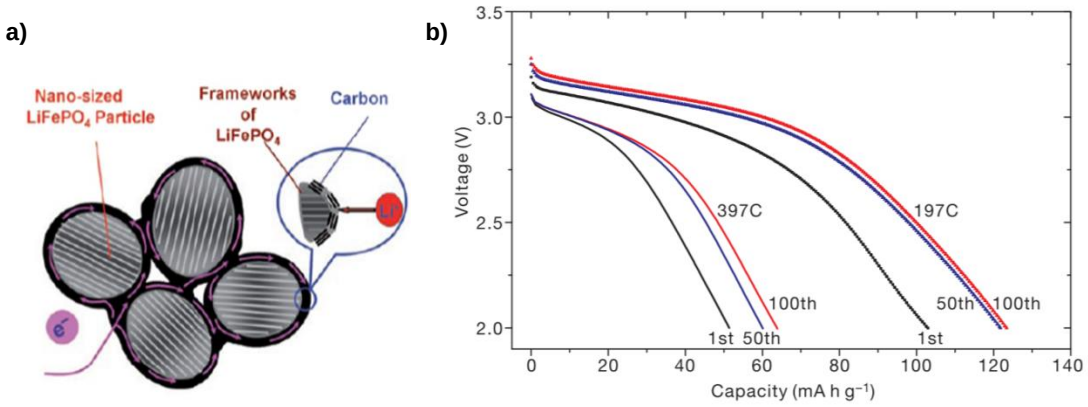

Fig. 3.7. a) Schematic of electron and ion transfer pathways for $LiFePO_4$ nanoparticles fully coated with carbon [125]. b) Ultra high rate capabilities achieved by increasing the mass loading of conductive carbon black in $LiFePO_4$ nanoparticles [126].

Although some of the figures and rate capabilities cited above are laboratory-scaled experiments, nanostructured LFP is the most recent cathode material that has gained commercial success in LIBs. With the initial studies carried out by Chung *et al.* [111] in 2002, A123 Systems, LLC, a battery company specialized in nanophosphate materials licensed from Massachusetts Institute of Technology was established. Indeed, due to its advantages and characteristics (later disclosed in Chapter **5**) a battery model of A123 is used in this thesis work.

Other high rate cathode materials based on spinel structures are considered promising because of their low price, relative safety and environmental friendliness. As with LFP, these materials are nanostructured to enhance Li-ion and electronic conductivity [100]. In general, contrary to the NE, most of the lithium intercalation compounds for PE in LIBs have been prepared in the form of controlled nanostructuring (e.g. nanoparticle, nanowire, nanotube, nanorods, etc. [100]) to enhance its properties. Still, various challenges to commercial high-rate batteries using controlled nanostructuring remain, including costs and scalability.

3.3. Li-ion battery fast charging methods

To achieve effective fast charging, the selected battery technology and architecture has to be complemented with the use of an optimum charging protocol. The charging protocol should aim to shorten the charging time, improve charging efficiency, minimize any performance attenuation and sustain a safe operation of the battery.

This section provides an overview of the most commonly used charging techniques in LIBs. Here we show that some charging protocols not always success to meet the aims of optimal fast charging. For example, some techniques shorten the charging time, but fail to maintain safe operation. In this section we analyze and point out the key parameters to develop a reliable charging protocol and establish fast charging fundamentals. The charging techniques reviewed in this section were carried out at ambient temperature.

3.3.1. Constant current–constant voltage (CC–CV) method

The most common process to charge LIBs is a consecutive two-step constant current (CC) - constant voltage (CV) charging process, CC–CV. In the first step, the battery is charged at CC at a given C-rate until the voltage of the battery reaches a predetermined cut-off voltage. In the second step, the battery is fixed to the cut-off voltage and the charging continues until the current declines to a pre-determined, end of charge (EOC) current value (see **Fig. 3.8**). The values of the CC rate and the predefined cut-off voltage depend on the LIB chemistry. These parameters are specified by the battery manufacturer to operate the battery under standard charging conditions. In contrast, the EOC current is independent of the battery chemistry, although most LIB manufacturers recommend a current of ~C/20 in the CV stage to reach full charge. Since the CC–CV method is easy to implement, performs efficient charges and is reliable at mid to low charging rates, it has been denoted as the standard charging method for LIBs.

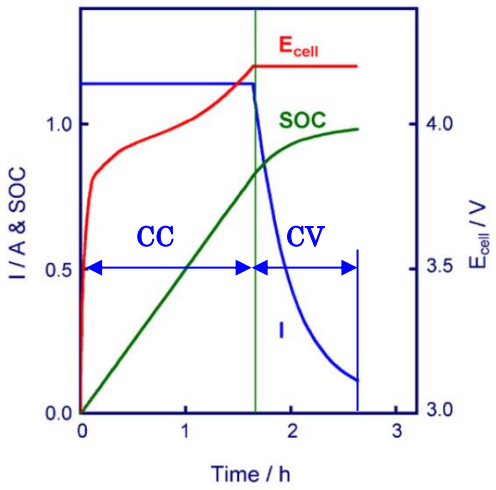

Fig. 3.8. Characteristics of the CC-CV charging protocol. Blue line represents the current, red the cell voltage and green the SOC [128].

Despite its advantages, one major drawback of the CC–CV method is that it takes long time (mainly in the CV stage) to fully charge the battery. Charging times of over 2 hours are common using the CC–CV method [128], [129]. To reduce charging time, high charging rates are required. However, high currents decrease the charging efficiency due to Joule heating, and may cause Li deposition at the end of the CC stage, as shown in [58]. Additionally, increasing the charging rate above a certain level does not reduce the charging time. This is because the increase of polarization reduces the charged capacity during the CC stage, where most of the capacity is charged (see **Fig. 3.8** green line). On the contrary, the

CV stage prolongs the charging time, as current decays. However, the CV stage is necessary to prevent overcharging, reduce battery's temperature and achieve full charge.

To summarize, the applicability of the CC–CV method for fast charging is limited and highly dependent on the LIB technology. Caution must be taken at high charging rates, as it may induce to Li deposition. However, for slow charging this method is reliable, efficient and easy to implement.

3.3.2. Constant voltage (CV) method

The constant voltage (CV) charging method was developed as the simplest strategy to reduce the charging time of the CC–CV standard method. The CV method skips the CC stage and starts charging the battery directly at CV, to terminate when the current drops below a certain level. Since it only consists of one charging stage, its design and concept is simple.

To study the possible advantages of the CV method, Sikha *et al.* [130] compared regular CC-CV vs. CV charging on commercial LCO cells. They found that although the CV method took half the time to recharge to 80% SOC, the capacity fade after 150 cycles was two times higher than that found on the CC–CV method. The capacity fade was associated to high initial charging rates (10C). To overcome such issues, Notten *et al.* [129] considered limiting the initial charging rates to 4.5C. They found that even if charging time can be reduced by half when compared to CC–CV, the capacity fade was at least 20% higher when charging at standard cut-off CV value (4.2 V), and more than 60% for higher CV set to 4.3 V (see **Fig. 3.9**). Both studies concluded that although the CV method can reduce the charging time, its effects are very detrimental to the life of the battery.

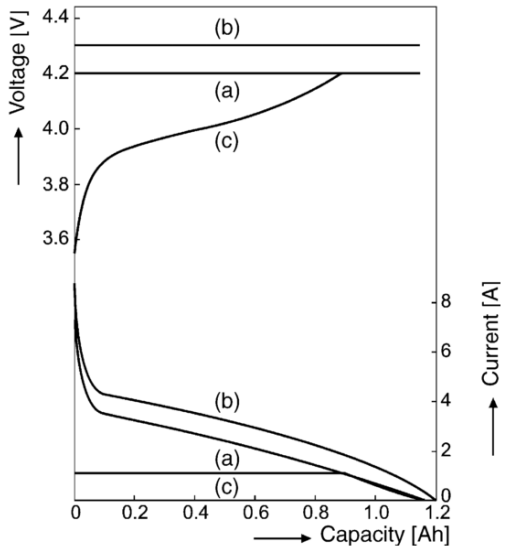

Fig. 3.9. Voltage and current characteristics of CV charging of a commercial LCO battery at V_{max} = 4.2 and 4.3 V (curves (a) and (b)), respectively. Standard CC-CV is shown in curves (c) for comparison.

Regardless of its simplicity, the main disadvantage the CV method is that demands very high initial charging currents rates. Due to the internal resistance (IR) of a LIB is in the mili Ohm range, a charging voltage within the 2.5 to 4.2 V range (commercial LIBs) can cause an initial current up to several tens of amps. Still, kinetic limitations occur within the battery and the amount of demanded current is limited by the intrinsic characteristics of the battery, and is reduced with the SOC. Similarly, charging continuously at the cut off voltage is detrimental to the battery, because electrolyte and active material decomposition leads to LLI and LAM [24], [36], [49], as seen in Chapter **2**.

To sum up, special cautions must be taken when fast charging using the CV method. Limiting the initial charging current and the pre-determined cut-off voltage may help to reduce both the charging

time and aging effects. Still, this charging protocol is not recommended to be carried out on a regular basis as it rapidly decreases the life of the battery.

3.3.3. Multistage charging method (MCM)

The multistage charging method was proposed to control the charging currents into different charging stages, either with stepwise descending and/or ascending currents. In general, to enhance the charging capabilities the design of the current stages is studied beforehand, taking into account the characteristics of the selected battery. Ideally, parameters such as the SOC, internal resistance evolution, or temperatures should be taken into consideration to design an optimal MCM. Therefore, this charging method is more advanced than the previous (CC–CV and CV). Experiments already started with Lead Acid [131] and Nickel batteries [132] for its potential use in EVs. Recently, MCM variations have been applied to LIB.

Multistage, boostcharging protocol was proposed by Notten *et al.* [129], based on the assumption that close-to-empty batteries can be recharged with very high currents for a short period of time without introducing major detrimental effects. The technique was carried out on LCO batteries, and consists on an initial CV stage limited to 5C and fixed to 5 min, followed by a standard 1 C, CC–CV stage (see **Fig. 3.10**a). The entire cycle was denominated CVCCCV charging. The results showed that a fully discharged battery can be recharged within 5 min to one-third of its rated capacity. However, to fully recharge the battery, the time is increased up to 60 min. Therefore, the capacity is mainly charged at the first CV stage, where the highest currents are applied. This method did not show significant impact on the battery cycle life.

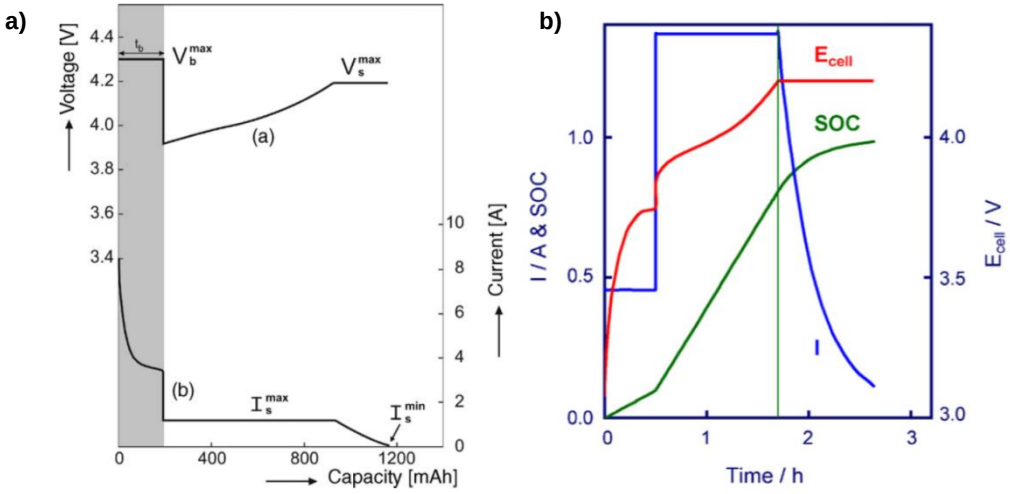

Fig. 3.10. a) Multistage boostcharging technique (CVCCCV), consisting of a limited boostcharge period (shaded region) followed by standard CC–CV charging [129], and b) multistage constant current-constant voltage (MCC-CV) charging technique [128].

A thorough study on the effects of the charging protocols on LCO batteries was carried out by Zhang [128]. The proposed multistage CC–CV protocol (MCC-CV, see **Fig. 3.10**b) was based on the analysis of the evolution of the IR with SOC and the consideration of the risk of Li deposition at high SOCs. The proposed strategy is to apply lower currents both at the beginning and near the end of charging, and higher current in the mid stage. Although this is a valuable strategy, the charging times were similar as regular CC–CV charging and the capacity fade was slightly higher. Indeed, the results showed Li plating caused by the mid CC stage, which lead to premature cell aging. Consequently, the study concluded that the protocol applied with the selected C-rates and cell technology was not effective or healthy. Still, the strategy reasoning is considered a good approach to enhance the charging capabilities. In fact, the rapid

capacity decrease was due to the use of rather high current rate in the second CC step which leads to Li plating.

Similarly, Liu *et al.* [133] proposed a multistage charging protocol based on an ant colony system algorithm, carried out in LCO batteries. Although the mathematical complexity of the algorithm is high, including positive feedback or distributed computation, the authors stated its applicability to real-life battery charging systems. In fact, the results showed a simple five step-wise, current decaying charging profile, which provided the battery with 25% more of cycle life than standard CC–CV charges, and achieved charges to 70% SOC in 30 min. Still, the computer load requirements appear to be high for its application on simple, yet reliable commercial battery chargers.

To our knowledge, the first fast charging protocol applied to LFP batteries was proposed by Huang *et al.* [134] in 2013. The design strategy is based on SOC evaluation and residual energy (amount of energy available) of the battery. The resulting charging profile is a multistage constant current based strategy (see **Fig. 3.11**). The LFP (1.1 Ah) cell charge starts with a slow initial CC stage at 0.5C for 30 min to avoid temperature rise, followed by a 1 min discharge pulse at 1C to eliminate cell overpotentials. This was followed by 5 min rest for battery relaxation. The last stage is a CC high rate charge (HRC) at 4C to finish the charging process. The results showed a notable reduction by half of the charging time, when compared to the standard C/2, CC–CV method. The cycle life evaluation up to 300 cycles showed no additional aging in terms of capacity fade. Still, in our opinion, although the protocol provides successful results, we shall remain conservative over the long term aging evolution, for various reasons: the protocol requires high currents of 4C, when the manufacturer recommends maximum rates of 0.5C. Also, the HRC stage is loaded at high SOCs for long time periods (20 min) with no voltage limitation. This causes the battery voltage to increase up to 4.5 V (3.65 V is the nominal). This high voltage could eventually lead to high electrolyte oxidation and decomposition, and lithium deposition in the NE. In our opinion, long-term evaluation should be carried out, since LFP batteries are designed to achieve long cycling periods of over 2,000 cycles [42]. In fact, "silent" degradation mechanisms that are enhanced during charge such as LAM_{deNE} could be developing, and cannot be deciphered through standard capacity evolution measurements [30], [31].

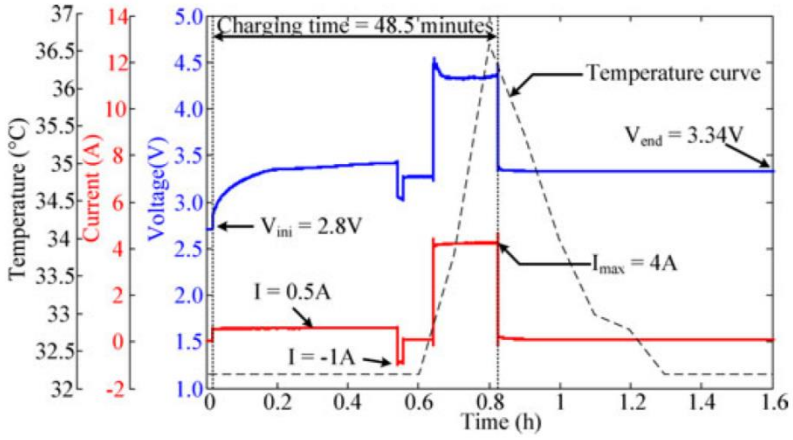

Fig. 3.11. Charge profile of the multistage charge method [134].

Recently (2014), a new multistage charging strategy was proposed by Vo *et al.* [135]. The battery technology selected was LMO (5.8 Ah) that permits maximum charging rates of 2C. The proposed strategy is based on a four stage constant current (FSCC) pattern, where each charging stage is set to 25% SOC (see **Fig. 3.12**). To select the optimal current rates (with the restriction of 2C as max. current), a mathematical approach based on the Taguchi method was developed, and the sequence of 1.8C, 1.3C, 0.9C and 0.5C was obtained. Similarly, this paper estimates the SOC of the cell to set the boundaries of the steps, through mathematical modeling. The results showed that the FSCC has better performance

than to standard CCCV, with a reduction of charging time of ~20%, and a slightly higher energy efficiency (1.5%) thanks to a smaller temperature variation (1.73ºC vs. 3.4ºC under standard charge).

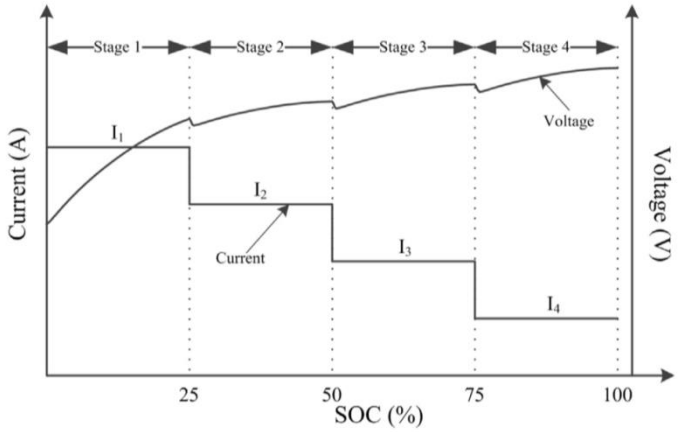

Fig. 3.12. Four stage constant current (FSCC) charging methods [135].

To sum up, the MCM is considered a high quality charging pattern, and can be applied using different methodologies. This method has important advantages to achieve both healthy and quick recharges, if applied properly. From the analysis, we suggest that the most convenient way to apply the MCM is through performing an early evaluation of the characteristics of the selected battery. Maximum charging rate and IR evolution with the SOC are key parameters. Applying low currents when the IR is at its higher values is recommended. Additionally, low currents must be loaded at high SOCs to avoid Li deposition. Similarly, exceeding the charging voltage limits must be avoided. Also, the length of the charging steps has to be determined through either experimental approaches or mathematical modeling.

3.3.4. Varying current method (VCM)

The charging process using varying current (VCM) consists in continuously modifying the charging current as the battery is being charged, based on different principles to optimize the charging process. For example, Chung *et al.* [136] optimized the charging process on a LMO battery, based on the theoretical models of lithium insertion into continuous non-porous electrodes. Although the model formulation is rather complex, the final results consisted on a simple, linear current decay profile (LCD) that performed faster charges by a factor of 2.5 than the standard method. However, several issues were found using this method; for example, Sikha *et al.* [130] on a study which compares several charging profiles, found that LCD method reduced the charging time, but also drastically reduced the cycle life of the LCO tested battery. This was caused by an overcharge of the positive electrode beyond the cut-off voltage. To avoid this problem, Sikha *et al.* [130] proposed a modified linear current decay (MLCD) protocol based on an empirical expression to reduce charging time avoiding cell overvoltage (see **Fig. 3.13**a). The obtained results were not satisfactory either: even though the charging time was reduced, the capacity loss after 150 cycles was two times higher than that found on the standard charging method. They suggested that possible electrolyte oxidation was caused by long charging periods within the cut-off voltage value, which lead to premature capacity fade and impedance increase. Interestingly, Purushothaman *et al.* [137] modelled the optimal charging profile of a LIB based on the maintenance of saturated interface concentration through the charging process, to obtain the maximum charging current without Li deposition on the NE. The optimal charging current profile exhibited a nonlinearity decrease, as shown in **Fig. 3.13**b, which is comparable as the one used by Sikha *et al.* [130] in **Fig. 3.13**a.

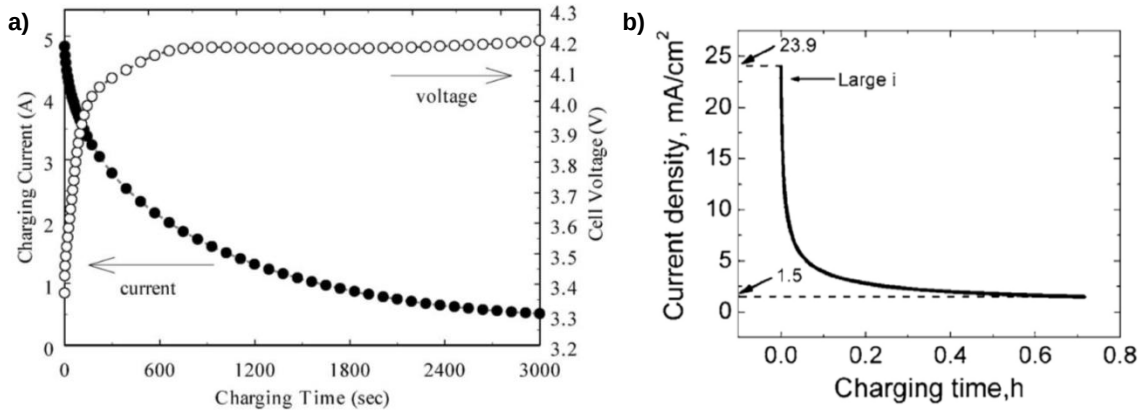

Fig. 3.13. a) current-voltage relationship of the modified linear current decay (MLCD) protocol [130] and b) optimal charging current profile based on the hypothesis of maintaining saturated Li concentration at the graphite electrode/electrolyte interface [137].

Recently (2014), a solid work by Z. Guo *et al.* [138], proposed a fast charging technique based on a nonlinear varying current profile. The charging profile is based on achieving an optimal fast and energy efficient charge that avoids CV step (see **Fig. 3.14**a). The strategy is based on impedance evolution with SOC coupled with a current decaying profile to accommodate the increase of Li ion transport overpotential in the electrolyte with SOC (see **Fig. 3.14**b). The charging parameters were derived from equivalent circuit modelling and algorithm optimization. The results showed better charging efficiency and cycle life than standard charging.

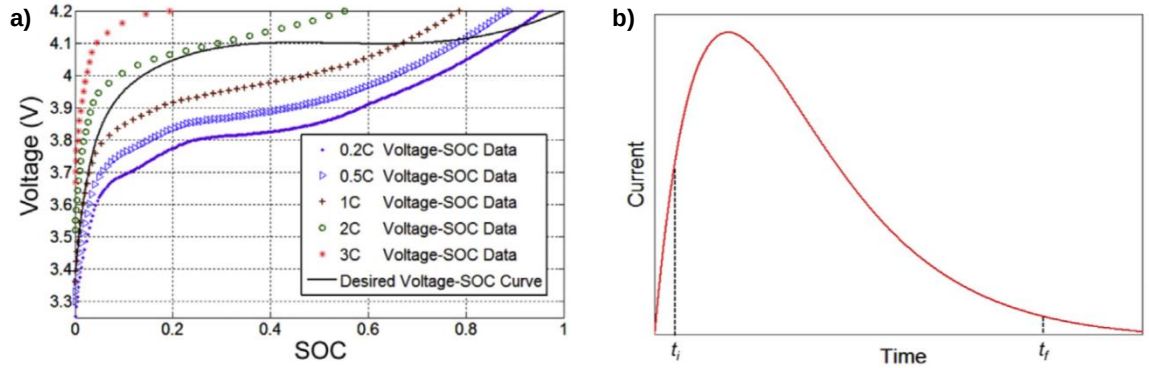

Fig. 3.14. a) Charging profiles at several C-rates and the desired charging profile to reach 100% SOC without CV step, and b) the charging current evolution for the proposed profile with nonlinear varying-current profile curve.

To conclude, the VCM methods are based on the optimization of charging process from a physical perspective. The problem is that quick recharges can be achieved, but with the risk of premature battery aging. Therefore, improvements must be carried out, so that the battery voltage never increases beyond the cut-off voltage [130] or the current accommodates to the polarization variations with SOC [138]. Additionally, as this method is based on physical models, it proves that low currents at high SOCs are favorable for quick recharges and to avoid Li deposition. This is in accordance with the analysis obtained from the previously described MCM method.

3.3.5. Pulse charging method

The pulse charging method consists in using short rest periods in the charging process, which can be accompanied by short discharge pulses. Relaxation time periods while charging allows Li ions to diffuse and distribute more evenly through the battery. Hence, this method is intended to eliminate concentration polarization at the electrode/electrolyte interface, to reduce the risk of Li deposition while

fast charging [81]. Due to its potential advantages, several authors carried out experiments. In general, there are various factors that may affect the functionality of this method, which shall be taken into consideration to optimize the charging process.

The effects of pulse charging on commercial LIBs were first studied in detail by J. Li *et al.* in 2001 [139]. The study compared three charging proposals: (1) pulse charging at 1C, (2) pulse charging at 0.5C and (3) standard 1C, CC–CV, carried out on LCO based batteries for 300 cycles. Unfortunately, the authors did not provide specific experimental information regarding the time length of the charging pulses, or the amplitude and length of the discharging pulses. Still, they showed that pulse-charging reduced the charging time to 1 h, while the standard CC–CV charge required 3.5 h. The XRD and SEM analysis showed that pulse charging reduced the effects of SEI build-up and surface cracking, both considered two major aging mechanisms [24], [36], [49]. They concluded that short relaxation periods accompanied by discharge pulses appeared helpful to eliminate concentration polarization, increase the power transfer rate and keep better electrode structural integrity.

Since the results obtained from J. Li *et al.* showed time reduction, additional works were carried out. In 2006, Purushothaman *et al.* [137] proposed various pulse charging profiles without discharge pulses. They found that pulse charging with constant pulse length and amplitude (see **Fig. 3.15**a) did not bring any potential benefit regarding inherent material transportation limitations in Li-ion batteries. On the contrary, continuously increasing rest durations (see **Fig. 3.15**b) or decreasing the pulse amplitudes (see **Fig. 3.15**c) was useful to relieve ion transportation limitations, and helped to reduce the charging time. Consequently, the depth of the region of the electrode affected by the pulses depends on the pulse length and pulse amplitude. In 2008, Chin *et al.* [140] carried out several experiments with positive charge pulses at various C-rates and rest periods. In addition to charging time reduction (< 1 h) when compared to standard CC–CV, pulse charging also showed benefits of decreasing the battery's heat generation. However, since the pulse charge experiments were not voltage limited, the batteries exceeded their (4.1 V) cut-off voltage up to 5.5 V. Consequently, they suggested possible Li-deposition appearance, along with other electrolyte oxidation. Hence, charging time was reduced at the expenses of cycle-life reduction.

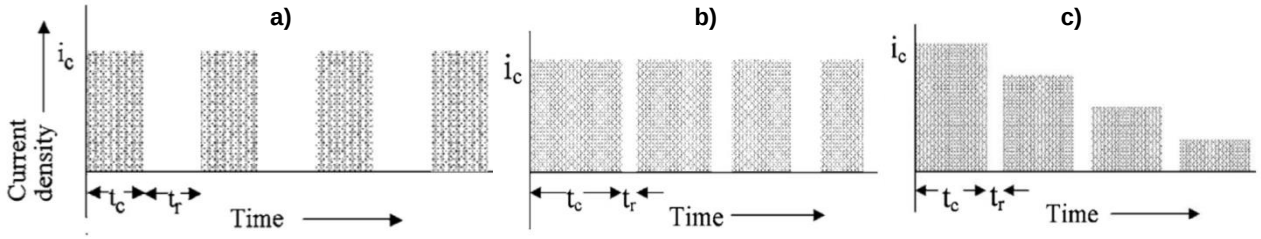

Fig. 3.15. a) Constant amplitude pulse charging with same rest durations, b) increasing rest durations, and c) with decreasing pulse amplitudes [137].

A recent study by Savoye *et al.* [141] on LFP batteries, showed the impact of pulse charging when combined with pulse discharging. The periodic pulse profiles were designed on the basis that the average current was the same as with the standard CC–CV method to facilitate comparison. The results showed that the current pulse profiles induce higher energy for charge and lower for discharge, hence reducing the overall cell performance. They concluded that for this particular chemistry, pulse profiles did not induce any positive effect on the cell materials or on electrochemical processes that could be related to cell performance.

To sum up, the pulse charging method is able to induce in some cases better charging results, produced by the relieving the ion accumulation at the electrode/electrolyte interface. However, from the literature, not any particular pulse charging profile leads to optimal charging results. Indeed, to date there is no proven method to determine the ideal pulse amplitude and rest period which produces the

best results on a specific LIB technology. Moreover, the pulse charging method likely provides different results upon the battery technology of choice. Hence, although this method can reduce charging time and energy losses, this can only be achieved by trial-and-error or by empirical methodologies, which may not always provide the expected results and, also, can be time consuming and complex.

3.3.6. Additional considerations for fast charging

Some other new charging methods have been proposed to reduce the charging time and/or eliminate unwanted safety and reliability concerns. In particular, thermal methods are focused towards safety. As commented in Section **2.3.4**, Li plating is a hazardous phenomenon that is enhanced at low temperatures during charge. To overcome this issue, pre-heating charging methods have been developed. Stuart and Hande [142], [143] proposed internally heating using high frequency AC currents that do not add capacity to the battery. Using this technique, it was possible to heat the pack from -20ºC to room temperature within 6 min by circulating 10-20 kHz AC currents. Pesaran *et al.* [144] also proposed heating the internal core of batteries with AC currents, as the fastest and most energy-efficient pre-heating method. In addition, the temperature distribution inside the battery was uniform in comparison with the irregular temperature distribution produced by external jacket heating. However, they commented that the impact of AC heating on battery life needs to be studied.

In general, battery thermal management has attracted considerable research and development efforts, as the overall battery cycle life is strongly dependent on temperatures (both high and low). In addition to the internal AC heating techniques mentioned above, most common management systems (for instance, used in EVs) include air or liquid thermal management systems (TMS) for effectively managing the heat dissipated from the batteries. There have been studies on the design of battery TMS [145] which illustrate the critical importance of including this systems in large, high power battery packs.

3.3.7. Summary of fast charging methods

Regarding the numerous fast charging methods found in the literature, the suitability for a given application is still very challenging to address. As shown, several factors affect the charging time, efficiency or aging of the battery. To facilitate the strengths and limitations of the analyzed charging methods, here is presented a table summarizing their main characteristics (see **Table 3-2**).

Table 3-2. Summary of charging methods found in the literature.

Charging method	Strengths	Limitations	References
Constant current, constant voltage (CC–CV)	Standard LIB charging method. Simple, high energy efficient and reliable at low C rates	Slow, may cause Li deposition if improper usage. CV stage prolongs the charging time while adding little charged capacity	[46], [58]
Constant voltage (CV)	Fast charge, easy implementation	Very detrimental, very high initial currents. Long CV stage is detrimental due to electrolyte oxidation. High peak currents during charge	[129], [130]
Multistage charging method (MCM)	Fast charge, healthy recharges, easy implementation, Li deposition can be avoided	Various methodologies. Need to carry out independent study for each method and LIB technology. Some methodologies based on mathematical algorithms may be difficult to implement in practical chargers	[128], [129], [133]–[135]
Varying current method (VCM)	Based on physical models to optimize the charging process. Good charging efficiency and cycle life	Risk of overvoltage if no cautions are taken, which leads to the reduction of the cycle life and impedance increase. Some of the charging profiles may be difficult to implement in practical chargers	[124], [130]–[132
Pulse charging	Eliminates concentration polarization at the electrode/electrolyte interface to reduce charging time and energy losses	Not any particular pulse profile leads to optimal charging results. Experiments carried out are not conclusive and many did not find any performance improvement and even damaged the battery	[137], [140], [141], [146]
Additional considerations	Necessity of thermal management systems (TMS) to avoid Li plating at low temperatures and reduce accelerated aging at high temperatures	External TMS are independent of the charging protocol when the range of the temperature working conditions is established. Hence the limitations are based on economical, mass/volume increases and added complexity of the system	[142], [144], [145]

3.4. Strategy to develop fast charging protocols in Li-ion battery systems

As shown, a universal protocol to achieve fast charging in LIB systems is very challenging. Still, it is possible to develop a strategy to attain fast charging, that can be applied in LIBs. The strategy proposed in this thesis is composed on a set of key points that allow the design of efficient, reliable and simple charging protocols, for its applicability in LIB systems. This strategy was developed on the base of two main elements: first, the selection of the proper LIB architecture optimized for high power applications, and second, the analysis of the strengths and limitations of the charging methods.

This section presents a universal step-by-step guide to design a fast charging technique adapted for any specific LIB application. It is important to point out that the various results can be attained. As shown, each particular fast charging LIB application has different targets on charging time, efficiency, cycle life, or may have sporadic usage. Similarly, the quantifications in C-rates or charging times are dependent on the selected LIB technology and the aforementioned targets. The results of applying these key points to develop a charging strategy are to develop efficient, safe fast charges. In fact, a fast charging protocol using this framework has been published [147], and is presented in the last section of this chapter as an applicability example.

The proposed strategy includes the key points described below and summarized in **Table 3-3**.

1. Selection of the LIB architecture optimized for fast charge: from the different electrode materials and battery configurations of choice, high power (HP) designed batteries accommodate best for fast charging. The choice of the HP battery considers the design of the cell from an engineering and basic science level.Cylindrical cells with large electrode area, reduced thickness of the electrodes, tabs distribution, loading ration, high electronic conductivity, high ionic conductivity and diffusivity and reduced ionic and electronic paths and charge transfer potentials can optimize the performance of HP. The use of high power chemistry active materials, coupled with nanomaterial techniques yield the best results. High power cell technology based on nanophosphates with coating layers is available on the market. Similarly, anode based LTO batteries also provide high charging current rates (up to 6C) and can work at low temperatures.

2. Pre-conditioning and battery evaluation testing: this stage is required to obtain experimental results that allow designers to evaluate the charging capabilities of the selected cells, under the expected temperature working conditions. The tests shall include charges under several C-rates, ranging from nominal to maximum. The temperature evolution, charging time, charging capability, energy efficiency and voltage evolution with SOC have to be evaluated. Moreover, voltage charging limits have to be established and never exceeded. It is also important to test the limits of the charging capabilities, being aware that some LIBs can exceed the recommended charging currents for short periods of time, usually stated as pulse charging capabilities. However, caution shall be taken to avoid Li plating, thus pulse charges have to be avoided at mid to high SOCs. Based on the analysis of these results, the development of the new charging strategy is carried out.

3. Internal resistance analysis as a function of the SOC: IR evolution as a function of the SOC has to be evaluated. Since IR is also dependent of current, several C-rates shall be applied to obtain the IR. From these results, the following design rule can be implemented: increase charging C-rates at lower IR values, and decrease the C-rates at higher IR values. This strategy aims to reduce Joule heating, hence providing better charging efficiency in the process. Similarly, the cell impedance shall increase towards high SOC, as the ability in moving the residual charge from the electrodes becomes more difficult. To measure and analyze the IR of a LIB, several techniques can be used [4], [9], [16], [148]–[153]. In this regard, Chapter **4** (Section **4.1**) provides additional details to measure the IR.

4. Multistage charging method (MCM) development: among the existing charging methods, the MCM is considered as a high-quality charging pattern with the advantages of long cycle life, high charge/discharge energy efficiency and short charging time. The VCM has similar strengths and sometimes similar current profiles, but its implementation in battery chargers may be more difficult. The rest of the charging methods did not show many advantages. Hence, here is opted to develop the fast charging technique based on the MCM. The combination of different levels of charging currents is adopted to achieve optimal fast charge: the maximum currents are applied to lower IR values, i.e. high currents at low to mid SOCs, and lower currents at high SOCs. A limited number of current steps has the advantages of simplifying the protocol design while providing fast charges The combination of current steps also helps to reduce the cell's internal temperature. The cell voltage cannot surpass the maximum voltage limit provided by the manufacturer, to prevent electrolyte and electrode oxidation, and accelerated aging. A last individual CV stage helps to prevent overcharging and reduce cell's temperature, but have to be limited in time to decrease risk of accelerated aging.

5. Temperature considerations: working temperatures are critical when designing fast charging techniques. Below zero temperatures increase the risk of Li plating, whereas high temperatures accelerate battery aging. Hence, the necessity of using a TMS to keep the battery operating at safe temperatures under extreme temperatures is fundamental.

6. Additional considerations and comments: more advanced techniques can be used to improve the charging capabilities. However, this is achieved at the expenses of adding complexity to the LIB system, increasing research time and experimental resources. In addition, the outcomes may not be always satisfactory. Still, it is important to disclose them: mathematical modeling to calculate maximum charging profiles with no Li deposition, based on Li ion transport in the electrolyte and through the porous electrode architecture. Battery chargers may include adaptive SOH evaluation, automatic IR and SOC calculations to automatically modify the charging profiles as the cell ages. Similarly, experiments with a three-electrode cell are beneficial. Tracking the voltage evolution of the NE and PE individually, leads to experimentally measure the Li plating limits and overvoltage, respectively. This allows quantifying the maximum C-rates as a function of the SOC than can be used for the current stages.

Table 3-3. Proposed strategy to achieve fast charge in LIB systems.

Fast charging design key points	Comments	References
1. Selection of LIB architecture optimized for fast charge	Commercial high power (HP) batteries with high power density and charge/discharge rates. Optimized HP design from engineering and basic science level. HP active materials. Low polarization resistances. Use of nanomaterials and coating layers to improve electrical conductivity.	[3], [18], [19], [100], [111], [117], [118], [125], [126]
2. Pre-conditioning and battery evaluation testing	Test and evaluate selected cell under several C-rates, ranging from nominal to maximum. Keep track of temperature evolution, energy efficiency, charging time, charged capacity and voltage evolution with SOC.	[16]
3. Internal resistance analysis as function of SOC and current	IR evaluation at different C-rates vs. SOC. Results to be used in fast charge protocol design rule: increase charging C-rates at lower IR values and decrease C-rates at higher IR values, to lower Joule heating.	[9], [16], [148], [152]
4. Multistage charging method (MCM) development	Current steps apply as: the maximum current to lower IR values: high current at low to mid SOCs, and lower current at high SOCs. This also helps to reduce cell's temperature. Use an optimum number of charging multistages yields best results and add simplicity to charger system). Avoid high currents at high SOCs to decrease risk of Li plating. Avoid surpassing cell voltage limits. Avoid long CV periods to decrease risk of electrolyte oxidation.	[36], [49], [128], [133], [135]
5. Temperature considerations	If the LIB system is to be operated at high or low ambient temperatures, consider including thermal management system. Below zero temperatures increase the risk of Li plating when fast charging. High temperatures accelerate cell aging	[36], [49]
6. Additional considerations and comments	If charger complexity is not a restrain, mathematical modeling to calculate optimal charging profiles, SOC, IR and/or adaptive SOH evaluation are optional. Similarly, experiments with three-electrode cell to track NE potential vs. Li are an asset.	[128], [133], [135], [138]

It is also important to point out that once the protocol has been designed, following the strategy proposed, it must be tested and evaluated. The evaluation shall include measurement of the target parameters such as charging time, efficiency, aging, etc. If targets are met, then the designed protocol is ready for long-term cycling and subsequent aging analysis. If the protocol requires improvements, modifications on key point #4 may be needed, such as modification in charging currents, for example.

Similarly, if the selected battery cannot provide the required basic targets, it is necessary to restart from key point #1, in order to select a suitable LIB for the application.

3.5. Design of a fast charge protocol for high power LFP batteries

Due to the increasing interest in LIB systems to achieve fast charging, one of the objectives of this thesis work is the design of an efficient and reliable fast charging protocol. A new fast charging protocol is presented in this section, describing design procedures and showing main results. The proposed technique achieves the general objectives of fast charge: quick recharges with minimal degradation effects, using a simple multistage charging method. The protocol was designed following the key points of the strategy previously presented in Section **3.4**. With the selected high power cell architecture and the designed protocol, full charges are accomplished within ~22 min. [147].

The first step to develop a fast charging protocol is to define the targets and working conditions of the tested cell. In this work, we aimed to carry out fast charges and discharges, to meet various key USABC long term goals. Long term USABC goals are considered challenging to be met by current LIB technology [154], and include charges that return 40% of SOC of the battery within 15 min; the complete charge/discharge process should also meet cycle life over 1,000 cycles, energy efficiencies above 80%, specific power during discharge above 400 W/kg, and specific energies above the mid-term goal (80 Wh/kg) [16]. Moreover, the charging protocol should be simple enough to be implemented in battery chargers and the tested cell should be cost effective. There were no restrains in the battery capacity values. In addition, the selected batteries should be suitable for several applications, including EVs, PHEVs or portable high power devices. The working conditions were set to the standard constant temperature of 23ºC.

As the targets are set, the next step is to evaluate the proposed strategies to achieve fast charge. For the particular case study, key points #5 (temperature considerations) and 6 (additional considerations) did not apply. This is because the tested cell is set to constant temperature (23ºC), and point #6 would add significant complexity to the battery charging system. Hence, by evaluating key points #1 to #4, an effective fast charging protocol is developed.

Key point #1 (selection of the LIB architecture optimized for fast charge) is crucial, as the selected cell has to achieve several targets to meet the objectives. Based on design rules established in key point #1, the selected battery was a nanophosphate based high power LFP cell, manufactured by A123 Systems. Material enhancement in these cells considerably improves their conductivity and rate capability in comparison to standard LFP cells [111]. According to the manufacturer, these cells allow fast charging and high discharging rates, and they are suitable for portable high power devices, EVs or ESS [155]. The manufacturer's product datasheet shows that these cells weigh an average of 70 g and have a capacity of 2.3 Ah. Moreover, the cost unit is low (10€/cell).

Continuing with key points #2 and #3, the selected cell was subsequently tested. Under nominal charge/discharge conditions (1C), the cell exhibited a capacity of 2.27 Ah, energy density of 98.8 Wh/kg and energy efficiency of 94%. The cell achieved maximum charges up to 10 A (4.3C), as stated by the manufacturer. The voltage limits are 3.6 V and 2 V for the EOC and EOD, respectively. According to point #3, measurements of the IR during charge were carried out. **Fig. 3.16** shows the results of the IR evolution versus the SOC for charging, calculated with the voltage curve difference method [4], [150]–[153] at 4C. The IR reaches its minimum immediately after starting the charging process. As the cell reaches approximately 10% SOC, the IR remains practically constant at 15-16 mΩ until 70% SOC is achieved, after which the IR value increases rapidly. This IR pattern has been also reported for LFP power cells from the same manufacturer [151].

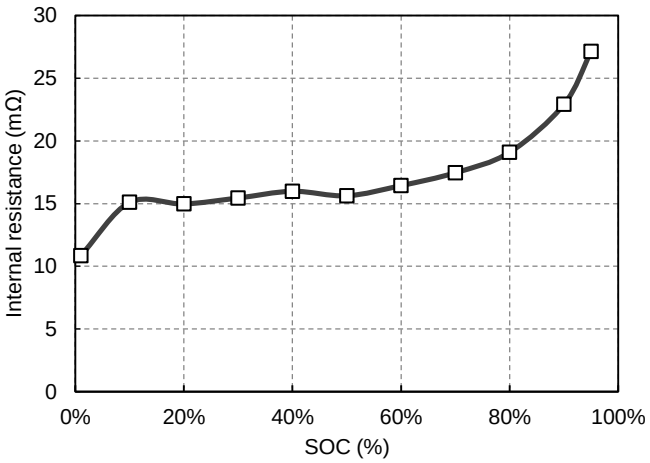

Fig. 3.16. Cell internal resistance evolution versus the state of charge, at 4C charging current.

Following key point #4, a MCM based technique was developed. The charging process is split into three different stages, referred as CC-I, CC-II and CV-I (see **Fig. 3.17**a-d). The first stage (CC-I) starts with CC at 4C to the charging cut-off voltage (3.6 V). The second stage (CC-II) consists of CC at 1C. Since the current in the second stage is lower than in the first, the cell voltage drops below 3.6 V (see **Fig. 3.17**b) allowing the charge to be extended, until the cell reaches again the charging cut-off voltage. The last stage (CV-I) is carried out at a CV of 3.6 V for a duration of 5 min. The SOC is shown in **Fig. 3.17**c; it increases linearly as the cell is charged at CC and asymptotically during the constant voltage stage. **Fig. 3.17**d shows the cell temperature evolution. The temperature is reminiscent of a symmetric bell curve over time: it starts at an ambient temperature of 23ºC, increases by 2.3ºC to its maximum at approximately half the charging time, and ends back at the ambient temperature.

The designed multistage technique is based on the evolution of the IR during the charging sequence. Because of the IR behavior, the highest charging current (4C) is applied when the cell's IR is at the lower values. This approach results in a more energy efficient charging process. The last two stages of the charging process are applied as the cell's IR increases rapidly; this procedure helps to decrease the cell's temperature to its initial value (see **Fig. 3.17**d). The charging current rate at 4C (9.2 A) was selected because it is close to the maximum charging current recommended by the manufacturer (10 A); a security margin of 8% was selected to avoid working at the limiting current, which reduced the likelihood of additional aging and overheating. The last stage (CV-I) provides better cell preservation by limiting the CV charging to 5 min, thus avoiding an acceleration of the aging process that occurs at high SOC values over longer periods of time, while at the same time reducing cell's temperature and achieving full recharge.

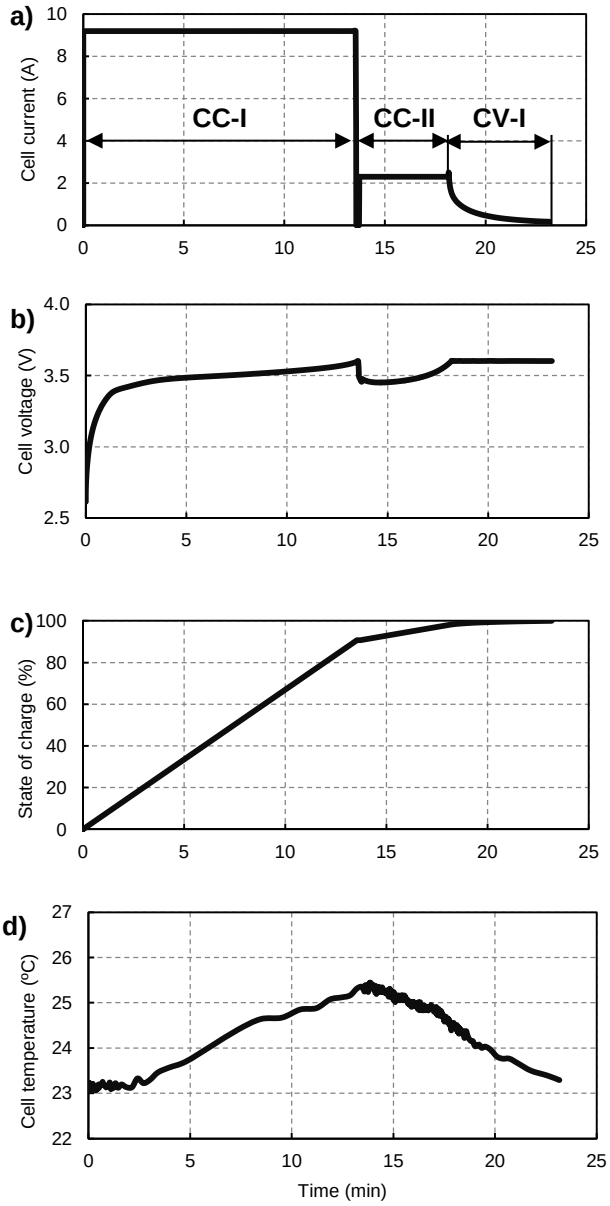

Fig. 3.17. a) Cell current, b) voltage, c) state of charge and d) temperature profiles for the fast-charging protocol.

Recharging can be performed very quickly with the proposed fast charging protocol on the selected cell architecture. The cell is charged from 0% to 40% of its capacity in approximately 6 min; this value meets the USABC goals regarding fast charging for EVs, and is an attractive short charging time for portable electronic devices. In addition, the cell is fully recharged in approximately 22 min. When compared to the standard charging procedure, the fast charging technique allows the cell to recharge in 1/3rd of the standard charging time (see **Fig. 3.18**).

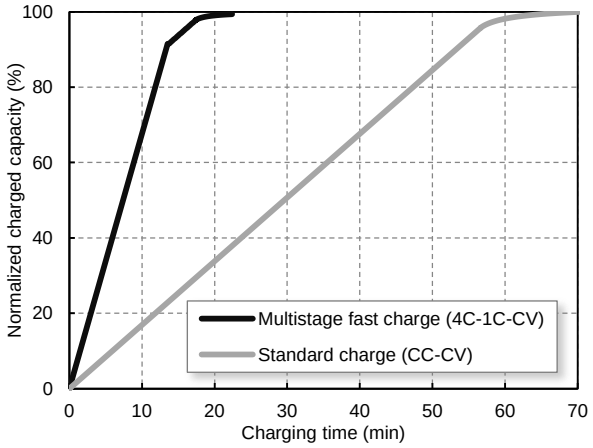

Fig. 3.18. Comparison of the normalized charged capacity versus charging time for the proposed fast charging technique and standard charge.

The design of a successful fast charge in LIBs is demonstrated here. The targets were challenging, including USABC long term goal of fast charge, cycle life, and others. Applying the key points of proposed strategy, we selected a HP cell and designed a simple, multistage charging protocol that allows the cell to be efficiently charged within 22 min.

The long term cycling test results (up to 5400 cycles) of the proposed charging technique and its comparison with standard CC-CV protocol are provided in Chapter **6**. Moreover, to complete the main objectives of this thesis, an extensive analysis on its performance and degradation analysis is provided in Chapter **7**.

3.6. Summary

This chapter presents an approach to implement fast charging in lithium ion battery (LIB) systems. Here we show the both battery architecture and the charging protocol have to be analyzed simultaneously to achieve fast charging on a specific application. In this chapter we also provide a step-by-step strategy for the design of efficient and reliable fast charge protocols. We finish the study presenting a new fast charging protocol applied on a high power (HP) lithium iron phosphate (LFP) battery.

An optimal fast charging process shall be quick and simple, adding the minimal detrimental effects to the battery. Fast charging is usually accepted when a battery system can be fully recharged in less than one hour. In addition, fast charging is highly dependent on the battery architecture design and the charging protocol. High power (HP) battery architectures are optimal for fast charging applications. As presented in Section **3.2**, the use of high power chemistry active materials, considerations in cell design and the use of novel nanomaterials yield the best results for fast charging capabilities. As shown, nanoscaling LFP provides very high rate capabilities (i.e. 60C) on laboratory-scaled tests, and 30C on commercially available LFP batteries.

Section **3.3** provides an updated overview and an analysis on the fast charging protocols found in the literature. Few protocols provided satisfactory results in the long-term cycling, when compared to standard charge. From the analyses, we derived the strengths and limitations of the studied charging protocols, and identified the main actions to take into account when fast charging, including: avoiding high currents at high state of charge (SOC) to reduce risk of Li plating, control cell voltage limits or avoid long constant voltage (CV) charging periods to decrease the risk of accelerated aging, to name a few. Also, from the analyses we concluded that the multistage charging method (MCM) is a high-quality charging pattern: when properly designed, MCM provides fast and healthy charges, using a simple multistage procedure.

The conclusions derived from the previous study provided us the required facts to build a general strategy to implement fast charging on LIBs. The strategy is divided into key points, including facts about LIB architecture selection, the importance of carrying out pre-conditioning and battery evaluation tests, and the design of multistage charging methods. The aim is to develop a simple, general step-by-step guide to design safe, fast charging techniques to any specific LIB application.

To validate the proposed strategy, a new fast charging protocol is presented here. The adopted technique is carried out using high power nanophosphate cells from A123 Systems, because of its advantages and fast charging capabilities. The charging profile is based on the evolution of the internal resistance during the charging sequence. Considerations to reduce high temperatures and reduce the risk of Li plating are considered. The profile consists on a multistage method of three charging stages (4C-1C-CV). The results met challenging long-term USABC goals (e.g. energy efficiency, fast charging capabilities, etc.), and safe charging was achieved within 22 min. achieving a time reduction of ~48 min. when compared to standard charge.

This page intentionally left blank

4. Techniques for Li-ion battery aging analysis

As presented in Chapter **2**, battery aging is caused by several, complex degradation mechanisms that can interact simultaneously. As a consequence, identifying battery aging mechanisms still remains very challenging today. However, several techniques, including *in situ* incremental capacity (IC) and peak area (PA) techniques can be used to estimate the state of a battery and its degradation modes. Although the use of these techniques is not straightforward, it can lead to successful outcomes. The aim is to obtain a first approach to identify the aging modes of lithium ion batteries (LIBs) both qualitatively and quantitatively through *in situ*, non-destructive techniques.

This chapter begins showing simple, yet effective well established methods to analyze capacity and power fade. As these methods are not powerful enough to identify the complicated aging patterns found in LIBs (e.g. loss of lithium inventory, loss of active material, etc.) more advanced, *in situ* techniques are presented. This includes the IC and PA techniques. Since the use of these techniques and further understanding of the derived results are not straightforward, here we provide a broad and descriptive analysis. We start describing the fundamental aspects of the IC and PA techniques. Next, we provide an individual analysis of the aging mechanisms and the particular signatures exhibited in terms of IC, PA, normalized cell capacity and half-cell electrode data. The outcome is a descriptive set of tools and degradation patterns that facilitate the aging analysis on commercial LIBs, particularized for LFP technologies. The identification of aging mechanisms through IC and PA analyses is completed with a summary in form of look-up tables. The presented analyses and techniques are extensively used in Chapter **6** and Chapter **7** to decipher the actual, more complicated aging modes that affect the tested cells. The last section provides a quick overview of commonly used *post mortem* techniques to identify LIB aging. Although these techniques are not used in this thesis, it is important to provide a brief summary, as they are often found in the literature to analyze battery aging.

4.1. Standard procedures for aging identification

This section presents the most commonly used techniques to identify battery aging. Although LIBs may degrade in very complex manners, the outcome is simple: a battery ages losing capacity and, in some degree power. The following techniques are simple and reliable tools to identify capacity fade and power fade in a battery. These techniques are widely used to provide a general, first quantification of battery degradation.

4.1.1. Capacity fade

The quantification of the capacity fade with cycling is evaluated by measuring the evolution of the nominal capacity as a function of the cycle number. Usually, the normalized capacity is stablished in the first reference performance tests (RPT) [7], [16], [147]. The results from the RPTs provide a nominal capacity which is established as the initial normalized cell capacity, i.e. 100%. As the cell is cycled, it loses capacity. The normalized cell capacity plotted versus the cycle number represents the capacity fade. This is shown in **Fig. 4.1**, where six identical LIBs were tested at the same C-rate, and different DODs [62].

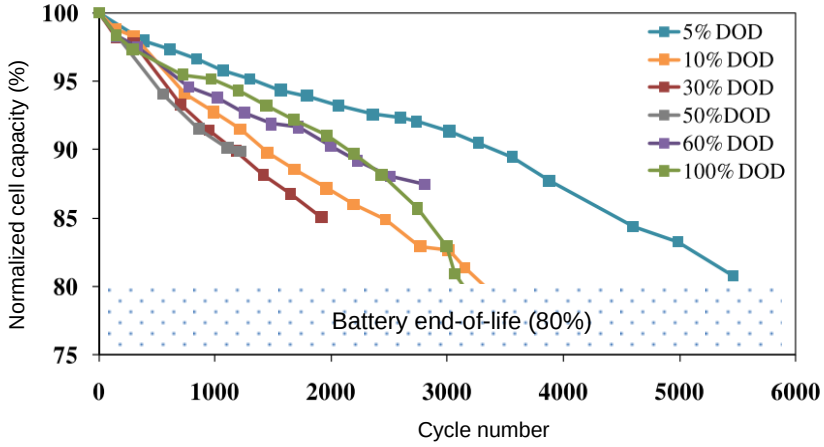

Fig. 4.1. Capacity fade in 6 commercial LIBs, cycled at different DODs [62].

As observed from **Fig. 4.1**, the capacity fade evolution quantifies the capacity loss in percentage. By definition, the end-of-life (EOL) is the point at which a specific test protocol cannot deliver more than 80% of its nominal capacity [16]. Hence, the capacity fade evolution quantifies in which cycle a tested cell has reached the EOL. However, from these measurements one cannot unveil power fade or the aging modes on the cell. Still, this representation is intuitive and the information that provides is essential to measure aging on a LIB. Therefore, it is always recommended to perform this analysis.

4.1.2. Specific energy and power fade

Both the specific energy (Wh/kg) and the specific power (W/kg) are key parameters to quantify battery aging. The specific energy quantifies how much energy is available, whereas the specific power quantifies how quickly that energy can be delivered. As an example, in EVs the specific energy loss causes range reduction, whereas specific power loss diminishes the acceleration. Hence, both parameters are important for quantifying battery aging. The relation of the specific energy and the specific power is represented in the Ragone plot, as shown in **Fig. 4.2**a. As the cell ages, less energy is delivered under the same specific power values.

To express the capacity of a battery in terms of the C-rate at which is charged or discharged, the Peukert plot is represented. The plot is constructed from the Peukert's law equation $C_p = I^k t$; where C_p is

the capacity at one-ampere discharge rate (expressed in Ah), I is the actual current (in amperes), k is the Peukert coefficient (dimensionless) and t the actual time to discharge the battery (in hours). To evaluate Peukert's law, the tests have to be conducted under constant currents and temperatures. The Peukert coefficient usually yields values between 1 and 2. An example of the Peukert plot is shown in **Fig. 4.2**b. The cell capacity is plotted versus the C-rate in discharge. As observed, the cell capacity decreases as the C-rate is increased. Similarly, as the cell ages, the capacity decreases and the Peukert coefficient is increased. An increase in the Peukert coefficient indicates that the cell attains less capacity as the C-rate is increased. This is observed in **Fig. 4.2**b, as the Peukert curves decrease more abruptly as the cell losses capacity.

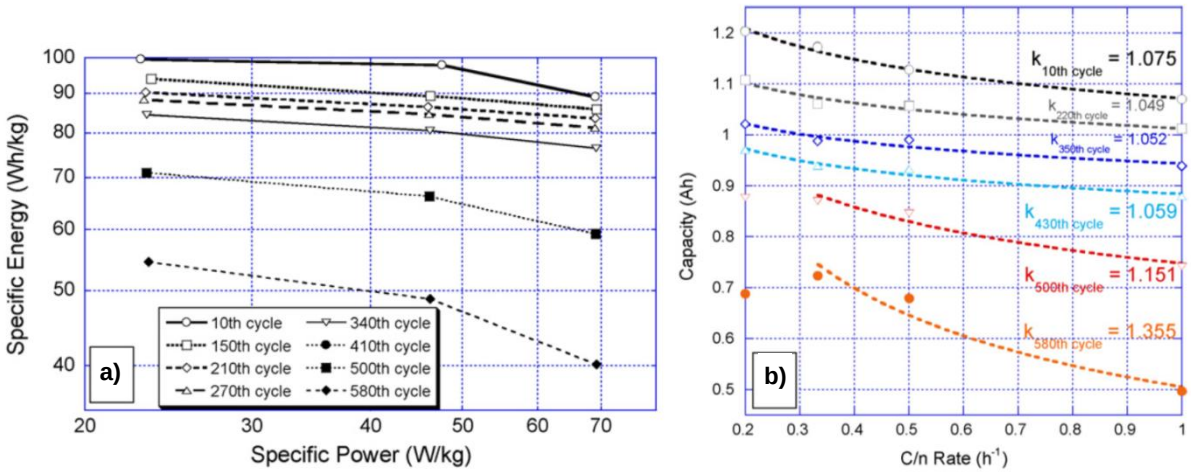

Fig. 4.2. Evolution of the a) Ragone and b) Peukert curves with cycling [7].

4.1.3. Internal resistance (IR)

Internal resistance (IR) is considered a key parameter in LIBs. It is directly linked to the power battery performance, including the ability to achieve fast charging, and is also related to the aging mechanisms of a battery, such as the SEI growth, or the physical degradation of the electrolyte and the electrode structure [24], [36], [42], [49]. The increase of the IR lowers the battery discharge voltage, resulting in less energy transferred to the load. It may also shorten the discharge time (and therefore the capacity). Also IR increase reduces the battery's power characteristics. Hence, measuring the IR provides useful information to evaluate battery aging.

The IR of a battery is a complex system, showing capacitive, resistive and inductive behavior interrelated among them [11], [148]. In addition, it is also dependent on several factors: from the battery capacity, constructive materials and its geometry, to physical and electrochemical phenomena [9], [31]. As a consequence, the IR of a battery is dependent of charge/discharge current rates, state of charge (SOC), state of health (SOH) and temperature.

To analyze the resistance of a battery, various methods have been proposed. Due to the importance of IR measurements, part of our previous works have been focused on IR measurement, evaluation, and applicability of the IR methods [152], [153]. We studied three different methods that share the advantages of relatively easy implementation, simple calculations, and give realistic results: voltage curve difference (VCD) [4], [150], [151], DC pulse current [9], [149], or the method proposed by the USABC [16], which has been widely adopted by battery manufacturers [149].

We concluded that the IR is not only dependent on the battery's architecture design, testing current conditions, SOH and SOC, but also on the IR methodology used. Indeed, the analyzed IR methods have advantages and disadvantages, in terms of the accuracy, current dependency or simplicity, to name a few

[152], [153]. For briefness, here we summarize various IR methods, paying special attention to the VCD, as is the method used in this thesis work to analyze the IR evolution of the tested cells.

Voltage curve difference (VCD)

The IR of a battery is defined as the opposition or resistance to flow an electric current within a battery. When a battery is connected to a load and a discharge current passes through the closed circuit, the voltage across the battery decreases, due to several sources of polarization:

$$V_{\text{Cell}} = E_{\text{OCV}} - \eta_{\text{ohmic}} - \eta_{\text{Ch.Tr}} - \eta_{\text{diff}} \tag{4.1}$$

As commented in Chapter **2**, ohmic polarization (η_{ohmic}), charge transfer ($\eta_{\text{Ch.Tr}}$) and diffusion (η_{diff}) compose the polarizations sources, and can be associated as R_{Cell} For a given SOH and at constant temperature, Eq. (4.1) can be rewritten as:

$$V_{\text{Cell}}(I, SOC) = E_{\text{OCV}}(SOC) - IR_{\text{Cell}}(SOC, I) \tag{4.2}$$

The E_{OCV} of a battery can be derived by calculating the pseudo-OCV (i.e. average of two thermodynamic curves at C/25). This yields to:

$$V_{\text{Cell}}(I, SOC) = V_{\text{pseudo-OCV}}(SOC) - IR_{\text{Cell}}(SOC, I) \tag{4.3}$$

reordering Eq. (4.3), the IR of a battery for a given SOC and testing discharge current (I) can be calculated using the expression:

$$R_{\text{Cell}}(SOC, I) = \frac{V_{\text{pseudo-OCV}}(SOC) - V_{\text{Cell}}(SOC)}{I} \tag{4.4a}$$

In battery engineering, it is considered $I > 0$ during charge, which yields $V_{\text{pseudo-OCV(SOC)}} < V_{\text{Cell(SOC,I)}}$. In contrast, during discharge, $I < 0$, which yields $V_{\text{pseudo-OCV(SOC)}} < V_{\text{Cell(SOC,I)}}$. As a result, the valid expression for $R_{\text{Cell}} > 0$, both during charge and discharge (taken into account $I > 0$ for charge and $I < 0$ for discharge) is:

$$R_{\text{Cell}}(SOC, I) = \frac{V_{\text{Cell}}(SOC, I) - V_{\text{pseudo-OCV}}(SOC)}{I} \tag{4.4b}$$

An example of IR measurement during discharge for the conditions SOC = 50% and I = 1C is depicted in **Fig. 4.3**.

One of the main advantages of the VCD method is that provides an IR value including the total polarization effects (i.e. ohmic, charge transfer and diffusion) at the specific tested rate and SOC, in a very simple, quick and accurate procedure. Possible drawbacks of this method are temperature and SOC dependency, especially at high C-rates. Because of its advantages, this IR method was used in this thesis work.

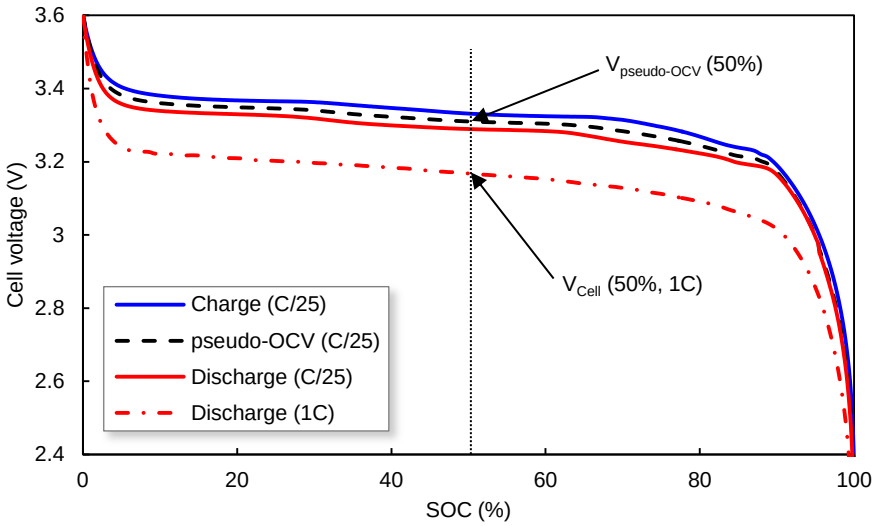

Fig. 4.3. Calculation of the IR at 1C, 50% SOC on a commercial LIB, using the voltage curve difference (VCD) method.

Similarly, other IR measurement methods have been developed. For example, USABC proposed a method for its applicability in EVs [16]. The method is based on measuring the voltage difference between a base current, and the IR testing current at 30 seconds. Because this method is not measured from thermodynamic conditions, the IR measurement includes charge transfer and diffusional effects from both testing currents, which decreases its accuracy. However, its implementation is online, simple and provides good accuracy of the measurements, particularly for the ohmic resistance [152], [153].

The DC current pulse performs IR measurements in true thermodynamic equilibrium. To achieve these conditions, the battery is put in rest at open circuit for 2 h before the 1 min testing current pulse is injected. The IR is derived from Ohm's law voltage difference at the testing current. Using rapid data acquisition systems (i.e. 500 μs), this technique can separately provide the ohmic, charge transfer and diffusional values. However, this IR technique is time-consuming, costly and more complex than the previous methods [152], [153].

Other technique to measure the IR is through electrochemical impedance spectroscopy (EIS) measurements. Although this method is widely used, it also has several drawbacks: it requires a set of specialized expensive instruments, the analysis is not straightforward, and it is usually very time consuming because some of the investigated electrochemical processes occur very slowly [156].

Overall, the measurement of the IR is important to quantify power fade and possible cell degradation. However, the IR does not address the issue of degradation in sufficient depth. To identify more complicated aging mechanisms, such as LLI and/or LAM, more advanced techniques have to be carried out. The following section describes using incremental capacity (IC) and peak area (PA) analysis can unveil complicated aging modes.

4.2. Incremental capacity and peak area techniques

Incremental capacity (IC) combined with peak area (PA) techniques are powerful diagnoses tools to identify cell degradation. Indeed, to date these are considered some of the most advanced non-invasive, *in situ* tools to trace the aging modes evolution of commercial LIBs [7], [31]. The analyses of the results derived from the IC and PA can decipher a first evaluation of the aging origins from a qualitative and quantitative perspective. In addition, IC and PA techniques are sufficiently efficient for the on-board control electronics, with minimal computation [7]. Still, the use of these techniques is not straightforward, and several considerations have to be carried out to make the most of them.

This section is to present the details to understand the basis of the IC and PA techniques. It also sets the foundations to identify aging modes (i.e. LLI, LAM, etc.) from IC and PA analyses, as later presented in Section **4.3**. The analyses carried out here are particularized to commercial GIC||LFP cells, because is the technology studied in this thesis. However, the approach is also valid with other commercially available LIB chemistries.

4.2.1. Incremental capacity (IC)

The incremental capacity (IC) is an electrochemical technique that can detect gradual changes with great sensitivity in cell behavior during life-cycle tests, by analyzing the evolution of the resulting IC peaks. The IC analyses are based on the original work by Thompson [157] in 1979, where the electrochemical potential spectroscopy was proposed as a new electrochemical measurement technique for studying electrode materials. It was later used in the 1990s by several authors, including Barker *et al.* [158], [159] and Dahn *et al.* [160], [161] to characterize carbonaceous materials. Only recently, Dubarry *et al.* [7], [30], [63], [150], [162]–[165] have extensively applied IC analysis on commercial LIBs and successfully monitored cell degradation without the need for *post mortem* analyses. Due to the advantages of the IC techniques, other authors have also carried out IC analyses to characterize cell degradation [32], [61], [96], [166]–[168] in LIBs. Still, the interpretation of the IC to reveal cell behavior and its degradation modes is not trivial, and has to be studied in detail.

The IC is an increment of capacity associated with a fixed-voltage step (i.e. $IC = \Delta Q/\Delta V$). To calculate the IC of a LIB, a constant current (CC) charge/discharge is carried out. By tracking the capacity increments associated with the fixed-voltage steps, the evolution of the IC vs. voltage is calculated. **Fig. 4.4** illustrates the procedure: a fixed-voltage step (ΔV) yields different capacities (Q_n), resulting from the cell voltage evolution. When applying $IC = \Delta Q/\Delta V$, it is found that $\Delta Q_2 > \Delta Q_1 > \Delta Q_3 > \Delta Q_4$. Hence, depending on the shape of the voltage curve, different intensity of IC peaks is formed. Indeed, voltage plateaus result in big capacity increases (ΔQ_2), which yields large IC peaks. Conversely, abrupt voltage changes result in little capacity increments (ΔQ_4). Most interesting, voltage plateaus and rapid voltage changes are directly related with the electrochemical reactions of the cell. Therefore, the analysis of the IC peaks can reveal information of electrochemical phenomena occurring in the cell.

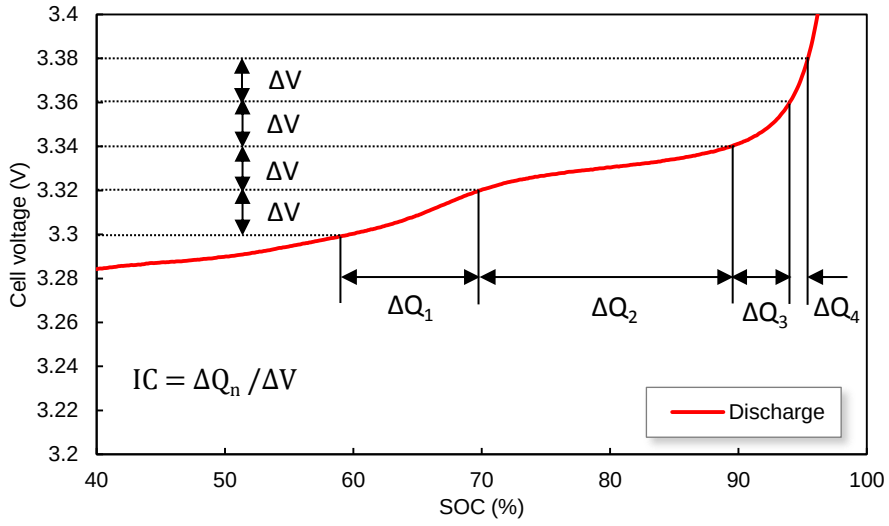

Fig. 4.4. Schematic representation to calculate the incremental capacity peaks for a given capacity interval in a lithium ion battery.

The sensitivity of IC peaks is dependent on the testing current rates. Under kinetic conditions, the voltage signatures of the cell may not exhibit distinctive IC peaks. This is because polarizations tend to inhibit the voltage plateaus. As a result, IC analysis under kinetics usually provides a single, bell-shaped

peak. Still, the IC analysis under kinetics can identify polarization resistances and kinetic degradation by measuring the shifting potential with cycling. Under thermodynamic tests (C/25), the reactions occur very slowly with minimal polarization effects. As a result, the electrochemical cell reactions are clearly distinctive into plateaus and curved-shaped voltage variations. Hence, the resulting IC curves have the largest sensitivity, with clear, distinctive IC peaks associated to its corresponding reactions. For these reasons, to identify cell aging modes with the best resolution and accuracy, the IC analysis shall be carried out under thermodynamic (C/25) testing conditions.

The testing equipment and experimental conditions also play an important role to achieve successful IC analyses (and also PA analyses, as they are directly derived from the IC curves). The IC curves are dependent on the accuracy and precision of the measurements of ΔV and ΔQ. Hence, voltage resolution and current accuracy are important factors to consider when designing the experiment [166]. It must be pointed out that the sampling rate has to obtain sufficient data to build the IC curves with enough resolution. The best way to achieve this is by sampling the cell curve evolution by a fixed-voltage interval. Data collection at 5 mV per step of variation is usually sufficient. Better accuracy may be achieved by reducing the sampling rate (i.e. 1 mV). However, noise and distortion of the IC curves may be produced due to the high sensitivity of the samples.

To illustrate the use of the IC technique and the electrochemical implications on a particular cell technology, **Fig. 4.5**a-b is presented. **Fig. 4.5**a shows the thermodynamic (C/25) charge/discharge curves of a commercial GIC||LFP cell, while **Fig. 4.5**b shows the associated curve with IC peaks labeled for the charge as (①, ②, ③, ④ and ⑤) and for the discharge (❶, ❷, ❸, ❹ and ❺). Each IC peak exhibits a particular shape and intensity, as the electrochemical process progress as the cell is charged or discharged. The IC peaks are the convolution of peaks associated with the electrochemical reactions in the active positive and negative electrode materials [169]. Hence, the IC peaks contain electrochemical signatures of both electrodes. As presented in Chapter **2**, for the particular application on GIC||LFP cells, the PE exhibits a two-phase transformation from $LiFePO_4$ to $FePO_4$ which results in a long, flat plateau at 3.43 V. Similarly, the staging phenomenon in the NE causes a series of voltage plateaus (two-phase coexistence) and voltage variations (formation of solid solutions), numbered from one to five. Since the five staging phenomena of the GIC are convoluted with the single, LFP potential plateau, five IC peaks are formed. As a result, all the peaks in **Fig. 4.5**b correspond to the staging phenomena in the GIC. Notice that the resulting peak signatures are specific for GIC||LFP cells. Other cell chemistries exhibit different IC peak signatures [32], [150], [162], [166], [170], [171].

The evolution of the IC peaks upon cycling yields key information on the cell behavior and its change as reflected by the chemistry [169]. Since each peak exhibits a particular shape, intensity and position, the IC peak evolution can qualitatively unveil different aging modes. To increase the power of this method, the IC analysis is coupled in the Section **4.3** with the Peak Area (PA) analysis that provides a quantitative perspective of aging modes

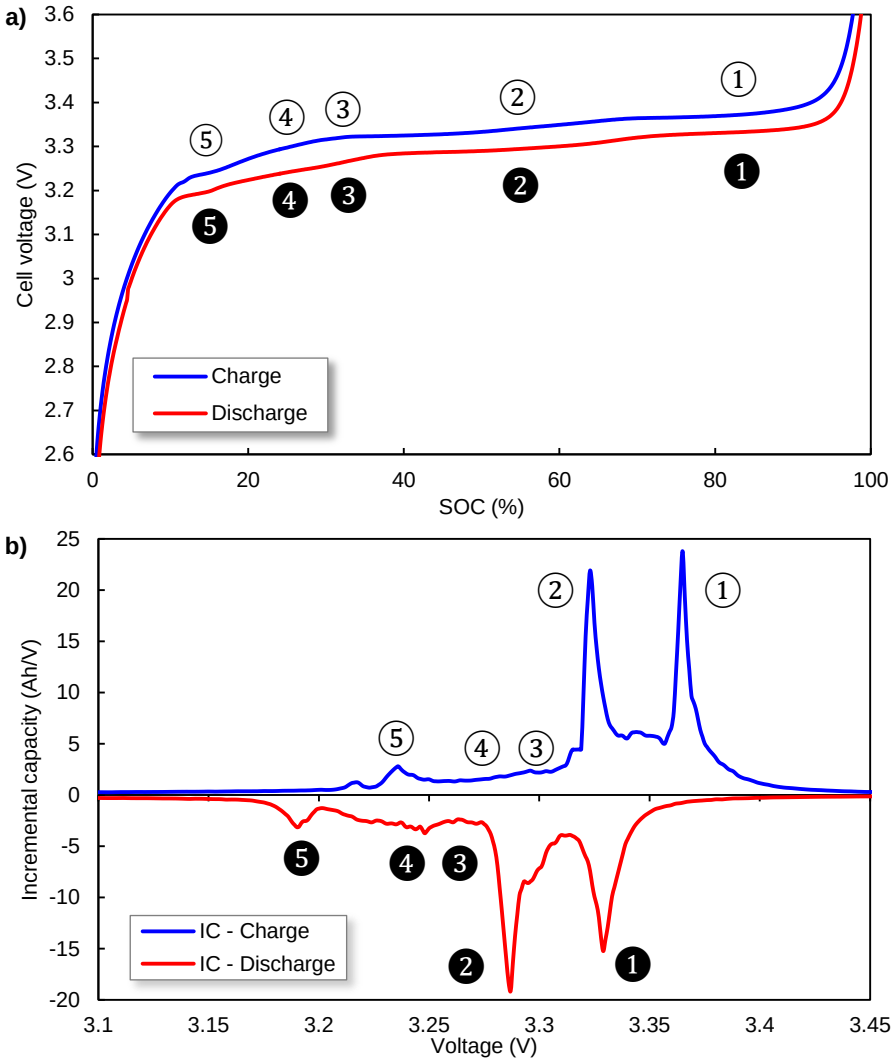

Fig. 4.5. a) C/25 charge/discharge curves of a commercial GIC||LFP cell, b) the corresponding incremental capacity curves.

4.2.2. Peak area (PA)

The peak area (PA) technique is a methodology derived from the IC curves that quantifies the aging modes ongoing on a cell. The technique is based on the area associated with each phase transformation occurring in the cell, detected from the inflection points (i.e. formation of solid solution) of the IC peaks [30]. In other words, the PA technique yields the capacity underneath the IC peaks between different voltage points. As commented, the IC peaks change in shape, intensity and position with aging. To quantitative keep track of those IC changes the PA analysis is carried out.

To further clarify the use of the PA technique on GIC||LFP cell technology, **Fig. 4.6**a-b is presented. **Fig. 4.6**a shows the same thermodynamic discharge curve (as previously presented in **Fig. 4.5**a) of a commercial GIC||LFP cell (red curve), derived from the potential subtraction of the PE (blue) minus the NE (black) electrodes. The PE is a long, flat plateau, whereas the NE has five marked plateaus attributed to the five (labeled from (❶ to ❺) staging reactions in the GIC. As observed, the staging phenomenon of the NE is directly reflected in the voltage's signature of the full cell. Most importantly, this effect is also translated to the IC peaks, as shown in **Fig. 4.6**b. The PA calculates the area of an IC peak (see dashed area in **Fig. 4.6**b), which is directly the capacity (in Ah) associated with the phase transformation.

The procedure to calculate the PA is carried out directly from the voltage vs. SOC (or capacity curve) (**Fig. 4.6**a, red curve) and its derived IC curve (**Fig. 4.6**b). To calculate peak area ❶ (i.e. ∫❶) the IC curves have to be previously generated. Secondly, the voltage inflection point between peak ❶ and ❷ is detected. Lastly, to calculate the capacity associated to ∫❶, the voltage inflection point is checked in the full cell curve, which has an associated discharged capacity (or normalized SOC, in this example). For this particular case, the ∫❶ corresponds to ~30% SOC_{PE}. The calculation of the peak area from peaks ❷-❺ (∫❷-❺) can be directly done by subtracting the cell capacity at the voltage inflection point minus the cell end of discharge capacity. The obtained results provide the capacity of ∫❶ and∫❷-❺. The capacity distribution is often provided in terms of percentage of the total cell capacity, or directly in Ah.

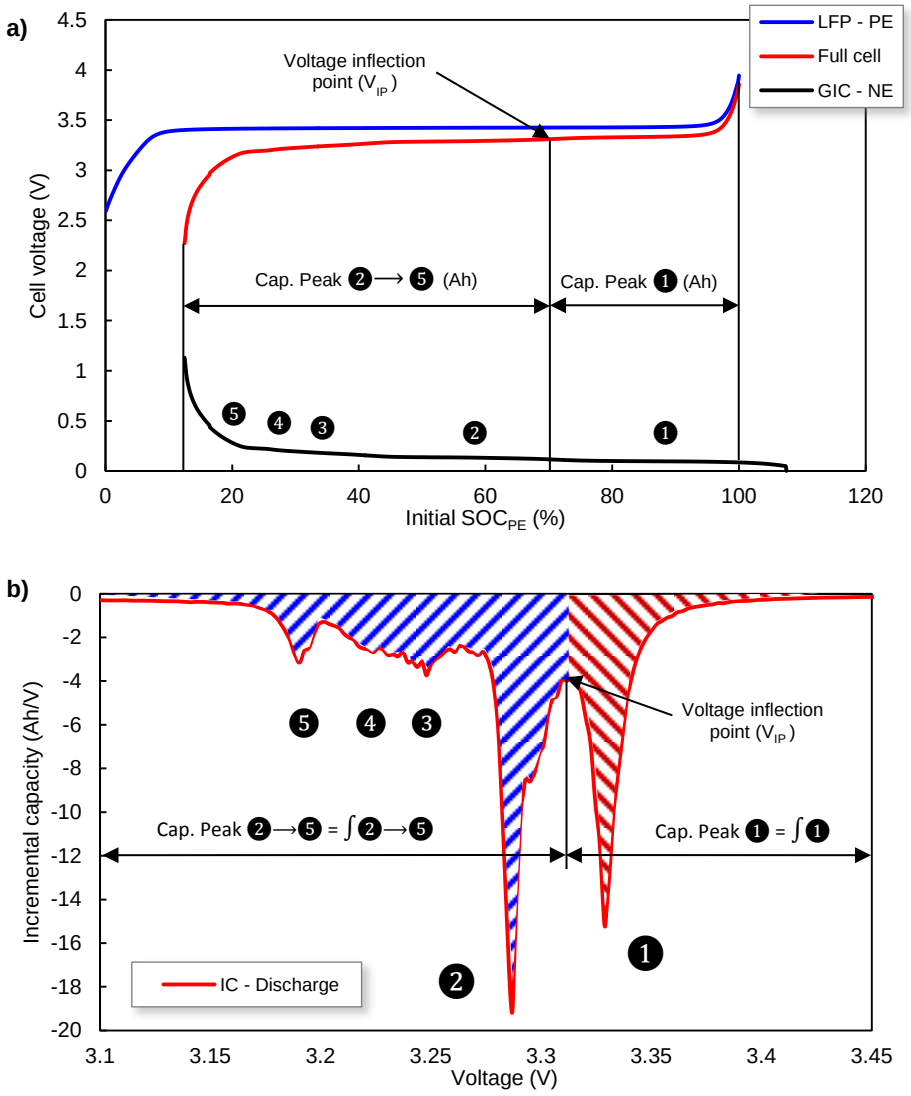

Fig. 4.6. a) C/25 discharge curve of a commercial GIC‖LFP cell showing the full cell (red), positive electrode (blue) and negative electrode (black) voltage profile. b) Schematic representation of peak area calculation, applied to peak ∫❶ and peak ∫❷-❺ individually.

For an appropriate comparison, we separately distinct the area underneath peak ❶ and the area associated under peaks ❷-❺. This particular association of areas facilitates the PA analysis and relates it with qualitative IC analysis, because some of the main degradation mechanisms affect peak ❶ and peaks ❷-❺ independently [31]. This particular aging association is unveiled in the next subsection. In addition, a better resolution is achieved when performing the analysis with this particular association: when the capacity area analysis is performed peak by peak, scattered results may be observed [61] due to the difficulty to identify the inflection points of the IC curves precisely.

4.3. Identification of aging mechanisms through incremental capacity and peak area analysis

As reviewed in Chapter **2**, the degradation of LIBs can be originated from various aging modes (e.g. LLI, LAM_{NE}, LAM_{PE}, etc.) which may act simultaneously or individually. This section presents how the aging modes individually affect the resulting IC signatures. The aim is to provide a set of tools (degradation patterns) that facilitate the degradation analyses on commercial GIC||LFP cells. For that, the previous IC analysis [31] is improving by adding the PA analysis and the effects that individual aging modes causes on cell capacity fade. In order to facilitate the applicability of IC and PA analyses, a summary is provided at the end of this section in look-up tables. These analyses are extensively used in Chapter **6** and Chapter **7** to decipher the actual, more complicated aging modes that affect the tested GIC||LFP cells.

To carry out the analyses, computer simulations were performed using a toolbox named *'Alawa*, developed in the Electrochemical Power Systems Laboratory (University of Hawaii at Manoa, USA). The mechanistic model implemented in *'Alawa* is described in [31] and the *Alawa's* features are presented in the experimental section (Chapter **5**). The simulation parameters used to obtain the results of this section were intentionally chosen to provide a realistic approach: thermodynamic cycling (C/25), a total of 1,500 cycles (represented in the figures in intervals of 250 cycles) with a degradation of 0.02% per cycle. The cycle number and degradation rate are selected to reach cell's end of life (EOL) in all aging scenarios. The constructive cell parameters are loading ratio (LR) = 0.95 and offset (OFS) = 12.5%. The simulated electrodes (NE and PE) were harvested from the commercial cells used in this thesis. It is important to point out that the quantitative results presented here are only valid for the simulation parameters used. However, the qualitative tendencies can be extrapolated to any GIC||LFP system.

4.3.1. Loss of lithium inventory

The loss of lithium inventory (LLI) results in an overall slippage of the NE over higher relative SOC_{PE} (see **Fig. 4.7**, inset figure). The slippage effect with cycling predominantly reduces the intensity (i.e. area underneath the peak) of peak ❶, as observed in **Fig. 4.7**. Peak ❷ only starts to lose intensity once peak ❶ is completely lost (cycle 1,250). This is because the GIC stage ❶ has been shifted outside the voltage window of the full cell. Peak ❺ is also affected by LLI, although in a small proportion. Upon aging, it tends to move towards higher potentials, although its intensity does not change. A similar effect occurs with peak ❷, where a small shifting towards higher potentials may occur. In contrast, peaks ❸ and ❹ are barely affected by LLI. Finally, the inflection point between peaks ❶ and ❷ remains practically constant in terms of voltage, although the IC value is reduced with aging.

Regarding the PA analysis, LLI causes linear capacity fade of peak ∫❶ until its area is completely lost. On the other hand, peak ∫❷-❺ remains constant, and only starts to lose capacity when peak ∫❶ is completely lost in cycle 1,250, as observed in **Fig. 4.8**a. From full cell perspective, LLI causes linear capacity fade from the first cycle, and remains constant even below the cell's EOL (see **Fig. 4.8**b). To sum up, in a first degradation stage, all the capacity lost in the full cell is reflected in peak ❶, both in the IC and PA analyses. Only under harsh degradation (i.e. below cell's EOL), peaks ∫❷-❺ are affected.

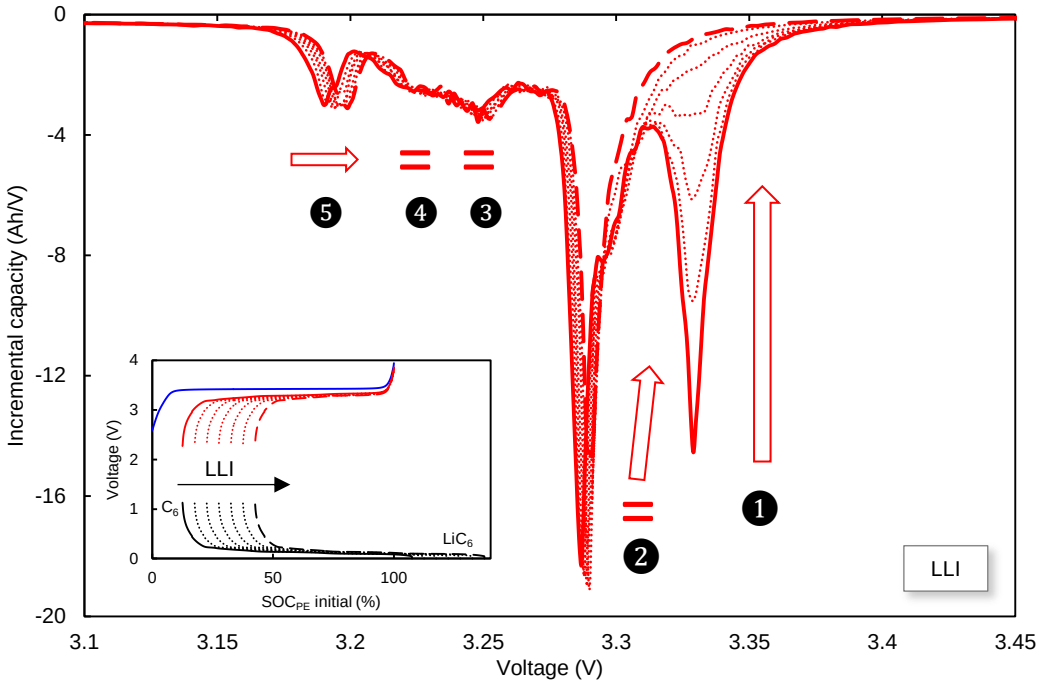

Fig. 4.7. IC signature evolution of LLI from the initial state (solid line) to the end of cycling (long-dash line), presented in 250 cycle intervals (small dotted lines). Inset figure shows LLI from the electrode perspective.

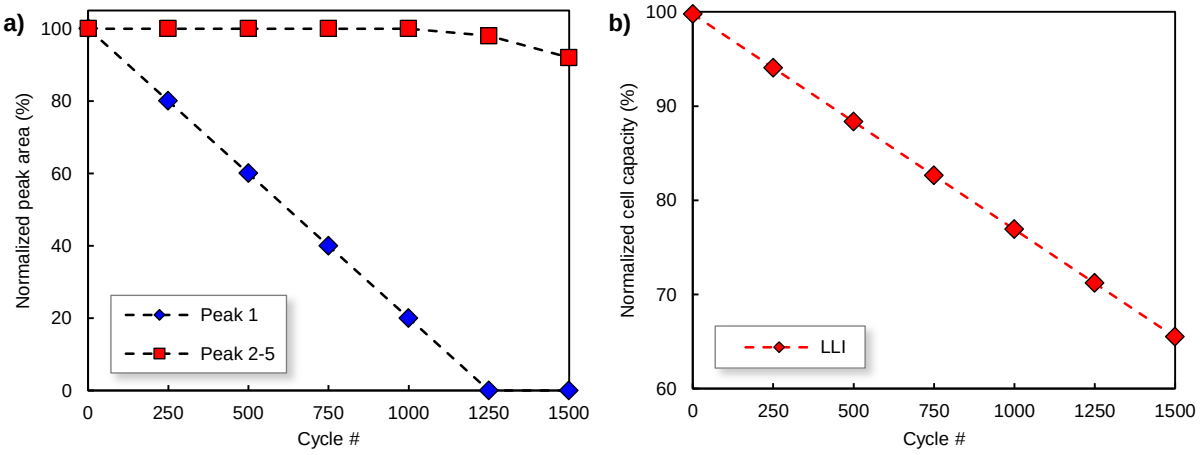

Fig. 4.8. Evolution of a) normalized peak areas and b) normalized cell capacity as a function of cycle number under LLI.

4.3.2. Loss of active material

This section individually presents the four modes of loss of active material (LAM) and its effects on the IC, PA and full cell capacity.

Loss of active material on the negative electrode delithiated (LAM$_{deNE}$) inducing Li plating

The aging mode LAM$_{deNE}$ results in a shrinkage of the NE (i.e. loss of capacity of the active material) starting from its lithiated state (LiC$_6$) or high SOC$_{PE}$, and is fixed at the delithiated state (C$_6$), or low SOC$_{PE}$ (see **Fig. 4.9**, inset figure). This shrinkage effect causes a reduction in all the IC peaks (since less graphite is involved in the reactions), except in peak ❶, that increases. This is because the NE has an excess of relative capacity outside the voltage window of the full cell (as the PE is the limiting electrode in charge). Therefore, with the shrinkage effect of LAM$_{deNE}$ starting from its lithiated state, more and more capacity in the staging ❶ plateau is accessible in the intercalation process. However, peak ❶ stops

growing at cycle 500, because thermodynamic Li plating occurs. From the inset figure (**Fig. 4.9**) this event occurs when the NE is reduced below 100% SOC_{PE}. The effect of Li plating on the IC signature may result in the appearance and subsequent growth of peak ⓪. Peak ⓪ emerges under reversible Li plating conditions. On the other hand, if all the deposited lithium is lost irreversible, peak ⓪ does not emerge. Hence, IC peak ⓪ shown in **Fig. 4.9** represents a theoretical 100% reversible Li plating process. The case of a thermodynamic Li plating process where both irreversible and reversible phenomenon interacts simultaneously would result in a smaller growth of peak ⓪. The growth depends on which process predominates. Regardless of the reversible or irreversible nature of Li plating, the evolution of peak ❶ and peaks ❷ to ❺ remains the same, i.e. reducing its intensity. It is important to point out that peak ❺ shifts towards lower potentials. Also, the inflection point between peak ❶ and ❷ is reduced in terms of IC height and slightly shifted towards lower potentials.

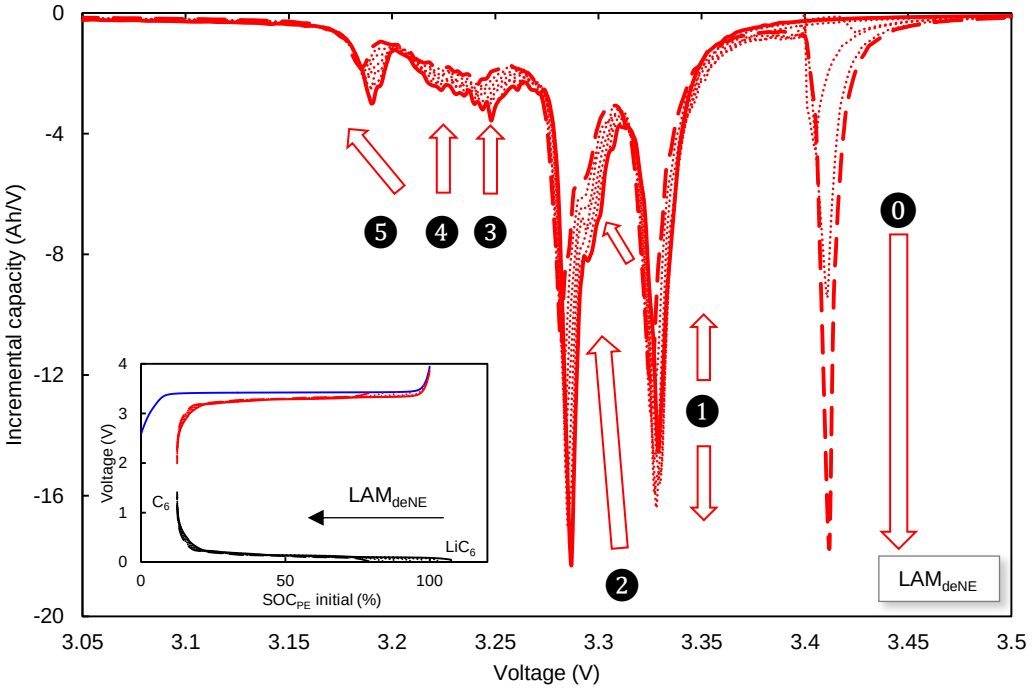

Fig. 4.9. IC signature evolution of LAM_{deNE} inducing reversible Li plating, from the initial state (solid line) to the end of cycling (long-dash line), presented in 250 cycle intervals (small dotted lines). Inset figure shows LAM_{deNE} from the electrode perspective.

The PA evolution under LAM_{deNE} is shown in **Fig. 4.10**a. Before Li plating occurrence (cycle 500), peak ∫❶ grows. Thereafter, it decreases following a linear degradation. Peak ∫❷-❺ follows a linear degradation, starting from the first cycle. Peak ⓪ evolution would appear at cycle 500, but it is not shown for the sake of clarity, as it depends on whether the mechanism is reversible and/or irreversible. The normalized cell capacity evolution under LAM_{deNE} has a peculiar behavior, as observed in **Fig. 4.10**b. During the first 500 cycles (i.e. no Li plating), the aging mode is not reflected in terms of capacity fade. The capacity that is lost under peak ∫❷-❺ is concurrently gained by peak ∫❶. Hence, this is a "silent" degradation mode, because the capacity remains unchanged, even though the cell is being aged. However, this "silent" mode may be identified by evaluating IC and PA peak ❶ growth. As thermodynamic Li plating appears, the process may be reversible and/or irreversible. The capacity fade evolution under the two cases is depicted in **Fig. 4.10**b. As commented with the IC peaks, a more likely scenario would show a capacity fade delimited within the two tendencies, as shown in the gray-dotted area.

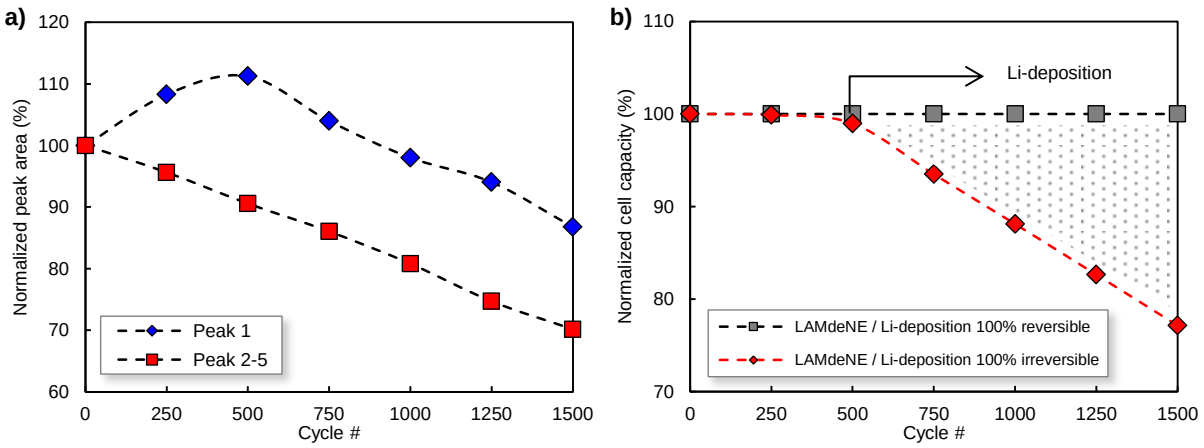

Fig. 4.10. a) Evolution of peak areas and b) normalized cell capacity as a function of cycle number, both under LAM_{deNE}.

Loss of active material on the negative electrode lithiated (LAM_{liNE})

The aging mode LAM_{liNE} results in a shrinkage of the NE towards a higher SOC_{PE}, starting from the NE delithiated state, and fixed at its lithiated state (see **Fig. 4.11**, inset figure). This shrinkage effect reduces all IC peaks proportionally as the cell ages with cycling. Only the reduction of peak ❺ is affected differently, as represented by the arrow over peak ❺ in **Fig. 4.11**. The inflection point between peaks ❶ and ❷ remains constant in voltage, though its IC value is reduced.

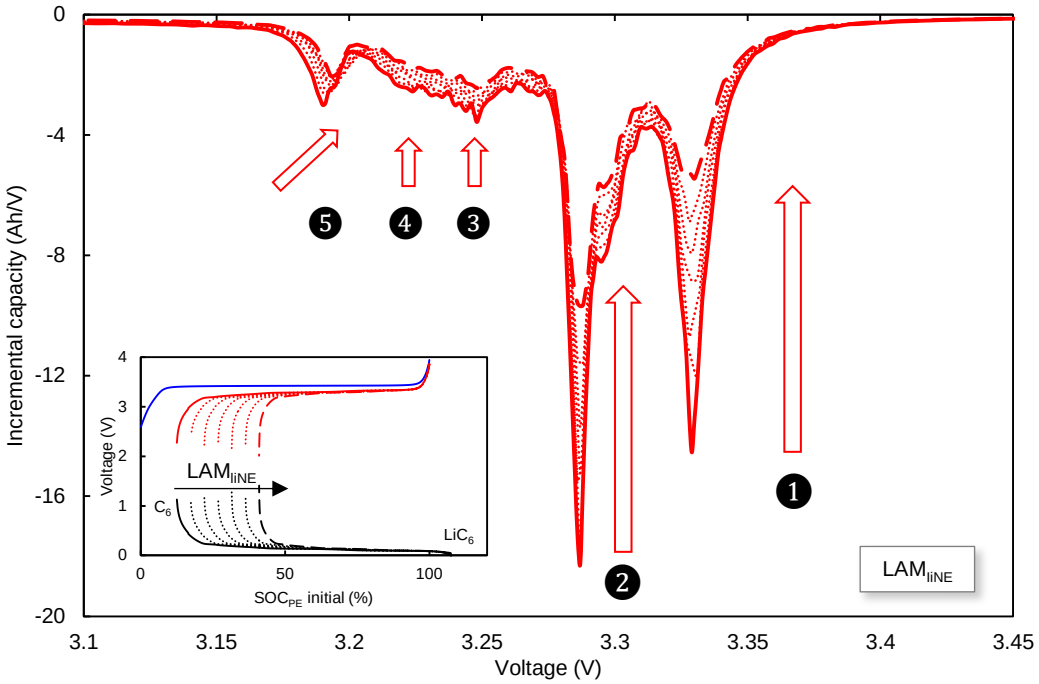

Fig. 4.11. IC signature evolution of LAM_{liNE} from the initial state (solid line) to the end of ccyling (long-dash line), presented in 250 cycle intervals (small dotted lines). Inset figure shows LAM_{liNE} from the electrode perspective.

Regarding the PA analysis, LAM_{liNE} causes linear capacity fade of peak ∫❶ and peak ∫❷-❺, as observed in **Fig. 4.12**a. The slope is however slightly less abrupt for peak ∫❷-❺ than that found on peak ∫❶. From a full cell perspective, LAM_{liNE} causes linear capacity fade from the first cycle, even below the cell's EOL (see **Fig. 4.12**b).

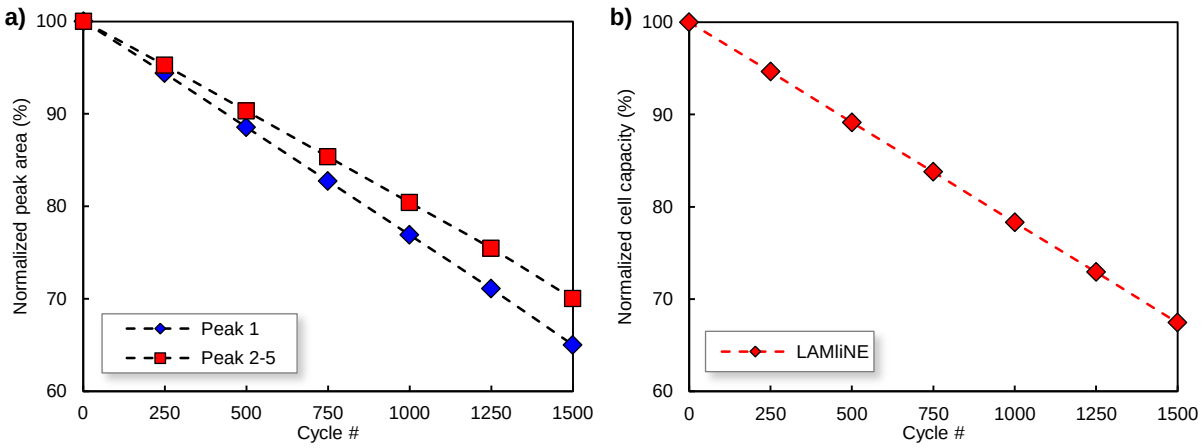

Fig. 4.12. a) Evolution of normalized peak areas and b) cell capacity as a function of cycle number under, both under LAM_{liNE}.

Loss of active material on the positive electrode delithiated (LAM_{dePE})

The aging mode LAM_{dePE} results in a shrinkage of the PE towards a higher SOC_{PE}, starting from its PE lithiated state (LFP) or low SOC_{PE}, and fixed at its delithiated state(FP) or high SOC_{PE} (see **Fig. 4.13**, inset figure). For these particular simulation parameters, during the first 250 cycles, LAM_{dePE} slightly affects peak ❺, by modifying its shape, towards lower potentials, as indicated by its corresponding arrow in **Fig. 4.13**. With no doubt, peaks ❶ to ❹ are not affected during the first 250 cycles, because the degradation of the PE is not within the full-cell signature limits (see **Fig. 4.13**, inset figure). As the cell ages, and the degradation of the PE is within the full-cell signature limits, peak ❺ is affected, and its intensity is reduced. As peak ❺ is more degraded, peaks ❹ and ❸ are also reduced, as they are very closely situated. Similarly, when peaks ❺ to ❸ are completely lost, peak ❷ would be reduced. For these particular parameters, this event occurs at cycle 1,500. While peaks ❺-❸ are being degraded, peaks ❶ and ❷ modify its shape, as indicated by the arrows. However, its intensity remains invariant, as confirmed from the PA analysis. Finally, the inflection point between peaks ❶ and ❷ is slightly affected, and shifts towards higher potential.

Regarding the PA analysis, as observed in **Fig. 4.14**a, the first 250 cycles do not cause any capacity loss on peak ∫❶-❺. After that cycle, peak ∫❷-❺ is reduced, following a parabolic degradation, continued by a linear degradation from cycle 750 onwards. However, peak ∫❶ remains invariant. From a full cell perspective, LAM_{dePE} does not cause any cell degradation during the first 250 cycles. Thereafter, a pseudo linear capacity fade is observed (see **Fig. 4.14**b). Hence, LAM_{dePE} causes "silent" degradation during the first cycles, caused by the particular degradation pattern of the PE. Only when the degradation of the PE is large enough to interact with the full-cell signature, the effects of LAM_{dePE} produces cell capacity fade.

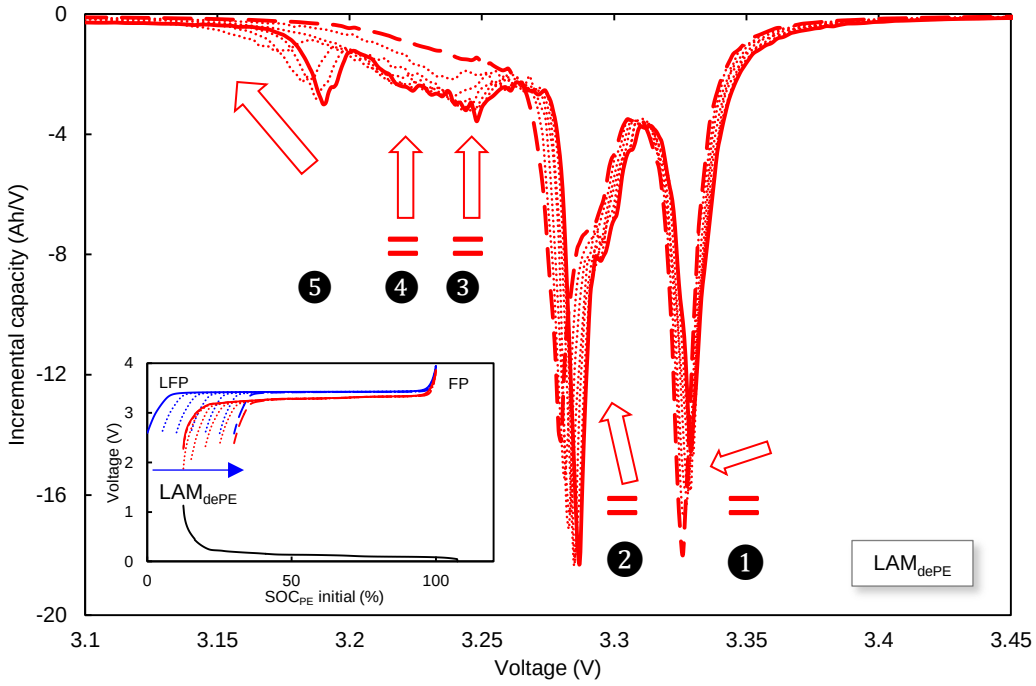

Fig. 4.13. IC signature evolution of LAM_{dePE} from the initial state (solid line) to the end of cycling (long-dash line), presented in 250 cycle intervals (small dotted lines). Inset figure shows LAM_{dePE} from the electrode perspective.

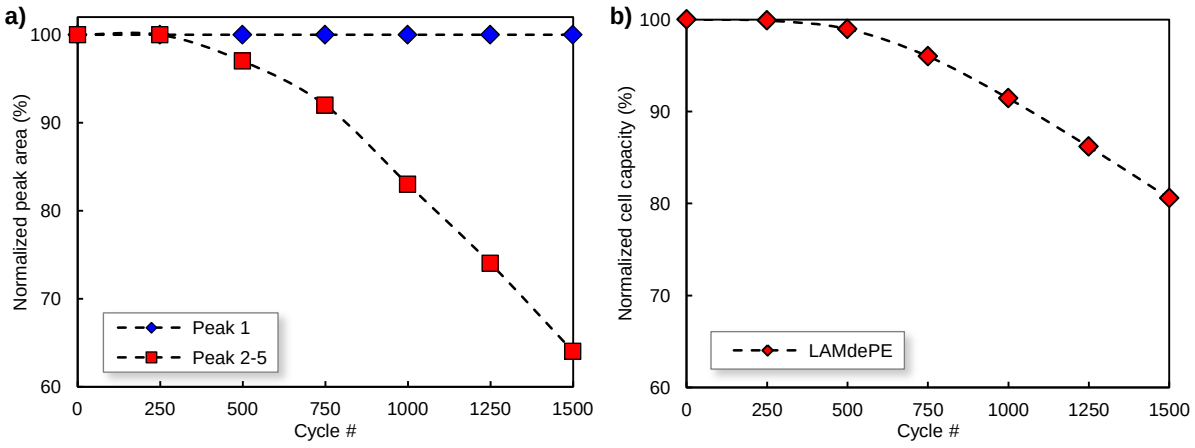

Fig. 4.14. a) Evolution of peak areas and b) normalized cell capacity as a function of cycle number, both under LAM_{dePE}.

Loss of active material on the positive electrode lithiated (LAM_{liPE})

The aging mode LAM_{liPE} results in a shrinkage of the PE towards a lower SOC_{PE}, starting from its PE delithiated state, and fixed at its lithiated state (see **Fig. 4.15**, inset figure). The shrinkage effect of the PE with cycling predominantly affects peak ❶, while peaks ❷-❺ remain invariant. As observed from **Fig. 4.15**, Peak ❷ only starts to lose intensity once peak ❶ is completely lost. For the selected simulation parameters, this event occurs at cycle 1,250. This is because the PE has reduced a large proportion of its capacity, and the stage ❶ in the GIC is now outside the voltage window of the full cell. The inflection point between peaks ❶ and ❷ remains constant in voltage, although is reduced as the cell ages.

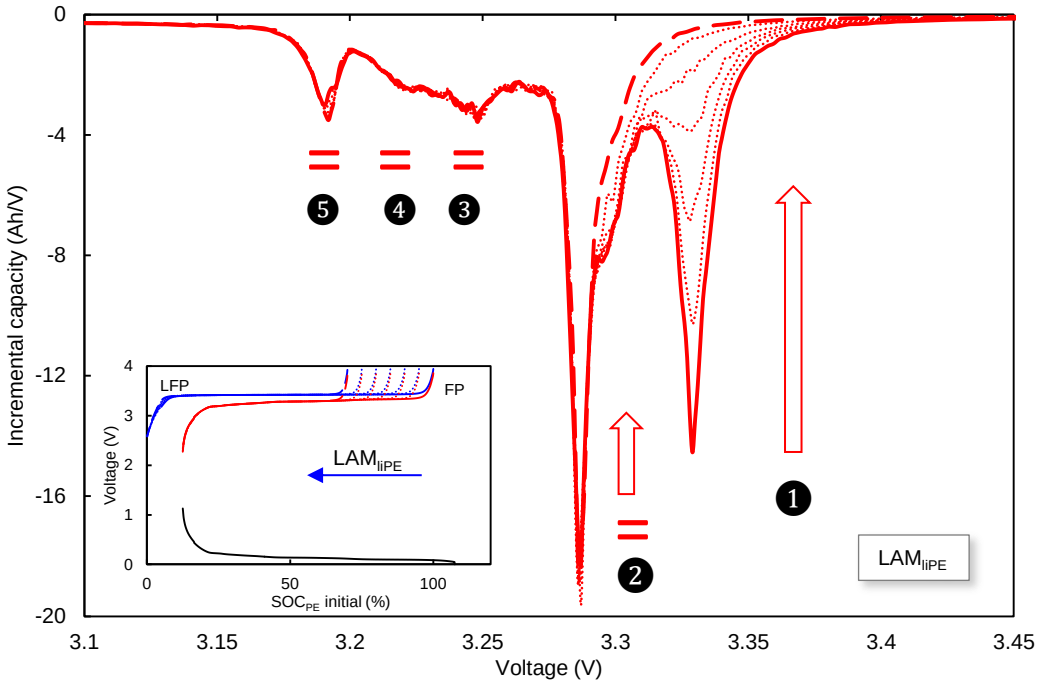

Fig. 4.15. IC signature evolution of LAM$_{liPE}$ from the initial state (solid line) to the end of cycling (long-dash line), presented in 250 cycle intervals (small dotted lines). Inset figure shows LAM$_{liPE}$ from the electrode perspective.

Regarding the PA analysis, LAM$_{liPE}$ causes linear capacity fade of peak ∫❶ until its area is completely lost. On the other hand, peak ∫❷-❺ remains constant, and only starts to lose capacity when peak ∫❶ is completely lost. This occurs at cycle 1,250 (see **Fig. 4.16**a). From a full cell perspective, LAM$_{liPE}$ causes linear capacity fade from the first cycle, and remains constant even below the cell's EOL (see **Fig. 4.16**b). To sum up, in a first degradation stage, all the capacity lost in the full cell is reflected in peak ❶ both in the IC and PA analyses. Only under harsh degradation (i.e. below cell's EOL), peaks ∫❷-❺ are affected. Most interestingly, LAM$_{liPE}$ and LLI have the same outcomes in terms of PA and normalized cell capacity. The IC peaks (particularly peak ❺) must be analyzed, among other techniques, to decipher whether the degradation origins are caused from LAM$_{liPE}$ or LLI.

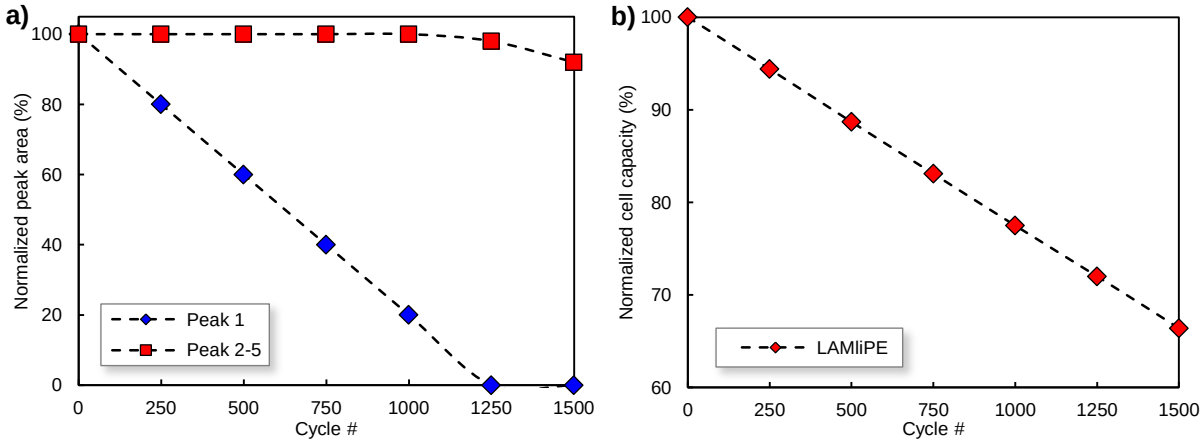

Fig. 4.16. a) Evolution of peak areas and b) normalized cell capacity as a function of cycle number, both under LAM$_{liPE}$.

4.3.3. Ohmic resistance increase

The aging mode ohmic resistance increase (ORI) affects the cell voltage. During charge, an ORI causes the cell voltage to increase, while on discharge is reduced. As a result, the energy delivered by the cell during discharge is reduced, while during charge is increased. Hence, the energy efficiency is reduced. The IC curves resulting from ORI at C/25 in a cell are shown in **Fig. 4.17**. The peaks are shifted towards higher potentials during charge, while on discharge is the opposite. Contrary to LLI and LAM modes, the effect of ORI does not cause direct capacity fade in the cell electrodes. Hence, the IC signatures do not show any loss of intensity, and remain constant in terms of shape. Similarly, since the IR does not cause direct capacity fade, normalized peak area capacity and normalized cell capacity are not shown, as they remain invariant. However, it is important to point out that large ORIs can indirectly reduce capacity on a cell. Under large ORIs (e.g. 100% increases) coupled with high C-rates (e.g. >2C), the predetermined cell cut-off voltage is reached earlier, and the cell may not completely reach full charge or discharge state. But the cell capacity is not lost. For example, thermodynamic C/25 rates, and even under ORIs of 200% as the ones shown in **Fig. 4.17**, the results did not show capacity fade.

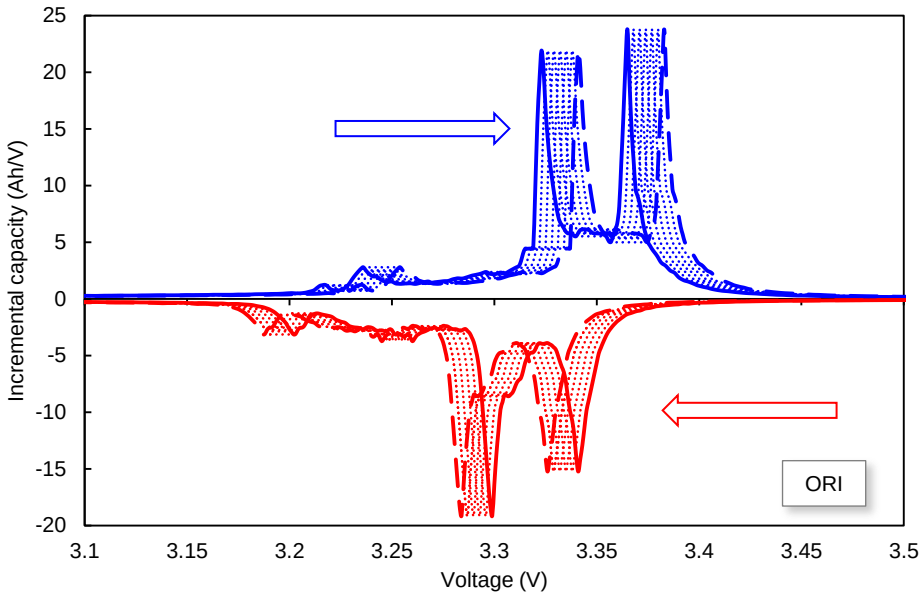

Fig. 4.17. IC signature evolution of ORI (200% of total increase) at C/25 from the initial state (solid line) to the end of cycling, presented in 250 cycle intervals (small dotted lines).

4.3.4. Summary of aging mechanisms identification through incremental capacity and peak area analyses

This section is to present a summary of the main outcomes derived from the IC, PA and capacity fade analyses for each individual aging mode. As previously shown, the different aging modes result in different IC and PA signatures. Some modes may even exhibit "silent" stages difficult to detect, and others (i.e. LAM_{deNE}) exhibit complicated patterns, with possibility of Li deposition. The identification of the aging modes on actual cells can be even more complicated because the aging modes are usually interrelated and may act simultaneously. Hence, to facilitate the IC and PA analyses on experimentally aged cells, a summary in form of look-up tables is presented here. The approach is to compare the tables presented here with the experimental IC and PA results of tested cells. By carefully analyzing and comparing the peak's signature evolution, the identification of the aging modes shall be clarified.

Table 4-1 summarizes the main degradation modes and their effects on the IC peaks for a GIC||LFP cell under thermodynamic discharges. The left column shows the possible degradation modes, whereas the first row indicates the IC peak numbers and the IC inflection point between peaks ❶ and ❷ (i.e.

$IP_{❶-❷}$). The upward and downward arrows indicate the reduction or the increase of the associated IC peak intensity respectively. Horizontal arrows indicate shifting of the IC peak positions; equal symbols indicate invariant IC signature. The symbols in red only apply when a second degradation stage takes place (e.g. when peak ❶ is completely lost during LLI then peak ❷ is reduced or after Li plating occurs under severe LAM_{deNE}). Peak ❿ only applies in the case of Li plating under LAM_{deNE}. As previously analyzed, peak ❿ appears under reversible Li plating.

Table 4-1. Summary of the main degradation modes and their effects in a GIC||LFP cell on discharge. Notice that arrow symbol ↑ indicates IC peak reduction.

Aging mode	❶	❷	❸	❹	❺	❿	$IP_{❶-❷}$
LLI	↑	= ↑	=	=	→	–	↑
LAM_{deNE}	↓ ↑	↑	↑	↑	↖	= or ↓	↑
LAM_{liNE}	↑	↑	↑	↑	↗	–	↑
LAM_{dePE}	= ↙	= ↑	= ↑	= ↑	↑	–	↖
LAM_{liPE}	↑	= ↑	=	=	=	–	↑
ORI	←	←	←	←	←	–	=

Table 4-2 summarizes the main results obtained from the peak area and normalized cell capacity aging mode analyses. It also includes the effects that the aging modes have on the internal constructive parameter LR and OFS. It also includes whether the aging mode is silent or can induce Li plating. Results in red color only apply when a second degradation stage takes place.

Table 4-2. Summary of the main characteristics derived from the peak area analyses.

	LLI	**LAM_{deNE}**	**LAM_{liNE}**	**LAM_{dePE}**	**LAM_{liPE}**
Peak Area ∫❶	Linear/ Depleted	Pseudo-linear increase/ Decreases	Linear	Not affected	Linear/ Depleted
Peak Area ∫❷-❺	Unchanged/ Linear	Linear	Linear	Unchanged/ Pseudo-linear	Unchanged/ Linear
Normalized cell capacity	Linear	Unchanged/ Unchanged or Linear	Linear	Unchanged/ Pseudo-linear	Linear
Loading ratio (LR)	Not affected	Decreases	Decreases	Increases	Increases
Offset (OFS)	Increases	Not affected	Increases	Reduces/ Negative	Not affected
"Silent" mechanism	No	Yes	No	Yes	No
Risk Li plating	No	Yes	No	No	No

To clarify the use of **Table 4-1** and **Table 4-2**, a simple example is provided. If in the resulting IC curves of a tested cell only decreases peak ❶, the aging mode may be LLI or LAM_{liPE}. However, this may be resolved by analyzing peak ❺. If there is a slight shift towards higher potentials, then the aging mode is LLI. Another example can show a reduction of peaks ❷-❺ from the first cycles. That indicates that a LAM_{NE} is undergoing. By examining evolution of peak ❶, one may detect LAM_{deNE} (if peak ❶ increases)

or LAM_{liNE} (if peak ❶ is reduced). Peak area analyses would also resolve the two aging modes and quantitative calculate the capacity lost by the aging mode. Notice that peak ❺ may be also helpful to identify different aging modes.

It is important to point out that the identification of the aging modes can be very challenging. The identification gets even more complex when several aging modes act simultaneously (i.e. LLI coupled with LAM_{NE} and/or LAM_{PE}, etc.) as can be the case in real life experiments. Under such circumstances, identifying and quantifying the aging modes is not always possible. To resolve this issue, IC and PA analyses shall be coupled with additional powerful tools. Such tools can be computational and/or through *post mortem* tests. In this thesis work, computational tools using the *'Alawa* toolbox are used to analyze the aging modes of the tested cells.

4.4. Characterization of battery aging through *post mortem* techniques

Further investigations to characterize battery aging and get some more understanding of the underlying aging phenomena may require *post mortem* physical analysis. Examples include structural analysis of the active materials by techniques such as X-ray diffraction (XRD), morphological and microstructural characterization with scanning electron microscopy (SEM), and transmission electron microscopy (TEM). Since in this thesis work we reference literature studies on *post mortem* analyses carried out on GIC||LFP cells, we find necessary to briefly cover the most common *post mortem* analyses to identify the aging.

Half-cell electrochemical testing

Electrochemical testing of the individual electrodes vs. lithium metal allows an assessment on the intrinsic capacity loss and/or resistance increase [59]. To examine the capacities of the electrodes, a cautious cell disassembling process inside a glove box is required. If precautions are not taken, possible artifacts in the measurements are likely to occur [76], [79].

In a GIC||LFP cell, the half-cell study consists of two half-cells (i.e. Li/LFP, Li/GIC cells) often assembled as Swagelok cells, or coin cells. Through electrochemical testing of the cells, the residual capacity of the electrodes can be measured. In the positive LFP electrode, the residual capacity corresponds to the amount of empty sites left in the $FePO_4$ framework when the full cell is fully discharged. As a consequence, the residual capacity would be a strong indication for the LLI [68], [76]. For the graphite electrode, the residual capacity corresponds to the amount of lithium left in this electrode when the full cell is fully discharged.

An example of the charge/discharge profiles of graphite and LFP electrodes recovered from different location areas for electrochemical evaluation is shown in **Fig. 4.18**a-b respectively. **Fig. 4.18**a, shows the effects of capacity and impedance degradation of the graphite (caused by non-uniform degradation). **Fig. 4.18**b displays the discharge capacities of the LFP electrode samples at same location for two current densities, where the polarization effects are observed when the samples are tested at higher current densities [68].

Chapter **5** includes a detailed section on half-cell procedures, materials and preparation. However, we shall point out that the half-cell tests carried out in this thesis were purposed for feeding the *'Alawa* simulation toolbox, and were not designed for battery aging characterization. Still, the procedures, materials and preparation also apply to characterize battery aging.

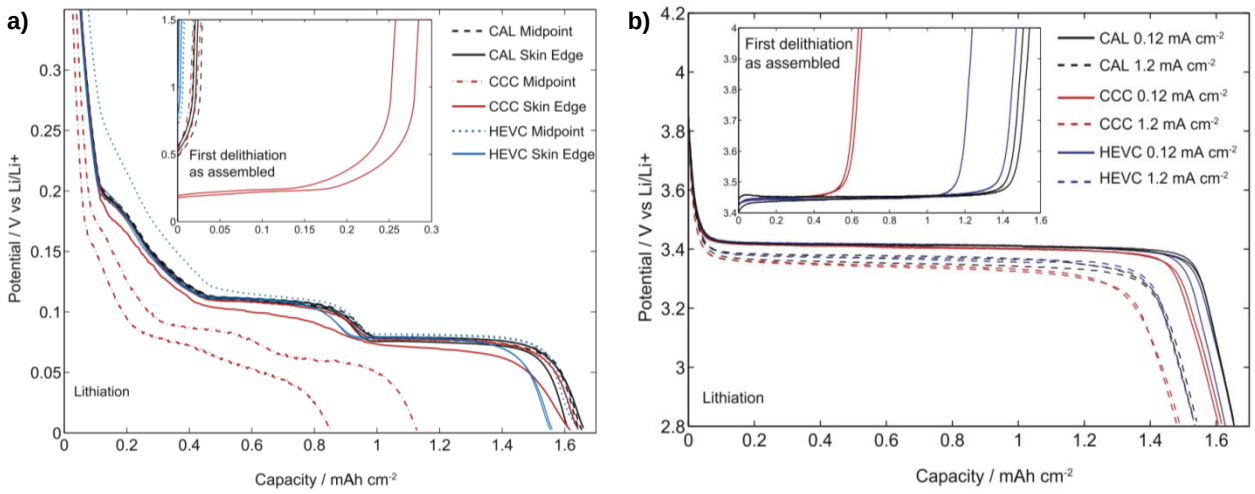

Fig. 4.18. a) Lithiation of the graphite electrode measured agains Li using constant current of 0.12 mA cm^{-2}, b) lithiation of LFP at currents of 0.12 and 1.2 mA cm^{-2} [68].

Morphology analyses

To investigate morphology, particle size, particle coatings, mixing efficiency and defects, microscopy techniques such as Scanning Electron Microscopy (SEM) and Transmission Electron Microscopy (TEM) can be used.

The SEM technique can be successfully applied to study the deterioration of electrode materials, including exfoliation phenomena, cracking of particles and delamination of the carbon negative electrodes. An example of SEM micrograph of a graphite anode, harvested from a commercial GIC||LFP cell is shown in **Fig. 4.19**a-b. **Fig. 4.19**a shows the SEM image of the graphite sample, harvested from a full cell when fresh (i.e. beginning of life, BOL). In contrast, **Fig. 4.19**b shows the SEM image of a harvested sample from the same type of cell, after being cycled at 2C, 80% DOD, 0ºC to reach end of life (EOL). As shown, **Fig. 4.19**b shows most pronounced microcracks in the surface, caused by cycling [59].

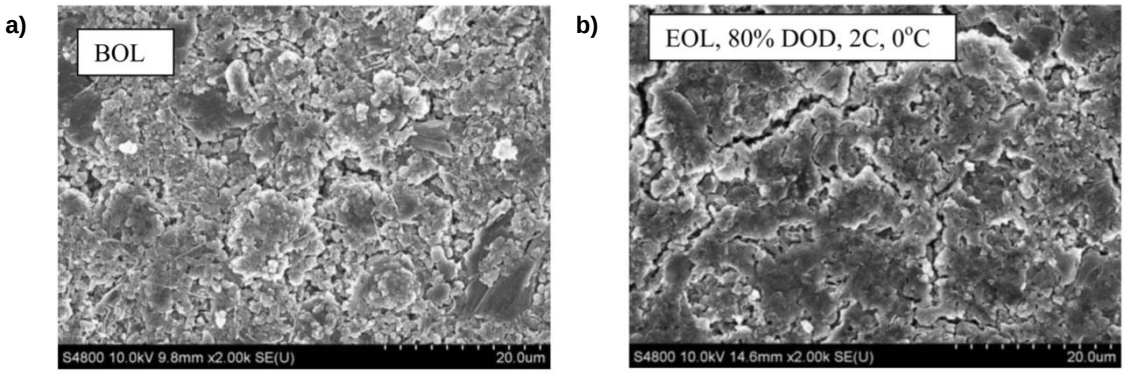

Fig. 4.19. SEM images of the graphite electrodes, extracted from a) an as-received cell, and b) cell cycled at 80% DOD, 2C, 0ºC, which showed pronounced microcracks [59].

TEM has better spatial resolution than SEM, and can execute additional analytical measurements, although they require more sample preparation. An example of TEM is shown in **Fig. 4.20**a-b. The images correspond to LFP electrodes, harvested from GIC||LFP cells when fresh (a) and aged (b). From the images it is observed that the particle size did not experienced major changes as the cell ages. The results shown here are in agreement with other works, for the same type of cell [110], [172]. The images

shown here correspond to an internal unpublished study carried out at the dependencies of the University of Oviedo and the National Carbon Institute (INCAR) [173].

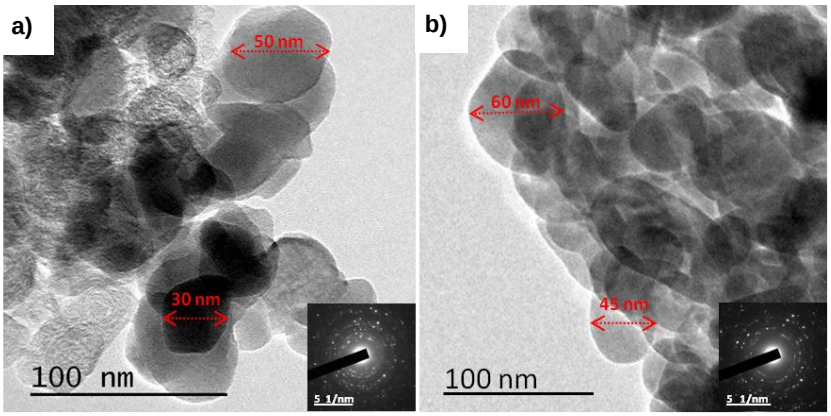

Fig. 4.20. TEM images for a) fresh and b) aged LFP cathode material to measure particle size.

An example of high resolution TEM (HRTEM) is shown in **Fig. 4.21**a-b. The images correspond to LFP and FP particles of the same harvested LFP cathode material. It is observed that HRTEM can measure the crystalline parameters (see **Fig. 4.21**a-b). Also, HRTEM can also be used to observe SEI layer thickness or Li dendrite growth on the NE. The images shown here correspond to an internal unpublished study carried out at the dependencies of the University of Oviedo and INCAR [173].

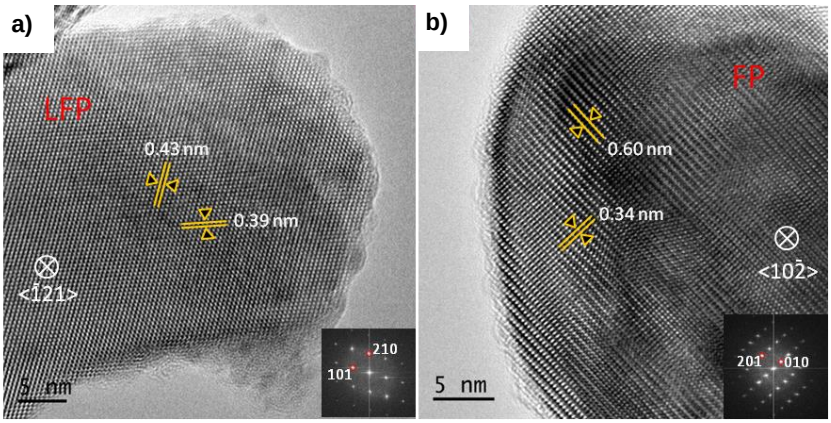

Fig. 4.21. HRTEM images measuring crystal lattice for a) LFP and b) FP cathode.

Structural analyses (X-ray diffraction, XRD)

X-ray diffraction is the most widely used technique used for studying long range structural ordering of materials and phase identification in LIB research. It is also used for quantitative analysis of phases, residual stress measurement, crystal structure, and three-dimensional material properties [64].

An example of XRD diffractograms of the LFP electrodes recovered from a fresh and a long-term cycled commercial GIC||LFP cell is shown in **Fig. 4.22.** The peak's positions indicate the presence of a mixture of LFP and FP crystals (y LFP + (1-y) FP) and not a solid solution LyFP, both on the PE of the fresh and aged cell. The area underneath the peaks (intensity) can be used to estimate the lithium content (the ratio y) in the fresh and aged electrodes. The results indicate that the aged PE contains less lithium than the fresh one, which is an evidence that LLI occurred throughout the cycling of the cell. This image corresponds to an internal unpublished study in collaboration with the University of Oviedo and the INCAR [173].

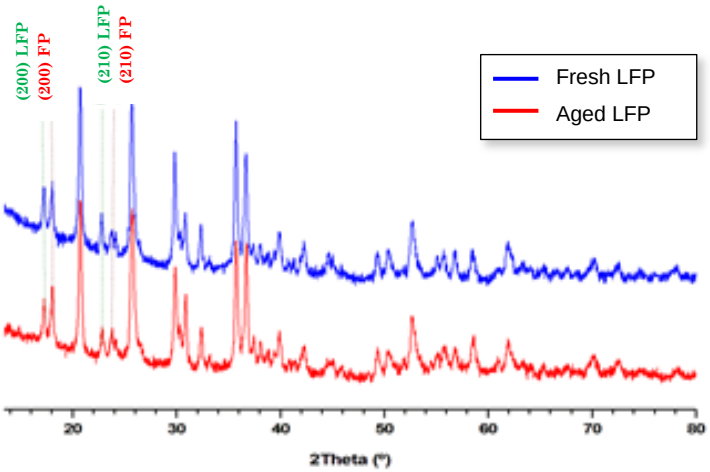

Fig. 4.22. XRD patterns of the LFP electrodes recovered from a fresh (blue) and aged cell after long-term cycling (red).

4.5. Summary

In this chapter, several techniques to analyze battery aging are examined. We started describing standard, well established techniques to evaluate capacity and power fade. The use of these techniques provides, for example, quantitative data to evaluate the end-of-life (EOL) of a battery. The internal resistance (IR) of a lithium ion battery (LIB) is considered a key parameter because it is directly related to power capabilities and battery aging. Here we provide a brief description of the most accurate IR measurement methods, highlighting its advantages and drawbacks. We concluded that the voltage curve difference (VCD) method is simple, yet accurate. Due to its advantages, this technique has been selected to carry out the IR measurements in the thesis. A detailed description of the VCD technique is provided in Section **4.1.3**.

The incremental capacity (IC) and peak area (PA) techniques are considered some of the most advanced, non-invasive *in situ* tools to trace a first qualitatively and quantitatively approach to decipher the aging modes of LIBs. However, the use and implementation of these techniques is not straightforward, and a full description is rarely found in the literature. Therefore, we carry out a study to understand the basis of the IC and PA techniques in Section **4.2**.

The analysis of the data derived from the IC and PA techniques can be challenging. To help in this task, Section **4.3** presents a broad analysis of the evolution with cycling of the effects that each aging mode causes on the IC, PA, cell capacity and half-cell electrode degradation. The analyses were performed based on a mechanistic model implemented in a toolbox named *'Alawa*, particularized for graphite, lithium iron phosphate (GIC‖LFP) batteries. To identify aging modes with the best resolution and accuracy, the analyses should be carried out under thermodynamic conditions (i.e. C/25). As an illustration, loss of lithium inventory (LLI), which is considered the main cause of degradation in LIBs, causes the reduction of IC peak ❶, linear capacity loss of $\int$❶, linear capacity loss of the full cell and a slippage of the negative electrode (NE). Another representative example is the loss of active material on the NE, when delithiated (LAM_{deNE}). Here we show the harmful effects of large $LAM_{deNE,}$ and how it may lead to Li plating. The analyses presented here also illustrate the effects that the aging modes cause on cell constructive parameters (i.e. LR and OFS), and how "silent" mechanisms may appear after a previous incubation stage. Overall, the analyses carried out here we aim to provide a set of tools to facilitate the degradation analysis in commercial LIBs.

Section **4.3** also shows how different aging modes result in particular, and sometimes complicated IC and PA signatures. However, these signatures are usually more complicated in real life LIBs, because the aging modes interrelate and can act simultaneously. To facilitate the analysis, we additionally provide a summary in form of look-up tables which is useful for the identification of the aging modes in real life applications.

The IC and PA analyses can be coupled with additional powerful tools to further analyze the aging mechanisms. Such tools can be computational and/or *post mortem* tests. In this thesis, computational tools using the *'Alawa* toolbox are used. Although *post mortem* analyses are outside of the scope of this thesis, we reference other works that used these techniques to clarify aging processes. Hence, a basic understanding of their capabilities is interesting. Therefore, to conclude the chapter, we briefly present the most commonly used techniques to characterize battery aging through *post mortem* physical analysis. Examples are half-cell electrochemical testing, Scanning Electron Microscopy (SEM) or X-ray diffraction (XRD), to name a few.

This page intentionally left blank

5. General procedures and materials

Nowadays, despite the development of battery models for simulation, battery testing is still necessary to characterize cell aging and performance. Indeed, battery manufacturers require extended cycle-life testing prior to battery commercial implantation. This validation is required by manufacturers of systems that include batteries. To illustrate an example, electric vehicle (EV) manufacturers require evaluating long-term battery testing procedures, including cycling, power or safety tests, before entering in production. This ensures that the selected cell technology is appropriated for the designed capabilities of the system. Hence, battery testing is fundamental.

Few characterization test methods have been developed by institutions and organizations. In addition, the existing tests are often too general and do not deal with the complex analysis of aging mechanisms. In particular, there was special interest to analyze the aging modes of lithium iron phosphate (LFP) cells under fast-charge and, also, combining fast-charge with dynamic stress discharges that emulate EV driving schemes. These working scenarios, coupled with an extensive cycling and further analysis of the degradation mechanisms, were yet to be reported in the literature.

In this chapter, we provide a set of long-term testing procedures designed specifically to enable the characterization of cell degradation and performance in a diverse manner. The multiple and extensive cycling is required to assess the power of the *in situ,* non-destructive techniques used in this thesis. Moreover, the testing schemes permit to evaluate cell performance, including parameters such as fast-charge capability and cell cycle-life, to name a few. Regarding cell performance, United States Advanced Battery Consortium (USABC) long-term goals are considered. In addition, half-cell testing procedures were carried out to be fed in the mechanistic computer simulation toolbox *'Alawa*. This innovative approach is later used to achieve accurate simulations, to further analyze the complex aging mechanisms found on the tested cells.

This chapter begins presenting the details of the cell type selected for testing in this thesis. Next, the proposed testing procedures are described, including the testing sequence throughout cells cycle life. To feed the mechanistic simulation model, half-cell testing procedures are presented next. The disassembling procedure and Swagelok cell construction requires careful considerations to avoid contamination and artifacts. Here we provide the required details to accomplish this objective. Following that, we present the testing equipment used in this thesis work. To finish the chapter, we present the mechanistic computer simulation toolbox *'Alawa,* together with an approach for coupling the experimental and simulation results and analyses to decipher the aging mechanisms.

5.1. Tested cell characteristics

Nanophosphate® high power GIC||LFP cells manufactured by A123 Systems were selected in this thesis, due to its advantages. This cell technology and architecture has fast charging capabilities, enhanced nanomaterials, high-power capabilities, is low cost and is suitable for its application on several LIB systems, including EVs, EESs and high power devices. An example of the tested cells is shown in **Fig. 5.1. Table 5-1** shows the main characteristics of the cell, obtained from the manufacturer's product datasheet. A total of 10 cells from the same batch (i.e. cell manufacturer identification number in sequence) were purchases from a vendor in a single order. This guarantees that all the cells have the same constructive characteristics from the manufacturing process. This is required to provide accurate and repeatable experimental results, not derived from cell-to-cell variations.

Fig. 5.1. Selected 2.3 Ah, high power GIC||LFP cell from manufacturer A123 Systems (model ANR26650M1).

Table 5-1. Main characteristics of the selected cells from manufacturer's datasheet.

A123 Systems	Characteristics
Model	ANR26650M1
Nominal cell capacity	2.3 Ah
Nominal cell voltage	3.3 V
Internal resistance (10 A, 1s DC)	10 mΩ
Standard charge method	2.3 A to 3.6 V CC/CV
Maximum discharge current (continuous)	70 A (30C)
Maximum charge current (continuous)	10 A (4.3C)
Cycle life at 10C discharge, 100% DOD	1000 cycles
Recommended charge and discharge voltage	3.6 V and 2 V
Cell weight	70 g

5.2. Battery testing procedures

Long-term, diverse and extensive battery testing procedures were designed to fully analyze the battery's aging mechanism and performance. Accordingly to the aims of this thesis work, first and foremost, extensive, diverse cycling allows us to assess the power of the *in situ,* non-destructive battery aging identification techniques used in this thesis work. Secondly, long-term, diverse battery testing is required to study the performance of the selected cell technology. Hence, three different cycling schemes were designed to accomplish the objectives of proper study of battery aging and performance.

The design of the battery testing procedures was carried out taken into consideration the United States Advanced Battery Consortium's (USABC) long-term targets. The test procedures evaluate the performance of advanced batteries for EVs, providing an unbiased measure of the cell's performance based on the goals of the USABC.

The battery testing procedures described here also include the sequence of reference test required to carry out the incremental capacity (IC) and peak area (PA) analysis. These are key tests, as they provide the data required to study battery aging. Overall, here is presented the experimental design in detail to both facilitate reproducibility of the tests and to judge the appropriateness of the experimental methods.

This section provides the detailed information of the main experimental procedures carried out on the selected GIC‖LFP cells. The testing procedures are divided into two sections. The first section (i.e. continuous cycling procedures) is the most important; the obtained data are used to analyze the aging modes of the tested cells. This is directly related with the main objectives of the thesis work. The second section deals with the calendar aging procedures, where the cells are set to rest and aging is analyzed.

Throughout testing, the cells were always cycled within the voltage limits recommended by the manufacturer (i.e. 2 V to 3.6 V). The same was applied for the testing currents. Data collection was set by voltage, at 5 mV/sample. The temperature for all testing, including continuous cycling and calendar aging was set to 23ºC.

5.2.1. Continuous cycling

Three cells were subjected to the continuous cycling test procedures. The framework of the procedures is shown in **Fig. 5.2**. As observed, each cell goes through the same testing stages; the difference is the type of cycling scheme implemented on each cell (i.e. standard, fast charge and dynamic stress). Reference performance tests (RPTs) evaluate the main cell characteristics after a pre-defined number of cycles (n = cycle number). The cycling number is sufficient to evaluate small aging intervals to later analyze the aging modes of the cells. Following the RPTs, the cycling process is resumed. The end of cycling is reached when the cells are close to, or surpass the battery's end-of-life (EOL). This ensures that the cell is fully characterized from its beginning of life (BOL) to EOL. Each procedure is commented below.

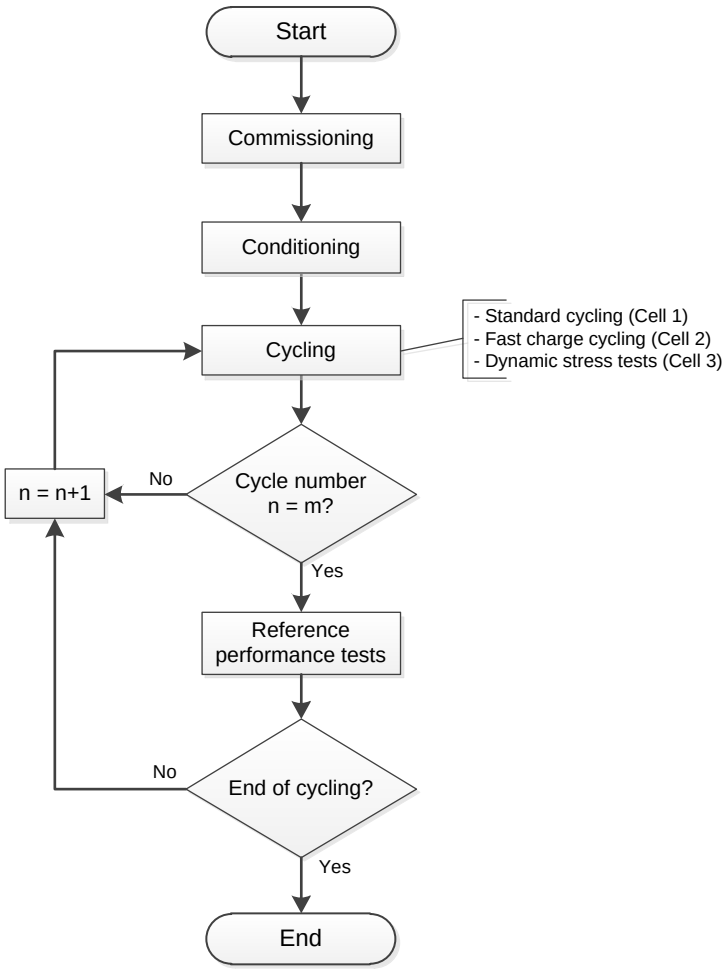

Fig. 5.2. Flow diagram of the continuous cycling procedure.

Commissioning

This stage is to identify, weigh and measure the OCVs voltage of the selected cells. The pre-test preparation is then carried out, which requires adjusting all the testing-machine software and hardware in order to achieve better reliability and improve the fidelity and accuracy of the measurements. Planning and scheduling the tests is also taken into account. Once these preparations are finished, the conditioning tests begin.

Conditioning

Prior to cycling, conditioning tests are performed to determine the effective capacity of the testing cells. The standard charging method consists of a CC-CV at 1C, until the termination current of C/20 is reached. The characterization test sequence is based on USABCs manual [16], and consists of performing groups of at least three different CC discharge cycles with the standard charging. Thus, three cycling at C/3, C/2 and C are performed. For subsequent testing, the battery capacity is considered stable when further three successive C/3 discharges agree within 2% [16]. Once the capacity has been stabilized, additional, thermodynamic tests at C/25 with 2h rest periods between cycles are also carried out. Thermodynamic tests provide the practical maximum capacity retention with minimal kinetic effects [7], [8]. The resulting C/25 capacity is adopted as the reference cell capacity. From the conditioning tests is also derived the initial internal resistance (IR) values, using the voltage curve difference (VCD) method. The conditioning tests are usually finished within 15 cycles.

Continuous cycling

Once the conditioning tests are finished, the cycling stage starts. The continuous cycling consists on a series of different continuous full charge and discharge cycles (100% DOD) for each cell, depending on the cycling protocol. The proposed cycling protocols are summarized in: standard, fast charge and dynamic stress test (DST) cycling.

1. Standard cycling (Cell 1): the standard cycling is a common, fundamental testing scheme which allows us to evaluate aging and performance under normal, expected testing circumstances. This testing scheme is also used as a "reference test scheme", since its results can be compared with other schemes. It consists of a sequence of continuous full charges and discharges at standard conditions. The standard charge is CC at 1 C (2.3 A) until the cell reaches the charging voltage (3.6 V), followed by a CV stage until the current declines to C/20 (110 mA), as seen in **Fig. 5.3**. The standard discharge is 1C until the cell reaches the cut-off voltage (2 V). This sequence is repeated for n = 300 cycles, followed by the RPT. Then again, the cycling is repeated.

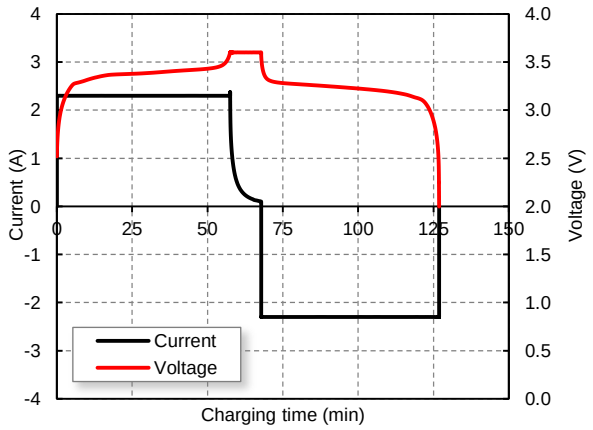

Fig. 5.3. Standard cycling procedure, showing cell current and voltage evolution vs. charging time.

2. Fast charge cycling (Cell 2): the fast charge cycling consists in performing both fast-charge and fast-discharge on a single cycle (see **Fig. 5.4**). Fast charge scheme was previously developed in Chapter **3**. This test is carried out to evaluate the performance of the fast charging protocol over long-term cycling, study the charging capabilities of the selected cell technology and architecture, and analyze how fast charging, coupled with rapid discharges affects battery degradation. The fast-charge protocol starts with a first phase (CC-I) at 4C constant current to 3.6V, followed by a second phase (CC-II) at 1C constant current to 3.6V. The last phase (CV-I) is a constant voltage step set to five minutes of length. After the fast-charging is accomplished, there is a 2 min rest, followed by the fast discharge at 4C constant current until the cut-off voltage of 2V is reached. During the discharge, the specific power delivered by the cell reaches values of 400 W/kg, meeting this long term USABC goal. Thereafter, the cell is again charged and discharged until the pre-defined cycle (n = 300) is reached. At this point, a RPT is carried out.

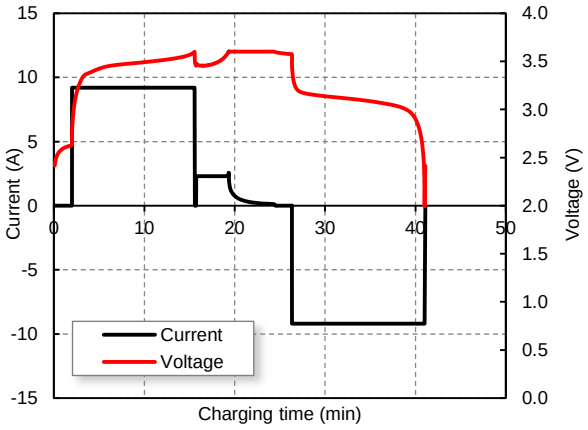

Fig. 5.4. Fast charge cycling procedure, showing cell current and voltage vs. charging time.

3. Dynamic stress tests (DST) (Cell 3): the DST cycling consists in performing both fast charge and dynamic stress tests discharges on a single cycle. Dynamic stress cycling is designed to evaluate the cell under "harsh", yet realistic electric vehicle (EV) driving cycling conditions. Here we expect to accelerate cell aging and cause additional degradation modes. This is especially interesting to evaluate the power of the battery aging identification methods. The charging process for this cycling test is identical as the explained above, that is the fast charging multistage protocol (4C-1C-CV). On the other hand, the discharge is carried out using a variable power discharge profile, developed by the USABC (Procedure #5B) [16]. This discharging protocol consists of a series of power pulses profiles mimicking discharge regimes and regenerative braking during a simulated vehicle driving, for a total of 360 s. The DST is scaled to the USABC long term power goal, set to 400 W/kg. The maximum power peak corresponds approximately to a 4C discharge current for the tested cell while 2C for the maximum charge peak power pulse. The DST profile is shown in **Fig. 5.5**a. The discharging sequence is finished when the voltage reaches the cell's cut off voltage (2 V). The profile of a complete charge and discharge cycle is shown in **Fig. 5.5**b. The sequence is repeated for n = 300 cycles, followed by the RPT.

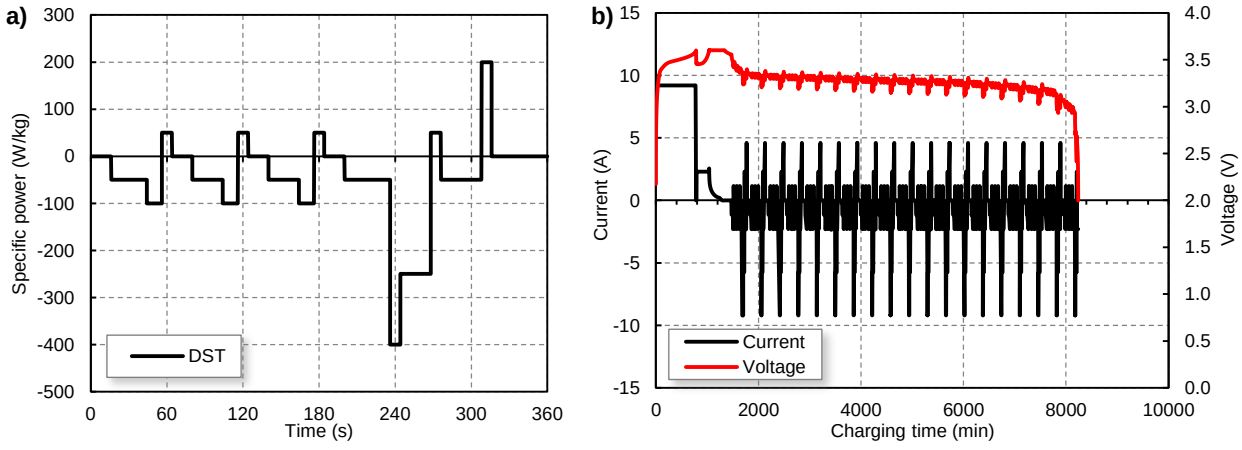

Fig. 5.5. a) Dynamic stress test (DST) protocol schedule and b) complete sequence of fast charge/DST cycle.

Reference performance tests

The RPT are used to characterize the degradation that occurs during the life of the subject test unit and to measure the cell's maximum achievable capacity, and the IR of the cells. From this testing sequence, the generation of the IC and PA curves is derived. The sequence includes at least two standard charges at 1C with CC discharges at 1C and C/3, and a final CC charge and discharge at C/25 with 2h

rest between cycles. From the reference tests, the IR is also calculated using the VCD method. Upon completion of the RPTs, internal cycling counter is set to zero (i.e. n = 0) and the end of cycling is evaluated. If end of cycling has not been reached, subsequent cycling is carried out, otherwise the procedure is finished.

Continuous cell tests matrix

Table 5-2 summarizes the continuous cycling procedures. All the tests are carried out at 23ºC.

Table 5-2. Test matrix for continuous cycling.

Cell number#	Continuous cycling Scheme	Charge	Discharge	RPT (cycling intervals)	Temperature (ºC)
1	Standard cycling	1C	1C	300	23
2	Fast charge cycling	4C-1C-CV	4C	300	23
3	Dynamic stress test cycling	4C-1C-CV	DST	300	23

5.2.2. Calendar aging

The calendar aging includes several calendar conditions, intended to maximize the understanding of the aging mechanisms that cells go under rest. For the calendar aging, a total of 8 cells were aged, including the Cells 1 to 3, previously used under the continuous cycling. It is important to point out that the objective of calendar aging is to decipher the aging evolution that the cells encounter only under rest conditions, and not to decipher the aging produced by the different testing conditions.

The framework of the calendar aging procedures is shown in **Fig. 5.6**. During the first stage, the cells went through the same commissioning and conditioning tests, to measure the effective capacity. Secondly, the cells either went to a calendar aging when they are fresh (i.e. Cell 1 and Cell 3), or directly to a continuous cycling procedure. As calendar aging while "fresh" is finished, cells are set to continuous cycling. The continuous cycling procedure structure is the same as presented in previous section, and consists of different continuous cycling schedules (described in the calendar aging test matrix), coupled with the RPTs. Once the cycling tests are finished, the cells can go to calendar aging (i.e. Cell 2 and Cell 4 to 8) or their aging study is finished (i.e. Cell 2 and 3). Upon completion of the rest time, a set of final RPTs are carried out. The final tests provide the data necessary to evaluate cell capacity and to generate the IC and PA curves to analyze aging evolution under rest.

Calendar aging cell tests matrix

Table 5-3 presents the calendar aging cell tests matrix. Each of the eight cells studied went through different cycling schemes for a number of cycles, prior to calendar aging at specific SOC conditions. For example, Cell 1 and Cell 3 underwent to the initial conditioning tests, and then were sent to rest for 12 and 13 months at 0 and 95% SOC respectively. The rest of the cells went through different cycling, and once they reached a determined number of cycles, were put to storage at a specific SOC. The calendar aging test matrix is designed to cover several storage conditions: some cells are more aged than others, different cycling number and the calendar storage conditions (i.e. rest time and SOC) differ for each cell. This situation may be more likely to be found in real-life applications, where cells are aged differently and then are sent to storage for different periods at several SOC conditions

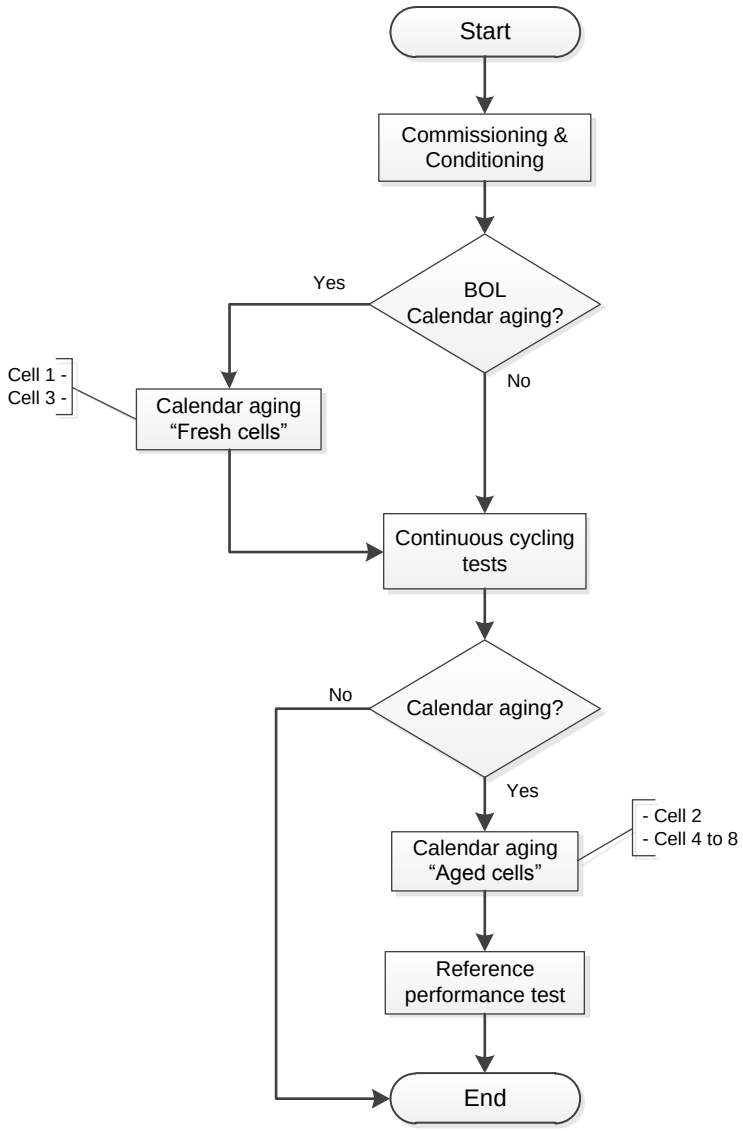

Fig. 5.6. Flow diagram of the calendar cycling procedure.

Table 5-3. Calendar aging cell test matrix.

Cell number#	Cycling scheme	Nº of cycles	Calendar storage duration (months)	SOC storage condition (%)	Storage temperature (ºC)
1	Conditioning	15	12	0	23
2	Fast charge cycling	5400	7	95	23
3	Conditioning	15	13	95	23
4	*	50	25	0	23
5	*	1000	36	0	23
6	*	900	34	50	23
7	*	700	31	20	23
8	*	2100	26	98	23

* Combination of various cycling schemes

5.3. Half-cell testing procedures

Half-cell testing procedures were carried out to be feed in the *'Alawa* computer toolbox. The objective is to provide an innovative approach where the *'Alawa* mechanistic model is constructed from the actual electrode materials of the tested cells. The procedure is to harvest half-cell data from another cell, which belongs to the same batch as the tested ones. The motivation behind this strategy is to obtain the highest resolution in the simulation procedures carried out with *'Alawa*. This is attained because the mechanistic model is constructed from real half-cell data. Hence, both the simulation process and the real-life experimental tests are carried out with the same basic electrode materials and properties. The meticulous processes needed to obtain half-cell data is described in this section.

All the experiments shown in this section were carried out at the Electrochemical Power Sources Laboratory (EPSL) at the Hawaii Natural Energy Institute, University of Hawaii, HI, USA. The disassembling procedure was previously designed by our research group at the University of Oviedo to carry out further investigations on post-mortem analyses. The results on this line of investigation are not shown here because is out of the scope of this thesis work.

5.3.1. Materials and preparation

The cell disassembling procedure was carried out on Cell 0, which was the same cell and same model as the tested ones. Cell 0 underwent to the commissioning and conditioning procedures to verify its resemblance with the tested cells. The cell was first fully discharged. The discharge procedure was CC at C/20 to 2 V, followed by a CV discharge set to 2 V until the current dropped to I<C/200. This ensures that the cell was fully discharged, and full delithiated state (C) on the NE was reached.

The cell was subsequently disassembled in an argon-filled glove box (<1 ppm H_2O, <10 ppm O_2). A rotatory tool equipped with a diamond coated (to avoid short-circuits) cutting disc was used to gently cut the central cylinder of the cell. Next, the electrode materials were properly harvested. Samples of both electrodes were stored in containers and saved in the glove box to avoid contamination. **Fig. 5.7**a-b shows an example of the cell disassembling procedures carried out inside the glove box.

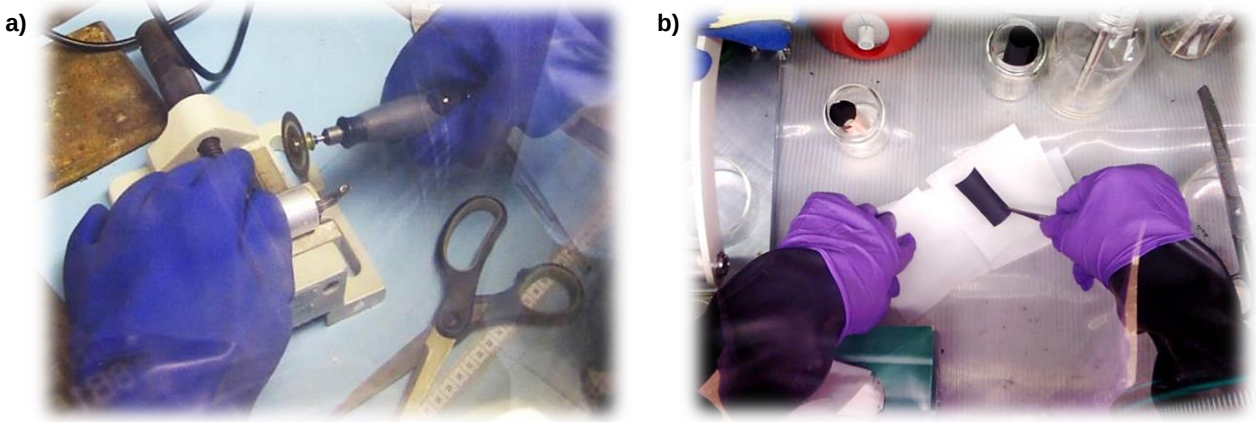

Fig. 5.7. Disassembling procedure inside the Argon-filled glove box. a) Shows the rotatory tool cutting the cell's shell, and b) shows a sample of the positive electrode material harvested from the commercial cell.

Once the disassembling process on Cell 0 was finished, the half-cell assembly process in a Swagelok cell began. To avoid any contamination, the Swagelok cell parts were previously cleaned in a chemical bath, and then vacuum-dried for 2 h at 110ºC in an oven. Thereafter, the Swagelok cell parts were placed inside the glove box.

The construction of the Swagelok cells and the choice of the selected materials were carried out according to the general procedures described in the literature [76], [79]. The Swagelok cell assembling procedure inside the glove box was carried out as it follows: the coating on one side of the electrode laminate was removed gently by rubbing it with a cotton tip soaked in 1-methyl-2-pyrolidinone (NMP). To avoid solvent seepage to the other side, i.e., the side on which the electrochemical measurements are made, the solvent was applied to the inner section of the back electrode, as described by Abraham *et al.* [79] and Safari *et al.* [174]. In addition, to decrease the risk of electrode contamination from the disassembling process [76], the electrodes (0.71 cm^2) were punched near the center of the jelly roll. Thereafter, in order to extract the lithium salt, the electrodes were rinsed in fresh dimethyl carbonate (DMC). Swagelok cells (1/2" PTFE-type) were then assembled with a lithium metal coated stainless steel pellet as counter electrode and two layers of Whattman GF/D borosilicate glass fiber sheet as separator. The electrolyte consisted of a 1 mol L-1/$LiPF_6$ in 1:1 (by weight) EC/DMC solution with 2%wt Vinylene Carbonate (VC) additive. Thereafter, the Swagelok cells underwent to a series of electrochemical tests. **Fig. 5.8** shows an example of the Swagelok cell assembling process in the glove box, where **Fig. 5.8**a shows the instant when the separator is to be inserted in the Swagelok cell, and **Fig. 5.8**b shows the electrolyte being added into the Swagelok cell.

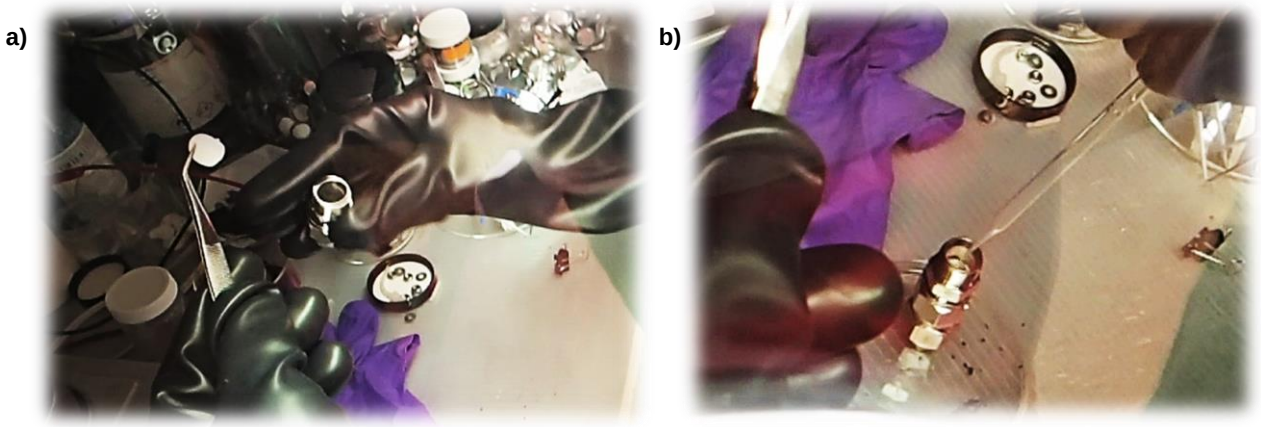

Fig. 5.8. Glove-box Swagelok assembling process. a) Shows the separator to be inserted in the Swagelok cell, and b) shows the electrolyte dropped into the Swagelok cell.

5.3.2. Electrochemical tests

As the Swagelok cells were built, a series of formation and reference tests were carried out, using CC: the LFP electrode was cycled from 1.8 V to 4 V, and the formation tests consisted on a single charge/discharge cycle at C/15, followed by 6 cycles at 1C, until capacity settles. The GIC electrode was cycled from 0.01 V to 1.8 V, and the formation tests consisted on two cycles at C/10. The reference test were the same for both electrodes, and consisted on a single charge/discharge cycle at C/30, C/25, C/10, C/5, C/2 and 1 C. Data collection was set to 2 mV to have sufficient details in the fast changing parts of the voltage (i.e. beginning and end of charge/discharge, formation of solid solutions). The electrochemical tests were carried out at ambient temperature (25ºC), in a temperature controlled laboratory. **Fig. 5.9** shows the image of a Swagelok cell under test.

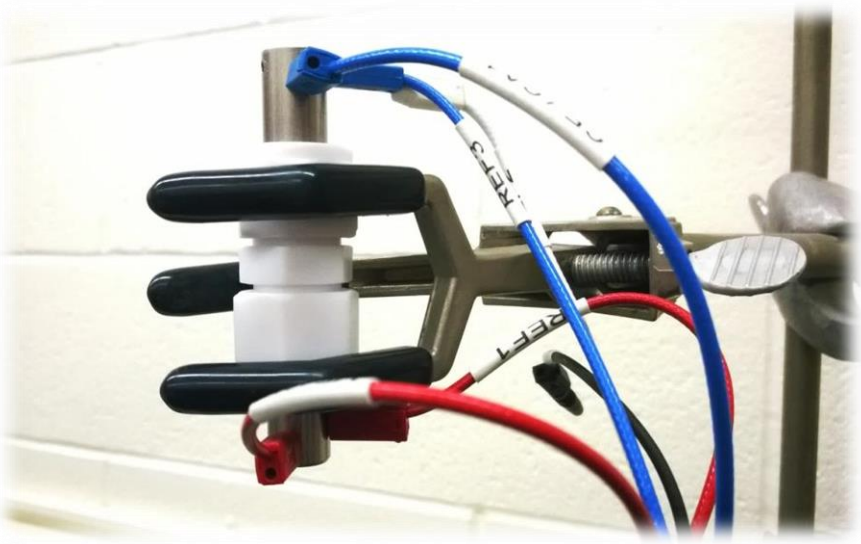

Fig. 5.9. Example of a Swagelok cell under test.

5.4. Test equipment

Here is presented the cell testing equipment used in this thesis work. The long-term cycling and the calendar aging tests were carried out at the Battery Research Laboratory at the Electrical Engineering Department, University of Oviedo, Spain. The testing equipment used was the Arbin BT-2000 battery testing machine and the Memmert 1CP-500 climate chamber. The electrochemical Swagelok cell tests was carried out at the EPSL at the Hawaii Natural Energy Institute, University of Hawaii, HI, USA. The testing equipment includes the VAC Nexus I glove box and the Bio-Logic (VMP3) potentiostat testing machine.

Battery testing machine: Arbin BT-2000

The tests for continuous cycling and calendar aging were carried out on a multichannel Arbin BT-2000 battery testing system (± 20 A), with four channels (see **Fig. 5.10**). The temperatures in the climate chamber and on the cells are measured with T-type copper-constantan thermocouples and logged into the Arbin system. The main technical characteristics of the machine are shown in **Table 5-4**.

Fig. 5.10. Arbin BT-2000 battery testing machine.

Table 5-4. Main technical characteristics of the Arbin BT-2000.

Characteristic	Arbin BT-2000
Number of channels	4
Current specification	High range -5 to 5 A Medium range -0.1 to 0.1 A Low range: - 0.01 to 0.01 A
Charge/discharge voltage range	-10 to 10 V
Input impedance	10GΩ
Sampling rate	<1 sec per scan
Rise time	<300 µs
Output accuracy	0.1% of FSR
Output resolution	0.05% of FSR
Voltage measurement accuracy	0.1% of FSR
Current measurement accuracy	0.1% of FSR
Measurement resolution	±0.006% FSR (14-bit transmission)
Signal ripple	<0.05% FSR

Climate chamber: Memmert 1CP-500

The long-term testing cycling and calendar experiments were carried out at a constant temperature of 23ºC±0.5ºC. The cells were located in a climate chamber from the manufacturer Memmert. The main technical characteristics are: power 500 W, volume 100 L and temperature range from 0ºC to 60ºC. **Fig. 5.11** shows the Arbin battery testing machine (upper left) and the Memmert climate chamber during testing.

Fig. 5.11. Arbin BT-2000 testing machine (upper left) and the Memmert 1CP-500 climate chamber.

Glove box: VAC – Nexus I

The cell disassembling process and Swagelok cell construction were carried out inside a glove box VAC – Nexus I (see **Fig. 5.12**). The argon-filled glove box purification capabilities are <1 ppm H_2O and <10 ppm O_2.

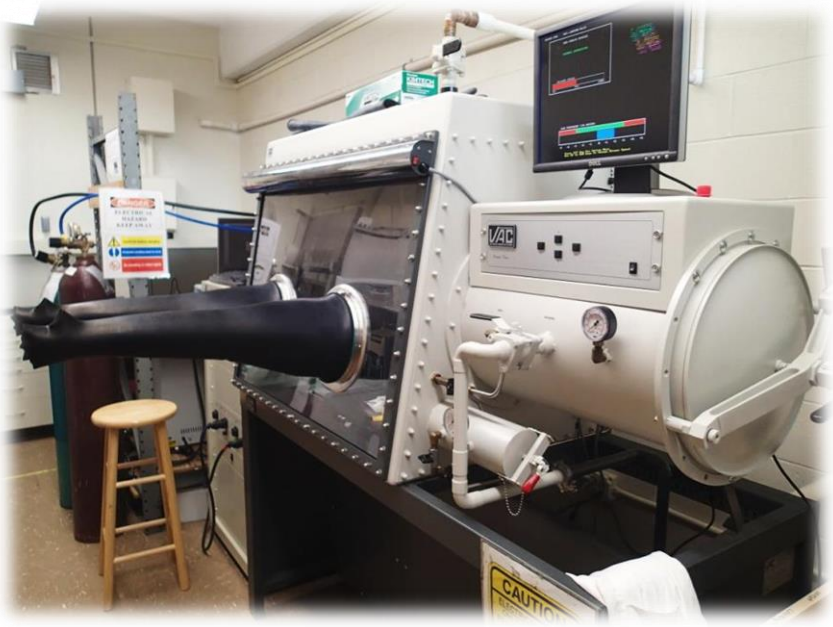

Fig. 5.12. Glove box VAC Nexus I.

Potentiostat testing machine: Bio-Logic (VMP3)

The electrochemical measurements on the Swagelok cells were carried out using a Bio-Logic (VMP3) potentiostat testing machine (see **Fig. 5.13**). The main technical characteristics of the machine are shown in **Table 5-5**.

Fig. 5.13. Potentionstat testing machine: Bio-Logic (VMP3).

Table 5-5. Main technical characteristics of the Bio-Logic (VMP3).

Characteristic	Bio-Logic (VMP3)
Number of channels	12
Current ranging	10 µA to 400 mA
Current resolution	760 pA
Low current	4 ranges 1 µA to 1 nA with resolution of 76 fA
Control voltage	20 V adjustable
Resolution	5 µV
EIS measurement	10 µHz to 1 MHz
Acquisition time	20 µs

5.5. Mechanistic simulation tests: the *'Alawa* toolbox

To attain a detailed aging analysis and to decipher the aging modes ongoing on the tested cells, computer simulations were performed using the proprietary *'Alawa* toolbox. The *'Alawa* is a unique Matlab© toolbox devoted to battery degradation diagnosis and prognosis, developed at the EPSL at the University of Hawaii. The mechanistic model behind the toolbox was described in detail by Dubarry *et al.* in [31]. The approach for this mechanistic model is based on half-cell modules that describe the electrode behavior. The cell performance is emulated from two separated half-cell modules (electrodes) constructed from laboratory experimental data. Hence, the system components are real data. This approach presents high-fidelity results that offer benefits for the study of LIBs. Further details of the model are discussed by Dubarry *et al.* [31].

This approach conceptually follows the one described by Christensen and Newman in the early 2000s [55], [175] and used by others such as Zhang *et al.* [176], [177]and Delacourt *et al.* [61], [172] to simulate cell degradation. Examples of instrumental achievements using the toolbox can be also found in [30], [99], [178], [179]. The toolbox is available for free for academic applications. To obtain the *'Alawa* toolbox, one can register through the toolbox webpage [180].

The *'Alawa* toolbox includes a user's manual with detailed information; for brevity, here we summarized the main characteristics. The *'Alawa* toolbox simulation window is shown in **Fig. 5.14**. The window is divided into three panels: the cell characteristics, the simulation options and the reporting options. In the cell characteristics, the individual positive and negative electrodes are selected for the simulation. The electrodes are previously loaded from the data obtained in the electrochemical tests. The cell constructive parameters (i.e. LR = NE/PE and SEI) are entered manually. The simulation options panel allows the user to choose the operating conditions to match the experimental tests, select the plausible degradation modes (both qualitatively and quantitatively), the simulation cycling number and the cycling intervals. The reporting options panel has several options (i.e. IC curves, capacity fade, etc.) to show the simulation results in different plots. It also has data export and import options.

In the example shown in **Fig. 5.14**, the PE is LFP, whereas the NE is GIC. The constructive parameters are set to LR = 0.9 and OFS = 12.5. As the cell is built, simulations began. The operating conditions are C/25 (-0.04) from 2 to 3.6 V. The degradation modes entered for the simulations are LLI = 0.01% per cycle, LAM_{deNE} = 0.005% per cycle and LAM_{liNE} = 0.002% per cycle. The simulations are carried out for 1,000 cycles and data is shown every 250 cycles. The results show the evolution with cycling of the PE, NE and full cell voltage signatures (upper panel) and the corresponding IC curves (lower panel). The results provide the final LR (0.88), OFS (24.4%) and capacity loss (15%). Other reporting options are

available. However, the PA analyses have to be carried out externally, by calculating the areas from the IC curves, as described in Chapter **4**.

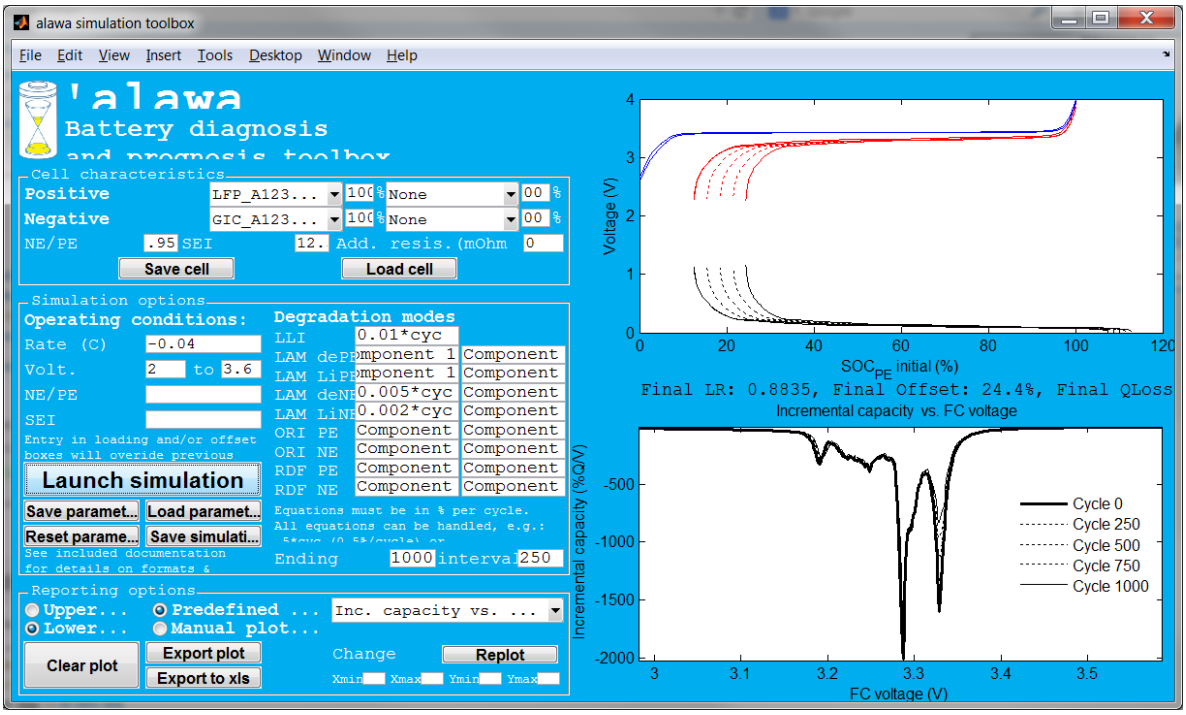

Fig. 5.14. Main *'Alawa* toolbox simulation window.

5.5.1. *'Alawa* approach description

The *'Alawa* simulation toolbox is based on a novel mechanistic model approach in which the degradation modes are the inputs to the simulations of the cell behavior in aging [31]. In other words, this is a "backward looking" approach where the "what if" aging modes of degradation are the inputs. The results from this particular "reverse engineering" approach unveil how the simulated cell with a particular cell constructive parameters and chemistry is aged under the proposed degradation modes. This strategy can handle complicated cell degradation paths and provides accurate results due to its flexibility by virtue of the mechanistic approach. Still, the accuracy of the results is directly related with the simulation inputs.

To achieve the greatest accuracy in the simulation process, a new approach was carried out to identify the aging modes: the computer simulations were performed using the Swagelok half-cell data harvested from Cell 0. Since the materials used in generating the half-cell data are the same as those used in the tested cells, the trends derived from the simulations precisely match the experimental full cell test results which provides maximum accuracy in degradation quantification.

The "what if" approach may lead to unresolved results or endless iterations if it is not applied correctly. The strategy to identify the aging modes consists in coupling the experimental cell results derived from the IC, PA and capacity fade analyses (as previously described in Chapter **4**) with the use of the *'Alawa* computer simulations. The aging modes from a qualitative and quantitative perspective are identified once the experimental and the computer results are equal. The approach applicability is shown in Chapter **7**, where the mechanistic diagnosis and prognosis analyses are carried out.

5.6. Summary

This chapter presents a particular set of experimental procedures and materials to achieve the main goals of this thesis work: the study of the aging mechanisms and performance of the selected high power lithium iron phosphate (LFP) batteries under diverse, realistic cycling schemes, by using *in situ*, non-destructive techniques. It must be pointed out that the methodology used in the design of testing procedures can be applied for the characterization of cell degradation and performance of other LIB technologies.

First, we present the selected cell technology, a high power nanophosphate cell manufactured from A123 Systems. We also address the importance of selecting the cells from the same production batch, to perform repeatable experiments and to avoid inaccuracies derived from cell-to-cell variations.

Next, the designed battery testing procedures are described. We propose three different continuous cycling tests (i.e. standard, fast charge and dynamic stress) to study the cells under various testing conditions. Standard cycling is used as a "reference" test. Fast charge cycling evaluates the long-term cycling capabilities of the cell under the designed fast charge protocol, and also includes fast discharges reaching the long term USABC power capability goal of 400 W/kg. Dynamic stress cycling consists of the designed fast charge protocol coupled with a realistic, electric driving scheme called Dynamic Stress Test (DST) discharge. The DST was developed by the USABC, and the testing is also set to the long term goal of 400 W/kg. With the designed tests, we aim to evaluate not only cell performance but also the capabilities of the *in situ*, non-destructive aging methodologies proposed. For this reason, the battery testing procedures include the sequence of reference tests required to carry out the incremental capacity (IC) and peak area (PA) analysis. These are key tests, as they provide the data required to study battery aging. Finally, we presented the calendar aging conditions.

An innovative approach to achieve accurate simulations of the aging mechanisms of the tested cells is used in this thesis. The strategy is based on feeding the *'Alawa* mechanistic model with real data, harvested from a cell from the same batch as the tested ones. Since both the mechanistic model and the tested cells have the same active materials, accurate simulations can be attained. However, the procedures to disassemble a commercial cell inside a glove box requires multiple, careful actions to be considered. Therefore, the details of these procedures and subsequent electrochemical testing are provided in Section **5.3**.

Accurate testing results and further analyses on the aging mechanisms are also directly related with the accuracy of the testing equipment used. Section **5.4** presents the testing equipment used in this thesis, including the main characteristics (e.g., accuracy, equipment range, resolution, etc.).

To finish this chapter, we present the *'Alawa* toolbox. This toolbox, based on a mechanistic approach, is extensively used in Chapter **7**, to analyze the aging modes ongoing on the tested cells from an innovative perspective, achieving high accuracy. Still, the use of this toolbox is not straightforward, and requires full understanding of both the experimental and the simulation results. Hence, a description of the approach to use the toolbox is provided in the last section.

6. Lithium iron phosphate battery performance and degradation: analysis of experimental results

This chapter investigates the performance and degradation of the cells tested under the proposed cycling schemes: standard, fast charge and dynamic stress tests. The investigations are carried out using *in-situ* cell degradation and performance analysis techniques, as presented in Chapter **4**. The aim is to provide a general, first evaluation and discussion of the effects that the proposed cycling schemes cause on the tested cells. Here we also aim to assess the convenience of using the proposed *in situ* techniques to decipher battery performance and degradation. This chapter also includes the results of calendar aging.

As presented in Chapter **2**, several aging modes can cause cell degradation. The main aging mechanisms are loss of lithium inventory (LLI), loss of active material (LAM), ohmic resistance increase (ORI) and Li deposition. Here we evaluate cell degradation by comparing the IC and PA signatures obtained from the experimental results, with the IC and PA signatures of the aging modes obtained from the mechanistic model (as presented in Chapter **4**). Using this approach, a first evaluation of the aging modes ongoing on the tested cells is obtained.

The results of the investigations of each cycling scheme are divided in two segments: The first provides the performance results. The aim is to decipher, for each proposed cycling scheme, the cell's end-of-life, and energy and power degradation. Standard procedures for performance identification are used in this first segment. The second segment estimates the aging modes. Here, incremental capacity (IC) and the peak area (PA) *in-situ* techniques are applied. The results of the evolution of the IC and PA signatures with cycling are provided here.

Once the battery performance and degradation results are shown, we carry out an analysis to draw conclusions on the significance of the obtained findings. First, we discuss the results from the IC and PA analyses, to estimate the aging mechanisms ongoing on the tested cells. Next, we carry out an analysis on the fast charging performance through long-term cycling, to evaluate its feasibility for safe, long-term and high power applications. Finally, to evaluate the cell's performance under the proposed cycling schemes, comparisons with the US Advanced Battery Consortium (USABC) long term goals are done. The comparisons help to validate the convenience of the selected cell technology for its use in electric vehicles (EVs).

6.1. Commissioning and conditioning tests

Prior to testing, all the cells underwent to commissioning and conditioning tests to determine the initial conditions. First, the cells were weighted, showing an average of 74.09 g with a deviation of 0.366 g (0.493%). From the conditioning tests, the discharged capacity at C/25 and 1C was obtained, as shown in **Fig. 6.1**a. The average capacity at C/25 was 2.300 Ah with a deviation smaller than 0.1 %. Therefore, the resulting C/25 capacity is adopted as the normalized cell capacity, i.e., $C_{norm.}$ = 2.300 Ah. The average capacity at 1C was 2.258 Ah with a deviation smaller than 0.5%. The initial internal resistance (IR) at 1C during charge and discharge is shown in **Fig. 6.1**b. The average IR during discharge measured at 50% SOC with the VCD method was 36.11 mΩ with a deviation smaller than 2%, while during charge was 32.52 mΩ with a deviation smaller than 3.5%.

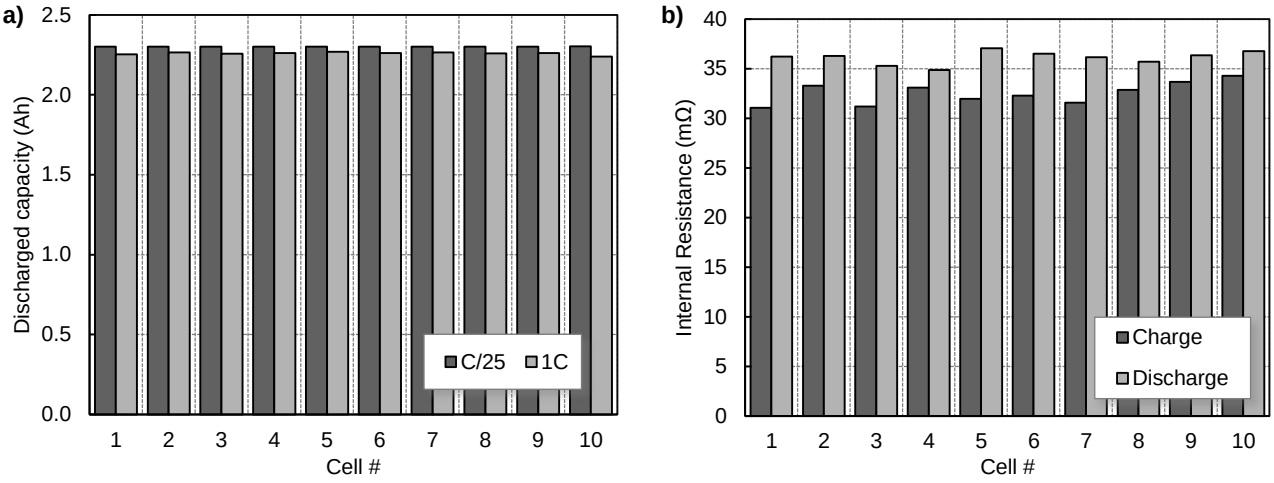

Fig. 6.1. Initial conditioning test results of the tested cells: a) discharged capacity at C/25 and 1C, b) internal resistance at 1C charge and discharge.

It is important to point out that the results obtained from the initial conditions showed minor cell-to-cell variations. The observed differences on this 10 cell-batch are lower or similar than those observed in other studies: Paul *et al.* [181] on a 20,000 batch LFP based cells measured a capacity deviation of 1.3% and IR deviation of 5.8%; Devie *et al.* [178] on a 60 batch LCO cells observed a capacity deviation of 1% and IR deviation of 2.5%; and, in a previous unpublished study carried out at the University of Hawaii on a 100 batch LFP based cells from the same manufacturer, a capacity deviation of 0.35% and IR deviation of 15% was measured. We are therefore confident that the batch used in this thesis work does not include any outliers and the results among cells are comparable.

During the conditioning tests, IC and PA curves were calculated to measure the capacity distribution per peak area. As shown, the tested cells showed minimal cell-to-cell variations, specifically at C/25. This was also directly translated when measuring the peak area for ∫❶ and ∫❷-❺. From the voltage sampling rate (5 mV), the construction of the IC curves and the subsequent calculations of the PA, measurements were 0.75 ±0.01 Ah and 1.54 ±0.01 Ah for ∫❶ and ∫❷-❺, respectively. The precision of the measurements is indeed very high and sufficient to carry out accurate analyses on the degradation modes. Since the capacity retention at C/25 was 2.300 Ah in the tested cells, peak ∫❶ corresponds to ~33%, while ∫❷-❺ ~67% of the full capacity, respectively. This peak area distribution is to be used in the PA analyses of each cell.

6.2. Standard cycling tests

This section provides the long-term cycling performance and degradation results from the standard cycling scheme. We use the techniques and analyses described in Chapter **4**, including capacity fade

evolution, IR measurements, or IC and PA techniques. The aim is to provide a general, first quantification on performance and degradation under standard cycling.

6.2.1. Standard cycling performance and degradation

Once the initial conditioning was finished, the cell tested under standard cycling was set to rest on discharge state (i.e. 0% SOC) for 12 months at 23ºC. After storage, the capacity retention only showed a minor change with an increase of capacity smaller than 0.1%, which are within the normal deviation. Therefore, the capacity retention at C/25 after storage remained constant at 2.300 Ah.

Capacity fade: standard cycling test

The discharged capacity fade under standard cycling tests, during RPTs (C/25) and continuous cycling is shown in **Fig. 6.2**. The discharged capacity is normalized to the adopted thermodynamic discharged capacity (i.e. 2.300 Ah). The capacity fade evolution followed a linear trend both for RPT and continuous cycling. The initial cycles during continuous cycling achieved 98.4% of the normalized discharged capacity. This capacity difference (~1.6 %) between thermodynamic and continuous cycling remains constant throughout cycling. This difference is because under thermodynamic conditions, the maximum attainable capacity of a cell is reached.

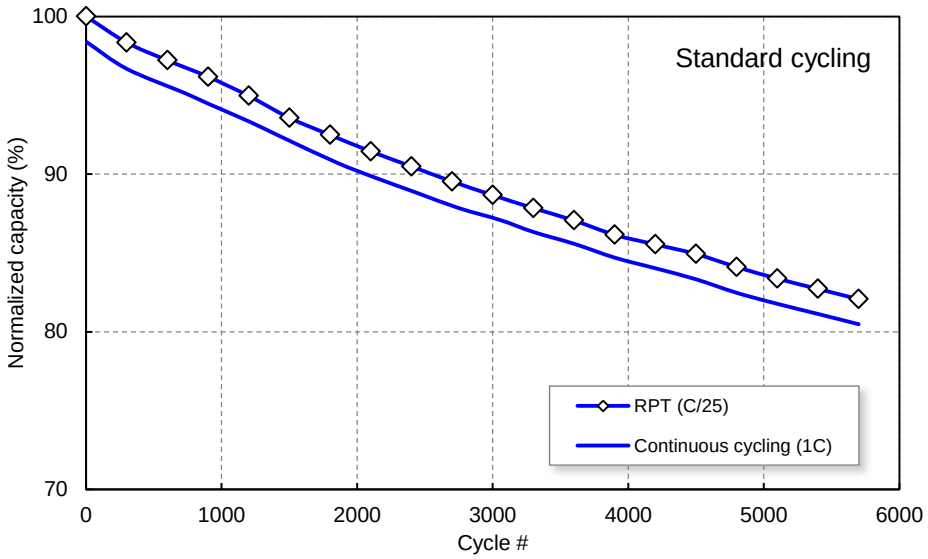

Fig. 6.2. Discharged capacity evolution under standard cycling, during RPTs (C/25) and continuous cycling (1C).

One of the most important figures of merit obtained from this representation is the end-of-life (EOL). The USABC defines the EOL of a cell as that point at which a specific test protocol cannot deliver more than 80% of its nominal capacity [16]. The long-term goal defined by the USABC for cycle life is set at 1000 cycles. Therefore, the cell tested under standard cycling surpasses the cycle life long-term goal, and will reach its EOL at approximately ~5900 cycles.

We also highlight that the degradation pace during continuous cycling was found to be equivalent to that shown in the manufacturer's datasheet [182], when tested at equivalent cycling conditions (1C, 25ºC). This fact reinforces that the tested batch does not include any outliers. Hence, the tendencies observed in the tested cells are indeed derived from the cycling scheme and not from cell-to-cell variation.

Energy and power performance: standard cycling test

The USABC defines the energy efficiency as the ratio of the net DC energy delivered by a cell during discharge to the total DC energy required to restore the initial SOC [16]. The long term goal of energy

efficiency is 80%. As observed in **Fig. 6.3**a, tested cell under standard cycling has an energy efficiency of 95.0% that remains invariant through cycling. Energy efficiency is related with cell temperature, as high cell temperatures lead to lower efficiencies. The cell temperature during standard cycling remained practically constant at 24ºC both for maximum or cell average (see **Fig. 6.3**b). The measured temperatures are only 1ºC above the thermal chamber temperature. Therefore, cycling under standard procedures does not cause significant cell temperature changes.

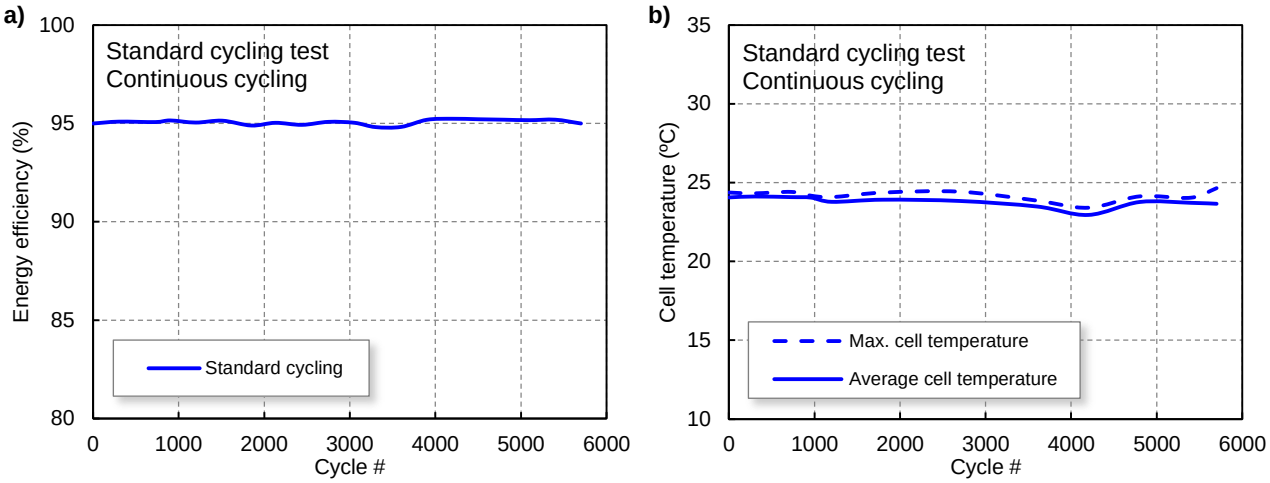

Fig. 6.3. Evolution under standard cycling of the a) energy efficiency and b) cell temperature.

Energy and power performance can be also evaluated from the accumulative energy throughput and the discharge time, as shown in **Fig. 6.4**a-b. The energy throughput (Wh) includes the effects of capacity (Ah) multiplied by the voltage (V). Hence, this representation relates not only the capacity loss, but also how much energy was delivered by the cell during cycling. This is important when large IR is observed: a battery may deliver similar capacity (i.e. without capacity loss) but at lower voltage (i.e. energy loss) due to IR increase. The results show that the cell cycled under standard cycling could deliver over 40 kWh before reaching EOL. **Fig. 6.4**b shows the total accumulated time the cell was under discharge. In total, standard cycling was discharging during 214 days. The total testing time, both including RPT and continuous cycling was ~25 months.

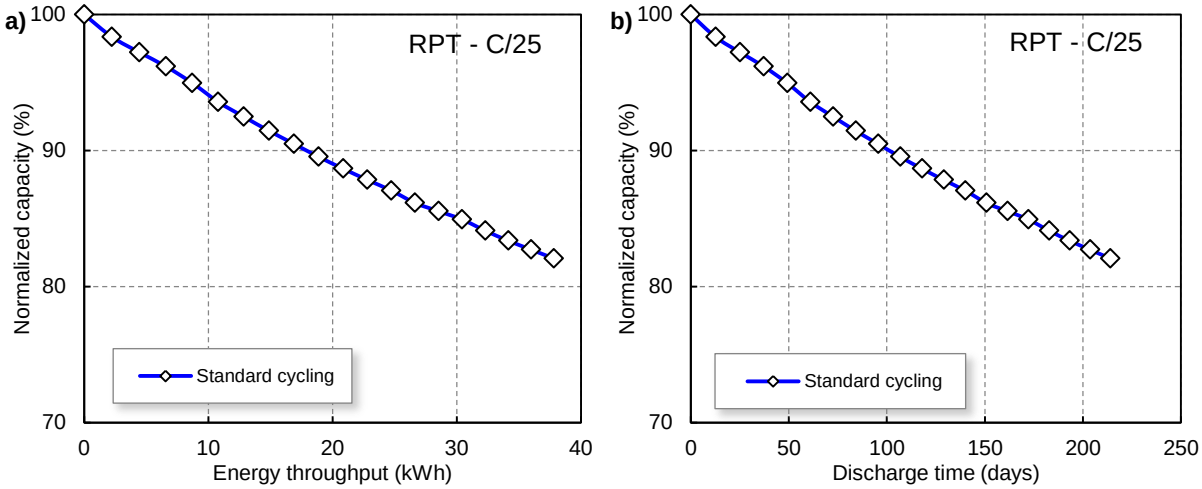

Fig. 6.4. Normalized capacity under standard cycling versus a) accumulative energy throughput and b) accumulative discharge time.

The Peukert curves (see **Fig. 6.5**a) depict the capacity retention pattern as a function of C rate, evaluated at different cycle number. As observed, only minor variations of capacity are measured from the thermodynamic (C/25) to the highest C-rate (6C). This is indeed a desired characteristic of quality HP cells. The Peukert coefficients (k) for the proposed cycling rates were calculated ($k_{Standard}$ = 1.004), showing great consistency with cycling. The Ragone plots **Fig. 6.5**b depict the power capability retention. The curves followed a downward trend: as specific power is increased (i.e. increase of discharge C-rate), the specific energy is reduced. Still, the reduction is small. The cell under standard cycling shows a specific energy reduction of ~15% throughout cycling, even under high specific power 560 W/kg (6C) conditions.

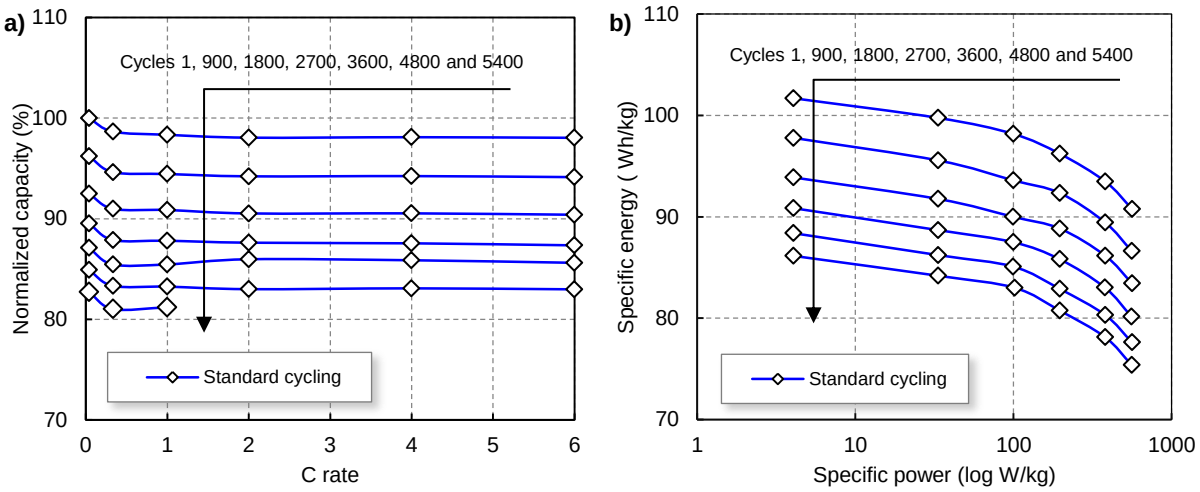

Fig. 6.5. Evolution of the a) Peukert and b) Ragone plots with cycle number under standard cycling.

The IR measurements during charge and discharge are shown in **Fig. 6.6**. The IR was calculated at 1C rate, 50% SOC using the VCD method, as presented in Chapter **4**. The results showed that IR did not increase with cycling, as the values at BOC and EOC remain close. The observed fluctuations (both during charge and discharged) are be derived from the IR measurement method. These fluctuations are within the average precisions of commonly used IR measurement techniques.

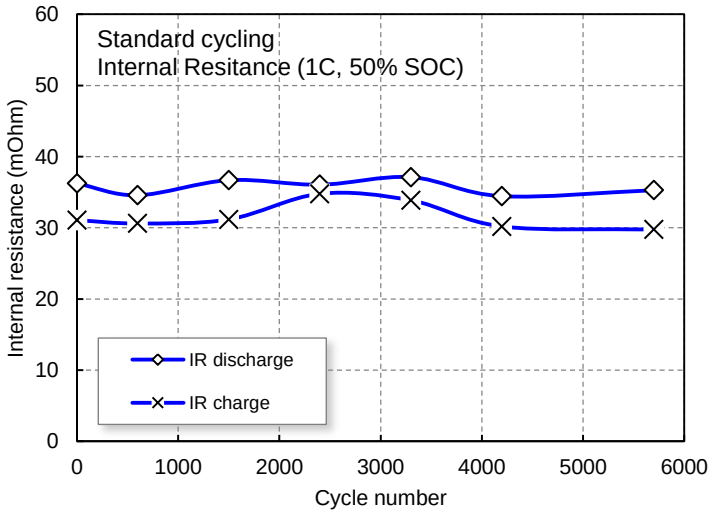

Fig. 6.6. Internal resistance evolution under standard cycling, at charge and discharge tests.

Fig. 6.7 shows the evolution with cycling of the cell voltage vs. the delivered capacity at 1C during the RPTs. This representation illustrates the cell's performance both from energy and IR perspective: the

areas underneath the curves represent the energy delivered by the cell, whereas the IR is represented by the vertical shift of the voltage evolution. As observed, the area underneath the curves (i.e. energy) is reduced due to capacity fade, and not due to IR increase. In fact, the shape of the discharge curve does not appreciably change as the cell ages; the position of the voltage plateau at ~3.3 V does not shift to lower voltages, which also confirms that the cell resistance did not increase.

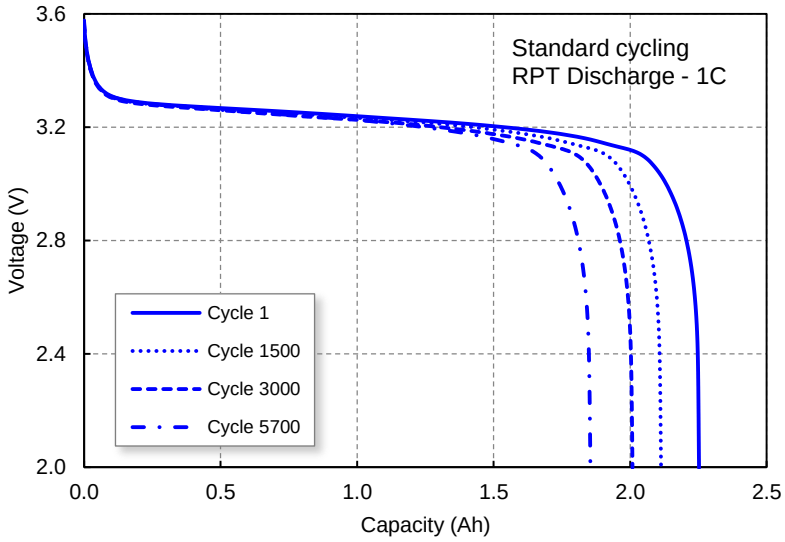

Fig. 6.7. Evolution under standard cycling of the voltage versus capacity, during RPT discharge at 1C.

To sum up, the cell tested under standard cycling was initially set to calendar aging for 12 months at 0% SOC, which did not cause any negative impact on capacity or IR. Thereafter, the standard cycling started, and the cell was tested for ~25 months, reaching ~5700 cycles and showing a capacity fade of 19.5%. Cell's EOL is to be reached at cycle ~5900. Both energy efficiency and cell temperature remained constant throughout cycling, at 95% and 24ºC, respectively. The power capabilities were not affected by capacity loss, as shown in the Ragone, Peukert and IR plots. Hence, the results showed that the cell ages primarily due to capacity loss, rather than IR increase.

6.2.2. Standard cycling degradation: incremental capacity and peak area results

This section shows the results of the IC and PA curves derived from the standard cycling test. A detailed description is carried out on thermodynamic (C/25) IC curves to attain the best resolution to identify cell degradation. To facilitate the understanding of aging from a kinetic perspective, the IC curves are calculated at C/3, 1C and 4C. Also, for an appropriate analysis, we separately distinct the area underneath the IC peak ❶ and the area associated under peaks ❷-❺.

Standard cycling: incremental capacity results

The evolution with cycling of the kinetic (i.e. C/3, 1C and 4C) IC curves derived from the cell tested under standard cycling are shown in **Fig. 6.8**a-b. From **Fig. 6.8**a, the kinetic consistency of the cell with cycling is shown: the IC peaks did not become broader, and the slope at which the first reaction (i.e. peak ❶) occurs did not change. This indicates that the kinetic effects remained invariant with cycling. The evolution of the cell's total sources of polarization resistance under kinetic conditions can be deciphered from **Fig. 6.8**b. The onset voltage at where the first reaction is taking place and the slope of the IC curves remain practically invariant with cycling, even for high 4C discharge rate. This indicates that the cell's polarization resistance was barely affected by aging under the proposed cycling scheme.

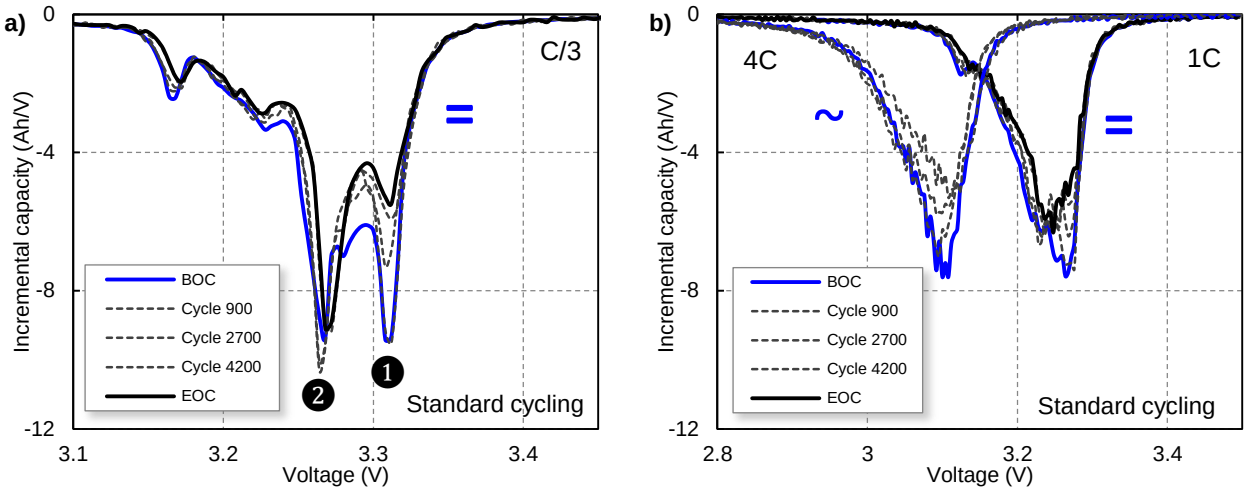

Fig. 6.8. Evolution under standard cycling of the IC curves at a) C/3 and b) 4C and 1C.

The evolution with cycling of the thermodynamic (C/25) IC signatures of the cell tested under standard cycling is shown in **Fig. 6.9**. The main feature observed in **Fig. 6.9** is the significant loss of intensity of peak ❶, as indicated by the arrow. The inflection point between peak ❶ and ❷ is also reduced, although with less intensity than peak ❶. When analyzing peaks ❷ to ❺, it was found that all peaks' intensities were reduced consistently, although in a much smaller proportion than the one found on peak ❶. Regarding peak ❺, the loss of intensity is also accompanied by a slight shift towards higher potentials. Similarly, peak ❷ exhibits minor width shrinkage, as indicated by its corresponding arrow.

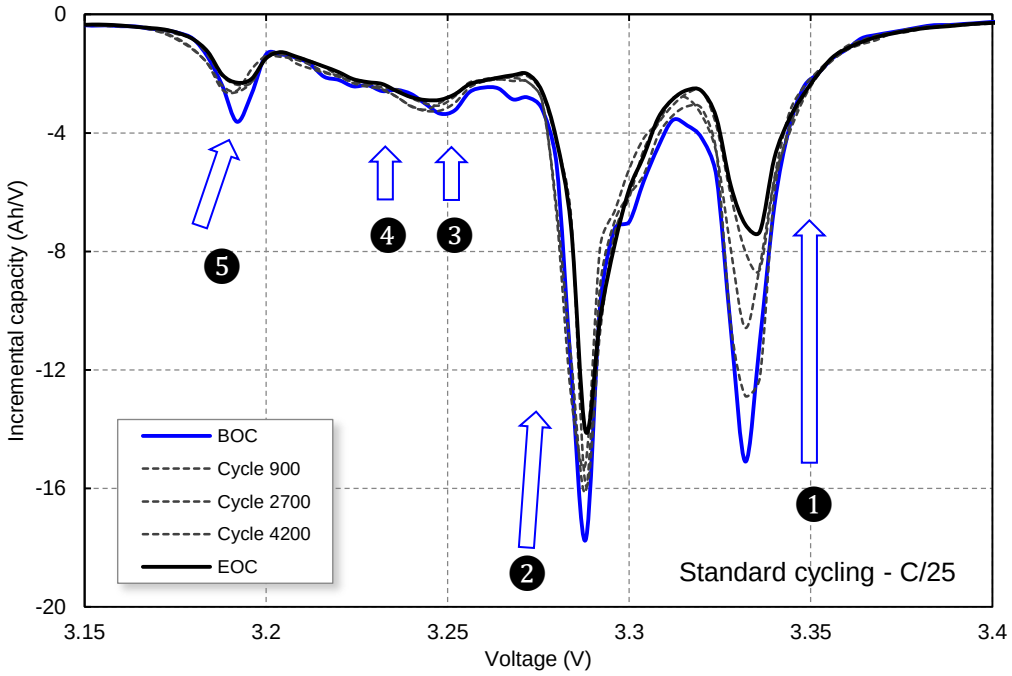

Fig. 6.9. Evolution under standard cycling of the IC curves at C/25.

Standard cycling: incremental capacity peak area results

Prior to calculating the PA evolution with cycling, we observed that the capacity degradation trend at C/25 under standard cycling can be divided into two linear stages, as shown in **Fig. 6.10**. Interestingly, from the linearized equations, the degradation rate during stage 1 is x1.6 larger than the one observed in stage 2. This effect was not caused by any external incident (e.g. temperature variations, calendar pause,

etc.). Therefore, this phenomenon is caused by internal cell factors originated by the proposed cycling conditions.

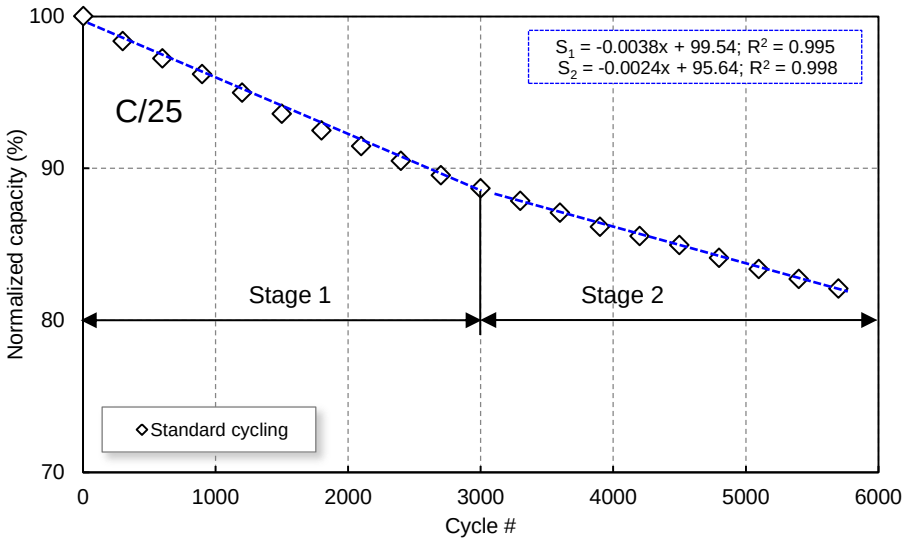

Fig. 6.10. Discharged capacity evolution trends for the standard cycling procedure.

The results of the IC peak area analysis of the cell tested under standard cycling are shown in **Fig. 6.11**. The normalized peak area evolution for both peak ∫❶ and peak ∫❷-❺ followed a linear reduction pattern, divided into two stages at cycle 3000 (see **Fig. 6.10**). The degradation rate for stage 1 is higher for peak ∫❶ than for peak ∫❷-❺ by a factor of x2.9. The subsequent cycling shows a reduction of the degradation trends, for both peaks ∫❶ and ∫❷-❺. The reduction of the degradation rate is more pronounced on ∫❶ (by a factor of x1.7) than for peak ∫❷-❺, which is x1.5. The cell showed a capacity fade of approximately 29% for peak ∫❶ and 13% for peak ∫❷-❺ at EOC.

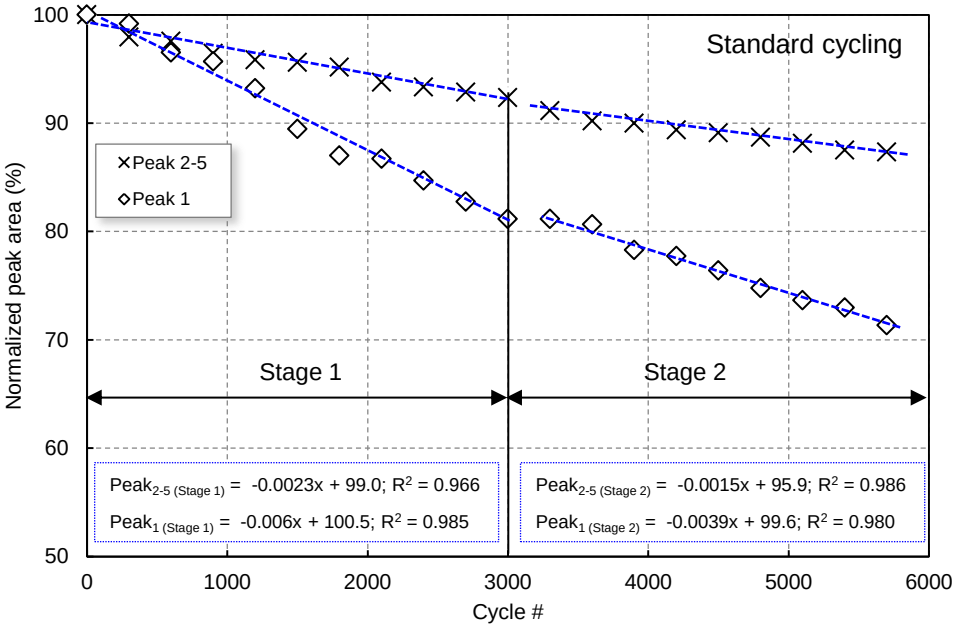

Fig. 6.11. Normalized peak area (peak ❶ and peak ❷-❺) at C/25, as function of cycle number for cell tested under standard cycling.

To sum up, standard cycling did not cause kinetic degradation on the tested cell, as observed on the kinetic IC curves. The thermodynamic IC curves primarily showed a reduction of peak ❶, accompanied by a reduction of peaks ❷-❺ in less degree. The PA results showed a two-linear stage reduction, where reduction of ∫❶ was larger than ∫❷-❺.

6.3. Fast charge cycling tests

This section provides the performance and degradation results from the fast charge cycling scheme. The fast charging scheme included a new multistage fast charging at 4C-1C-CV, followed by a high-rate discharge (4C) that reached long-term USABC specific power goal (400 W/kg). Here we use the analysis techniques including capacity fade evolution, IR measurements, or IC and PA techniques, to provide a general, first quantification on performance and degradation under fast charge cycling.

6.3.1. Fast charge cycling performance and degradation

Once the initial conditioning was finished, the cell tested under fast charge cycling was directly set to cycling. The normalized capacity (C/25) was 2.300 Ah.

Capacity fade: fast charge cycling test

The discharged capacity fade under fast charge cycling, during RPTs (C/25) and continuous cycling is shown in **Fig. 6.12**. The capacity fade followed a linear trend both for RPT and continuous cycling. The initial cycles during continuous cycling achieved 97.9% of the normalized discharged capacity. This capacity difference (~2.1%) between thermodynamic and continuous cycling remains constant throughout cycling. The cell's EOL under the proposed cycling scheme was reached at cycle ~4500.

The sudden decrease observed at cycle 4500 during the fast charge cycling was caused by a 65-day calendar pause, with Cell 2 left at 95% SOC. When cycling was resumed, 2% of capacity loss was observed under continuous cycling. However, capacity was partially recovered during the next ~200 cycles, to return to a similar capacity fade trend as before the calendar pause.

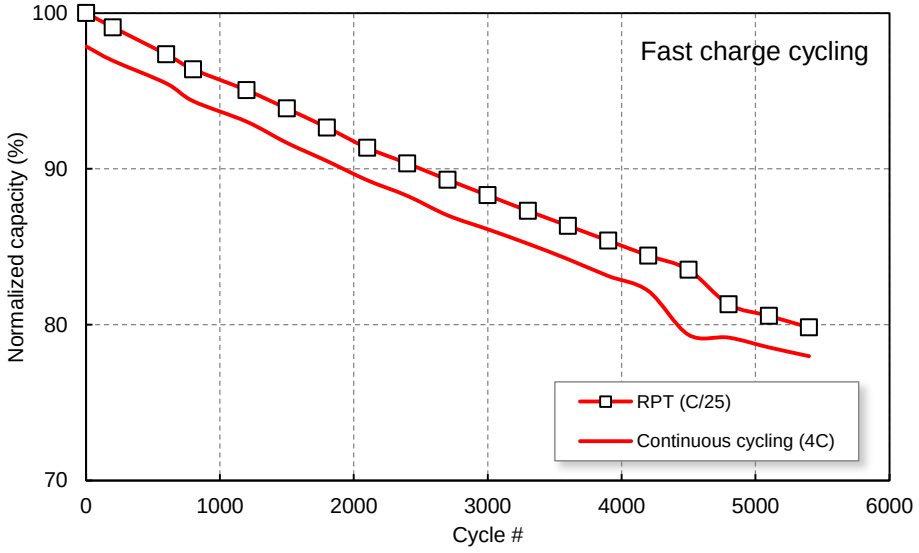

Fig. 6.12. Discharged capacity evolution under fast charge cycling, during RPTs (C/25) and continuous cycling (4C discharge).

Energy and power performance: fast charge cycling tests

As observed in **Fig. 6.13**a, tested cell under fast charge cycling has an energy efficiency of ~88% that remained invariant through cycling. The cell temperature evolution with cycling is shown in **Fig. 6.13**b.

The average cell temperature is ~27.2ºC, while the maximum cell temperature (reached at the end of the discharge at 4C) was ~28.2ºC. The average temperature is about ~4ºC above the thermal chamber temperature. These temperatures remain nearly invariant throughout cycling.

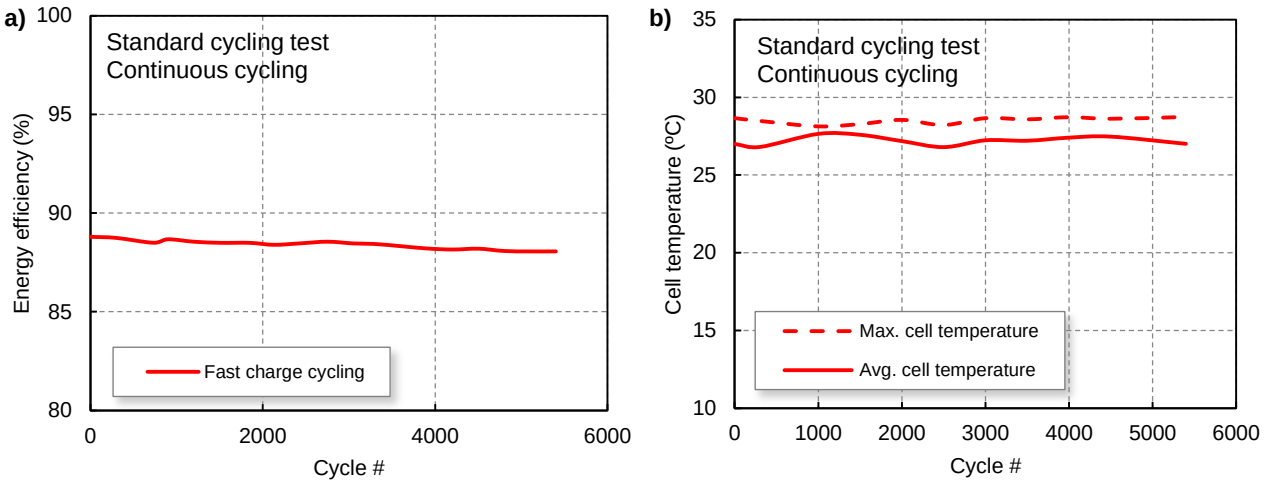

Fig. 6.13. Evolution under fast charge cycling of the a) energy efficiency and b) cell temperature.

The accumulative energy throughput and the discharge time for fast charge cycling are shown in **Fig. 6.14**a-b. The results show that the cell could deliver about 33 kWh before reaching EOL, quite a remarkable figure. The total discharging time for fast charge cycling was ~70 days, as observed in **Fig. 6.14**b. The total testing time, including RPTs, the 65-day calendar pause and continuous cycling was ~12 months.

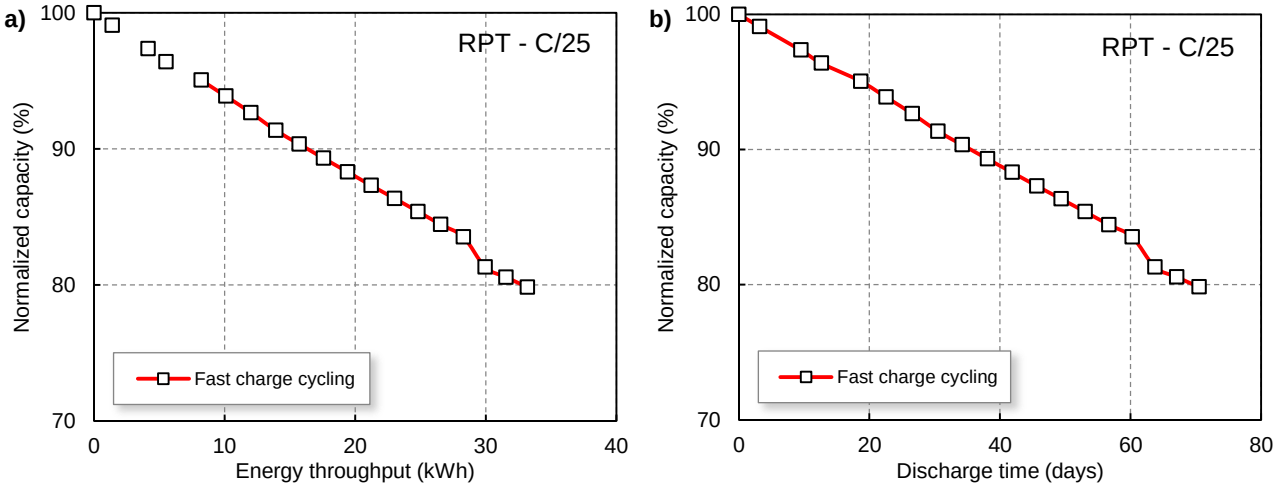

Fig. 6.14. Normalized capacity under fast charge cycling versus a) accumulative energy throughput and b) accumulative discharge time.

As observed in the Peukert curves (see **Fig. 6.15**a), only minor variations of capacity are measured from the thermodynamic (C/25) to the highest C-rate (4C). The Peukert coefficients (k) for the proposed cycling rates were calculated (k_{Fast} = 1.005), showing great consistency with cycling. The Ragone curves (see **Fig. 6.15**b) followed a downward trend: as specific power is increased (i.e. increase of discharge C-rate), the specific energy is reduced. Still, the reduction is small. The cell under fast charge cycling cell shows a specific energy reduction of ~20% throughout cycling, even under high specific power 400 W/kg (4C) conditions.

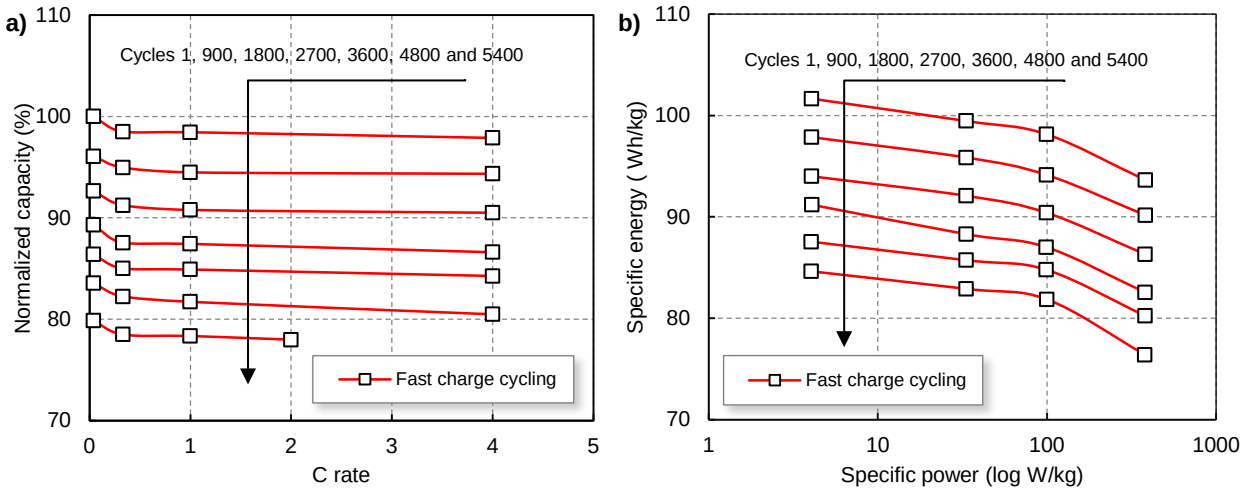

Fig. 6.15. Evolution of the a) Peukert and b) Ragone plots with cycle number under fast charge cycling.

The IR measurements during charge and discharge are shown in **Fig. 6.16**a. The results showed that IR did not increase with cycling, as the values at BOC and EOC remain close. The IR values, measured at 1C, 50% SOC averaged ~34 mΩ throughout cycling.

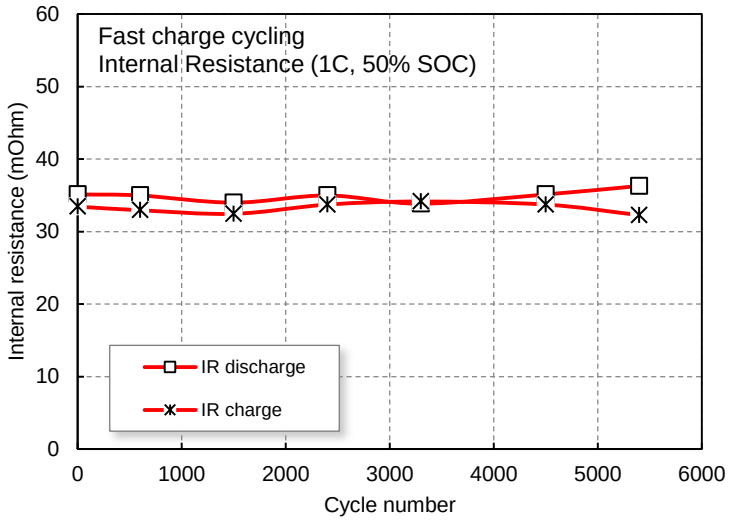

Fig. 6.16. Internal resistance evolution under fast charge cycling, at charge and discharge tests.

Fig. 6.17 shows the evolution with cycling of the cell voltage vs. the delivered capacity at 1C during the RPTs. As observed, the area underneath the curves (i.e. energy) is reduced due to capacity fade, and not due to IR increase. In fact, the shape of the discharge curve does not appreciably change as the cell ages; the position of the voltage plateau at ~3.3 V does not shift to lower voltages as the cell ages, which also confirms that the cell resistance did not increase. We must remark that the results obtained here are equal to those found on the standard cycling scheme.

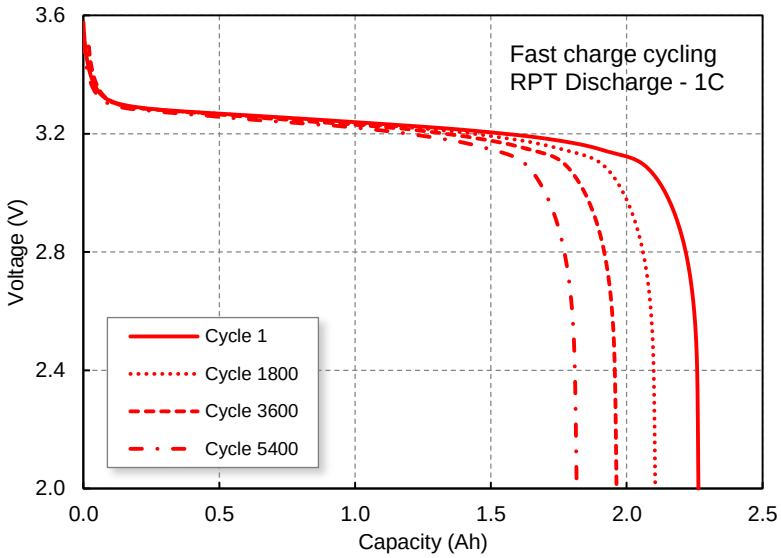

Fig. 6.17. Evolution under fast charge cycling of the voltage versus capacity, during RPT discharge at 1C.

To sum up, the cell tested under fast charge reached EOL at cycle ~4500. Both energy efficiency and cell temperature remained constant throughout cycling, at 88%, and 27.2ºC on average, respectively. The power capabilities were not affected by capacity loss, as shown in the Ragone, Peukert and IR plots. The results showed that the cell ages primarily due to capacity loss, rather than IR increase. We must point out that the performance and degradation results obtained under fast charge cycling are very similar as the ones previously shown for standard cycling.

6.3.2. Fast charge cycling degradation: incremental capacity and peak area results

This section shows the results of the IC and PA curves derived from the fast charge cycling test. A detailed description is carried out on thermodynamic (C/25) IC curves to attain the best resolution to identify cell degradation. To facilitate the understanding of aging both from a thermodynamic and kinetic perspective, the IC curves are calculated at C/3, 1C and 4C.

Fast charge cycling: incremental capacity results

The evolution with cycling of the kinetic (i.e. C/3, 1C and 4C) IC curves derived from the cell tested under fast charge cycling are shown in **Fig. 6.18**a-b. The kinetic consistency of the cell with cycling remains unaltered (see **Fig. 6.18**a), as the IC peaks did not become broader, and the slope at which the first reaction occurs practically did not change with cycling: only a small reduction in the slope is observed at EOC, which is considered negligible for this analysis. In terms of the evolution of the polarization effects, from **Fig. 6.18**b is observed an invariant of the onset voltage under 1C, and a small shift towards lower potentials at 4C. The voltage shift of the slope at 4C between BOC and EOC is ~20 mV. From a high discharge current of 4C (9.2 A), the resulting resistance variation was calculated to be 2.1 mΩ. This value corresponds to a small variation of ~5% of the initial IR. This indicates that the cell's polarization resistance is affected in a small proportion only under high discharge rates.

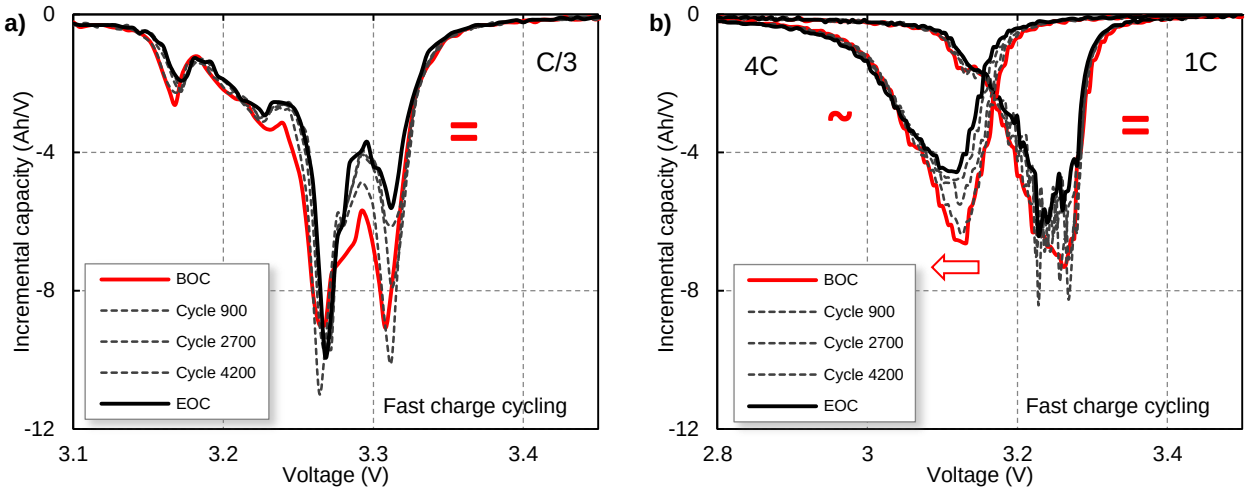

Fig. 6.18. Evolution under fast charge cycling of the IC curves at a) C/3 and b) 4C and 1C.

The evolution with cycling of the thermodynamic (C/25) IC signatures of the cell tested under fast charge cycling is shown in **Fig. 6.19.** The main feature observed in **Fig. 6.19** is the significant loss of intensity of peak ❶, as indicated by the arrow. The inflection point between peak ❶ and ❷ is also reduced, although with less intensity than peak ❶. When analyzing peaks ❷ to ❺, it was found that all peaks' intensities were reduced consistently, in a much smaller proportion than the one found on peak ❶. Regarding peak ❺, the loss of intensity is also accompanied by a slight shift towards higher potentials. Similarly, peak ❷ exhibits a slight shrinkage, as indicated by its corresponding arrow.

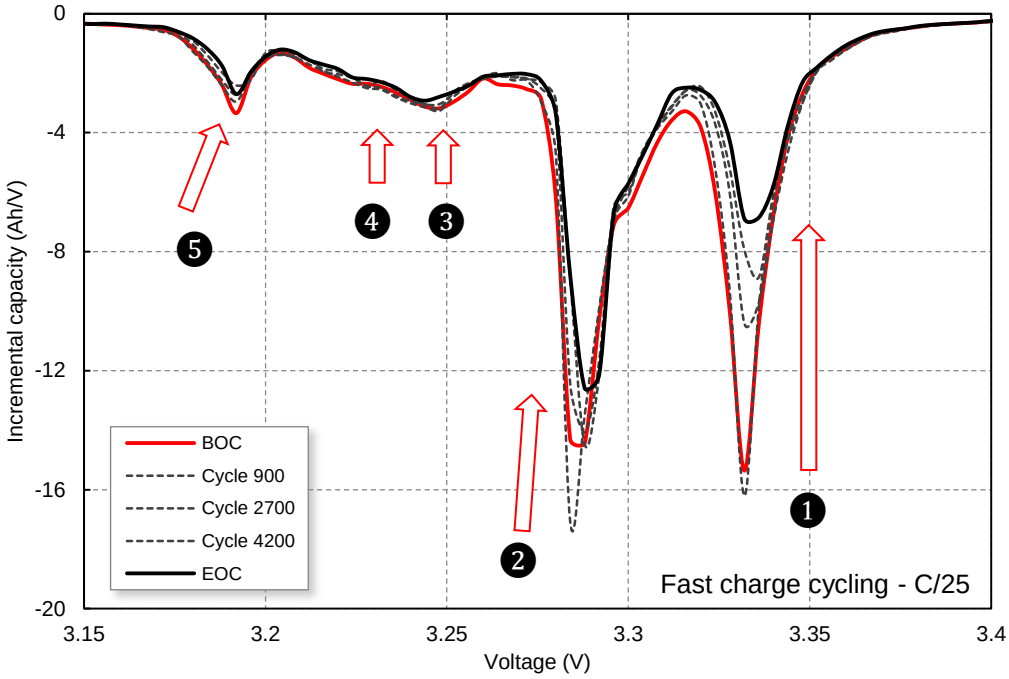

Fig. 6.19. Evolution under fast charge cycling of the IC curves at C/25.

An example of further reasoning required to analyze the IC curves and resolve imprecisions is provided here. In **Fig. 6.19**, the height of peak ❷ at BOC appears to be smaller than at cycle 900. This seems self-contradictory; as described in Chapter 4, no aging mechanisms increase the height of peak ❷, and simultaneously reduce peaks ❸ to ❺. Similarly, subsequent cycling shows the fact that peak ❷ has to be reduced. This minor glitch was probably derived from the testing equipment sampling the voltage data. It is observed that peak ❷ is unusually wider at its top, where it ought to be thinner. This type of

reasoning shall be used when the IC curves show unusual signatures to decipher possible errors. It is important to point out that this inaccuracy does not affect the IC peak area analysis. Hence, the analyses must be derived from the tendency of several curves with cycling, to eliminate possible outliers that may lead to incorrect conclusions.

Fast charge cycling: incremental capacity peak area results

The linearity of the capacity fade patterns may be subdivided into two stages, on account of the 65-day calendar pause. The capacity degradation trend at C/25 under fast charge cycling followed a linear trend that remained constant until cycle 4500 (see **Fig. 6.20**). As commented, the capacity degradation at cycle 4500 was caused by a 65-day calendar pause. The subsequent measurements at C/25 show that the capacity fade is not fully recoverable. Still, the second stage shows a slightly less abrupt linear degradation pattern than stage 1 (see equations, inset **Fig. 6.20**).

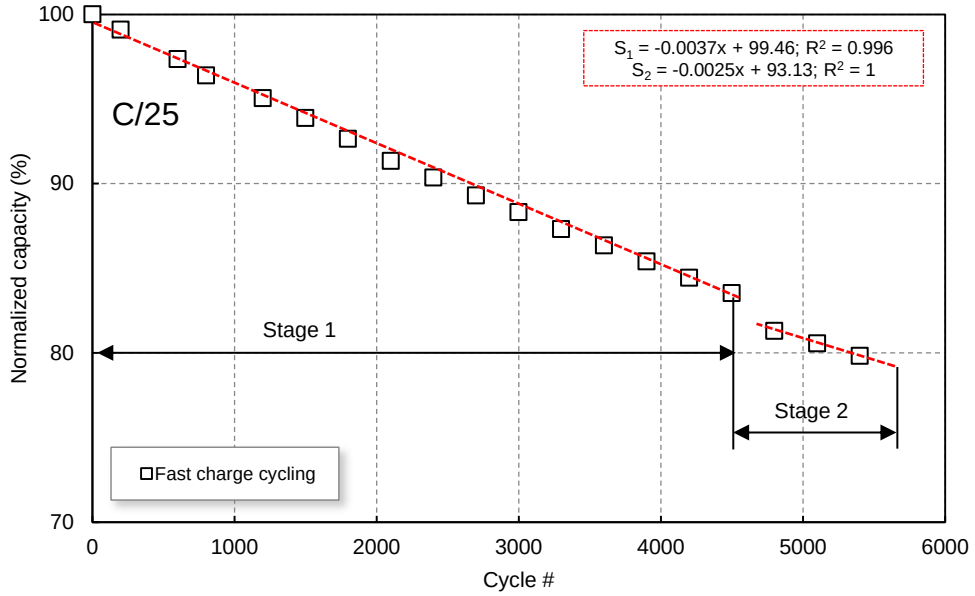

Fig. 6.20. Discharged capacity evolution trends for the fast charge cycling procedure.

The results of the IC peak area analysis for the cell tested under fast charge cycling are shown in **Fig. 6.21**. The normalized peak area evolution for both peak ∫❶ and peak ∫❷-❺ followed a linear capacity fade trend, until cycle 4500, where a second stage appeared. The degradation rate for stage 1 is higher for peak ∫❶ than for peak ∫❷-❺, by a factor of x2.6, until stage 2 appeared. During stage 2 only peak ∫❶ is affected, slightly reducing its degradation rate. In contrast, peak ∫❷-❺ remains invariant throughout cycling. The cell showed a capacity fade of approximately 33% for peak ∫❶ and 13% for peak ∫❷-❺ at EOC.

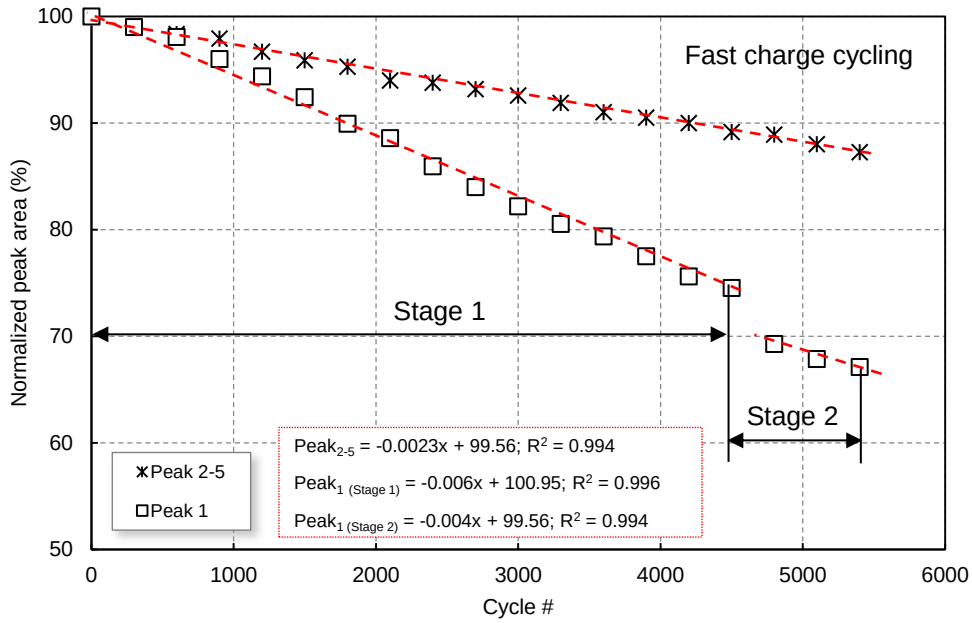

Fig. 6.21. Normalized peak area (peak ❶ and peak ❷-❺) at C/25, as function of cycle number for cell tested under fast charge cycling.

To sum up, fast charge cycling did not cause kinetic degradation on the tested cell, as observed on the kinetic IC curves. The thermodynamic IC curves primarily showed a reduction of peak ❶, accompanied by a reduction of peaks ❷-❺ in less degree. The PA results showed a two-linear stage reduction, where reduction of ∫❶ was larger than ∫❷-❺.

It may have been noticed that the description carried out in the IC paragraph is the same as the one indicated on standard cycling. In fact, when comparing the IC (C/25) figures (see **Fig. 6.9** standard cycling, **Fig. 6.19** fast charge cycling), both tendencies and quantitative values are very similar. In other words, from the IC curves, the qualitative analysis suggests that the standard and fast charge cycling affect the aging of the cells in a similar manner, even if the charging schemes are very different.

In addition, it is important to point out the great similarity of the peak area results showed on the standard and fast charge cycling schemes, particularly before entering degradation stage 2. When comparing both figures (see **Fig. 6.11** standard cycling, **Fig. 6.21** fast charge cycling) up to cycle 3000, peak ∫❶ of standard cycling showed a capacity fade of 18%, whereas fast charge cycling showed 17%. The differences are even smaller when calculated for peak ∫❷-❺. In other words, from the PA results, the quantitative analysis suggests also that the standard and fast charge cycling affect the aging of the cells in a similar manner (particularly in the first degradation stages), even if the charging schemes are very different.

6.4. Dynamic stress cycling tests

This section provides the performance and degradation results from the dynamic stress cycling scheme. The stress testing scheme included fast charging (4C-1C-CV), followed by a dynamic stress test (DST) discharge scaled to the long-term USABC specific power goal (400 W/kg). Here we use the analysis techniques including capacity fade evolution, IR measurements, or IC and PA techniques, to provide a general, first quantification on performance and degradation under dynamic stress cycling.

6.4.1. Dynamic stress cycling performance and degradation

As the initial conditioning was finished, the cell tested under dynamic stress cycling was set to rest on charged state (i.e. 95% SOC) for 13 months at 23ºC. After storage, the capacity was reduced from 2.300 Ah to 2.240 Ah (~2.6%).

Capacity fade: dynamic stress cycling

The discharged capacity fade under dynamic stress cycling during RPTs (C/25) and continuous cycling discharges (DST) is shown in **Fig. 6.22**. The discharged capacity is normalized to the adopted initial thermodynamic discharged capacity (i.e. 2.300 Ah). Due to the calendar aging, the initial cycling started at 97.4% for the C/25. The capacity fade evolution followed a non-linear linear trend both for RPT and continuous cycling. Under dynamic stress cycling, the differences from thermodynamic and DST continuous cycling are larger than those previously observed in standard and fast charge cycling. Also, the normalized capacity under thermodynamics and DST did not remain constant with cycling: in the early cycling stages, the differences are within ~4%. However, at EOC, the capacity difference was ~12%. The cell's EOL of was reached at cycle ~1100.

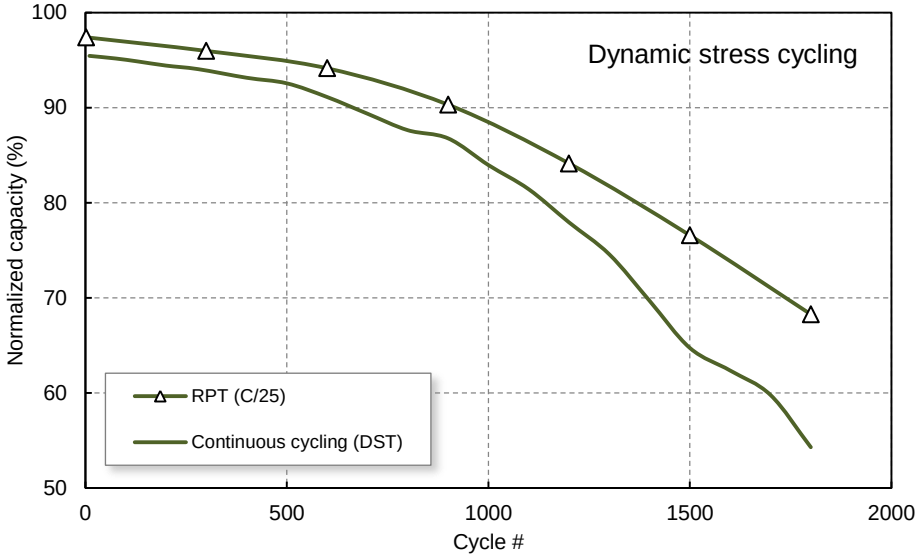

Fig. 6.22. Discharged capacity evolution under dynamic stress cycling, during RPTs (C/25) and continuous cycling (DST discharge).

Energy and power performance: dynamic stress cycling tests

The energy efficiency of the cell tested under dynamic stress cycling is shown in **Fig. 6.23**a. During the first 600 cycles, the efficiency remains rather constant at 92.4%. The subsequent cycles (600-900) experiment a decrease (-1%), then partially recovered to finally follow a constant decrease to reach 90.7% (-1.78%). The cell temperature evolution with cycling is shown in **Fig. 6.23**b. The average cell temperature is ~24ºC and remains rather constant throughout cycling. The maximum cell temperature (reached at the end of the 4C charging stage) was ~28.2ºC, although it decreases with cycling to ~26ºC. The reason for this temperature decay is the reduction of the charging time at 4C as the cell ages.

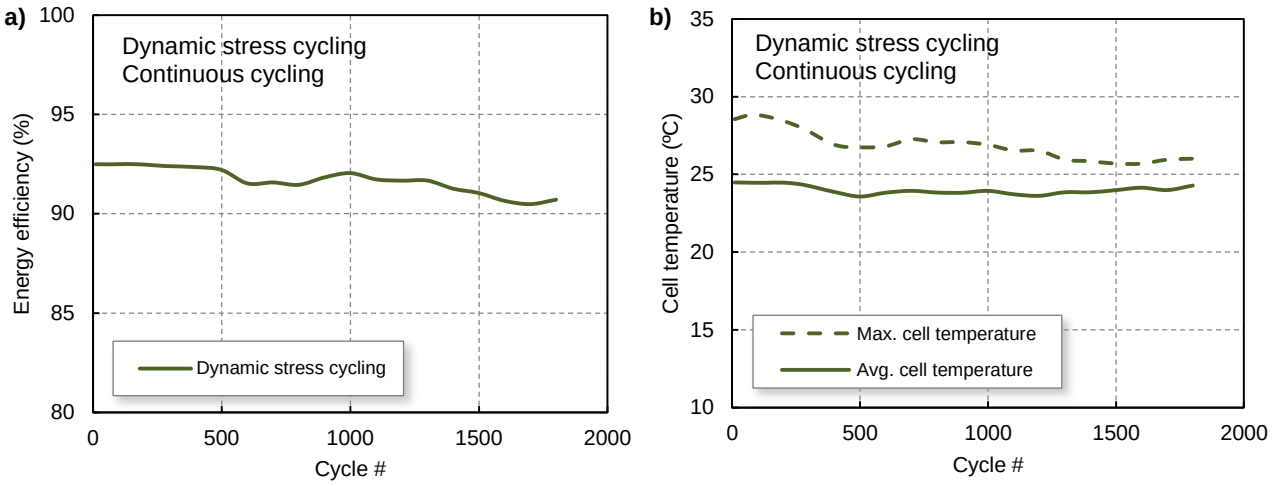

Fig. 6.23. Evolution under dynamic stress cycling of the a) energy efficiency and b) cell temperature.

The accumulative energy throughput and the discharge time for dynamic stress cycling are shown in **Fig. 6.24**a-b. The results show that the cell could deliver about 11 kWh before reaching EOL (see **Fig. 6.24**a). The total discharging time for fast charge cycling was ~70 days, as observed in **Fig. 6.24**b. The total testing time, including RPTs, and continuous cycling was ~8 months.

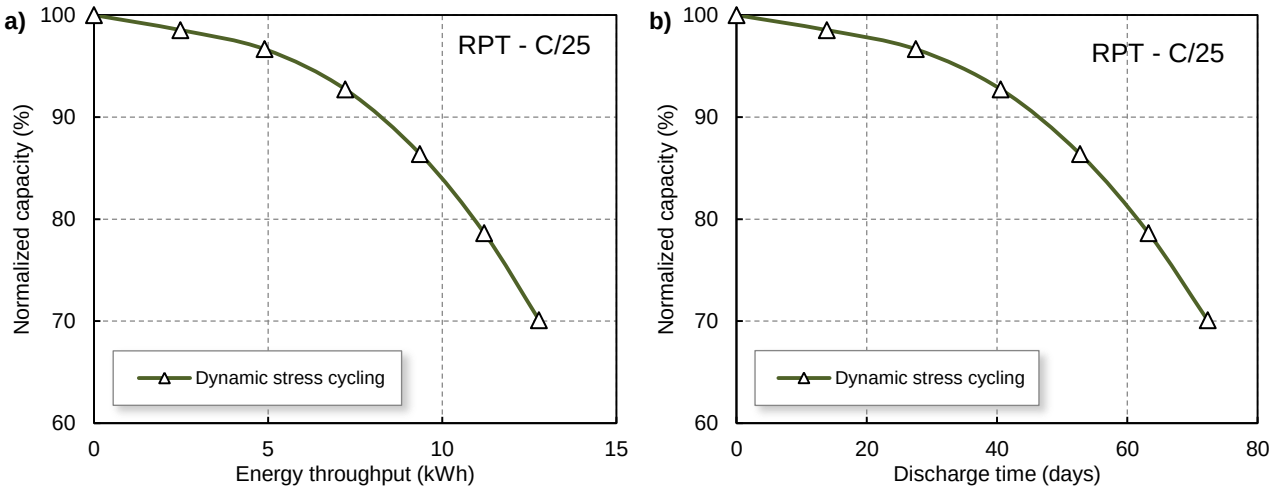

Fig. 6.24. Normalized capacity under dynamic stress cycling versus a) accumulative energy throughput and b) accumulative discharge time.

The Peukert curves (see **Fig. 6.25**a) depict the capacity retention pattern. As observed, small variations of capacity are measured from the thermodynamic (C/25) to the highest C-rate (1C). The Peukert coefficients (k) for the proposed cycling rates were calculated ($k_{Dynamic}$ = 1.009), showing great consistency with cycling. The Ragone plots (see **Fig. 6.25**b) depict the power capability retention. The curves followed a small downward trend. Since cell under dynamic stress cycling was limited to 1C discharges on the RPTs, power capability retention was not quantified in sufficient detail with the Ragone plot. However, with additional measurements of IR and with the IC analysis, kinetic (and therefore power) degradation can be evaluated. These findings are unveiled in the next subsection.

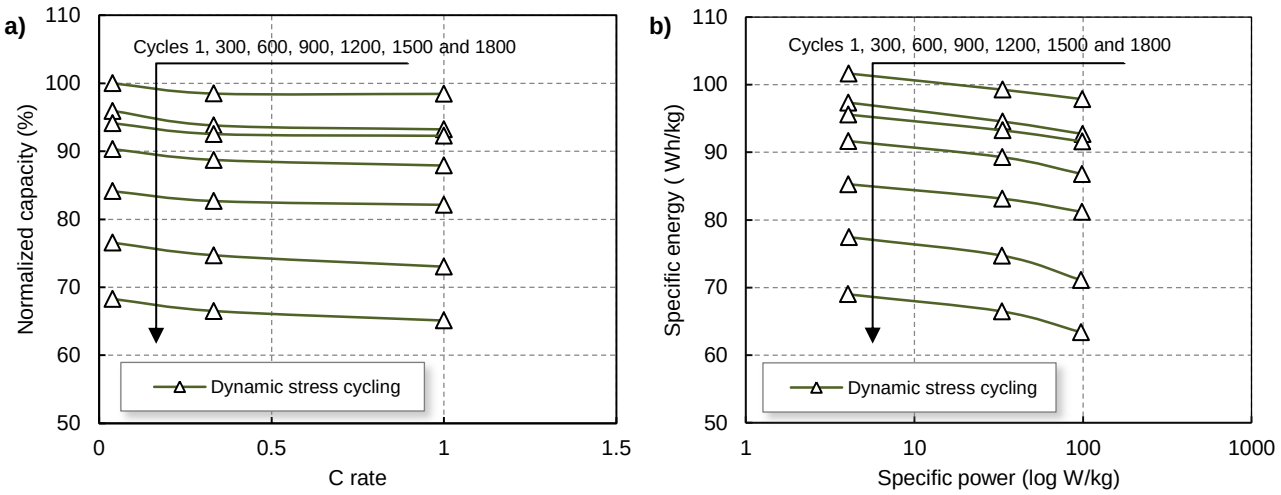

Fig. 6.25. Evolution of the a) Peukert and b) Ragone plots with cycle number under dynamic stress cycling.

The IR measurements during charge and discharge at 1C, 50% SOC using the VCD method are shown in **Fig. 6.26**. The results showed that the IR of the cell tested under dynamic stress cycling experienced a large IR increase, close to 100%. There are two rapid IR increases, one after cycle 600 and the other after cycle 1200.

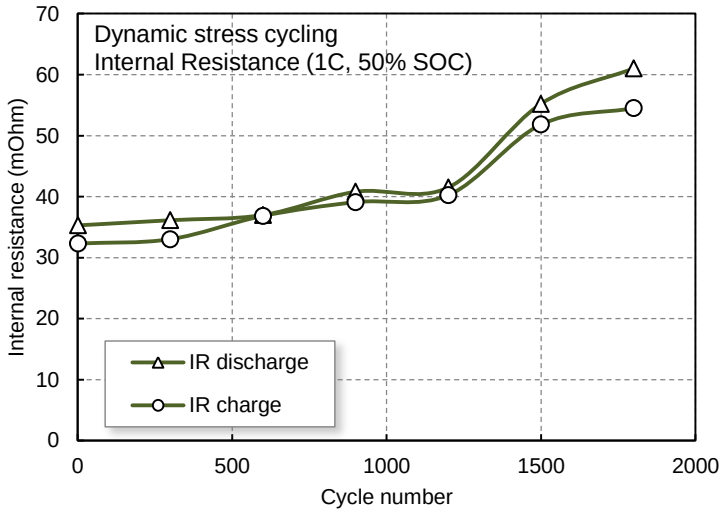

Fig. 6.26. Internal resistance evolution under dynamic stress cycling, at charge and discharge tests.

Fig. 6.27 shows the evolution with cycling of the cell voltage vs. the delivered capacity at 1C during the RPTs. As observed, and contrary to the results shown on standard and fast charge cycling, the area underneath the curves (i.e. energy) is reduced both due to capacity fade and IR increase. The shape of the discharge curve changes as the cell ages, in particular on cycle 1200 and 1800. Also, the position of the voltage plateau at ~3.3 V is shifted for cycles 1200 and 1800 to lower voltages as the cell ages, which also confirms an increase of the cell IR.

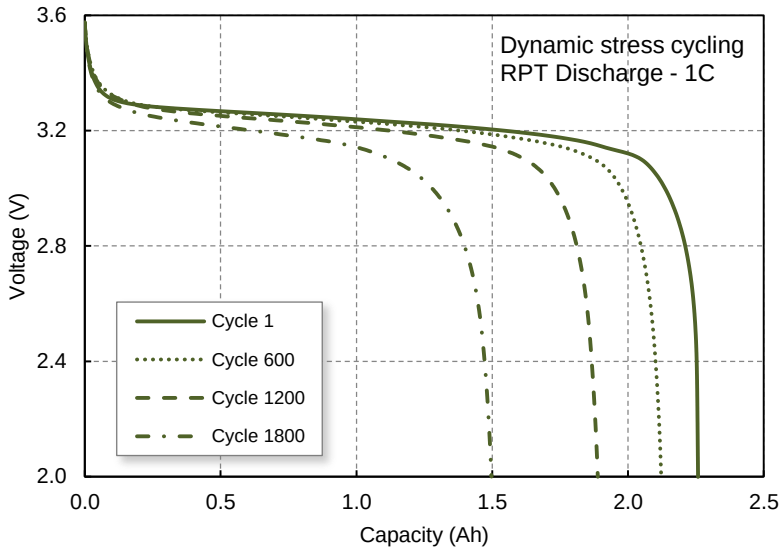

Fig. 6.27. Evolution under dynamic stress cycling of the voltage versus capacity, during RPT discharge at 1C.

To sum up, the cell tested under dynamic stress cycling was initially set to calendar aging for 13 months at 95% SOC, which caused a capacity reduction of 2.6%. Thereafter, the dynamic stress cycling started, and the cell was tested for ~8 months, reaching ~1800 cycles, showing a capacity fade of 32.5% when measured at C/25. Cell's EOL was reached at cycle ~1100. Both energy efficiency and maximum cell temperature showed a small reduction with cycling. The power capabilities were negatively affected, because the cell showed an increase of 100% on the IR. Further examinations of kinetic degradation are carried out in next subsection. In conclusion, the results showed that the cell ages due to capacity loss and IR increase.

6.4.2. Dynamic stress cycling degradation: incremental capacity and peak area results

This section shows the results of the IC and PA curves derived from the dynamic stress cycling test. A detailed description is carried out on thermodynamic (C/25) IC curves to attain the best resolution to identify cell degradation. To facilitate the understanding of aging both from a thermodynamic and kinetic perspective, the IC curves are calculated at C/3 and 1C.

Dynamic stress cycling: incremental capacity results

The evolution with cycling of the kinetic (i.e. C/3 and 1C) IC curves derived from the cell tested under dynamic stress cycling are shown in **Fig. 6.28**a-b. **Fig. 6.28**a shows the kinetic degradation of the cell: the IC peaks become much broader, and the slope of the first reaction is abruptly reduced. In fact, the initial three distinctive peaks showed at BOC became indiscernible at EOC. Similarly, **Fig. 6.28**b shows a large polarization resistance increase with cycling, even at 1C rate. The observed shift of ~80 mV produces an IR increase of 34 mΩ, which corresponds to an increase of 100%. It has to be noticed that the evolution of the kinetic degradation is not linear: the first 900 cycles show a more progressive, pseudo-linear evolution, whereas the subsequent cycles show much rapid kinetic degradation.

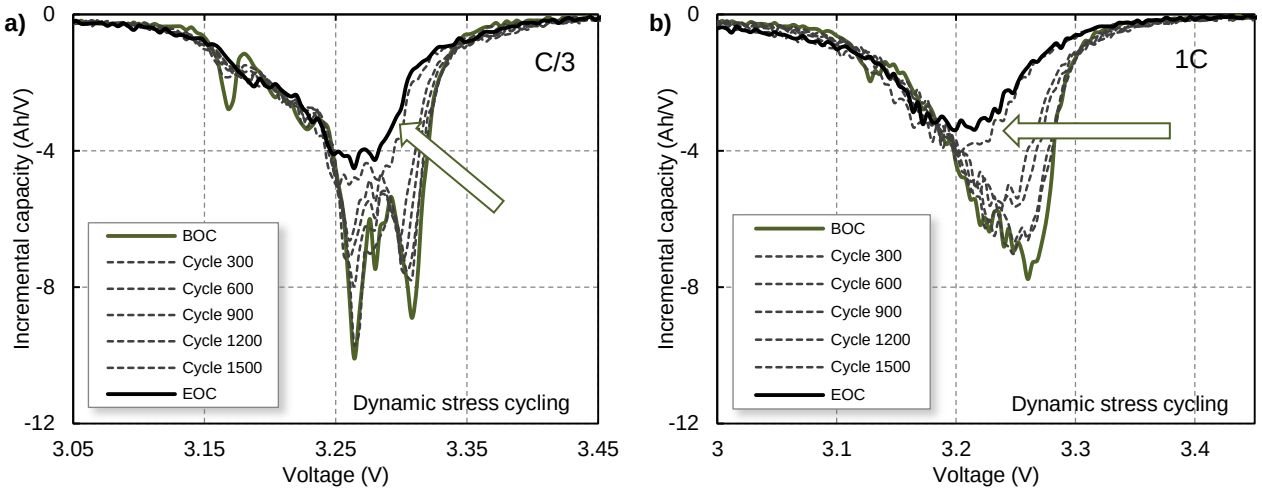

Fig. 6.28. Evolution under dynamic stress cycling of the IC curves at a) C/3 and b) 1C.

The evolution with cycling of the thermodynamic (C/25) IC signatures of the cell tested under standard cycling is shown in **Fig. 6.29**. The main features observed are the strong reduction of the IC peaks (from ❶ to ❺), and the significant appearance of peak ❿. We shall begin the analysis with peak ❿: during the first cycles is not presented, and only after cycle 900 is clearly observed, to continue its gradual growth until the EOC. The intensity of peak ❶ is also reduced, although its reduction rate is rather slow during the first 600-900 cycles, to thereafter increase its reduction rate until EOC. Similarly, its shape is shrunk towards lower potentials, as indicated by the small arrow. The inflection point between peaks ❶ and ❷ is reduced and shifted towards lower potentials. The intensity of peaks' ❷ to ❺ is reduced abruptly. Similarly, peak ❷ is shrunk and shifted towards lower potentials, as indicated by the arrows, whereas peak ❺ is almost vanished at EOC.

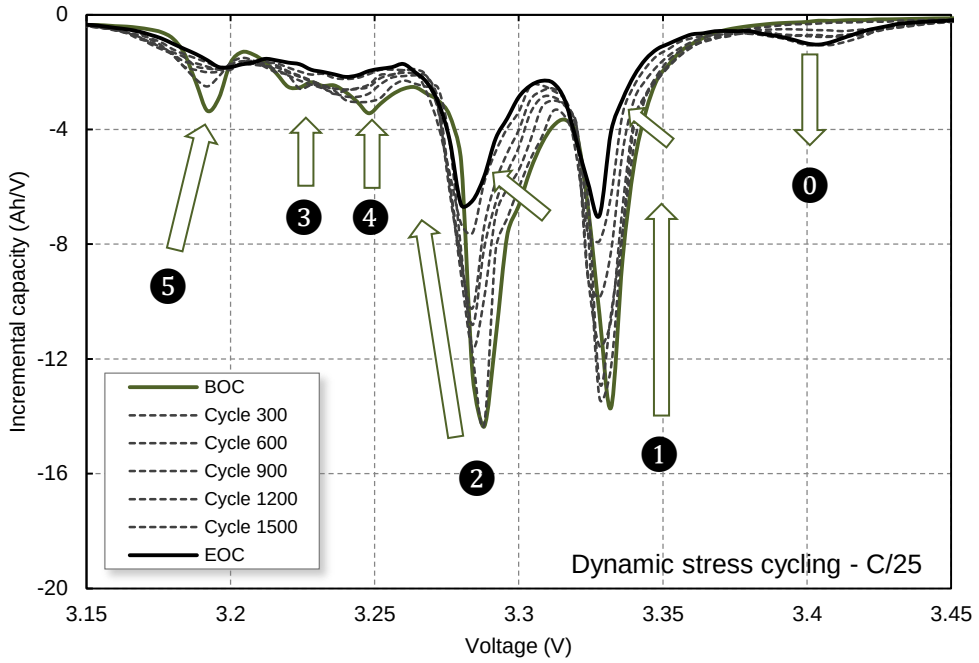

Fig. 6.29. Evolution under dynamic stress cycling of the IC curves at C/25.

Fast charge cycling: incremental capacity peak area results

Capacity retention under dynamic stress cycling appeared highly non-linear. However, the trend can be divided into two well defined stages that followed a linear trend, as shown in **Fig. 6.30**. From the linearized equations, stage 1 shows a degradation rate which is x1.5 faster than that shown on the standard and fast charge cycling. During stage 2 the degradation rate is rapidly increase with respect to stage 1, by a factor of x4.4. The gap between stage 1 and 2 (i.e. between cycle 600 and 900) could contain a nonlinearity process event that produces the sudden trend change.

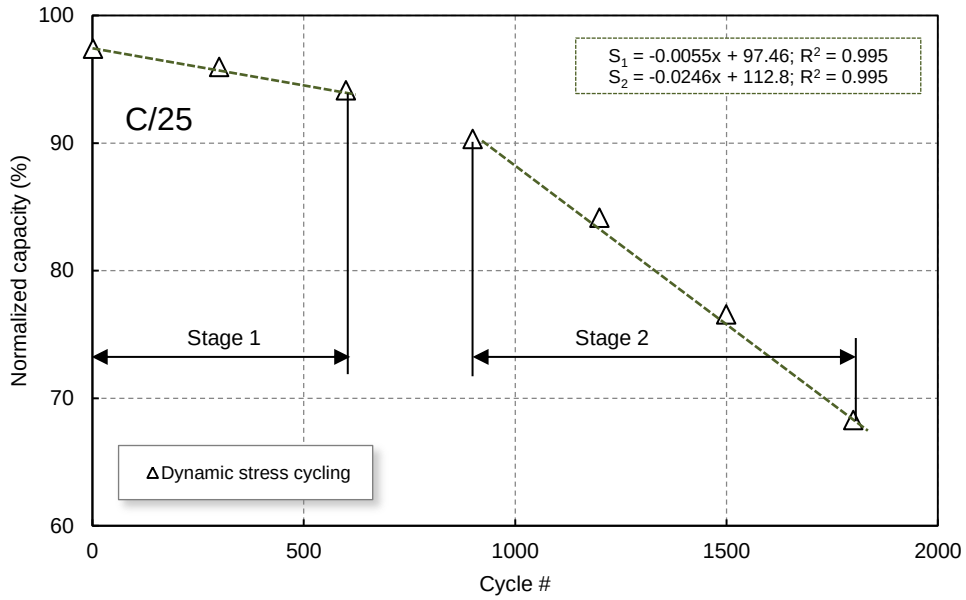

Fig. 6.30. Discharged capacity evolution trends for the dynamic stress cycling procedure.

The results of the PA analysis for the cell tested under dynamic stress cycling are shown in **Fig. 6.31**. The first aspect to be noticed is the starting point: peak ∫❶ is reduced by ~8%. The reason behind this lays in initial condition results. As previously shown, the capacity of the cell was reduced to 2.240 Ah (~2.6% of capacity reduction) due to calendar aging. However, this reduction is not equally distributed among peak ∫❶ and peak ∫❷-❺, and only peak ∫❶ is reduced. Once continuous testing started, during the first 600 cycles (i.e. stage 1) peak ∫❶ linearly grew, whereas peak ∫❷-❺ linearly faded. As previously observed, the degradation pattern under dynamic stress could contain a nonlinearity process event that produces the sudden trend change. The inflection point between cycle 600 and 900 is where the peak ∫❶ tendency changed. Considering cycle 900 as the beginning of stage 2, peak ∫❶ followed a linear degradation trend, which is more abrupt (x1.7 factor) than that showed by peak ∫❷-❺. The degradation pattern for peak ∫❷-❺ followed a linear trend which remained invariant throughout cycling. The cell showed a capacity fade of approximately 27% for peak ∫❶ and 33% for peak ∫❷-❺ at EOC.

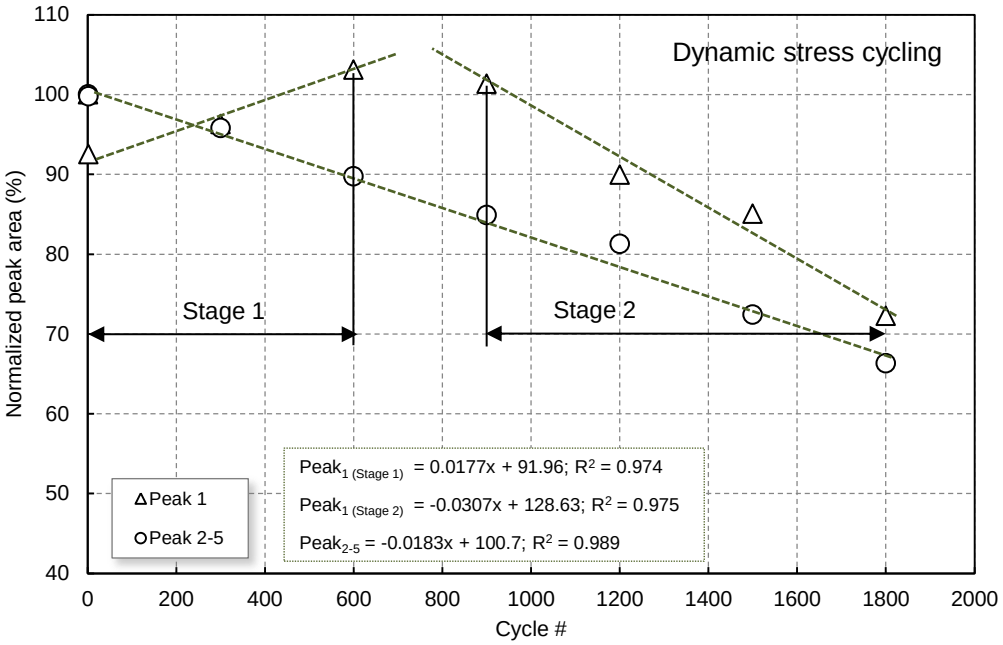

Fig. 6.31. Normalized peak area (peak ❶ and peak ❷-❺) at C/25, as function of cycle number for cell tested under dynamic stress cycling.

To sum up, dynamic stress cycling caused abrupt kinetic degradation on the tested cell, as observed on the kinetic IC curves. The thermodynamic IC curves primarily showed an abrupt reduction of peaks ❷-❺, accompanied by a reduction of peak ❶ in less degree. From the IC results we observed the appearance of peak ❿ hardly discernible at cycle 600, but measurable from cycle 900 onwards. The PA results showed a two-linear stage reduction, where ∫❶ grows until cycle 600-900, to later decrease. The ∫❷-❺ showed a linear degradation. The reduction of ∫❷-❺ was larger than ∫❶.

6.5. Lithium iron phosphate battery performance and degradation: discussion

In this section we discuss the performance and degradation of the cells tested under standard, fast charge and dynamic stress cycling. We first analyze the main findings of the IC and PA results, and put them into context to decipher the aging modes ongoing on the tested cells. Next, we analyze the fast charging protocol, to study its performance and degradation on the long-term cycling. This helps to draw conclusions on the feasibility of the proposed fast charging design strategy. To finish the study, a general evaluation of the performance of the tested cells is carried out. The obtained results (e.g., cycle life, power capability, energy efficiency, etc.) are compared with the long-term USABC goals, in order to validate the selection of this battery technology for its use in EVs.

6.5.1. Incremental capacity and peak area analyses

Here we discuss the results obtained from the IC and PA carried out on the cells tested under standard, fast charge and dynamic stress cycling. The discussion set into context the main findings and importance of IC and PA analyses.

Incremental capacity analysis

The results in this chapter showed the IC curves (both under kinetic and thermodynamic conditions) derived from the cells tested under the proposed cycling schemes. By analyzing the kinetic IC curves, it was possible to examine the kinetic degradation of the cells: the kinetic effects of the cells tested under standard (see **Fig. 6.8**a-b) and fast charge cycling (see **Fig. 6.18**a-b) remained practically invariant with

cycling, whereas the cell tested under dynamic stress (see **Fig. 6.28**a-b) was abruptly degraded from a kinetic perspective. These results are in agreement with the IR test results: the cells under standard and fast charge showed only minor IR changes, whereas dynamic stress cell abruptly increased its IR values. The analysis of the thermodynamic curves was more complicated, as all the IC peaks are affected, following various patterns. From a wide perspective, it is clear again that cells under standard and fast charge schemes are less aged than dynamic stress cell.

To facilitate the thermodynamic analysis of the IC peaks and the significance of the alterations, **Table 6-1** was done, derived from **Fig. 6.9** (standard cycling), **Fig. 6.19** (fast charge cycling) and **Fig. 6.29** (dynamic stress cycling). Readers may also refer to Chapter **4** to bring to mind the degradation patterns that each individual aging mode causes on the IC curves.

Table 6-1. Schematic representation of the IC peaks degradation patterns obtained at C/25, for the cells tested under standard, fast charge and dynamic stress cycling.

Cycling test	❶	❷	❸	❹	❺	⓪	$IP_{❶-❷}$
Standard	↑	↑	↑	↑	↗	–	↑
Fast charge	↑	↑	↑	↑	↗	–	↑
Dynamic stress	↑	↑	↑	↑	↗	↓	↑

The similarity of the aging patterns of standard and fast charge cycling was previously highlighted, as capacity fade, power capability and kinetic degradation was very close. In fact, when comparing the IC peaks, the similarity of the degradation patterns is again very close (see **Table 6-1**). Hence, the analysis of the IC signatures can be merged for both cells.

When comparing the obtained IC signatures of standard and fast charge tests (see **Table 6-1**) with the summary of the aging modes identification presented in Chapter **4**, we observe that the degradation of peaks ❷-❺ should only be caused by LAM acting on the NE. Moreover, the reduction of peak ❶ could be derived from LLI, LAM_{liNE} or LAM_{liPE}. However, as suggested by the *post mortem* analyses in the literature [59], [61], [68], [76], [78], [93], [174], cell degradation caused by LAM on the PE on LFP cathode materials is very unlikely. In contrast, the majority of the literature reports agree that LLI is usually found as a major aging mode [7], [24], [32], [36], [55], [59], [63], [76], [183]. If these two considerations are taken into account, and the facts derived from the IC signatures, it is indeed very likely that the cells aged due to LLI + LAM_{NE}. Similarly, the reduction and direction of peak ❺ may also suggest the effect of LLI (shifting) added with reduction caused by LAM_{NE}. However, deciphering the magnitude of LLI or which of the possible LAM_{NE} mode (i.e. LAM_{deNE} or LAM_{liNE}) is predominant is still very challenging.

The IC degradation pattern of cell tested under dynamic stress shows a distinctive feature: the appearance of peak ⓪ (see **Table 6-1**), that emerges under reversible Li plating conditions. In addition, peak ⓪ emerges after cycle 600-900, and is a plausible cause of the stage 2 in the capacity fade trend, observed after cycle 900. Also, after cycle 900, the cell IR is increased more abruptly, and during cycles 600 to 900 the energy efficiency is slightly decreased. These evidences suggest Li plating occurrence on the cell tested under dynamic stress. As presented in Chapter **2**, Li plating is considered one of the most detrimental aging mechanisms, may lead to second degradation stages and even cause safety issues. We observe that peak ⓪ should only be caused by LAM_{deNE} from all the LAM aging modes. To decipher if LAM_{deNE} is acting alone, we shall refer to peak ❶: if LAM_{deNE} was the only aging mode, peak ❶ would initially grow, to later decrease. However, IC peak ❶ shown an initial, slow rate of decrease of peak ❶ (see **Table 6-1**). This could be caused by the additional effect of LLI, which counteracts the growth of ❶

caused by LAM_{deNE}. This suggestion also agrees with the previous proposal, where LLI is to be found a major aging mode, as supported by the literature. Comparing these IC curves with the standard and fast charge cycling IC curves, we may suggest that LAM_{deNE} is now a more prominent degradation mode, by the effect of peak ⓪ and large shrinkage of peaks ❷-❺. Still, we cannot yet quantify the effects of LAM_{deNE}. Moroever, from the IC curves it may be possible that LAM_{liNE} is acting simultaneously, as it also contributes to the reduction of peaks ❶ to ❺.

The analyses carried out in this section are useful to provide a first approach of the plausible degradation modes that affected the tested cells, from a qualitative perspective. The next subsection presents the results of PA results, to give a first quantifying approach of the aging modes ongoing on the cells.

Peak area analysis

The results presented in this chapter showed the degradation patterns with cycling of each peak area association (i.e. peak ∫❶ and peak ∫❷-❺). The main results derived are summarized in **Table 6-2**. Words in red indicate second degradation stages. As previously commented, to facilitate the analyses of the PA, we shall refer to the contents provided in Chapter **4**.

Table 6-2. Summary of the main characteristics of the PA degradation patterns, obtained at C/25 for the cells tested under standard, fast charge and dynamic stress cycling.

	Standard cycling	**Fast charge**	**Dynamic stress**
Peak Area ∫❶	Linear	Linear	Linear increase/ Decrease
Peak Area ∫❷-❺	Linear	Linear	Linear
Deg. Rate ∫❶ > ∫❷-❺ ?	Yes	Yes	No
Normalized cell capacity	Linear	Linear	Linear/ Abrupt linear
Risk Li plating	No	No	Yes

The similarity of the aging patterns of standard and fast charge cycling is again showcased from the PA degradation analysis, particularly for the first 3000 cycles. This indicates that the cells seem to age in a similar manner; both from a qualitative and quantitative perspective. However, due the slight changes of the slopes in the different stages, and the effect that calendar aging causes on fast charge cell (cycle 4500), the PA analyses shall be provided separately.

The PA linear degradation pattern of cell tested under standard cycling is more pronounced for ∫❶ than for peak ∫❷-❺. By examination of the mechanistic models, LLI, LAM_{liNE} and LAM_{liPE} show this condition. However, none of them show the same pattern. LLI and LAM_{liPE}, do not affect peak ∫❷-❺. In addition, LAM_{liPE} is rather unlikely, as previously commented. Similarly, the separation trends between ∫❶ and ∫❷-❺ under LAM_{liNE} are much closer than the ones showed in the experimental results. Hence, as derived from the IC curves, it is indeed very likely that the degradation trends are derived from the effects of various aging modes. The suggestion that LLI and LAM_{NE} are taking place simultaneously is very plausible, as peak ∫❶ reduces its intensity (but not as much as if was acting alone), and peak ∫❷-❺ is being reduced from the effects of LAM_{NE}.

To analyze the plausible degradation patterns of the cell cycled under fast charge cycling, we shall proceed identically as with standard cycling. Both cells show the same patterns, only with minor

variations in the numerical tendencies. Hence, LLI and LAM_{NE} are likely to be taking place simultaneously during fast charge cycling. The change of tendencies after the 65-day calendar pause only affects peak ∫❶. By comparison with the mechanistic simulations, LLI and LAM_{liPE} cause this type of degradation. However, the cell is at rest, and LAM is therefore very unlikely. On the other hand, the studies on calendar aging indeed agree that calendar aging causes SEI growth [24], [94], [97], [98], which consumes cyclable lithium (LLI). These facts are in agreement with what is observed from the PA results.

The cell tested under dynamic stress also suffered from LLI during the initial calendar aging. This is shown by the initial reduction of peak ∫❶ by ~8%. Thereafter, the cell showed a PA degradation pattern that is remarkable similar to that shown for a cell aged under severe LAM_{deNE}. The main difference is that under LAM_{deNE}, the cell does not start to loss capacity until Li plating emerges. This outcome was not observed in the tested cell under dynamic stress, which lost capacity from the first cycle. Hence, LAM_{deNE} has to be accompanied by additional aging modes. As previously analyzed with the IC results, it is very likely that LAM_{deNE} is accompanied at least by LLI. In fact, a combination of LAM_{deNE} + LLI could match with PA degradation pattern exhibited by the cell under dynamic stress cycling. Due to the complexity of the degradation patterns shown in this cell, further analyses are needed to decipher the degradation modes from a qualitative and quantitative perspective. Only upon further analysis of PA coupled with mechanistic simulations, it can be possible to unveil the aging modes from a qualitative and quantitative perspective. Finally, when cell tested under dynamic stress is compared with the fast charge cycling scheme, it is clear that the DST discharge is the responsible for the rapid degradation of the cell. In fact, fast charge cycling and dynamic stress cycling have the same charging protocol; by comparison with standard cycling, the fast charging protocol does not cause significant degradation on the cell. Hence, the DST seems responsible for the rapid capacity fade, power capability reduction and IR increase.

The IC and PA analyses carried out here provided a notable, first approach of the cell's performance and degradation. Applying the analyses carried out in Chapter **4** to the experimental results, we suggested LLI + LAM_{NE} on the cells tested under standard and fast charge, and a combination of LAM_{deNE} + LLI for the cell tested under dynamic stress cycling. The ability to decipher these aging modes through *in situ* techniques is a remarkable achievement. These findings also validate the applicability of the individual aging analyses carried out in Chapter **4**, to decipher real world, more complicated aging signatures. This allowed us to evaluate cell aging, estimate what are the main aging modes ongoing on the cells, or even find solid evidences of Li plating evolution which could affect cell safety. Still, in this thesis we aim to attain the most advanced aging evaluation and quantification, in order to provide: the level of detail to analyze the amount of capacity that is loss to each mechanism (in a quantitative value of % per cycle), the nature of LAM_{NE} (i.e. if the observed degradation is caused by LAM_{deNE} and/or LAM_{liNE}) and the advanced study of Li plating. To achieve this complete and challenging aging study, more advanced techniques and analyses are required, which are used in synergy with the results shown here. These analyses are provided in Chapter **7**, under a mechanistic simulation approach.

6.5.2. Fast charging performance and degradation analyses

Here we discuss the overall performance of the designed fast charging protocol. To carry out the analyses, we compare the performance and degradation of the fast charging protocol with the results of standard cycling, where nominal charging conditions were used.

Fast charging performance

The charging time evolution for the standard cycling and the fast charge cycling is depicted in **Fig. 6.32**. The charging time at standard cycling took 67 min at beginning of cycling (BOC), and evolved following a downward linear trend, reducing the charging time to 54 min at the end of cycling (EOC). The

fast charge cycling scheme took 22 min at BOC, and evolved with cycling remaining practically constant, only decreasing its charging time to 20 min at EOC.

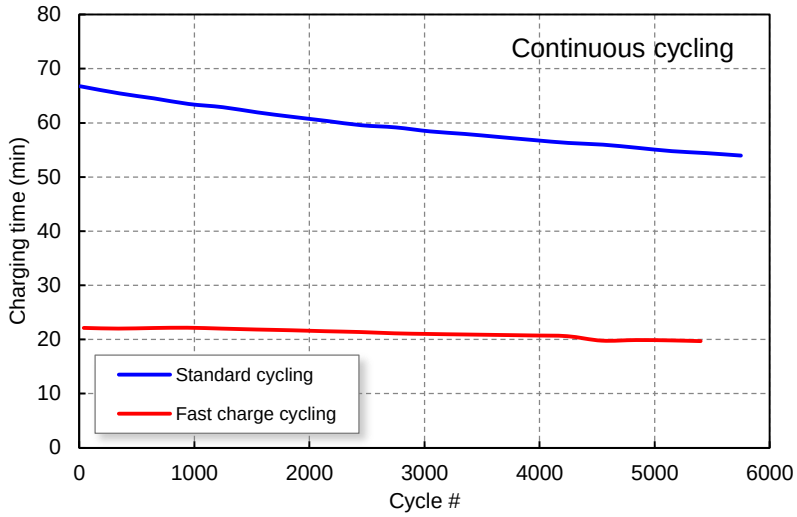

Fig. 6.32. Charging time evolution during continuous cycling.

It would seem common that, as shown with standard cycling (see **Fig. 6.32**), when a cell reduces its capacity, the charging time is also reduced. This occurs because less capacity to be charged takes less time (if keeping the same charging current). However, this is not observed with the fast charging scheme (4C-1C-CV). To further decipher this behavior, the evolution with cycling of the percentage of charging time and charging capacity of the different charging stages is described in the following figures (see **Fig. 6.33**a-d).

The charging time under standard cycling (see **Fig. 6.33**a-b) is clearly defined by the CC charging stage at 1C. Indeed, the 1C stage took an average of ~87% of the total charging time through cycling, to charge above ~97% of the total cell capacity. The CV stage took ~13% and charged the rest ~3% of the total cell capacity. The tendencies remained constant through cycling, even if the total charging time was reduced by 17 min from BOC to EOC.

The charging time under fast charge cycling (see **Fig. 6.33**c-d) is characterized by the first charging stage at 4C: the charging time under this stage slightly decreased with cycling (i.e. 3 min). Still, on average, the charging time at 4C remains within the ~55% (~11 min) of the total charging time. Yet this stage provides up to ~90% of the total charged capacity. This indicates that the long-term USABC goal for fast charging (recharged up to 40% of capacity within 15 min) is surpassed throughout cycling. The second charging stage at 1C takes ~22% (~4 min) and provides ~8.5% of the total cell capacity. Finally, the third charging stage at CV is fixed to 5 min (~22% of charging time) and provides the rest ~1.5% of the charged capacity. These two last stages charged ~9% of the total cell capacity. In addition, the use of the last two stages has a positive effect to achieve full recharges throughout cycling. As observed in **Fig. 6.33**c-d, the charging time and charged capacity of 1C and CV is slightly increased with cycling, as it compensates the reduction of the charging time at 4C. As a result, the full recharges remain practically constant (and in the same charging time) throughout cycle life.

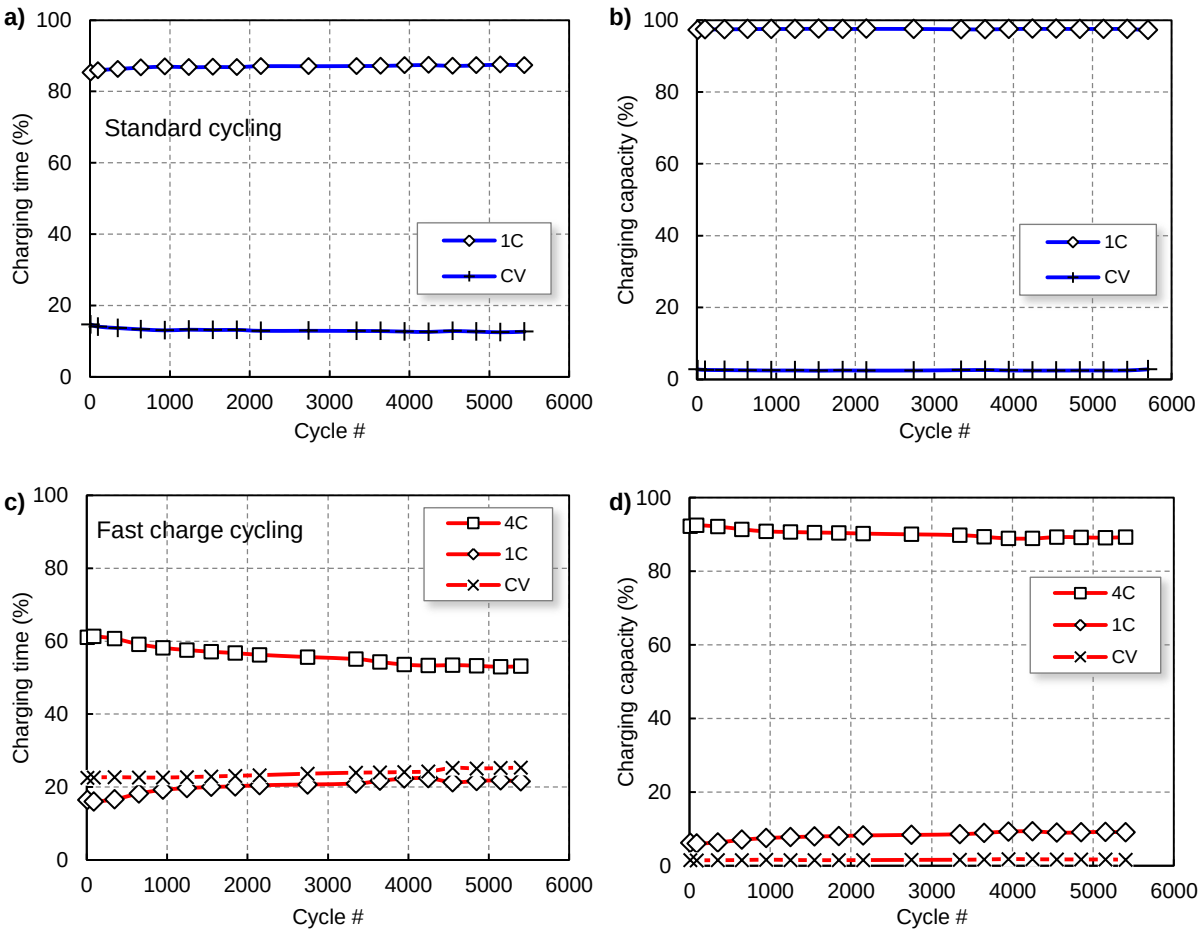

Fig. 6.33. Charging time and capacity evolution with cycling for the (a-b) standard charge and (c-d) fast charge.

With a charging stage at 4C that charges up to 90% of the total cell capacity, it would be possible to avoid stages 1C and CV, and still achieve the long-term USBAC fast charging goal. However, these two stages (i.e. 1C and CV) allow the cell to decrease its temperature rapidly, while still being charged. This is observed in **Fig. 6.34**. The cell temperature increased rapidly during the 4C discharge cycles, to reach the maximum temperature value (~28ºC). During charge, with the first stage at 4C, the temperature rose again after a slight decrease, until it was approximately the value at the end of each discharge cycle. The lower current in the last two stages (1C-CV) allowed the cell temperature to decrease abruptly to its lower values (~24ºC), which are near the thermal chamber preset point (23ºC±0.5ºC). Hence, the use of 1C and CV stages decrease the thermal stress and the risk of cell overheating. This avoids further deterioration, while provides full charging of the cell.

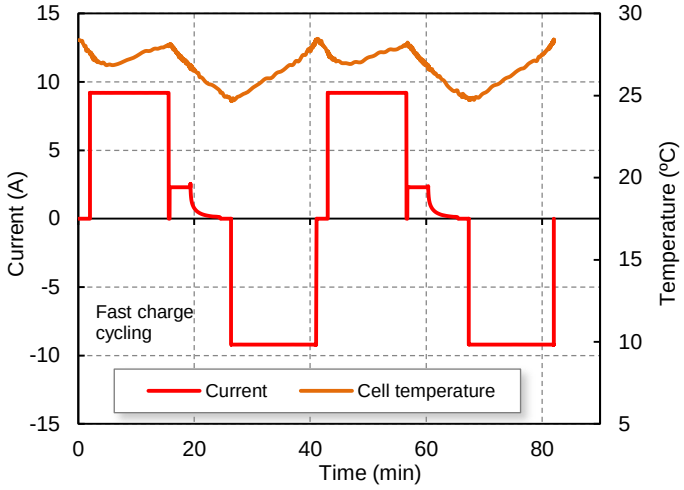

Fig. 6.34. Current and cell temperature evolution for the fast charge protocol.

Fast charging degradation

When compared with standard cycling, the fast charge protocol did not cause additional capacity degradation. This is shown in **Fig. 6.35**. The tested cells degrade with the same trend, showing minor differences (<0.5%), even if the cycling conditions widely differ. This is particularly true until cycle ~3000. Thereafter, the trends tend to diverge slightly until cycle 4500. This is a first observation that reveals the significant positive performance features of the fast charging protocol.

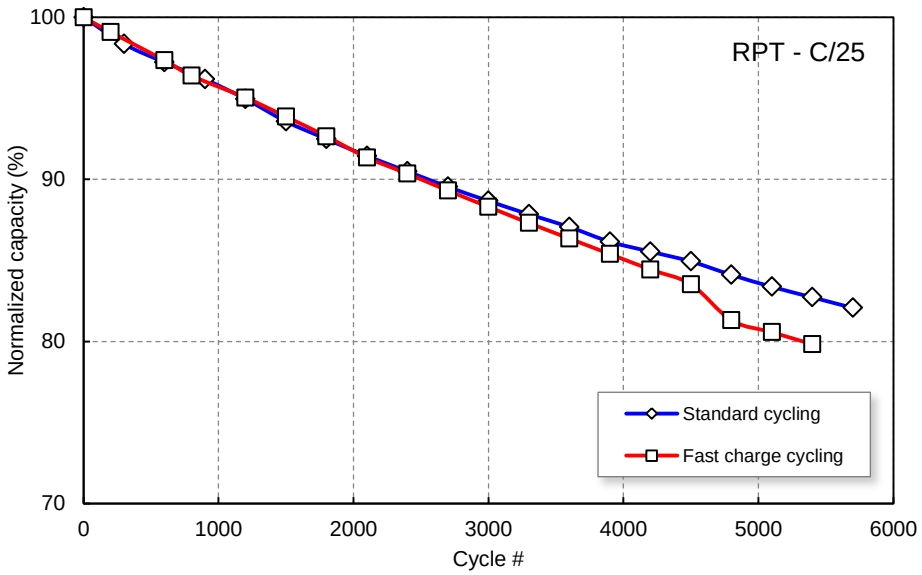

Fig. 6.35. Discharged capacity evolution with cycling at C/25 rate, determined in the RPT.

In terms of power capabilities, the fast charge protocol did not cause any significant degradation. This was shown when comparing the Peukert, Ragone and IR plots of both testing schemes (see **Fig. 6.5**a-b and **Fig. 6.6** for standard cycling, see **Fig. 6.15**a-b, **Fig. 6.16** for fast charge cycling). Fast charging did not produce IR increase in the cell. With these results we concluded that both testing schemes caused cell aging primarily due to capacity loss, rather than IR increase in a very similar manner.

To further evaluate the degradation of fast charge cycling both qualitatively and quantitatively, we examined the IC and PA curves. When compared with those derived from the standard cycling, we found

again great resemblance. In fact, the qualitative IC analyses showed the same degradation patterns, and we estimated LLI + LAM_{NE} as the degradation modes. Moreover, the quantitative PA analyses showed again practically the same degradation values for ∫❶ and ∫❷-❺, during the first 3000 cycles.

When we tried to compare with other fast charging protocols, we found that very few studies were proposed on LFP cells (see Chapter **3**). An example was the fast charging scheme proposed by Huang *et al.* [134]; we found that it could cause degradation in the mid-term cycling, because high current rates (8 times above recommended by manufacturer) were applied at high SOCs, increasing cell voltage up to 4.5 V. The cycle life evaluation was 300 cycles, insufficient to compare the results with the obtained from our tests. Although not specifically designed for fast charging purposes, in the study of Klett *et al.* [68] the same type of cell was tested at room temperature with 3.75C charging rate, using CC to 3.6 V followed by CV stage. The discharge was carried out at 3.75C CC to 2 V. This cycling scheme is very close as the one proposed in the fast charging cycling. However, it does not include the multistage CC stage at 1C. When results were compared, the cycle life of the cell at 3.75C/3.75C was approximately 1800 cycles, much smaller than the 4600 cycles obtained with the proposed fast charging (4C-1C-CV/4C) scheme. The introduction of the charging stages (4C-1C), together with the time limitation to 5 min. in the CV stage are therefore important to achieve fast charge without causing rapid degradation.

Recently, Khandelwal *et al.* [184] carried out an study on LFP cells to facilitate the design of efficient charges, using thermally coupled models. They found through numerical simulations that boost or multistep charging can charge battery faster and, also, the importance of the thermal effects due to the charging profile. Among the studied protocols, Khandelwal *et al.* studied our proposed 4C-1C-CV fast charging scheme in comparison with direct 4C-CV (with no limiting CV time) from a thermal perspective. They observed thermal advantages in our proposed protocol and reduction in charging time. Hence, this study also helped to validate our findings on the thermal advantages of the designed fast charging technique.

In conclusion, the performance and degradation results validated the feasibility of the designed fast charging protocol, to achieve safe, efficient fast charges. We showed that with a proper selection of cell chemistry and architecture, coupled with an efficient and reliable fast charging protocol, it is possible to achieve fast, safe charges throughout the cell's cycle life.

6.5.3. Lithium iron phosphate battery evaluation

The results provided in this chapter showed the long-term cycle aging evolution of three equal HP, GIC||LFP cells under different cycle aging conditions: standard, fast charge and dynamic stress cycling. The cells were initially studied to ensure the consistency of the selected samples. With these verifications, the results between the tested cells were therefore comparable. Hence, the aging evolution is caused by the proposed cycling scheme, and not due to cell-to-cell variations.

To analyze the battery performance, several measurement techniques and representations were implemented. This helped to quantify the cell's end-of-life for each proposed cycling scheme, energy and power degradation, temperature evolution with cycling and charging time. This evaluation was also compared to the long term USABC goals, when possible.

Table 6-3 shows the main USABC long-term goals evaluated for the tested cells under the proposed cycling schemes. With the exception of the specific energy goal, the selected cells achieved the long term USABC goals. The long-term specific energy goal (200 Wh/kg) remains in general quite demanding for LIB technologies, particularly for EV applications. Although various laboratory-based approaches have been explored to reach energies up to 440 Wh/kg [185], studies suggest that commercial LFP batteries are unlikely to achieve the specific energy USABC long-term goal in the near future, with their actual chemistry composition and design [154].

Table 6-3. USABC long-term goals evaluation for the proposed cycling schemes.

Cycling scheme	Specific Energy (Wh/kg)	Specific Power (W/kg)	Cycle life (cycles)	Fast-charge (min)	Cycling efficiency (%)
USABC goals	80*	400	1000	40% SOC in 15 min	80%
Standard cycling	98/79	>570	5900	Not tested	95
Fast charge cycling	98/78	>400	4600	Achieved	88
Dynamic stress test	98/75	Not tested	1100	Achieved	92/90

* Mid-term goal. Slash symbol: BOC/EOC at 1C from RPT

In terms of specific power, the long-term goal was successfully achieved when the cells were set to high rate tests. In addition, the cells under standard and fast charge did not show IR increase with cycling, and both power performance tests showed invariant capabilities throughout cell cycle life. This is indeed a desired characteristic of quality HP cells.

For the cycle life requirements, the cells tested under standard and fast charge cycling exhibited a remarkable long cycle life (up to 5900 and 4600 cycles, respectively), much above the long-term USABC goal. In addition, the long cycle life performance was attained under two different cycling schemes, which is also a good indicator of both the fast charging protocol and selected cell technology. On the contrary, the tested cell under dynamic stress reached 1100 cycles. This may seem rather unsatisfactory when compared to standard cycling. However, it must be pointed out that the cell achieved important long-term USABC goals (including cycle life), even under such demanding cycling scheme (we shall recall that DST was scaled to the long-term USABC goal, 400 W/kg).

The fast charging goal throughout cycle life was validated by examining the charging time of cells under fast charge and dynamic stress testing. In addition, on account of introduction of multistage (4C-1C-CV) charging sections in the design of the protocol, full recharges were attained throughout cycling, and the total charging time remains within the expected values (~22 min). The evolution with cycling of the charging time and capacity with aging allows the battery to be fully charged, while keeping the cell under safe charging conditions.

The energy efficiency throughout cycling also achieved the long-term USABC goals, showing high values (up to 95% under standard cycling) that are required, for example, to achieve effective EV driving. Although not shown here for simplicity, the energy efficiency at C/25 during the RPT remains within 99% throughout cycling, for all cycling schemes.

In addition to the performance analysis, one of the main drawbacks for LIBs is, in general, the final cost of the system. For this particular case, even if LFP is a cost-effective battery (10€/unit for the tested cell) when compared to other technologies, the final price of a full system is still in the 800-1000€/kWh, whereas the USABC goals set the prices at lower than US$100 per kWh. We must understand that wholescale sellers would get a reduced price, and EV manufacturers are attaining battery system costs around the US$400 per kWh, with 8% of cost reduction rate per year [186].

Interested readers in the performance of LFP batteries for EV applications may refer to [154], where an evaluation of several LFP batteries (including high power, high energy and large capacities) are studied under various testing scenarios and the obtained results are compared with the USABC goals. The findings of the current study are consistent with those of [154], where the tested LFP batteries

successfully met some important USABC goals, but the increase of energy density or the reduction of the final cost are two of the major technical challenges to be addressed.

6.6. Calendar aging

To complete the results on battery performance and degradation, a calendar aging diagnosis is presented in this section. The motivation behind this analysis is that LIB systems may remain long periods of time at rest. Indeed, applications such as EVs or second-life use of batteries are examples where the LIB system may remain long periods of time at rest. The aim of this section is to evaluate capacity fade and decipher the aging modes acting on the tested LFP cells while on rest.

In this section we present the analyses on 8 cells, which were set to rest under the same temperature, but at several storage conditions, as presented in Chapter **5**. The aging analyses are carried out by evaluating the capacity fade vs. time. Similarly, IC and PA analyses are also performed to evaluate the aging modes that are undergoing while the cells are at rest. The results provided in this section are useful to enhance our understanding on calendar aging and the possible issues that battery second life applications may encounter.

Capacity fade

Table 6-4 shows the calendar aging cell test matrix, including the capacity retention and cycle number of the cells before calendar storage. The cells were cycled for a given number of cycles under different cycling schemes, always within the voltage limits and current limits recommended by the manufacturer and at ambient temperature (i.e. 23ºC). The capacity retention prior calendar storage is provided. Although not shown here for simplicity, none of the tested cells showed IR increases before the calendar aging. Similarly, the capacity degradation trend was linear throughout cycling for all the tested cells. Hence, the tested cells lost performance due to linear capacity fade, whereas the power capabilities remained invariable.

Table 6-4. Calendar aging cell test matrix, including capacity retention prior the calendar storage.

Cell number#	Cycling scheme	Nº of cycles	Capacity retention prior calendar storage (%)	Calendar storage (months)	SOC storage condition (%)
1	Conditioning	10	100	12	0
2	4C-1C-CV/4C	5400	79.87	7	95
3	Conditioning	10	100	13	95
4	*	50	99.8	25	0
5	*	1100	98.3	36	0
6	*	800	98.5	34	50
7	*	700	95.2	31	20
8	*	2100	90.8	26	98

* Combination of various cycling schemes

Fig. 6.36 shows the normalized discharged capacities measured at C/25 and 23ºC, for the 8 cells set to calendar under different storage conditions of SOC and capacity retention. There are two main distinctive groups of cell testing conditions: cell# 1, 3, 4, 5 and 6 were set to rest at high capacity retention (i.e. above 98.4%). In contrast, cell# 2, 7 and 8 were set to rest at lower capacity retention (i.e. below 96%). Upon storage, the cells with lower capacity retention prior calendar aging showed the larger capacity fade, as observed by the slope of their corresponding degradation trends (see **Fig. 6.36**). Indeed, Cell# 2 showed a capacity degradation trend during storage which is x2.2 higher than that found on Cell # 8. Both cells have practically the same SOC storage conditions (i.e. 95% and 98%, respectively).

The cells also showed dependence upon SOC storage conditions and cycle number, as both conditions influence the capacity loss evolution during storage. This is specially perceived at the SOC extremes on fresh cells (i.e. Cell# 1, 3 and 4). As observed, Cell# 3 was stored for 13 months at 95% SOC and lost 2.6% of its normalized capacity. In contrast, Cell #1 and Cell #4 were stored at 0% SOC for longer periods (up to 25 months Cell #4) and did not show any noticeable capacity loss. On the other hand, Cell# 5 and 6 were set to rest at 0% and 50% SOC respectively, although both showed the same capacity fade with time. Similarly, Cell# 7 was stored at 20% SOC. showing a larger capacity fade than Cell#6, which was stored at 50% SOC. Overall, the results suggest that when the cells are fresh, high SOC conditions are more dominant on capacity degradation. However, when the cells are cycled, the SOC is less dominant, and capacity retention prior to cycling coupled with cycle number, are the main factors.

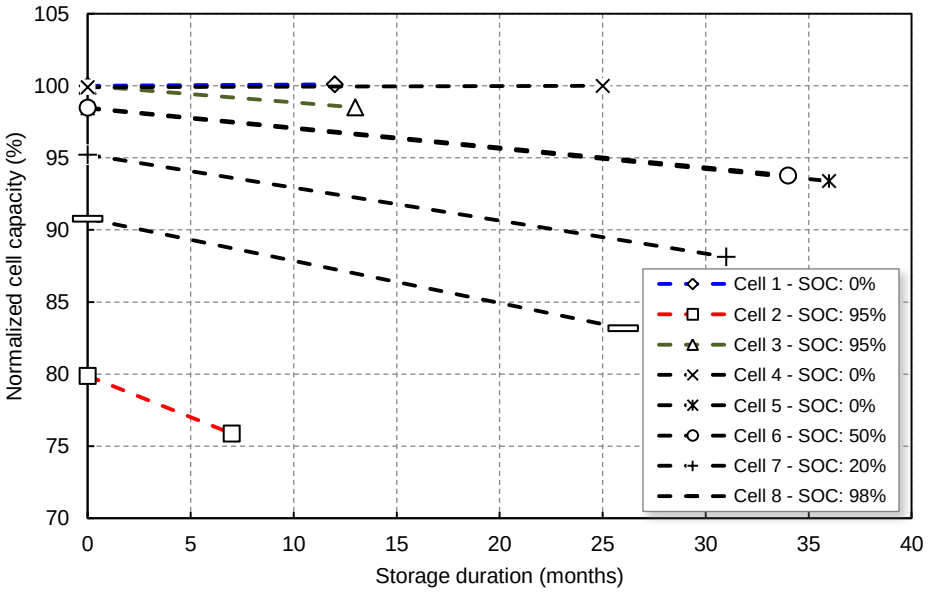

Fig. 6.36. Discharged capacities measured at C/25 and 23ºC for the 8 cells under different storage conditions of SOC and capacity retention.

Aging mechanisms

To decipher the aging modes that the cells encountered during storage, we carried out the PA analyses. Although not shown here for simplicity, the PA analyses were derived from the IC results. The PA results provide a clearer vision of the nature of the aging degradation. As observed in **Fig. 6.37**a-b, the capacity fade is attributed to peak ∫❶ instead of peak ∫❷-❺. This is a clear signal that the capacity fade was caused by the aging mode LLI instead of LAM. No evidences of LAM were measured, as peaks ∫❷-❺ were not reduced during storage. These findings are in agreement with the work of Kassem and Delacourt [76], in which using post-mortem techniques confirmed LLI as the main source of calendar aging on LFP cells.

The results of this investigation can be applied to actual LIB applications. In general, fresh LIBs that are not used should be stored at low SOC to minimize degradation. Similarly, when aged LIBs are used for second-life applications, it is recommended that the storage duration is minimized, to reduce capacity fade. Although not covered in our experiments, high temperatures also play a critical role on storage aging, as covered in the literature [76], [95]. Overall, to reduce the aging during storage one shall store the LIBs at low temperatures and low SOCs. Similarly, for second-life LIB applications it is more convenient to recover batteries with high capacity retention and low cycle life.

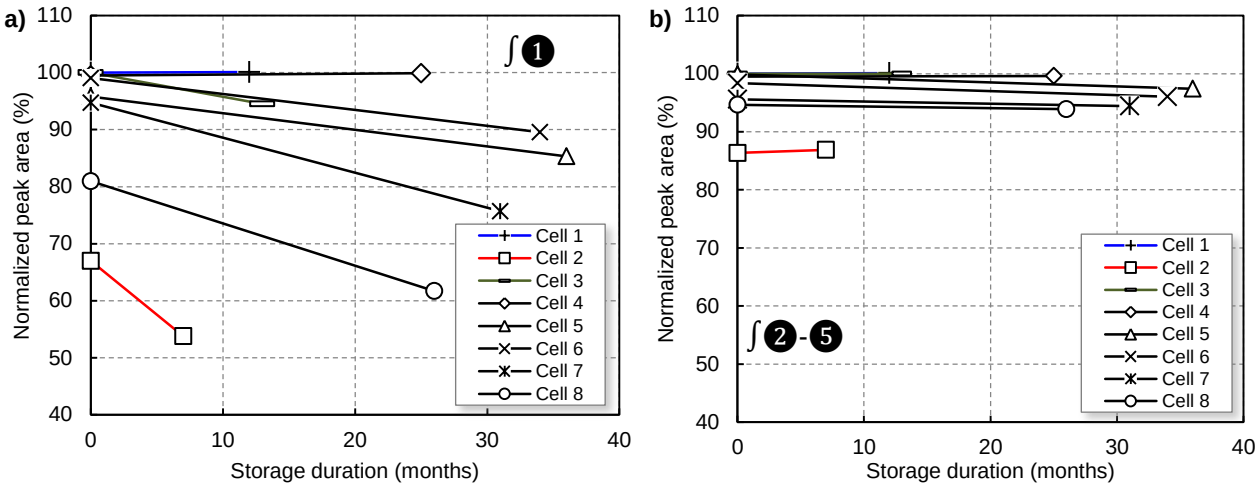

Fig. 6.37. Peak area results of the cells during storage for a) peak ∫❶ and b) peak ∫❷-❺.

To sum up in this section, a brief study of the calendar aging was carried out on 8 cells set to rest under different storage conditions. The temperature was kept at 23ºC during the whole experiment. The extent of capacity loss was found to be related with the capacity retention and cycle number prior storage. The results showed that long-term cycled aged cells were more affected by calendar storage. Similarly, storage at high SOC also plays a significant role, although its effects are more prominent only on fresh cells.

6.7. Summary

This chapter presents the experimental results and analyses carried out on the cells tested under the proposed schemes. We conducted a series of *in situ* performance and degradation analyses to provide a broad study on the cell's performance, and a first approach to decipher the main aging modes ongoing on the tested cells.

From the initial conditioning results, it was shown that the batch used in this thesis does not include outliers and the results between cells are comparable, showing minor cell-to-cell variations. Also, capacity evolution under standard cycling was confirmed to match with the experimental values provided by the manufacturer. This ensures that the results of cell performance and degradation are caused by the proposed testing schemes and not due to cell-to-cell inaccuracies.

Both from the performance and degradation analyses we observe that the cells tested under standard and fast charge showed remarkably similar behavior (particularly for the first 3000 cycles), even under broadly different testing schemes. These similitudes were confirmed from qualitative and quantitate analyses; both cycling schemes caused a linear degradation trend on the tested cells, which only differ by less than 0.5%. Also, the power capabilities were not affected by capacity loss, as shown in the Ragone, Peukert and internal resistance (IR) plots. The results confirmed that the cells aged primarily due to capacity loss, rather than IR increase. The aging modes were deciphered from the *in situ* incremental capacity (IC) and peak area (PA) results, and showed the same degradation pattern for both cells, dominated by loss of lithium inventory (LLI), and in less degree, loss of active material on the negative electrode (LAM_{NE}). This indicates that the cells seem to age in a very similar manner; both from a qualitative and quantitative perspective.

The performance of the cell cycled under dynamic stress cycling was deteriorated more rapidly due to the use of the dynamic stress test (DST) discharge scheme. The DST was scaled to the USABC long term goal (400 W/kg), which is considered very demanding for the current cell technology. Still, the cell achieved 1100 cycles at end-of-life. Due to the nature of the cycling scheme, composed by multiple charge/discharge repetitions, we deciphered that large LAM occurs on the tested cell. The aging analysis showed LAM_{deNE}, possibly accompanied by LLI. Similarly, Li plating was detected and was the plausible cause of the second degradation stage starting within the cycles 600-900. As Li plating emerges, the cell performance rapidly decreases, leading to rapid capacity degradation and IR increase.

Fast charging was validated throughout cycling, by examining the charging time evolution, overall performance and the analyses of the degradation modes. The proposed fast charging scheme achieved full recharges within ~22 min. throughout cycle life, reaching a considerable time reduction of ~48 min. with respect to the standard charge. When analyzed, fast charging was energy efficient (88%), showing results above the United States Advanced Battery Consortium (USABC) goals throughout cycling. Most importantly, when compared to standard cycling, fast charging did not introduce further aging. This is indeed a solid indicator of the convenience of the applicability of the fast charging protocol on the selected cell technology. We conclude that with a proper selection of cell chemistry and architecture, coupled with the design of an efficient multistage fast charging protocol, it is possible to achieve fast, safe charges throughout the cell's cycle life.

To analyze battery performance, we conducted a comparison study of the tested cells performance, versus the long term USABC goals. These goals are oriented towards EV applications, and helped us to evaluate the cell's end-of-life for each proposed cycling scheme, energy and power degradation, etc. The results from continuous testing showed that the cells exhibited an overall good performance. The cells surpassed cycle life, fast charging, specific power and cycling efficiency long term goals. However, specific energy goal was only achieve in the mi-term USABC goal. Indeed, the specific energy goal still remains

very challenging for LIB technologies in general. Hence, the reduction of weight is a major objective to be improved in commercial LIBs for electric vehicle (EV) applications.

A study of calendar aging was carried out for 8 cells under several aging stages and SOC storage conditions. The results showed that aged cells (i.e. less capacity retention and more cycles-life), were more affected by calendar storage. Under storage, the cells showed capacity loss caused by LLI, showing no evidences of LAM. Hence, for second-life LIB applications, it is recommended that the storage duration is minimized to reduce capacity fade.

Finally, the analyses carried out in this chapter provide a first approach to decipher the main degradation modes that affected the tested cells. Also, the applicability of using *in situ* techniques is verified here. Even though the aging analyses obtained in this chapter are a remarkable achievement, in this thesis we aim to further analyze the details of the degradation modes ongoing on the tested cells from a qualitative and quantitative perspective. These analyses are provided next, in Chapter **7**.

This page intentionally left blank

7. Lithium iron phosphate battery performance and degradation: a mechanistic analysis via diagnosis and prognosis

To effectively manage and control a battery system, battery performance and aging mechanisms have to be evaluated. The identification and further analyses of the aging mechanisms in real life lithium ion battery (LIB) systems through *in situ* techniques is the fundamental objective of this thesis work because of its importance: these findings allow efficient, reliable and safe operation of LIB systems. In the same way, battery prognosis is a powerful tool to effectively manage battery systems, aiming to provide accurate prediction of battery performance, aging evolution and life estimation. Hence, in this chapter we present the results and analyses of the mechanistic approach via diagnosis, carried out on the cells tested under standard, fast charge and dynamic stress cycling. This chapter also includes a prognosis approach particularized for the fast charge cycling scheme, due to its relevance in this work.

The results in Chapter **6** showed the long-term cycle aging evolution of the tested cells, under the proposed cycling conditions. There, we analyzed the performance results and the aging modes ongoing on the cells. Overall, all indications suggested that the following degradation modes were acting on the tested cells: loss of lithium inventory (LLI) and loss of active material on the negative electrode (LAM_{NE}). In addition, clear symptoms of Li plating were observed on the cell tested under dynamic stress cycling. Even if these findings are relevant, here we aim to the improve battery aging identification via diagnosis and prognosis mechanistic analyses.

Despite the recent understanding on LIB aging mechanisms, online diagnosis of the aging effect in a battery system remains lacking. Furthermore, a detailed study of the degradation modes ongoing on the proposed cycling schemes is relevant. Indeed, the detailed disclosure of fast charging degradation and the study of Li plating through *in situ,* online techniques could be quite enlightening for the development of diagnosis and prognosis models to study the performance and useful service life of LIBs.

With this aims in mind, in this chapter we provide a broad analysis to decipher, both qualitatively and quantitatively the aging modes ongoing on the tested cells. We combine incremental capacity (IC) and peak area (PA) analyses with mechanistic model simulations (*'Alawa* toolbox simulations with harvested half-cell data) to quantify the degradation modes on the tested cells. To attain the demanding aims of this chapter, here we develop original approaches, which are required, for example, to build the mechanistic model and attain realistic, high accuracy simulations, or to decipher the complex nature and evolution of Li plating.

7.1. Full cell reconstruction using '*Alawa* toolbox

To further decipher degradation modes of the tested cells from a detailed qualitative and quantitative perspective, *'Alawa* simulations are carried out. In order to lunch the simulations, it is first required to build the simulated cell mechanistic model. This model is to behave as close as possible from the experimental cells to achieve the best accuracy in the analysis of the degradation modes. However, the procedure to build the model is not straightforward. Hence, in this section we present an innovative approach to reconstruct the model with accuracy. The approach is based on the IC and PA analyses of the results derived from the Swagelok half-cell disassembling process, coupled with IC analyses from the simulated model. The objective is to build a model that successfully resembles the commercial GIC||LFP tested cells. Consequently, the results obtained from the aging simulations reflect the experimental ones with accuracy.

7.1.1. Loading ratio (LR) and offset (OFS) estimation

The first step of the simulation process is to virtually reconstruct the cell behavior as close as possible to the tested ones. According to the *'Alawa* model [31], the reconstruction of the cell behavior of a battery is accomplished by composing the half-cell characteristics of the PE and NE and adjusting two parameters: the loading ration (LR) and the initial offset (OFS). As commented in Chapter **2** (see **2.2.5**), the LR is defined by the ratio of the capacity in the NE (Q_{NE}) over the capacity in the PE (Q_{PE}), i.e. LR = Q_{NE}/Q_{PE}, whereas the initial OFS is defined by the electrode slippage. These parameters are actually coupled and can be expressed as LR = f (OFS) [30]. We shall recall from Chapter **2**, that the initial OFS is determined by the SEI formation process as a result of irreversible capacity loss in the first few cycles on the electrolyte/electrode interface via side reactions. The reconstruction of the cell consists in feeding into the *'Alawa* toolbox the obtained voltage vs. capacity curves of the Q_{NE} and Q_{PE}, and the cell constructive parameters (LR, OFS).

The accuracy of the *'Alawa* simulations is directly related to the accuracy of the cell construction parameters (i.e. Q_{PE}, Q_{NE}, LR and OFS). Unfortunately, these parameters cannot be directly measured on a commercial cell. Thus, a new strategy is proposed here to resolve this issue. Using direct and indirect electrochemical measurements, GIC intercalation process fundamentals and IC analyses, it is possible to calculate the cell constructive parameters.

To calculate the cell constructive parameters, an estimation of LR = f (OFS) can be yield by evaluating the Q_{NE} and the total full cell capacity Q_{FC}. If the NE is limiting in discharge, we can write:

$$Q_{\mathrm{PE}} = Q_{\mathrm{FC}} + OFS * Q_{\mathrm{PE}} = \frac{Q_{\mathrm{FC}}}{(1 - OFS)} \tag{7.1}$$

since LR = Q_{NE}/Q_{PE}, we can now rewrite Eq. (7.2) to obtain:

$$LR = \frac{(1 - OFS)Q_{\mathrm{NE}}}{Q_{\mathrm{FC}}} \tag{7.2}$$

where OFS is expressed as a percentage of Q_{PE}. The results should give only one possible LR and OFS couple. An example of the OFS and cell construction parameters is shown in **Fig. 7.1**. To resolve Eq. (7.2), Q_{FC} and Q_{NE} have to be measured. In addition, a realistic LR can be obtained through a series of iteration values for OFS.

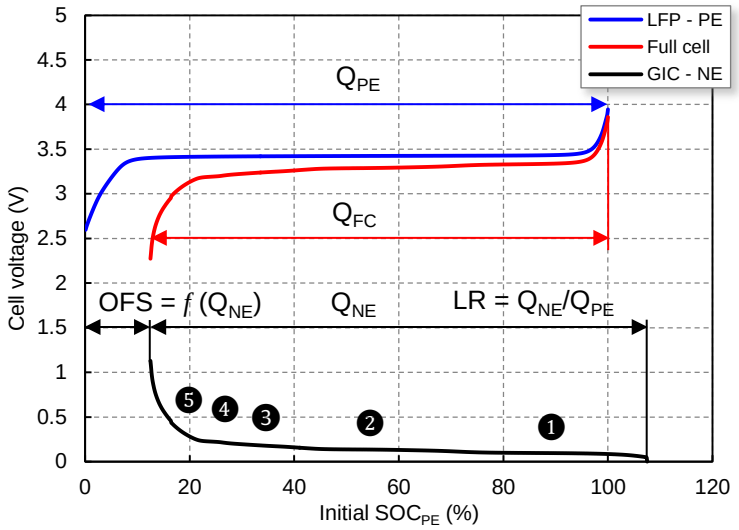

Fig. 7.1. Simulation at C/25 of the GIC||LFP cell with the harvested electrodes, as a function of SOC_{PE} (%), with the formation of the initial offset set to OFS = 12.5% and LR = 0.95.

To estimate LR = *f* (OFS), two approaches can be used; in the first case it can be derived from full cell data and in the second case from the Swagelok half-cell data. Due to its relevance, we shall discuss both approaches to unveil further details.

To estimate the initial LR = *f* (OFS) from the commercial cells, full cell capacity (Q_{NE}) at C/25 of the experimental cells can be measured when fresh (i.e. 2.300 Ah). However, Q_{NE} cannot be measured to its full extent, because the NE is the limiting electrode during discharge, and PE is the limiting electrode during charge on a fresh cell (if no Li-plating is observed). Still, a theoretical approximation could be used to indirectly measure Q_{NE}: the work from Dahn *et al.* [26] showed that in pure graphite materials, plateaus ❷-❺ corresponds to the phase transformations from LiC_{12} to C; therefore, $Q_{❷-❺}$ should account for half of Q_{NE}, i.e. $Q_{NE} = 2*Q_{❷-❺}$. Since $Q_{❷-❺}$ can be directly measured to its full extent in a full cell (see **Fig. 7.1**), a good estimation of Q_{NE} could be yield. Hence, from commercial cells, LR = *f* (OFS) can be calculated with certain confidence. However, this method is only accurate if $Q_{NE} = 2*Q_{❷-❺}$. In fact, the capacity composition ($Q_{NE} = 2Q_{❷-❺}$) is to be found primarily in pure graphitic materials [26], [187]. Nevertheless, graphite compounds usually found in commercial cells may have different plateau composition ranges depending on the choice of carbon materials [188]. This is attributed to several factors, including graphitic structural order, degree of crystalline orientation, morphology, textural properties, or the use of different binders, to name a few [22], [121], [188]. In other words, even if a good approximation of LR = *f* (OFS) can be obtained from full cell data, the best results are obtained when Q_{NE} is directly measured, i.e. from the Swagelok half-cell experiments.

To estimate LR = *f* (OFS) from half-cell experiments, the composition range associated with plateaus ❶ and ❷-❺ of the Swagelok cell has to be measured. Since the amount of active material in the Swagelok cell accounts for that found only on 0.71 cm^2, a proper capacity escalating in percentage was performed. This process facilitates the comparison of the full cell experimental data with the Swagelok half-cell data. Since half-cell measurements are carried out on GIC vs. Li^+/Li, to properly compare the results with the C/25 discharge process in full cell, the half-cell is charged. To measure the capacity composition of the GIC at C/25, we calculate the IC curves of the GIC vs. Li^+/Li to measure the PA distribution (see **Fig. 7.2**a-b). The results showed $Q_{❶}$ = 39% and $Q_{❷-❺}$ = 61%. Since $Q_{❷-❺}$ can be directly measured in the full cell (1.54 ±0.01 Ah), it therefore corresponds to 61% of the total Q_{NE}. With the obtained GIC capacity proportions and $Q_{❷-❺}$, the capacity $Q_{❶}$ = 0.98 ±0.01 Ah can be calculated. Therefore, the total capacity on the NE, derived from direct half-cell measurements is $Q_{NE} = Q_{❶} + Q_{❷-❺}$ = 2.52 ±0.02 Ah.

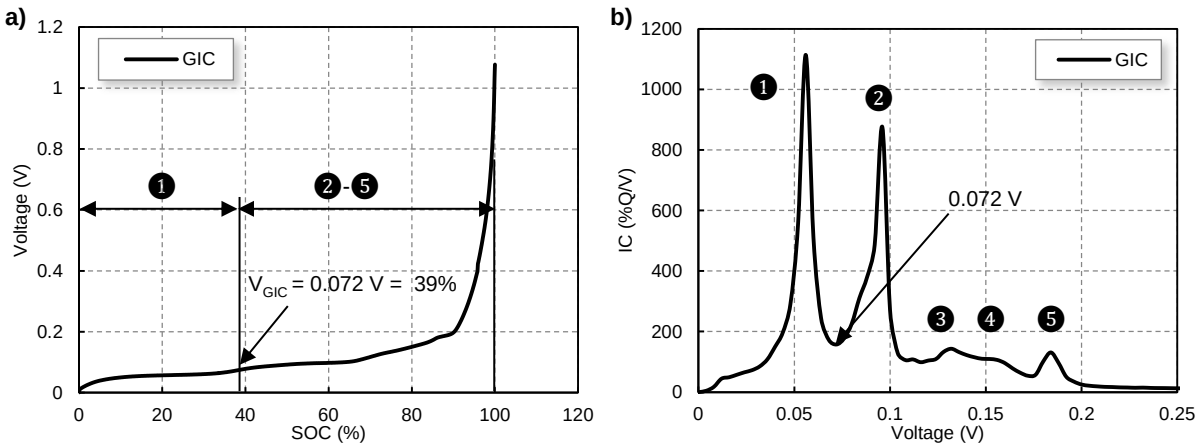

Fig. 7.2. a) GIC vs. Li^+/Li delithiation process of the harvested half-cell and b) its corresponding IC curve.

At this point, since Q_{NE} (2.52 ±0.02 Ah) and Q_{FC} (2.300 Ah) were measured, it is possible to obtain the relation LR = *f* (OFS) from Eq. (7.2). This is done through a series of realistic iteration values for LR and OFS, as shown in **Fig. 7.3**. The dashed lines indicate the minor tolerance errors in the LR = *f* (OFS) calculations derived from the half-cell measurements and calculations.

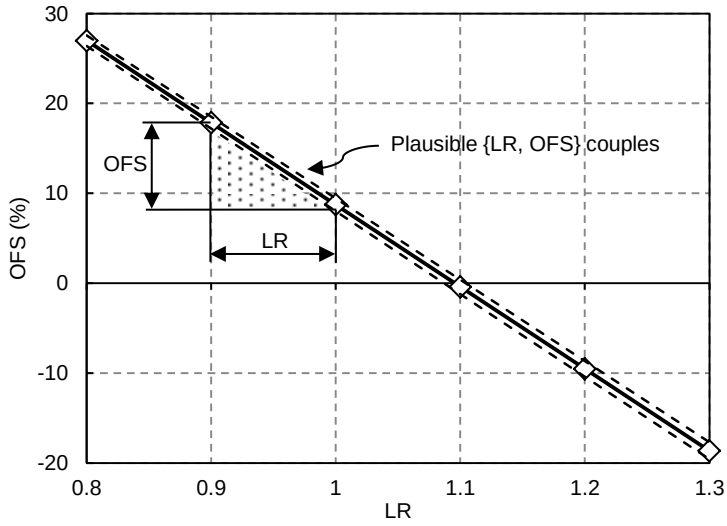

Fig. 7.3. OFS vs. LR relation of the test cells derived from the half-cell data.

As shown in **Fig. 7.3**, there are numerous {LR, OFS} couples that could match the experimental full-cell data. However, only one {LR, OFS} couple is the best match. To yield a first estimation, we can refer to other works on same cell technology, which, through different post-mortem techniques calculated the initial capacity loss on the NE through the SEI formation (i.e. OFS). Indeed, it is common to find values within the 10-15% range [30], [32], [76]. A first estimation of the plausible {LR, OFS} couples is shown in **Fig. 7.3** in the dotted area, resulting in values of LR between 0.9 and 1. However, to complete the simulation model, we still have to find the particular {LR, OFS} couple that matches the experimental cells. To achieve this, it is required to compare the simulation model with the experimental cell results. The highest accuracy is reached through IC analysis.

7.1.2. Full cell reconstruction trough incremental capacity analysis

To complete the validation of the simulation model, various {LR, OFS} couples derived from the Eq. (7.2) are used to obtain the simulated full-cell curve. To compare the simulated full-cell with the experimental cells, the corresponding IC curves derived from the voltage vs. capacity curves are

generated. Due to the higher sensitivity of the signature revealed by the IC peaks than those of the voltage vs. capacity ones, the IC analysis provides more information to validate the simulation results.

Fig. 7.4 compares the C/25 discharge IC curves from the experimental data (continuous red line) when fresh, and the simulated curves at various combinations of {LR, OFS} couples, derived from Eq. (7.2). The height and onset voltages between the experimental and the simulated IC curves agree well from peak ❶ to peak ❹. Only a small discrepancy at the inflection point between peaks ❶ and ❷ was observed, which was considered negligible for the purpose of this analysis. However, discrepancies between the simulated and the experimental IC curves are noticed in peak ❺. Indeed, the differences in peak ❺ help to identify the suitable {LR, OFS} couple to validate the model.

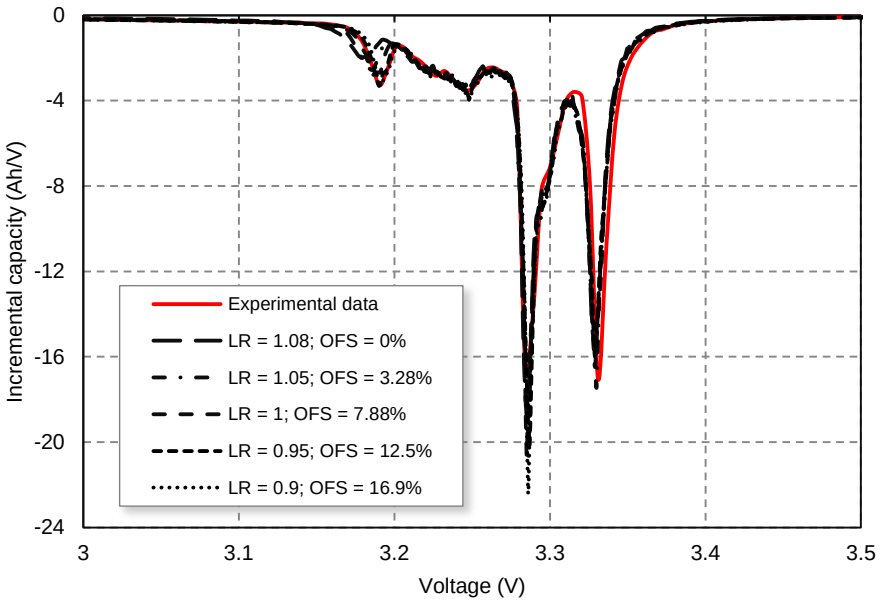

Fig. 7.4. Comparison of IC curves at C/25 for experimental data (solid line) and simulated data with various LR = *f* (OFS) relations (dashed lines).

In a typical GIC||LFP cell, peak ❺ is formed by the convolution of the LFP reaction with GIC in its phase transformation ❺, which corresponds to the graphite staging phenomena from $Li_{0.04}C_6$ to C. Depending on the LR and OFS values, the PE can be convoluted with graphite staging ❺ under two possible scenarios: when the PE is in the $FePO_4$ – $LiFePO_4$ phase transformation (i.e. the voltage plateau) or in the formation of the Li_yFePO_4 solid solution (i.e. the curve-shaped portion on the discharge curve). As a result, the shape of peak ❺ would be sharper when the convolution occurs in the phase transformation (i.e. large OFS values), or broader if it is in the solid solution region (i.e. smaller OFS values). This fact is shown in **Fig. 7.5**, where peak ❺ from **Fig. 7.4** was zoomed in. As observed, the intensity and shape of peak ❺ has the best match with LR = 0.95 and a corresponding value of OFS = 12.5%. Indeed, peak ❺ appears to be too broad for the {1, 7.88} couple and too sharp for the {0.9, 16.9} couple.

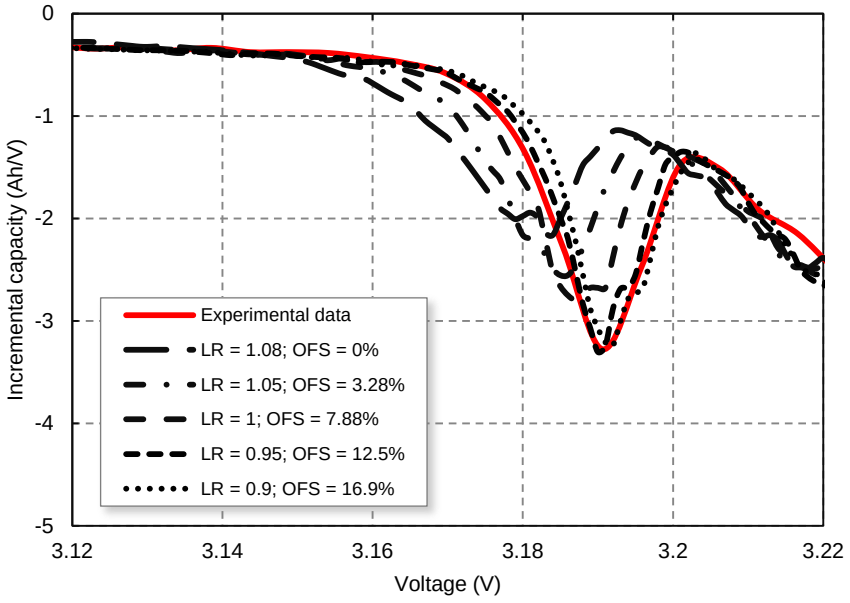

Fig. 7.5. Comparison of Peak ❺ zoomed from the IC curves at C/25 for experimental data (solid line) and simulated data with various LR = *f* (OFS) relations (dashed lines).

7.1.3. Full cell reconstruction using *'Alawa* toolbox: discussion

The cell constructive parameters required to carry out the simulations were obtained by using a new approach to reconstruct the cell behavior as close as possible to the experimental ones. By comparisons of both experimental and simulated curves, the results showed that LR = 0.95 and OFS = 12.5% match the experimental cell data. Moreover, through half-cell analysis, we calculated LR = Q_{NE}/Q_{PE} = 0.95. The simulated full cell (Q_{FC}) with these obtained values was intentionally shown in **Fig. 7.1**. On account of the reproducibility and minor cell-to-cell variations of the experimental cells (as exposed on Chapter **6**), the obtained mechanistic model with LR = 0.95 and OFS = 12.5% matches nicely with the experimental values. Hence, these parameters are to be used in the simulations for all the cells to decipher the aging modes.

Similarly, it is significant to find out LR<1 for a commercial HP GIC||LFP cell, when other studies often suggest values within 1.2 to 1.45 [189] in HP format cells. However, we shall state that our calculations of the LR are performed after SEI formation, whereas in general, the LR is given as a cell constructive parameter (i.e. before cell assembling). Thus, the initial SEI formation also produces a certain amount of graphite loss (LAM_{NE}) in the first formation cycles [31], [79], [161], [190] that reduces the initial LR. Although not directly stated on other works, the calculated {LR, OFS} cell constructive parameters were found to be in accordance with the half-cell data (same cell model), provided courtesy of [61], and comparable to other post-mortem analyses on high power GIC||LFP cells [76], [93], [174]. Additionally, post-mortem studies on GIC||LFP cells have reported similar findings with regards to composition proportions of the NE [61], [68], [76] as the ones presented here.

We showed the significant advantages of the new strategy carried out here to yield an accurate LR = *f*(OFS) relation. Swagelok half-cell measurements on the harvested electrodes from the same batch-tested cells, coupled with the proposed full cell reconstruction including IC and PA analyses, made possible to accurately identify the total Q_{NE} and, as a result of this, to obtain an accurate LR = *f*(OFS) relation. This validates the requirement of cell disassembling on commercial cells when fresh (as described in Chapter **5**) to achieve accurate simulation results. Finally, with the use of *'Alawa*, and its flexibility of comprising half-cell data into a full cell, we were able to perform a proper cell adjustment, avoiding complicated analyses and possible artifacts inherent on the cell disassembling processes. In addition, on account of the minor cell-to-cell variations, only one cell was required for the disassembling

process, whereas the derived results are valid for subsequent simulations on this type of cell model. This has great advantages, because labor-intensive activities and resources are substantially reduced. It must be pointed out that this new strategy provides a level of accuracy and quickness which is unlikely to be achieved by traditional post-mortem analysis.

7.2. Standard cycling: mechanistic analysis of aging

This section presents the analysis of the aging modes affecting the cell tested under standard cycling. The *in situ,* nondestructive techniques used to decipher the aging modes are the mechanistic *'Alawa* toolbox, coupled with the IC and PA analyses. We start with single-mode and multiple-mode simulations to decipher the qualitative aging modes. Subsequently, additional simulations verified versus experimental data lead us to obtain the quantitative results. Several representations of cell degradation are provided to get insight into details of the effects that the aging modes cause on the cell electrodes. The analyses and simulations are performed at C/25 to be compared with the experimental results obtained from the RPTs, also at C/25. This ensures a maximum level of accuracy to decipher the aging modes undergoing on a cell. The designed strategy provides the detailed results of the aging modes from a qualitative (i.e. the identification of the aging modes) and quantitative (i.e. the degradation per cycle of the aging modes) perspective.

We shall point out that the procedures of aging analyses carried out in this section are also shared with the cells tested under fast charge and dynamic stress cycling. Here is provided a step-by-step analysis that is to be used on the analyses of the tested cells; for simplicity, only this section provides the description of the procedures, avoiding repetitive analyses.

The last section presents the concluding remarks, with a discussion of the proposed techniques and the obtained results. This enhances the understanding of the implications that the aging modes have on the tested cells, and demonstrates the potential of the *in situ* techniques used to decipher cell degradation.

7.2.1. Standard cycling: analysis of the degradation mechanisms

A first approach to find out which particular degradation mechanism was undergoing on the cell tested under standard cycling consisted in reproducing the experimental results through '*Alawa* simulations. The simulation analyses are divided into two subsections: the first one is to simulate single-mode degradation modes, and the second one simulates multiple-mode degradation mechanisms.

Although from the IC and PA analyses carried out in Chapter **6** we suggested that aging was caused by two aging modes simultaneously ongoing on the cell (i.e. LLI + LAM_{NE}), it is important to corroborate this suggestion by the mechanistic simulations. Subsequently, in the second subsection we carry out the simulations with multiple degradation modes. The results of the simulations with the proposed aging modes are verified with the PA results of the experimental data. Hence, the degradation modes are obtained both qualitatively (aging modes identification) and quantitatively (through PA verification).

Single-mode degradation mechanisms simulation

The first step consisted in simulating each degradation mechanism individually, to match the experimental cell degradation. The results are shown in **Fig. 7.6**, where the capacity fade of the experimental data (at C/25) and the individual simulated aging scenarios are compared, all matching the final capacity loss. From the numerical *'Alawa* outputs, a degradation separated into two stages (i.e. stage 1 and stage 2) of 0.0033% + 0.0018% per cycle (i.e. cyc^{-1}) of LLI, 0.0032% + 0.002% cyc^{-1} of LAM_{liNE}, or 0.0032% + 0.0018% cyc^{-1} of LAM_{liPE} match with the 18% of total capacity loss for that cycling. In contrast, the aging modes LAM_{dePE} and LAM_{deNE} show an initial steady stage that does not cause capacity fade. As commented, although these degradation modes cause degradation on the electrodes

(causing loss of active material) they remain "silent" in terms of full cell capacity loss. Thereafter (~1800 cycles), both modes enter an abrupt degradation stage to reach the final capacity point. Since no ORI or kinetic degradation was found in the experimental results, these degradation modes were not simulated.

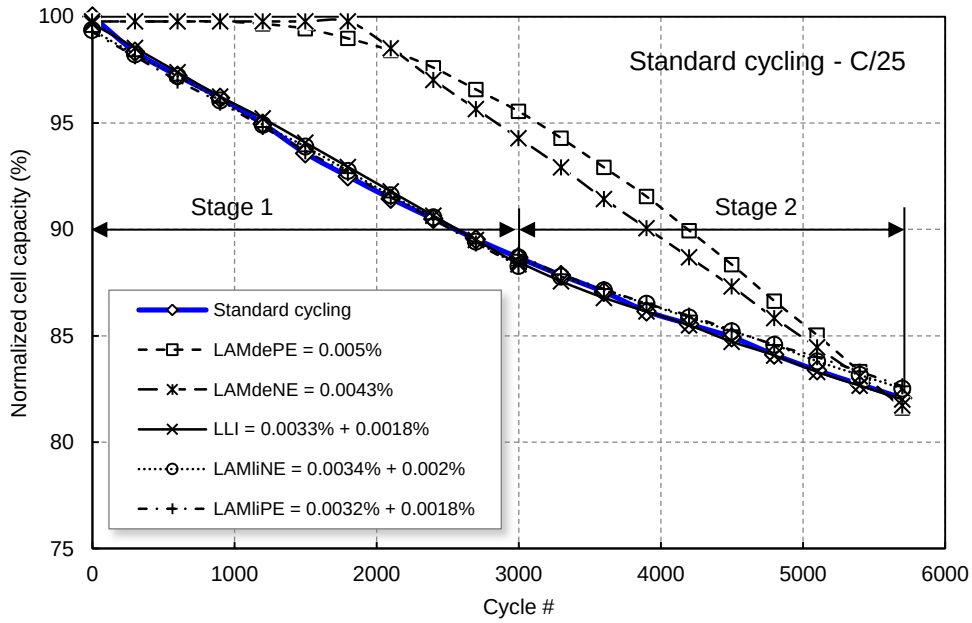

Fig. 7.6. Capacity fading trend predictions for standard cycling at C/25 according to '*Alawa* model simulations. The two numerical terms on LLI, LAM_{liNE} and LAM_{liPE} indicate the degradation values on stage 1 and stage 2, respectively.

From the simulations shown in **Fig. 7.6**, degradation modes LAM_{dePE} and LAM_{deNE} involve a material loss that does not cause initial capacity loss on the full cell signature. For this reason, the degradation trend does not match the experimental results. This fact excludes them from being the main degradation mode contributing to the capacity loss. On the other hand, LAM_{liPE}, LAM_{liNE} and LLI show a linear degradation process, which matches the trend of experimental capacity fade.

To decipher if one of the aging modes (LAM_{liPE}, LAM_{liNE} and LLI) acting alone is the actual degradation mechanism, the PA results derived from the IC simulation curves are analyzed. The results shown in **Fig. 7.7** compare the PA of the experimental cell and that of the simulated results. As observed, none of the aging modes match the experimental results. Therefore, the suggestions obtained from Chapter **6** are confirmed: more than one aging mode is acting simultaneously and causing degradation on the tested cell.

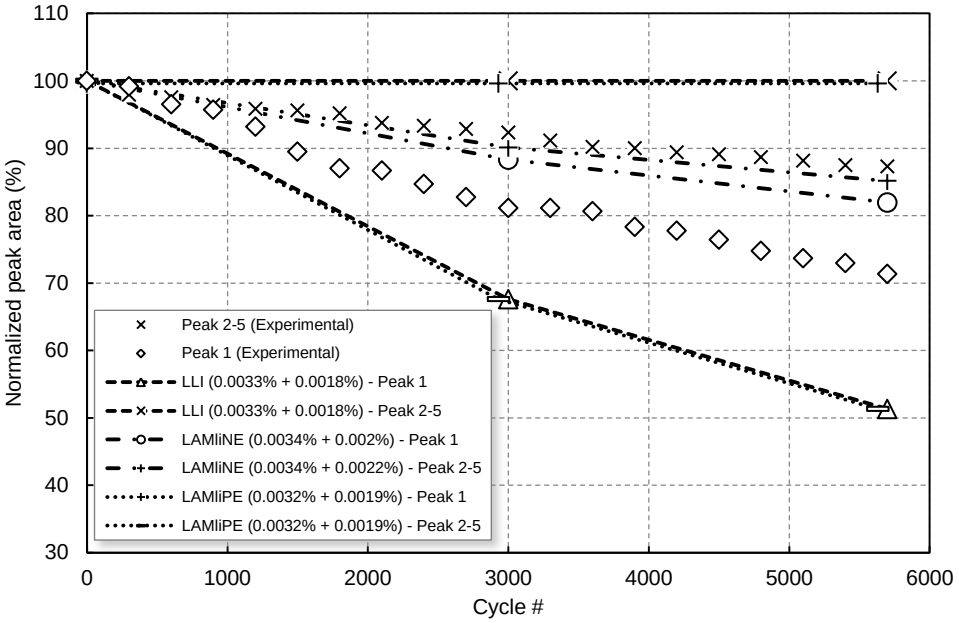

Fig. 7.7. Normalized peak area trends for peak ❶ and peak ❷-❺ of the experimental and the simulated results particularized for LLI, LAM_{liNE} and LAM_{liPE}. The terms in parenthesis indicate the degradation values on stage 1 and stage 2, respectively.

Multiple-mode degradation mechanisms simulation

To resolve the fact that more than one degradation mode is taking place on the tested cell, we shall first recapitulate the plausible aging modes affecting the cell tested under standard cycling. From the IC and PA analyses derived from Chapter **6**, LLI was suggested to be the main source of aging, mostly attributed to the ongoing formation of the SEI layer on the graphite [7], [24], [32], [36], [55], [59], [63], [76], [183]. Moreover, degradation on the PE was discarded, as suggested by the *post mortem* analyses in the literature [59], [61], [68], [76], [93], [174]. This is because of the high stability and long-cycle life of the LFP materials. Hence, LLI + LAMNE should be acting simultaneously on the tested cell.

To decipher which aging mode on the NE (i.e. LAM_{deNE} or LAM_{liNE}) accompanies LLI, we can refer to **Fig. 7.8**, where peak ∫❶ and peak ∫❷-❺ are shown for the experimental and individual simulation of LLI at 0.0033% + 0.0018% cyc^{-1} for stage 1 and 2, respectively. As observed, LLI only causes degradation on peak ∫❶, leaving peak ∫❷-❺ unaltered. To match the experimental values, peak ∫❶ has to slow down its degradation rate, whereas peak ∫❷-❺ has to increase its degradation rate. From the aging modes on the NE, only LAM_{deNE} compensates this degradation. Indeed, LAM_{deNE} produces peak ∫❶ growth and peak ∫❷-❺ reduction, as observed by the arrows depicted in **Fig. 7.8**. The combination of LLI and LAM_{liNE} could reduce the area of peaks ∫❷-❺ as well, but it would induce to more capacity fade on peak ∫❶. All these arguments lead to the conclusion that LLI + LAM_{deNE} are the aging modes ongoing on the tested cell.

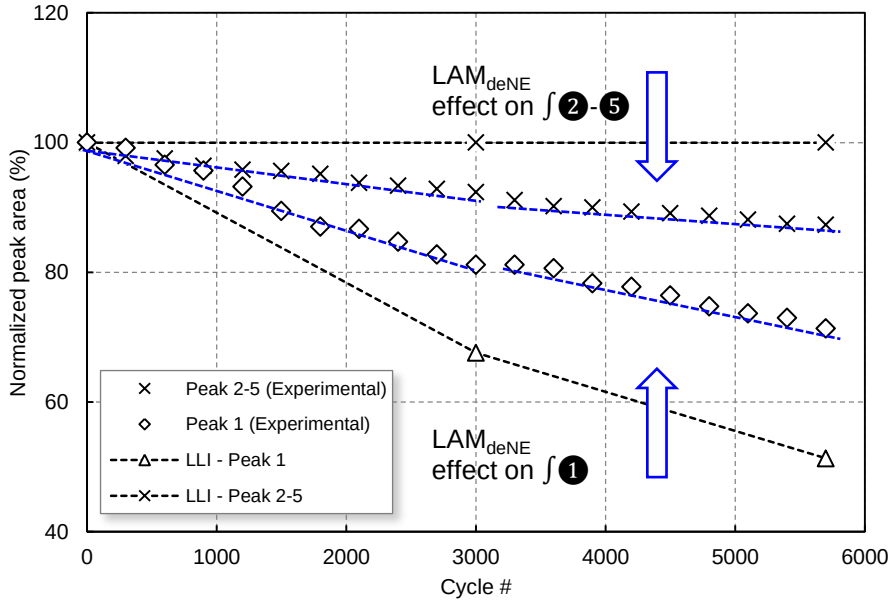

Fig. 7.8. Normalized peak area trends for peak ❶ and peak ❷-❺ of the experimental and the simulated results particularized for LLI at 0.0033% + 0.0018% cyc^{-1}.

The previous analyses identify LLI and LAM_{deNE} as the aging mechanisms undergoing on the tested cell, from a qualitative perspective. However, these analyses did not quantify to what extent each mechanism individually contributes to the full cell degradation. This complicated issue can be resolved by performing further simulations with the *'Alawa* toolbox.

The simulations were carried out with the following settings: both NE and PE were the actual electrodes harvested from the same model, same batch cell as the experimental ones. The cell constructive parameters required to reproduce the experimental cells were previously obtained in the full cell reconstruction section; LR = 0.95 and OFS = 12.5%. To be compared with the experimental data, the simulations were performed at C/25 discharge rate. Finally, the degradation modes loaded in the *'Alawa* toolbox were LLI and LAM_{deNE} and the results of the simulations were validated against the experimental peak area results.

The simulations were split into two stages, to follow the experimental degradation trends. The results for stage 1 revealed that a combination of 0.0033% cyc^{-1} of LLI and 0.0023% cyc^{-1} of LAM_{deNE} match nicely with the experimental data, as observed in **Fig. 7.9**a-b (blue dashed lines). Several combinations of LAM_{deNE} were performed, but they fail to match with the experimental values (see **Fig. 7.9**a-b, black discontinuous lines). To simulate stage 2, the partial cell constructive values after the first stage (i.e. $LR_{Partial}$ = 0.86, $OFS_{Partial}$ = 22.4%), were feed into the *'Alawa* toolbox as the beginning point of simulation of stage 2 (i.e. cycle 3000 to 5700). The simulations were performed by approximately applying the reduction factor found on the experimental data for stage 1 to stage 2 (x1.7 for peak ∫❶ and x1.5 for ∫❷-❺). The results showed that a combination of 0.0018% cyc^{-1} of LLI and 0.0016% cyc^{-1} of LAM_{deNE} agree with the experimental data, as seen in **Fig. 7.9**c-d.

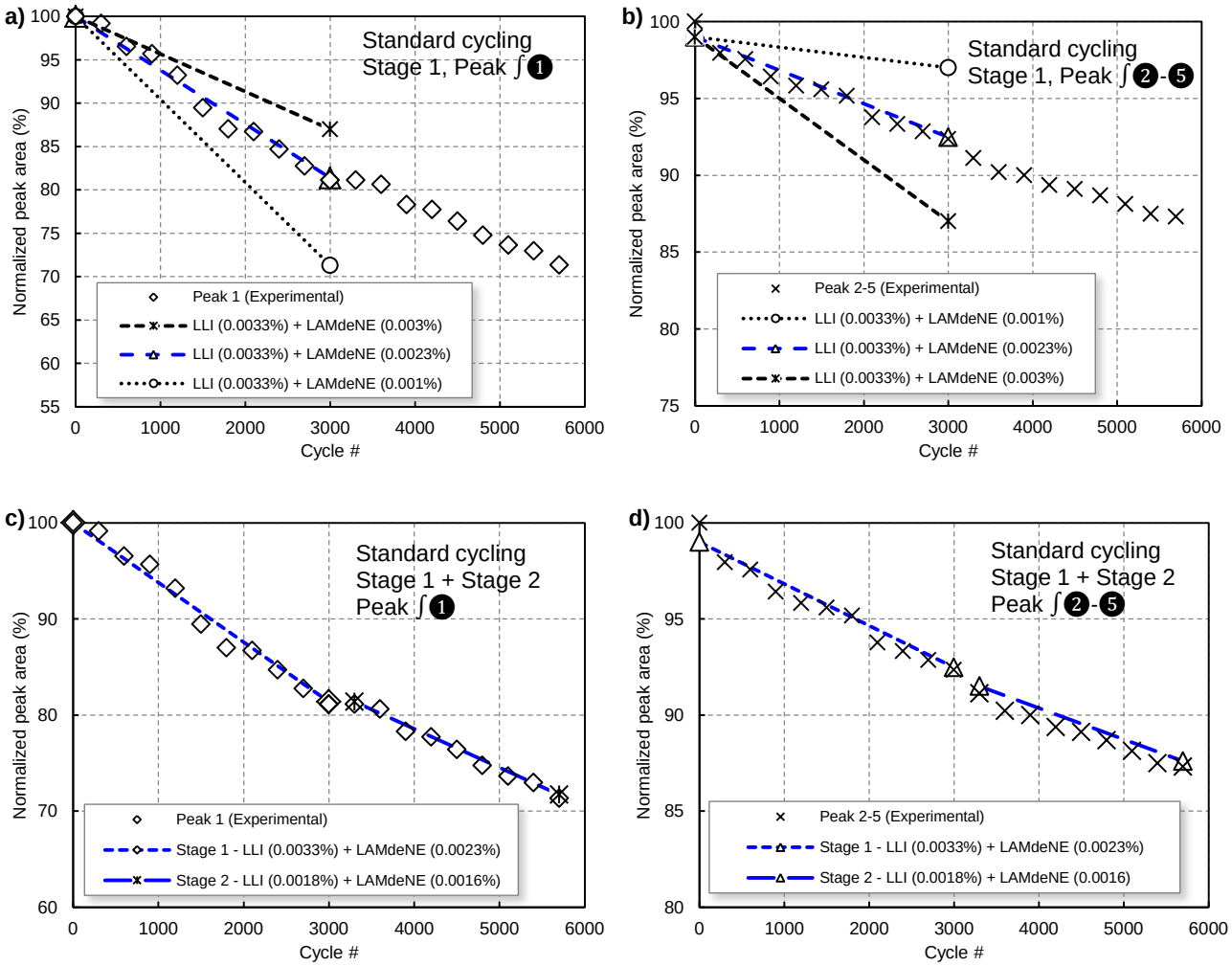

Fig. 7.9. a) Normalized peak area for peak ❶ and b) peaks ❷-❺ as a function of cycle number for stage 1. Same representation is adopted for stage 2 (c-d). The experimental data are in symbols, whereas the simulated results are dotted or dashed lines. The simulated results are exhibited for different combinations of LLI + LAM_{deNE} for both stages. The best matches between experimental and simulated results are shown in blue dashed lines.

The capacity degradation with cycling of the experimental and simulated results is compared in **Fig. 7.10**. As observed, the simulated aging modes (blue dashed lines) match nicely with the experimental data. The degradation modes ongoing on the cell tested under standard cycling are a combination of 0.0033% cyc^{-1} of LLI and 0.0023% cyc^{-1} of LAM_{deNE} for the first 3000 cycles and a combination of 0.0018% cyc^{-1} of LLI and 0.0016% cyc^{-1} of LAM_{deNE} from cycle 3000 to cycle 5700. Therefore, the aging modes were identified both qualitatively (LLI + LAM_{deNE}) and quantitatively (% cyc^{-1} value).

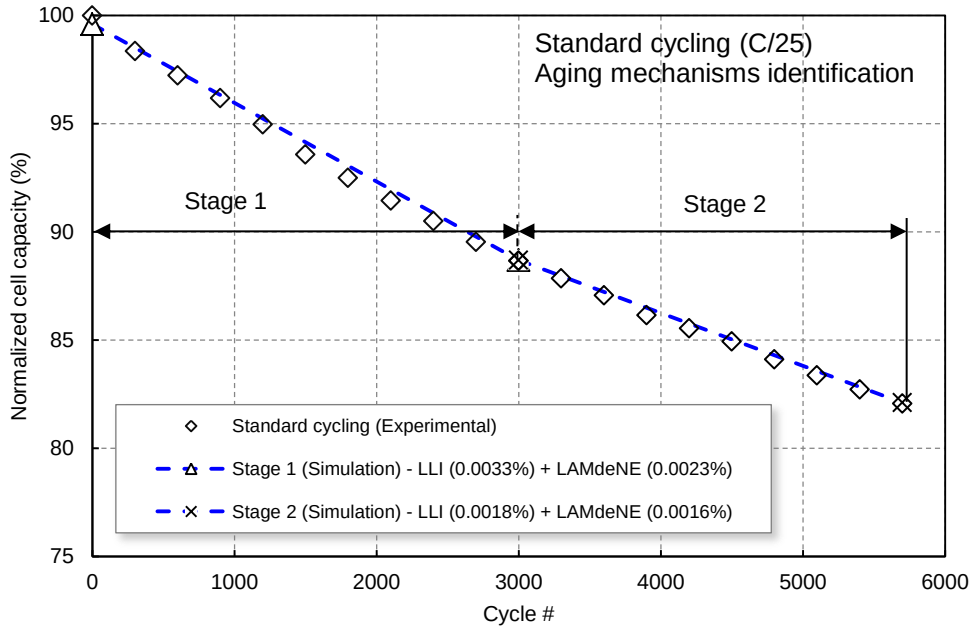

Fig. 7.10. Comparison of the normalized cell capacity evolution trends for the experimental standard cycling procedure (◊) and the obtained simulated degradation modes with LLI + LAM_{deNE} (dashed blue lines).

7.2.2. Standard cycling half-cell analysis

Another distinctive feature of *'Alawa* simulation is that reveals the effects that different degradation mechanisms cause on each individual electrode through cycle aging. Since the effects of LLI and LAM_{deNE} modify the LR, OFS and Q_{NE} of the full cell [31], a quantification of these parameters is carried out to provide a better understanding on how these degradation modes affect the electrodes. The results are depicted in **Fig. 7.11**, showing the evolution of the correspondence of the electrodes balance with aging, based on the degradation modes. The solid lines are the initial state of cycling (BOC), the dotted lines show the evolution at cycle 1500, 3000 and 4500 and the dashed lines show the final results at cycle 5700.

Depending on the degradation modes, the fading affects differently each electrode (PE or NE) and the corresponding full cell (FC). In this case, the actual state of the PE at the beginning and the end of cycling remains intact ($Q_{PE\ final} = Q_{PE\ initial}$). The NE is affected from both the LLI and LAM_{deNE}. The effects of LLI are translated into a constant slippage of the NE correspondence towards higher initial relative capacity. At a 0.0033% cyc^{-1} during the first 3000 cycles, the NE reaches a partial $OFS_{Partial}$ of 22.4%. From cycle 3000 to 5700, with LLI at 0.0016% cyc^{-1}, the final OFS_{Final} is 27.1%. In contrast, the effects of LAM_{deNE} are translated into a shrinkage of the NE curve commenced from the lithiated (LiC_6) stage and remaining constant at the delithiated (C_6) state [31]. At 0.0023% cyc^{-1} during the first 3000 cycles, the NE suffered a total reduction of its active material by 6.9%, whereas from cycle 3000 to 5700 the reduction was 4.3 %. The total AM reduction on the NE was 11.2%. Therefore, the combination of both modes of degradation, as LLI predominates, results in an overall slippage of the NE correspondence towards a higher relative capacity (see **Fig. 7.11**). The LR varied from 0.95 to 0.84, showing the effect of LAM_{deNE}.

Another interesting result observed in **Fig. 7.11** is how LAM_{deNE} affects a portion of the NE that falls outside the capacity range of the PE. As a result, for the calculated degradation rate, the LAM_{deNE} effects remain "silent" on the full cell signature, explaining why there is no discernible loss of capacity on the full cell. Hence, only by quantitatively tracking LAM_{deNE} was possible to decipher this hidden loss.

The numerical values of the capacities of the NE, PE and FC can be calculated from the obtained results. $Q_{NE\ initial}$ was calculated to be 2.52 Ah, whereas $Q_{PE\ initial} = Q_{PE\ final} = 2.65$ Ah. The final capacity of the NE can be calculated, since the total reduction was 11.5% (i.e. $Q_{NE\ final} = 2.21$ Ah). The final usable FC range was diminished by 18%, which agrees with the observed experimental capacity loss.

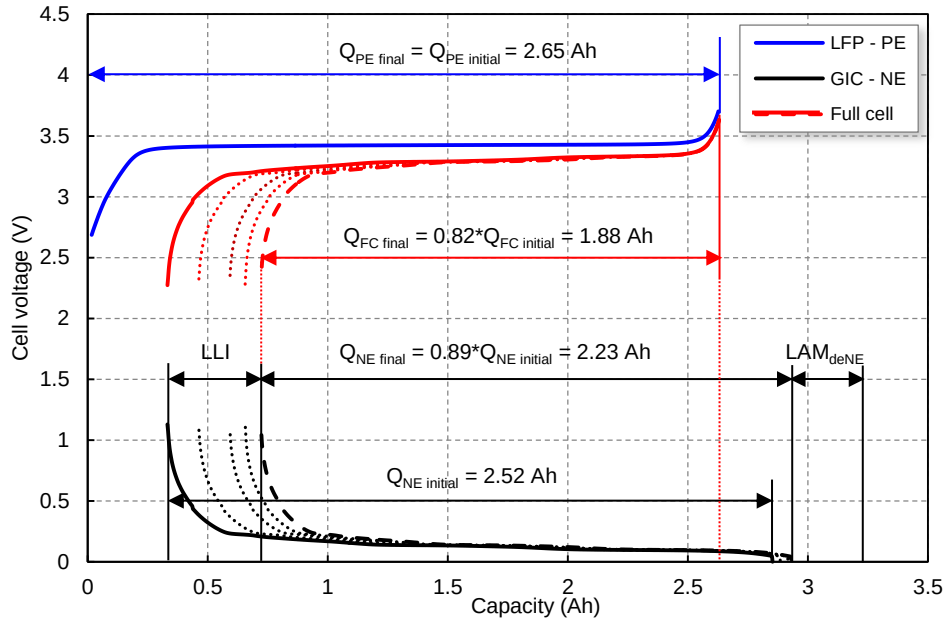

Fig. 7.11. Schematic representation of the GIC||LFP cell tested under standard cycling, showing the evolution with cycling of the simulated results for LLI at 0.0033% $cycle^{-1}$ and LAM_{deNE} of 0.0023% $cycle^{-1}$ (cycle 0 to 3000) and LLI at 0.0018% $cycle^{-1}$ and LAM_{deNE} of 0.0016% $cycle^{-1}$ (cycle 3000 to 5700).

As a final verification of the simulation vs. the experimental results, the cell voltage vs. capacity evolution with cycling is plotted in **Fig. 7.12**. The simulated results with the proposed degradation modes, again agree nicely with the experimental values.

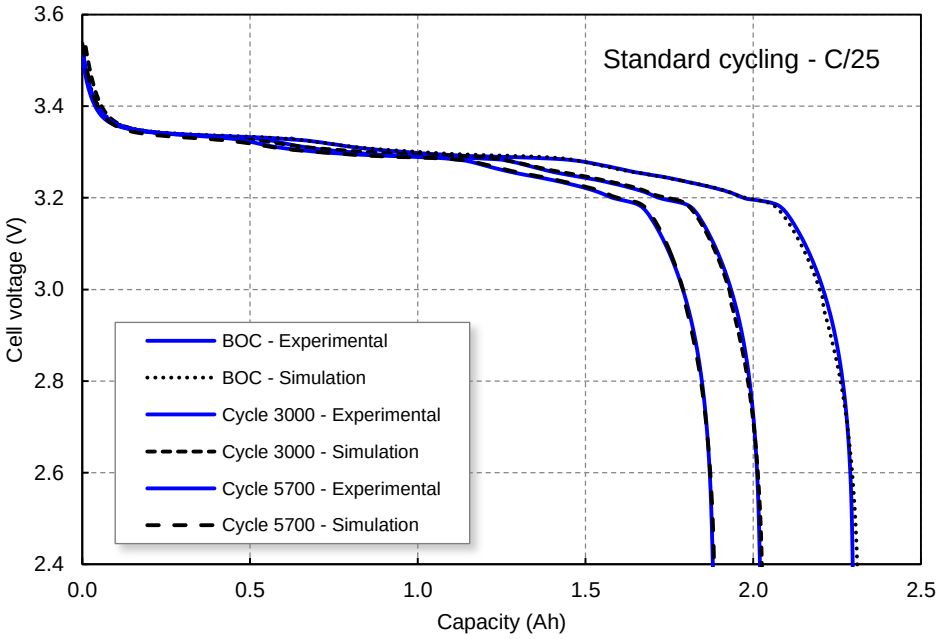

Fig. 7.12. Evolution with cycling of the voltage vs. capacity curves for the experimental and the simulated results.

7.2.3. Mechanistic analysis of aging under standard cycling: discussion

In this section, we deciphered the aging modes of the cell tested under standard cycling, both qualitatively (LLI + LAM_{deNE}) and quantitatively (% cyc^{-1} value). We used an approach based on *in-situ* nondestructive analyses and *'Alawa* simulations. The first step in this approach was to corroborate that multi-mode degradation mechanisms were undergoing. Although a solid approach was performed through previous IC and PA analyses, the simulations confirmed the suggestions previously obtained in Chapter **6**: LLI + LAM_{NE} were detected. Next, deciphering whether LAM_{liNE} or LAM_{deNE} were the actual modes that accompanied LLI was required. This was done through the comparison of the experimental peak ❶ and peak ❷-❺ evolution against the simulated results of LLI degradation. It was observed that only LAM_{deNE} compensated the PA signature to match the experimental values. As the aging modes were obtained (LLI+LAM_{deNE}), the next step was to decipher the quantitative values. This was done through *'Alawa* simulations. The simulated values were validated with the experimental peak area results, and also showed the evolution of the voltage vs. capacity curves of the experimental and simulated results. In conclusion, the cell tested under standard cycling was found to have the aging modes: LLI at 0.0033% $cycle^{-1}$ coupled with LAM_{deNE} of 0.0023% $cycle^{-1}$ (stage 1, cycle 0 to 3000) and LLI at 0.0018% $cycle^{-1}$ coupled with LAM_{deNE} of 0.0016% $cycle^{-1}$ (stage 2, cycle 3000 to 5700).

The qualitative and quantitative findings provided here are significant. The majority of the reports in the literature agree that LLI is usually found as a major aging mode [7], [24], [32], [36], [55], [59], [63], [76], [183]. Similarly, other works [30], [32], [59], [61], [68] reported LLI as the main source of aging, accompanied with LAM on the NE to a less extent, usually through post-mortem analyses [59], [61], [68]. However, through the *in-situ* analyses and *'Alawa* simulations carried out in this section, we were able to enhance the results from previous reports: here a qualitative distinction of the aging mode on the NE (i.e. LAM_{deNE}) was provided and the quantitative evolution of LLI and LAM_{deNE} (i.e. % cyc^{1} value) calculated.

The half-cell evolution of the NE, PE and FC is also a significant approach as reveals the effects that the different aging modes cause on the individual electrodes. Even if through post-mortem analyses it is possible to decipher the final state, here not only the evolution with cycling is provided, but also the evolution of the shifting and shrinking effects of the NE is deciphered. In addition, by calculating the initial LR and OFS values from the full cell reconstruction, it is possible to decipher the LR and OFS evolution with cycling. Hence, the actual capacity of the NE, PE and FC, escalated to Ah can be calculated. Indeed, the voltage vs. capacity curves of the simulated FC with the calculated aging modes matches nicely with the experimental one. This information cannot be drawn from conventional post-mortem analyses.

7.3. Fast charge cycling: mechanistic analysis of aging

This section presents the mechanistic analysis of the aging modes affecting the cell tested under fast charge cycling. To decipher the aging modes, here we use the same approach and *in situ* techniques as previously commented on the cell tested under standard charge. The results of the aging modes from a qualitative and quantitative perspective are provided.

As suggested from previous IC and PA analyses carried out in Chapter **6**, the cell under fast charge cycling presents similar aging patterns as the cell tested under standard cycling. Here we provide additional comparative analyses through a mechanistic perspective to provide a solid conclusion. Similarly, the analyses through a mechanistic perspective help us to enhance the understanding of the effects that fast charging cause on the individual electrodes. Finally, the concluding results validate the feasibility of the proposed fast charging scheme.

7.3.1. Fast charge cycling: analysis of the degradation mechanisms

The evolution of the normalized integral areas of peak ❶ and peak ❷-❺ as a function of cycle number is presented in **Fig. 7.13**. The experimental data at C/25 (diamond and square symbols) are compared with those predicted by *'Alawa* model (dashed red lines) for the aging modes based on LLI + LAM_{deNE}. The simulations were split into two stages, to follow the experimental degradation trends.

According to the simulations, the results shown that a degradation of LLI at 0.0033% cyc^{-1} + LAM_{deNE} at 0.0023% cyc^{-1} (stage 1, cycle 0 to 4500) and LLI at 0.002% cyc^{-1} + LAM_{deNE} at 0.0023% cyc^{-1} (stage 2, cycle 4500 to 5400) matched nicely with the test data. Notice that peak ❷-❺ was not affected by the 65-day calendar pause provoked at cycle 4500. Hence, the degradation rate of LAM_{deNE} remained constant throughout cycling. Similarly, we shall point out that the degradation rates found during the first 4500 cycles (i.e. 0.0033% cyc^{-1} + LAM_{deNE} at 0.0023% cyc^{-1}) for the cell tested under fast charging are the same as those found in the cell tested under standard charging during its first degradation stage (i.e. up to cycle 3000).

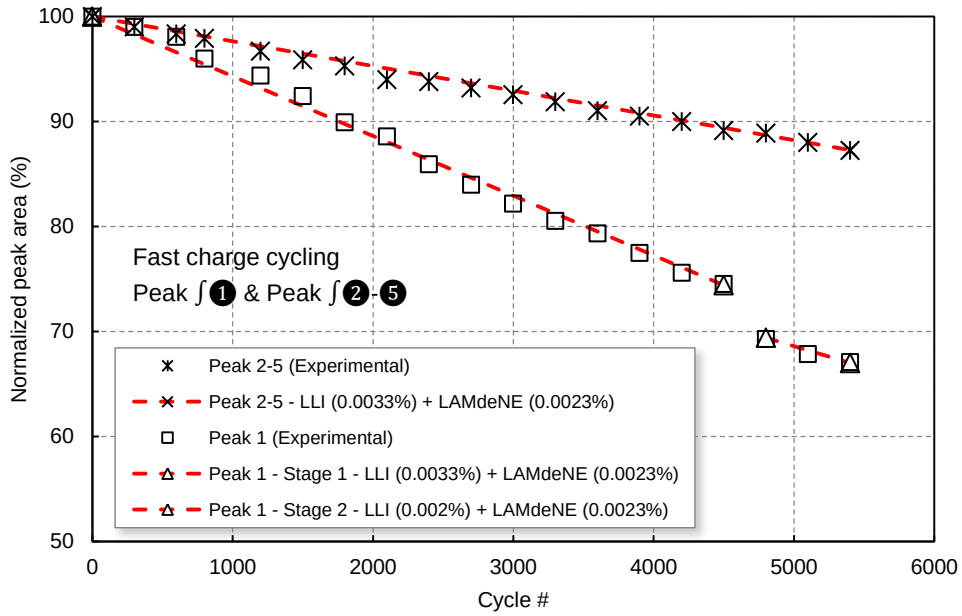

Fig. 7.13. (a) Normalized peak are for peak ❶ and (b) peaks ❷-❺ as a function of cycle number. The experimental data are in symbols, while the simulated results are red dashed lines. The simulated results are exhibited for the matching combination of LLI + LAM_{deNE}.

The evolution of the cell capacity with cycling for the experimental and the simulated data is compared in **Fig. 7.14**. As observed, the simulated aging modes (red dashed lines) match nicely with the experimental data (squared symbols). Hence, the aging modes of the cell cycled under fast charge were identified, both qualitatively (LLI + LAM_{deNE}) and quantitatively (% cyc^{-1} value).

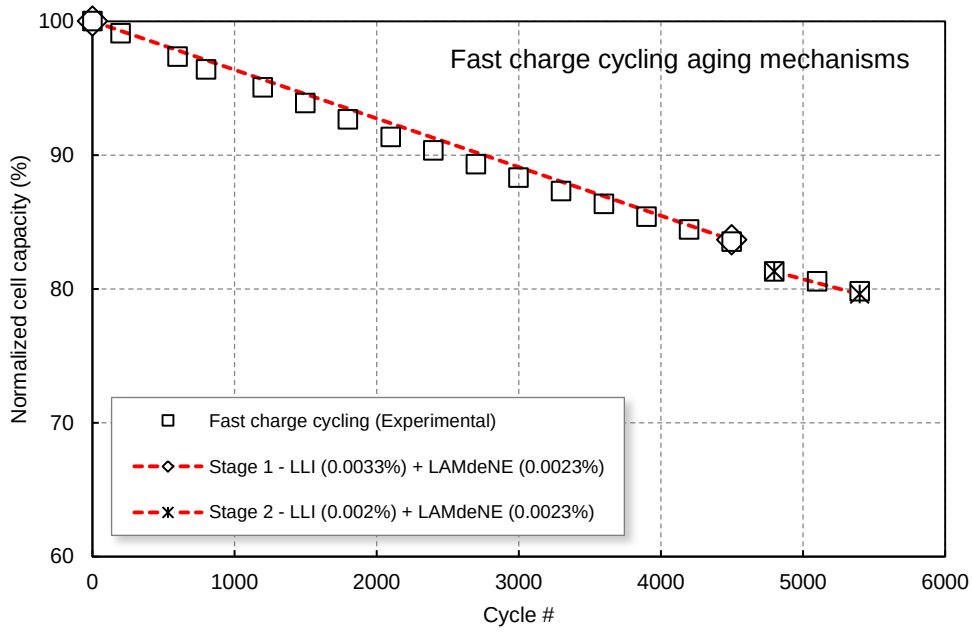

Fig. 7.14. Comparison of the normalized cell capacity evolution trends for the experimental fast charge cycling procedure (□) and the obtained simulated degradation modes with LLI + LAM_{deNE} (dashed red lines).

7.3.2. Fast charge cycling half-cell analysis

The evolution of the correspondence of the electrodes balance with aging is depicted in **Fig. 7.15**. The solid lines are the initial state of cycling (BOC), the dotted lines show the evolution at cycle 1500 and 3000, the dashed-dot lines shows cycle 4500, whereas the final result at cycle 5400 is shown with dashed lines.

The aging modes derived by the fast charge cycling on the tested cell were LLI and LAM_{deNE}. As commented, the effects of LLI are translated into a slippage of the NE: at LLI = 0.0033% cyc^{-1} during the first 4500 cycles, the NE reaches a partial $OFS_{Partial}$ of 27.3%. From cycle 4500 to 5400, with LLI reduced to 0.002% cyc^{-1}, the final OFS_{Final} is 30.3%. The effects of LAM_{deNE} are translated into shrinkage of the NE towards the delithiated state. With LAM_{deNE} at 0.0023% cyc^{-1} throughout cycling, the NE suffered a total reduction of its active material by 12.4%. As LLI predominates, this results in an overall slippage of the NE correspondence towards a higher relative capacity, as observed in **Fig. 7.15**. The LR varied from 0.95 to 0.83, showing the effect of LAM_{deNE}. From **Fig. 7.15** is also observed that the degradation rate of LAM_{deNE} only affects a portion of the NE that falls outside the capacity range of the PE. As a result, at the calculated degradation rates, the effects of LAM_{deNE} remain "silent" on the full cell capacity.

The numerical values of the capacities of the NE, PE and FC can be calculated from the obtained results. The $Q_{NE\ initial}$ was calculated to be 2.52 Ah. Since no degradation was estimated on the PE, $Q_{PE\ initial} = Q_{PE\ final}$ = 2.65 Ah. Similarly, the final capacity of the NE can be calculated from the LR reduction of 12.4% (i.e. $Q_{NE\ final}$ = 2.20 Ah). The final usable FC range was diminished by 20.1%, which agrees with the observed experimental capacity loss.

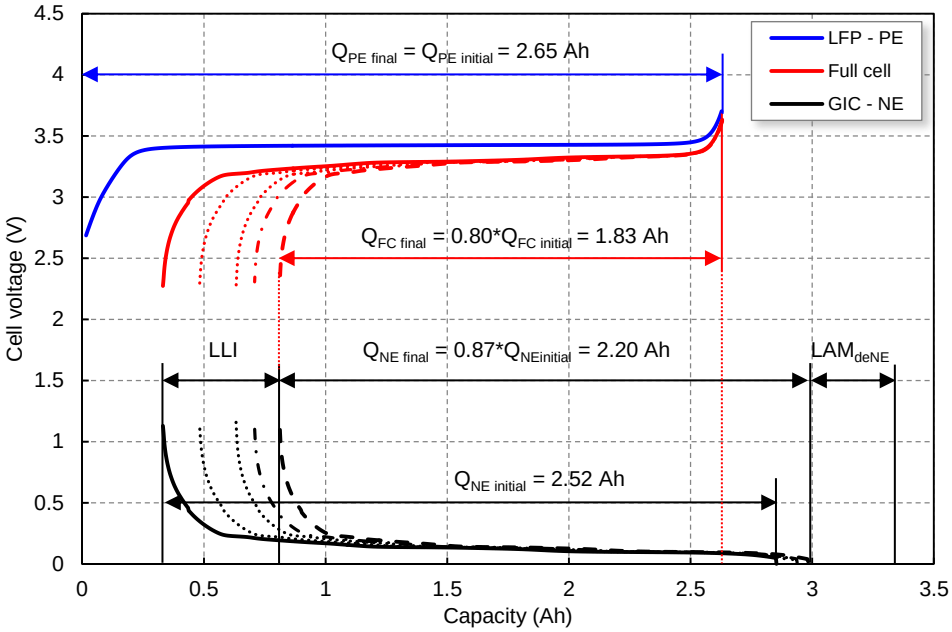

Fig. 7.15. Schematic representation of the GIC||LFP cell tested under fast charge cycling, showing the evolution with cycling of the simulated results for LLI at 0.0033% cycle^{-1} and LAM_{deNE} of 0.0023% cycle^{-1} (cycle 0 to 4500) and LLI at 0.002% cycle^{-1} and LAM_{deNE} of 0.0023% cycle^{-1} (cycle 4500 to 5400).

As a final verification of the simulation vs. the experimental results, the cell voltage vs. capacity evolution with cycling is plotted in **Fig. 7.16**. The simulated results with the proposed degradation modes, again agree nicely with the experimental values.

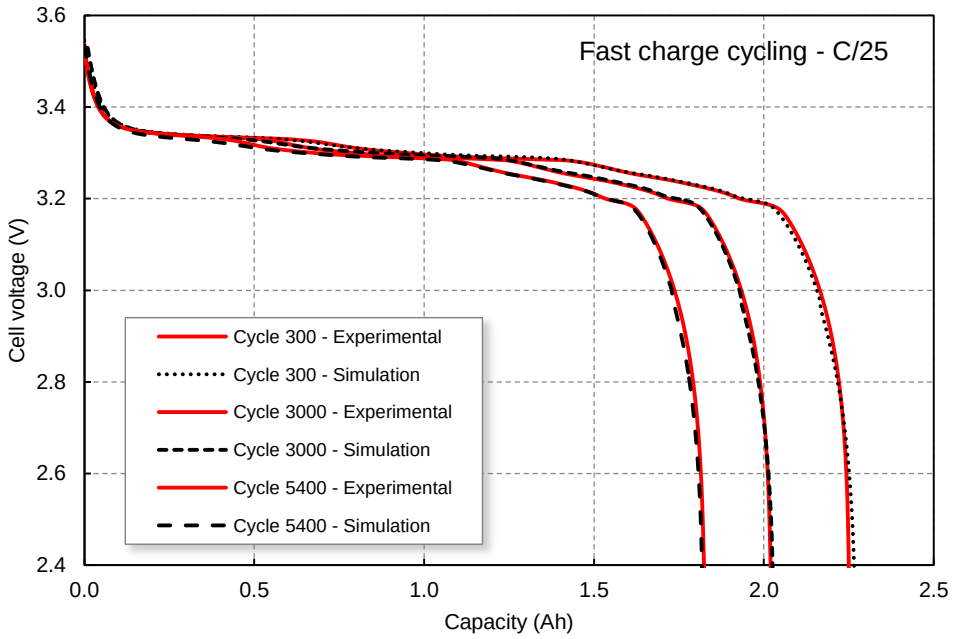

Fig. 7.16. Evolution with cycling of the voltage vs. capacity curves for the experimental and the simulated results.

7.3.3. Mechanistic analysis of aging under fast charge cycling: discussion

Through the *in-situ* analyses and *'Alawa* simulations carried out in this section, the cell tested under fast charge cycling was found to have the aging modes: LLI at 0.0033% cycle^{-1} coupled with LAM_{deNE} of

0.0023% cycle^{-1} (stage 1, cycle 0 to 4500) and LLI at 0.002% cycle^{-1} coupled with LAM_{deNE} of 0.0023% cycle^{-1} (stage 2, cycle 4500 to 5400).

The cell's degradation rate remained linear with cycling, with the exception of the 65-day calendar pause at cycle 4500. As analyzed, the calendar pause only affected peak ❶ whereas peak ❷-❺ remained unaltered. Hence, only LLI was observed during the calendar stop. This is in agreement with the literature reports on calendar aging [24], [94], [97], [98]. As the cycling was reestablished, LAM_{deNE} remained unaltered, whereas the LLI rate was slightly reduced, by a factor of ~1.6. The factor reduction of LLI after calendar pause was obtained from last three data points. Thereafter, the cell reached its EOL and it was set to rest. The tests were executed as planned, but it would be interesting to find out whether the LLI factor reduction would have remained invariant with cycling or, if in contrast, it would have been increased again. To our best knowledge, there has not been works published in the literature dealing with these conditions. Hence, we remain cautious with providing any suggestion on the tendency rate that LLI would follow in subsequent cycling.

To validate the feasibility of fast charging from a mechanistic perspective, we shall discuss the relation of the fast charging scheme with the half-cell results. As previously shown in **Fig. 7.15**, the slippage of the NE correspondence towards a higher relative capacity has important consequences: under such conditions, the NE would not be fully lithiated when the PE completely released all its Li ions [31], [58]. Thus, Li plating could be avoided [36], [60]. This result indicates that the cell tested under the proposed fast charging scheme and cycling conditions, should not encounter any risk of thermodynamic Li plating. More broadly speaking, since no significant ORI or kinetic degradation was observed during the experiments, the risk of Li plating under the proposed cycling aging conditions is slim. This findings are is significant, since Li plating is considered detrimental degradation mode associated with fast charging [24], [36], [57], [74], [81], [82]. Indeed, these findings confirm from a mechanistic perspective that the designed fast charging scheme on the selected cell technology is safe.

The convenience of the applicability of the fast charging scheme is also validated through comparison with the cell tested under standard cycling. Both aging modes show a similar pattern (especially for the first 3000 cycles which are the same), even under broadly different testing schemes. Hence the proposed charging protocol did not originate accelerated aging to the tested cell, in addition to provide quick and safe charges.

7.4. Dynamic stress cycling: mechanistic analysis of aging

This section presents the mechanistic analysis of the aging modes affecting the cell tested under dynamic stress cycling. As suggested from the previous IC and PA analyses carried out in Chapter **6**, the cell under dynamic stress test presented evidences of Li plating. In addition, the IC and PA evolution showed more complicated patterns than those found on the standard and fast charging tested cells. This causes that the aging diagnosis is much more challenging.

To overcome such difficulty, the following steps were taken. First, the nature of Li plating that affects the cell is presented. Second, quantitative analyses are carried out to decipher the plausible aging modes ongoing on the cell. Due to the nature of Li plating and the complicated degradation patterns that this cell exhibits, further analyses are required: quantitative measurements of peak ❶ are provided to measure the reversible Li plating. And third, the results of these measurements allow us to simulate the degradation modes from a half-cell perspective with better accuracy. All this provides information of the aging modes both qualitatively and quantitatively.

7.4.1. Nature of Li plating on cell tested under dynamic stress cycling

In general, Li plating can be originated due to (1) hazardous cell operation conditions, (2) cell constructive defects and/or (3) conventional aging of the cell.

Hazardous cell operation conditions are referred to low temperature operation (below 0ºC) and strenuous charges [36], [57], [74], [81], [82], [87]. Under such conditions, Li plating could suddenly appear. However, these conditions were not found on the cell tested under dynamic stress: the temperature during testing was always kept at 23ºC. With respect to the charging rates, the proposed fast charging scheme is safe and does not cause further aging, as previously verified. Similarly, although the DST has charging intervals (i.e. regenerative braking), the maximum charging rate is 2C for 8 seconds per DST cycle. Hence, we conclude that the origin of Li plating is not caused by hazardous cell operation conditions.

Cell constructive defects are referred to poor cell balance, geometric misfits and/or poor electrolyte formulation [36], [57], [58]. Cell balance was calculated from the mechanistic full cell reconstruction: LR = 0.95 and OFS = 12.5%. Under such cell constructive parameters, the NE cannot be fully lithiated when the PE completely released all its Li ions, so Li plating is avoided. In addition, this type of cell was successfully cycled for over 5000 cycles under standard and fast charge regimes. Therefore, since all the tested cells exhibited minimum cell-to-cell variations, this verifies that no evidences of geometric misfits and/or poor electrolyte formulation are to be found. Hence, we can conclude that conditions on point (2) are not found on the selected tested cells.

All this leads to conclude that Li plating was originated due to gradual cell degradation. Indeed, the IC and PA analyses showed evidences of progressive cell degradation towards Li plating: the gradual growth of peak ∫❶.

The origin of Li plating can be also studied from its kinetic and thermodynamic components. As described in Chapter **2**, kinetic Li plating occurs under strenuous charging rates, subzero temperatures and ORI on the NE. As previously commented, strenuous charges or subzero temperatures are discarded. Similarly, the IR analyses showed that only after cycle 900 the IR starts to grow more rapidly. During the first 600 cycles, the IR increase is considered small (~5 mΩ over 35 mΩ). Indeed, between cycle 600 and 900 we suggested that Li plating occurs. Thus, the IR increase is a direct consequence of Li plating appearance, and not vice versa.

Under normal operating conditions and no ORI increases, Li plating can be induced by the studied degradation mechanisms. From the four possible LAM modes, Li plating appears when LAM_{deNE} is significant to reach a condition where overcharging the NE occurs [31]. No other LAMs directly cause Li plating. When this phenomenon occurs, it is very likely that the capacity of the full cell enters a second stage of degradation, accelerating its capacity fade and IR increase [31], [47]. This was observed on the experimental data.

Therefore, we can conclude that the origin of Li plating is originated by progressive cell degradation. The degradation causes large LAM_{deNE} that eventually produces Li plating on the cell. The study to decipher the effects of LAM_{deNE} is carried out through thermodynamic conditions in the mechanistic simulations.

7.4.2. Dynamic stress cycling: analysis of the degradation mechanisms

To proceed with the analysis of the degradation mechanisms, it is first required to load the cell constructive parameters to reproduce the experimental cell. Due to initial calendar aging of the cell, the OFS at the BOC was affected. Hence, we calculated the initial parameters OFS_{BOC} = 14.7% and LR_{BOC} = 0.95 which are loaded to simulate the cell.

The evolution of the normalized integral areas of peak ∫❶ and peak ∫❷-❺ as a function of cycle number is presented in **Fig. 7.17**a-b respectively. The experimental data at C/25 (diamond and square symbols) are compared with those predicted by *'Alawa* model (dashed lines) for the aging modes based on

LLI + LAM_{deNE}. The simulations were split into two stages, to follow the experimental degradation trends.

The simulation results for stage 1 (which accounts from BOC up to cycle 750), revealed that a combination of approximately 0.0045% cyc^{-1} of LLI and 0.017% cyc^{-1} of LAM_{deNE} is the best match with the experimental data for peaks ∫❶ and ∫❷-❺, as observed in **Fig. 7.17**a-b. The simulated degradation modes on the FC also matches nicely with the experimental cell capacity fade. The combination of aging modes was intentionally projected up to cycle 750 (green, dashed line), where we suggest that approximately, Li plating emerges. Indeed, from the IC and PA analyses, peak ❼ started to be quantifiable at cycle 900, but hardly discernible at cycle 600. Since the PA degradation patterns are more complex than in the previous cells, in this analysis peak ∫❶ is evaluated only during stage 1.

From cycle 750 onwards, peaks ∫❷-❺ (see **Fig. 7.17**b) entered the second stage. Since peaks ∫❷-❺ are directly affected by LAM_{deNE} and not by LLI, the degradation rates of LAM_{deNE} can be calculated independently: ~0.025% cyc^{-1} from cycle 750 to 1800. In contrast, **Fig. 7.17**a, the PA results after Li plating contain the capacity sum of peak ∫❶ and peak ∫❼. Therefore, to analyze how the aging modes affect ∫❶ it is first necessary to separate peak ∫❼ and peak ∫❶ quantitatively.

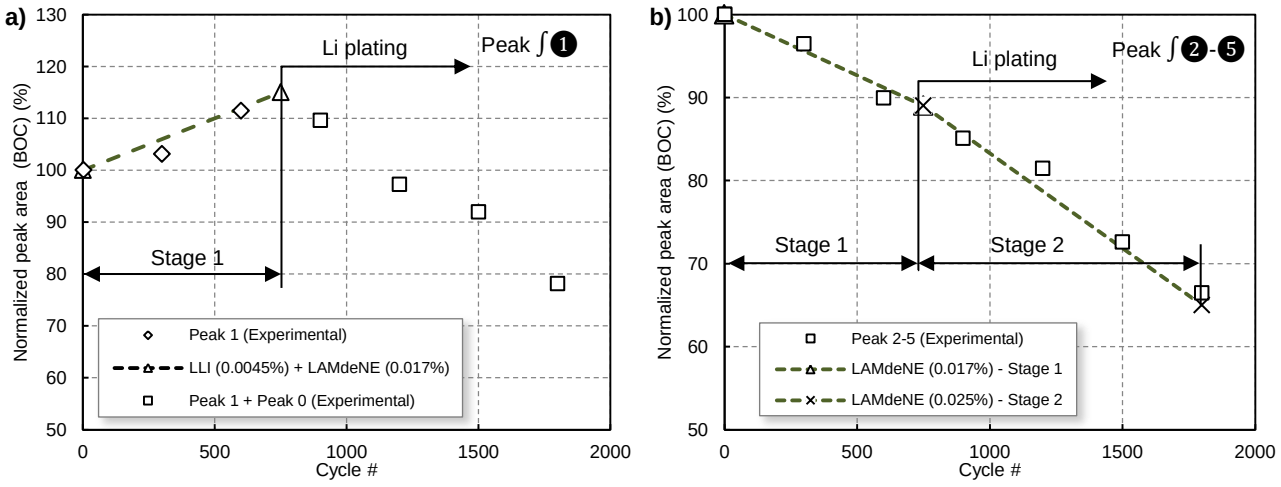

Fig. 7.17. Normalized peak area for (a) peak ❶ and (b) peak ❷-❺ as a function of cycle number. The experimental data are in symbols (diamond and squares), whereas the simulated results are in dashed lines. The simulated results are exhibited for LLI + LAM_{deNE} for both stages.

The results of the experimental cell capacity degradation and its corresponding PA analysis, as a function of cycle number, are shown in **Fig. 7.18**. To facilitate the analysis, here the PA of each peak is presented in terms of capacity (Ah), and not in terms of normalized peak area. As observed, the cell and peak ∫❷-❺ loss capacity with cycling. In contrast, the capacity of peak ∫❶ is increased during the first 600 cycles. Thereafter, as Li plating emerges, peak ∫❶ is reduced rapidly. Based on previous reasoning, we estimate that Li plating emerges around cycle 750. This is shown in **Fig. 7.18**. The first accurate PA measurement on IC peak ❼ was performed at cycle 900. Thereafter, the capacity of ∫❼ remains rather constant with cycling. Indeed, peak ∫❼ was measured to be 0.124 Ah at cycle 900 and 0.140 Ah at cycle 1800 (which corresponds to 5.8% and 8.9% of the total cell capacity, respectively). Hence, even if peak ∫❼ remains rather constant in terms of capacity, its presence in relative values of full cell capacity is slightly increased with cycling.

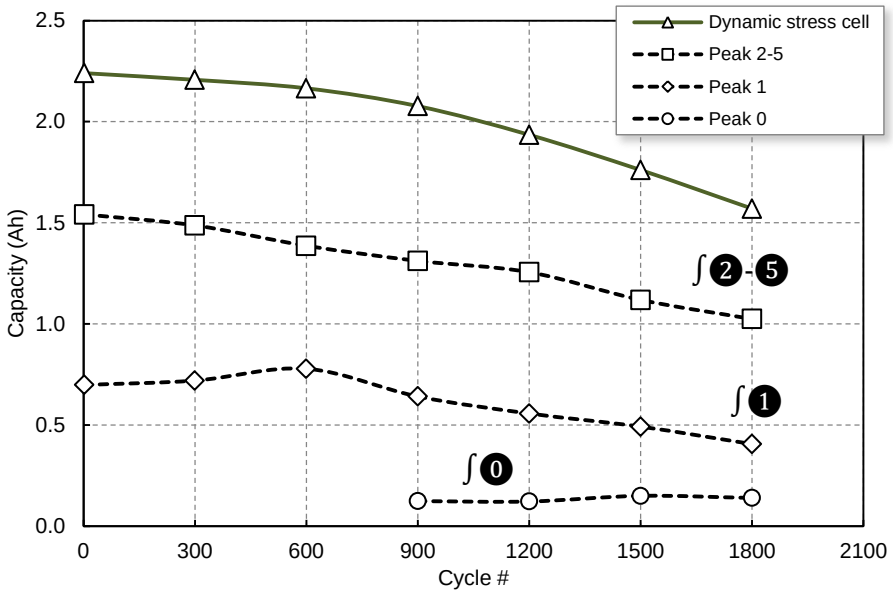

Fig. 7.18. Capacity evolution with cycle number for the cell tested under dynamic stress cycling (green continuous line) and its contribution of each peak area capacity evolution (dashed lines).

The nature of Li plating can be further divided into reversible and irreversible. The irreversible plated lithium is the main responsible for the capacity losses and the subsequent detrimental effects. In contrast, reversible Li plating does not cause direct capacity loss as it is possible that part of the metallic lithium deposited can be recovered [57], [74], [90]. Moreover, the reversible plated lithium is reflected in the growth of peak ❼ of the IC curves. Hence, the measured capacities of peak ∫❼ provided here account for the part of Li plating that is reversible.

The ability to measure peak ∫❼ in terms of absolute capacity (and relative percentage) is of great importance to carry out further mechanistic simulations. Indeed, the degradation analyses based on PA simulations are much complicated after Li plating, since LLI and irreversible Li plating are taking place simultaneously. However, by using a reverse simulation strategy, which consists in introducing the experimentally measured amount of reversible Li plating into the half-cell model, the aging modes can be also calculated.

7.4.3. Dynamic stress cycling half-cell analysis

The evolution of the correspondence of the electrodes balance with aging, based on the simulation of the degradation modes are depicted in **Fig. 7.19**a-d. Four representative aging stages are depicted: (a) shows the half-cell at initial stage and after initial calendar aging (BOC). In (b), the evolution of the electrodes is shown from BOC to cycle 750, where Li plating approximately begins. Finally, (c) and (d) show the aging evolution with Li plating, from cycles 750 to 1200 and 1200 to 1800 respectively. For each stage, the solid lines represent the initial conditions, whereas dashed lines represent the final state. Each figure shows the effect of the degradation modes ongoing on the cell, referenced for each particular stage.

Fig. 7.19a shows the effects that calendar aging caused on the cell. Due to the calendar aging stage (13 months) carried before BOC, the cell reduced its capacity by 2.6%. The capacity fade was attributed to LLI. Since LLI is translated in a shifting of the NE, this degradation affects directly the NE and hence the OFS value at BOC (i.e. OFS_{BOC}). The OFS_{BOC} can be easily calculated from the mechanistic model, since all the initial cell constructive parameters are known. The calculated result was OFS_{BOC} = 14.7%. Since calendar aging only affects LLI, the LR remains unaltered, hence LR_{BOC} = 0.95. The BOC cell constructive values were loaded into the *'Alawa* toolbox to begin with the cycling simulations.

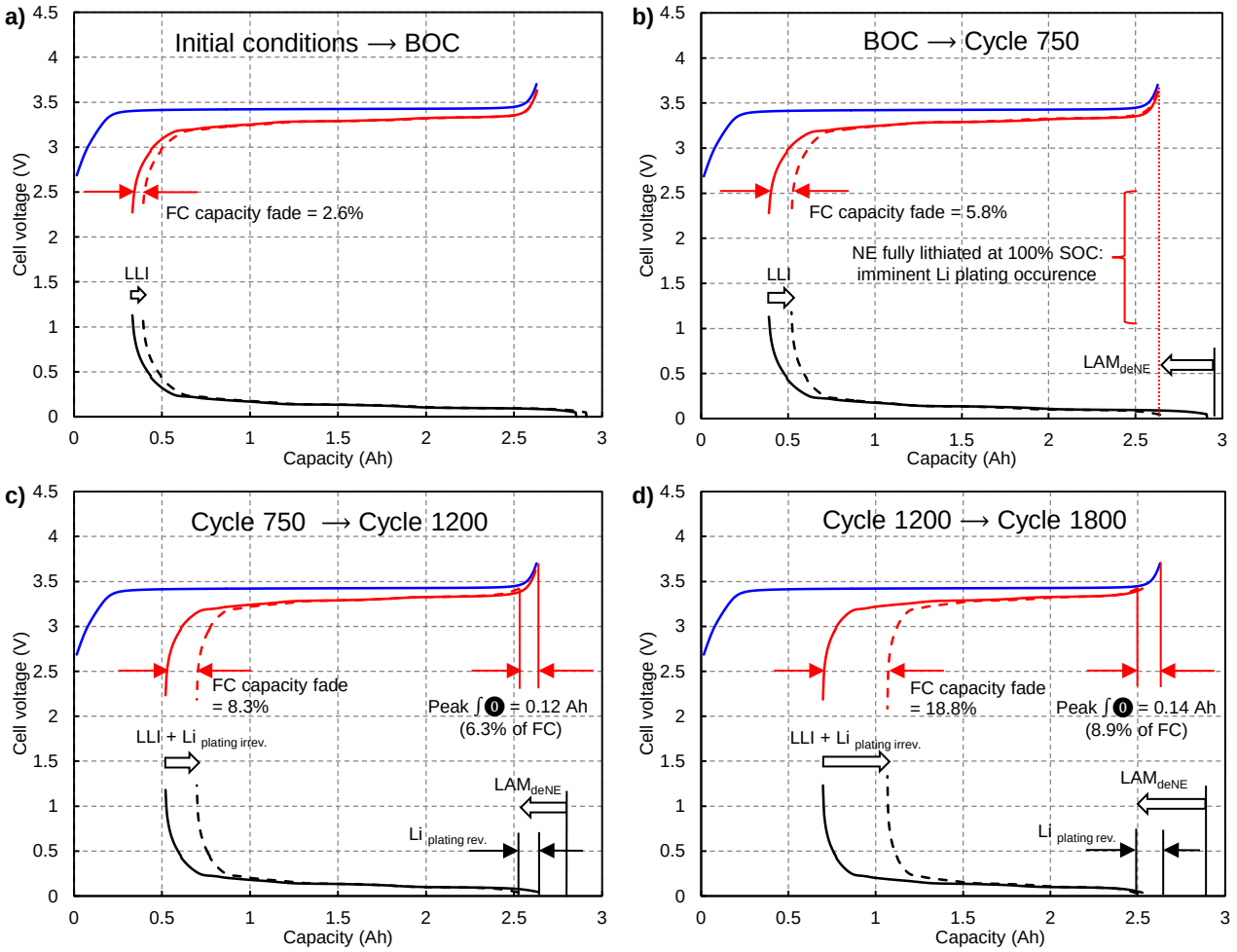

Fig. 7.19. Schematic representation of the GIC||LFP cell tested under dynamic stress cycling, showing the evolution with cycling of the simulated aging modes for a) initial conditions to BOC, b) BOC to cycle 750, c) from cycle 750 to 1200, and d) from cycle 1200 to 1800.

Fig. 7.19b shows the effects that the degradation modes LLI + LAM_{deNE} cause on the cell, from BOC to cycle 750. As previously obtained from the simulations, LLI = 0.0045% cyc^{-1} and LAM_{deNE} = 0.017% cyc^{-1} were found to approximately match the experimental data. Although LAM_{deNE} was ~3.7 times larger than LLI, the FC capacity fade of 5.8% was entirely attributed to LLI. This is because the effect of LAM_{deNE} remains "silent" as it falls outside the area of the PE (see **Fig. 7.19**b). Moreover, it is important to point out the state of the NE when fully lithiated, at cycle 750: the stage of LiC_6 matches with the fully delithiated state of the PE ($FePO_4$), as seen in **Fig. 7.19**b (vertical red line). In other words, an imminent Li plating situation is presented here: subsequent cycling at a rate of LAM_{deNE} larger than LLI would induce the cell to Li plating. This is because the NE stage LiC_6 would be reached before the PE releases all its Li ions. This is an important finding, because based on simulations that agree with the experimental data, we estimated that Li plating occurrence appears within the cycle 750. On account of the LLI + LAM_{deNE} aging modes, the constructive parameters at cycle 750 were: OFS_{750} = 19.6% and LR_{750} = 0.8. These parameters were set to simulate the cell from cycle 750 to 1200.

Fig. 7.19c-d show the evolution of the correspondence of the electrodes balance in the case of aging with Li plating, for cycle 750 to 1200 (c) and from 1200 to 1800 (d), respectively. As the degradation rate of LAM_{deNE} is larger than that of LLI, Li plating appears, in form of reversible ($Li_{plating\ rev.}$) and irreversible ($Li_{plating\ irrev.}$). The reversible part of Li plating does not contribute to capacity fade on the FC. As a result, peak ∫0 is generated. As observed in **Fig. 7.19**c-d, the simulation results of peak ∫0 agree with the measured experimental values. The irreversible part of Li plating contributes to capacity fade;

the plated lithium promotes progressive growth of the SEI [52], [58], [128] and also tends to isolate Li metal grains which become inactive [82]. Similarly, the subsequent surface film formation causes capacity losses which are not distinguishable from irreversible plating [74]. Hence, in the mechanistic model we attribute the SEI growth as a "shifting" of the NE, whereas the material isolation as a shrinkage effect (i.e. LAM_{deNE}). This is shown in **Fig. 7.19**c-d: Li $_{plating\ irrev.}$ causes capacity losses, hence SEI growth is added to the ongoing LLI. Similarly, according to the simulations, the rate of LAM_{deNE} as Li plating appears was increased from ~0.017% (up to cycle 750) to 0.025% cyc^{-1} (cycle 750 to 1800). On account of the LLI + Li plating + LAM_{deNE} aging modes, the final cell constructive parameters at cycle 1800 were: OFS_{Final} = 40.2% and LR_{Final} = 0.54.

Fig. 7.20 shows the evolution of the half-cell based on the simulation of the degradation modes, referenced from the initial conditions to final state (as indicated by arrows). The solid lines are the initial state, the dashed lines show the BOC and cycle 750, whereas the dotted lines show cycle 1200 and the final cycle, 1800. As shown in **Fig. 7.20**, the degradation on the PE did not show any noticeable degradation, even if the cell shows large capacity fade coupled with Li plating. This can be validated through various approaches: first, because of the intrinsic high stability and performance of nanostructured LFP materials [42]. Second, under LAM_{liPE} the PE would reduce its capacity starting from its delithiated state (high SOC) towards lower SOC. However, this effect would reduce peak ∫❶, which fails to match the simulation with the experimental results. And third, literature on *post mortem* analyses [68], [78] concluded that GIC||LFP cells, even when exhibiting Li plating and large cell impedance increase, did not show any distinctive change of the LFP material. Only LAM_{dePE} could cause degradation without affecting the FC signature. However, this scenario is unlikely, on account of the previous statements. Therefore, even if this cell experimented large capacity fade coupled with Li plating, we remain confident that the PE did not show any noticeable degradation throughout cycling.

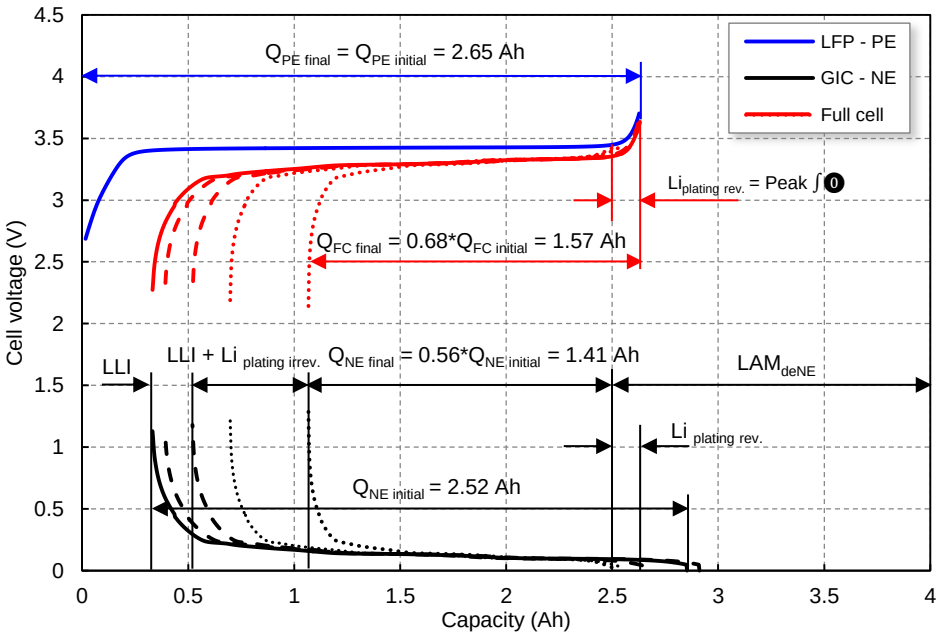

Fig. 7.20. Schematic representation of the GIC||LFP cell tested under dynamic stress cycling, showing the evolution with cycling of the simulated results.

The shrinkage effect on the NE caused by the large LAM_{deNE} aging mode is clearly observed in **Fig. 7.20**. Contrary to the cells previously analyzed under standard and fast charge, here the degradation ratio of LAM_{deNE} is larger than that of LLI. This causes that the predominant effect on the NE is translated into shrinkage instead of a slippage. The shrinkage effect eventually causes Li plating, as the NE stage LiC_6 is reached before the PE releases all its Li ions.

The numerical values of the capacities of the NE, PE and FC can be calculated from the mechanistic simulations. The results are shown in **Fig. 7.20**. The final usable FC range was diminished by 32%, which agrees with the observed experimental capacity loss.

Fig. 7.21 shows the evolution with cycling of the experimental cell capacity together with the distribution of the aging modes. During the first stage (up to cycle 750), the capacity fade on the cell was attributed only to linear LLI at 0.0045% cyc^{-1} (black dotted area). Although LAM_{deNE} exhibited a greater rate (i.e. 0.017% cyc^{-1}) than that of LLI, its effect on the FC signature remained "silent". During the second stage, Li plating is presented on the tested cell. With a degradation rate on LAM_{deNE} of approximately 0.025% cyc^{-1}, we can run simulations to obtain the maximum FC capacity loss that the cell would encounter if the Li plating effect was 100% irreversible. The theoretical maximum value is displayed with the green dashed line. In addition, the Li $_{plating\ rev.}$ capacity was quantified from the experimental data through peak $\int$❶. The deduction of the maximum theoretical Li plating effect (i.e. 100% irreversible) from the experimental reversible plating effect (i.e. peak $\int$❶) results in the actual capacity of the experimental cell. This is shown with the solid green line. Hence, the total cell capacity loss during stage 2 was caused by the effects of LLI + Li $_{plating\ irrev.}$ at a rate of ~0.02% cyc^{-1}, as shown in **Fig. 7.21**, in the red dotted area.

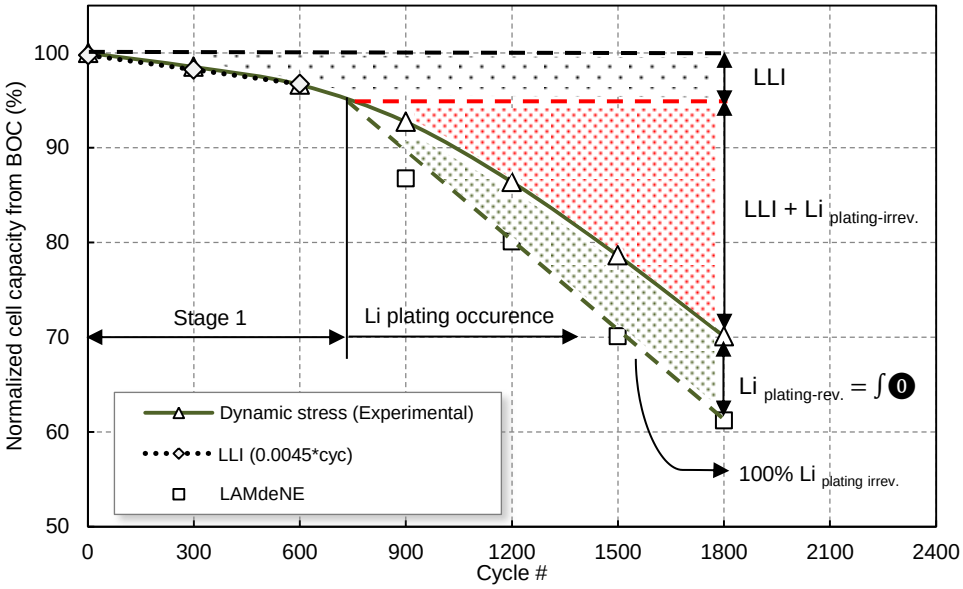

Fig. 7.21. Normalized capacity evolution with cycle number for the of dynamic stress cycling (green, solid line), indicating the LLI during the first stage (grey, dotted area), and the reversible Li plating (green, dotted area) and LLI + Li plating irreversible aging modes (red, dotted area).

Fig. 7.22 compares the evolution with cycling of the cell voltage vs. capacity curve of the simulation and the experimental results. The simulated results agree in good terms with the experimental curves. The accuracy is relatively lower than in previous analyses on cells under standard and fast charge schemes, because of the complexity of Li plating effects.

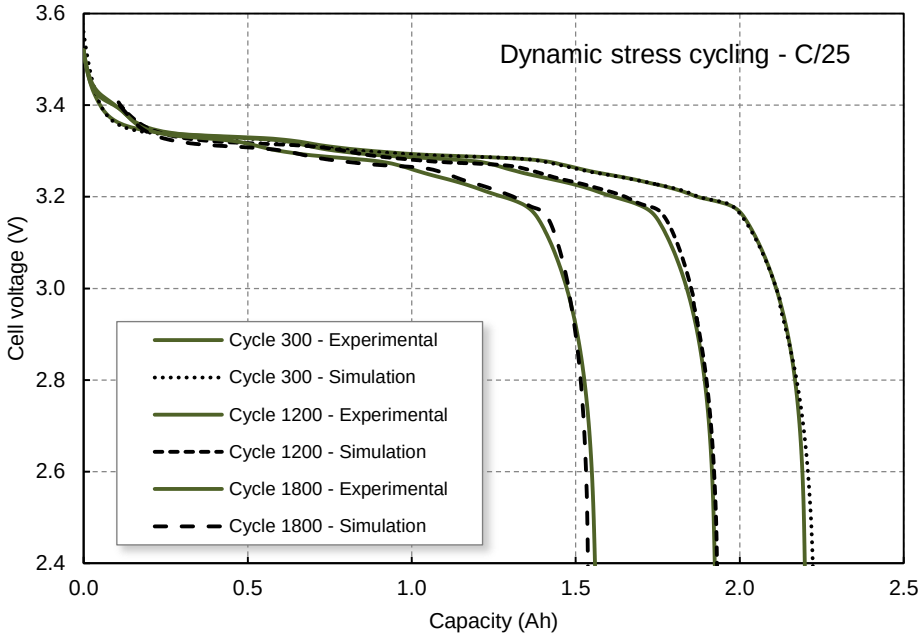

Fig. 7.22. Evolution with cycling of the voltage vs. capacity curves for the experimental and the simulated results.

7.4.4. Mechanistic analysis of aging under dynamic stress cycling: discussion

In this section, the aging modes affecting the cell tested under dynamic stress were deciphered, both qualitatively and quantitatively. The cell exhibited a nonlinear capacity evolution, divided in two stages (i.e. before and after Li plating occurrence). During the first stage (up to approx. cycle 750), the aging modes were LLI at 0.0045% cyc^{-1} and LAM_{deNE} at 0.017% cyc^{-1}. The second stage (cycle 750 to 1800) presented Li plating on the NE. The aging modes during the second stage included LLI + $Li_{\text{plating irrev.}}$ at approx. 0.02% cyc^{-1} and LAM_{deNE} at 0.025% cyc^{-1}.

The quantification of Li plating required previous investigations to decipher its nature origins. Li plating was originated from progressive cell degradation (and not by a sudden, isolated incident), associated with the large LAM_{deNE} aging mode occurring during the first stage. Next, through PA analyses, the evolution with cycling of the capacity of peak ❶ was measured. This allowed us to quantify the amount of reversible Li plating. Then, half-cell simulations were performed. The simulations of the proposed aging modes during the first stage showed an imminent Li plating occurrence within cycle 750. Subsequent simulations were carried out by taking into account the reversible part of Li plating measured experimentally (i.e. peak ∫❶) and comparing it with the simulated results. This allowed us to validate the obtained degradation modes. Finally, in the mechanistic simulations we attributed the $Li_{\text{plating irrev.}}$ part which produces progressive SEI growth, as a slippage of the NE, whereas the material isolation as a shrinkage effect associated with LAM_{deNE}. The $Li_{\text{plating rev.}}$ caused by LAM_{deNE} was attributed to peak ∫❶.

From a broader perspective, as Li plating emerges, it induces more degradation on the cell. Li metal is known to be very reactive toward electrolytes which should form additional SEI and isolate Li metal grains. This causes an increase of the LLI and LAM_{deNE} rates which also explains the observed cell performance loss and rapid IR increase during Li plating occurrence.

The majority of the reports that study Li plating effects agree in that Li plating causes performance loss, SEI growth and rapid IR increase [36], [57], [68], [78], [81]. This is commonly found through *post mortem* analyses. Yet in this study, we are able to provide *in situ* quantitative and qualitative analysis of Li plating and its evolution with cycling by using the proposed strategies coupled with the mechanistic

simulations. These significant findings enhance the understanding on how Li plating can raise from its "silent", incubating stage, how it appears, and its effects on the cell. We additionally provide the half-cell projection, which allows us to study the effects of the reversible and irreversible components of Li plating and its evolution with cycling. Still, due to the complexity of Li plating effects, the simulations have intrinsic inaccuracies. However, we are confident that for the majority of battery applications the results provided here surpass the common requirements in terms of accuracy and precision. Therefore, the potential of using the IC and PA analyses, coupled with the *'Alawa* toolbox with harvested half-cell data, is demonstrated: diagnosis of cell's aging modes can be deciphered, even under complex degradation mechanisms such as Li plating.

Li plating is considered a harmful aging mechanism which may lead to safety deterioration. This is because the metallic lithium deposits may result in the formation of dendrites which eventually can pierce the separator, produce short circuit in the cell and cause thermal runaway. However, thermal runaway was not observed on the tested cell, even when cycled bellow EOL. Moreover, since the reversible Li plating capacity (i.e. $\int 0$) and the LAM_{deNE} rate remained rather constant during the second cycling stage, safety deterioration does not seem to be increased. Similarly, *post mortem* studies on same type GIC||LFP cells [68], [78] exhibiting Li plating and large cell impedance increase, did not show any distinctive dendrite growth or separator pierce. Therefore, the safety and durability of this cell technology and architecture was not affected, even under harsh detrimental conditions. This is crucial for any battery application (especially for industrial applications, EVs and EES), where safety is imperative.

As previously suggested in Chapter **6**, the rapid performance decrease observed on the cell was caused by the DST discharging scheme. The main reason behind this rapid degradation can be related to the vast number of repetitive intercalation/deintercalation processes that the cell underwent. Indeed, on a single DST cycle, 10 intercalation/deintercalation processes occur. In addition, 16 DSTs are contained on a full discharge when the cell is fresh. Hence, at least 160 intercalation/denitercalations occur per full cycle. When the cell is aged, 10 DSTs are contained on a full discharge. In round numbers, after 1800 cycles the cell was subjected to over 250,000 intercalation/deintercalation processes. This vast number of partial charge/discharges can affect the structure of the electrodes (e.g. by volume changes, stress, etc.), thus reducing the active material on the NE [24], [28], [36], [60], [71]. This reasoning is in concordance with the aging modes found on the cell tested under dynamic stress: LAM_{deNE} experienced an increase by a factor of x10 when compared with the LAM_{deNE} rate found on standard or fast charge cycling. Hence, DST cycling particularly affects the aging mode LAM_{deNE}. This verifies that DST cycling is very detrimental to the cell and causes rapid performance degradation.

Finally, the approaches carried out here allowed us to detect Li plating during operation (i.e. online) through *in situ* techniques and nondestructive analyses. The study of the evolution of the IC peaks and PA with cycling, coupled with the quantification of LAM_{deNE} with *'Alawa* simulations allowed us to estimate the presence of Li plating, even before it occurred. Hence, a prognosis approach can be carried out with the presented methods and simulations. This important topic is discussed in the next section.

7.5. Aging prognosis

Nowadays, prognostic techniques in LIBs remain very challenging, due to the inherent complexity of the electrochemical processes that take place within a battery. Still, several attempts in battery prognosis technologies have been developed. Recently, Rezvanizaniani *et al.* [191] reviewed the last advances in battery prognostic technologies, and observed that the current prognostic techniques are generally based on data-driven and/or physical-model approaches. Although both approaches have certain advantages and drawbacks, the main challenges to be addressed remain the uncertainty in the analysis of durability and safety during battery life. Aiming to overcome such challenges, here a different approach is used, based on the *'Alawa* mechanistic model. By using inference techniques, the *'Alawa*

toolbox is capable of revealing how different degradation scenarios may affect the cell beyond the current cycling state. As a result, cell aging prognosis can be derived.

Hence, in this section we perform an aging prognosis based on the mechanistic *'Alawa* model. The study is particularized for the cell tested under fast charge cycling conditions, to show the plausible effects of fast charging over long term cycling. The prognosis analysis was carried considering that the cell would be cycled under normal conditions (i.e. fast charging scheme) and did not consider anomalous conditions (i.e. strenuous charges and/or charge at low temperatures). The simulations up to cycle 10000 are carried out under two given "what if" representative prognosis scenarios:

Scenario 1: steady degradation. The calculated aging mechanisms remain intact (i.e. LLI = 0.0033% cycle^{-1} and LAM_{deNE} = 0.0023% cycle^{-1}), thus the cell keeps aging at the same rate as observed

Scenario 2: Li plating appearance. The LLI remains intact (i.e. LLI = 0.0033% cycle^{-1}) but the cell starts to show Li deposition at cycle 4500

The results and concluding remarks derived from these simulations help to understand the plausible tendencies that the cell under fast charging may encounter in subsequent cycling, and the characteristics and advantages of mechanistic approaches for aging prognosis.

7.5.1. Scenario 1: steady degradation

The results of the simulations up to cycle 10000 are presented in **Fig. 7.23**a-b. **Fig. 7.23**a compares the normalized cell capacity evolution with cycling (left axis) and the degradation modes with cycling (right axis). Thicker lines show the "diagnosis" part of the simulation, whereas thinner lines present the "prognosis" results. The dashed lines show the actual capacity fade that each particular degradation mechanism causes on the full cell. **Fig. 7.23**b shows the evolution of the half-cell data electrodes under scenarios steady degradation. The data evolution of the half cells is shown again with the thicker lines for the "diagnosis", and the thin ones for the "prognosis". The initial (cycle 1) and final (cycle 10000) are presented in solid lines, whereas the dashed ones results in 2000 cycle increments.

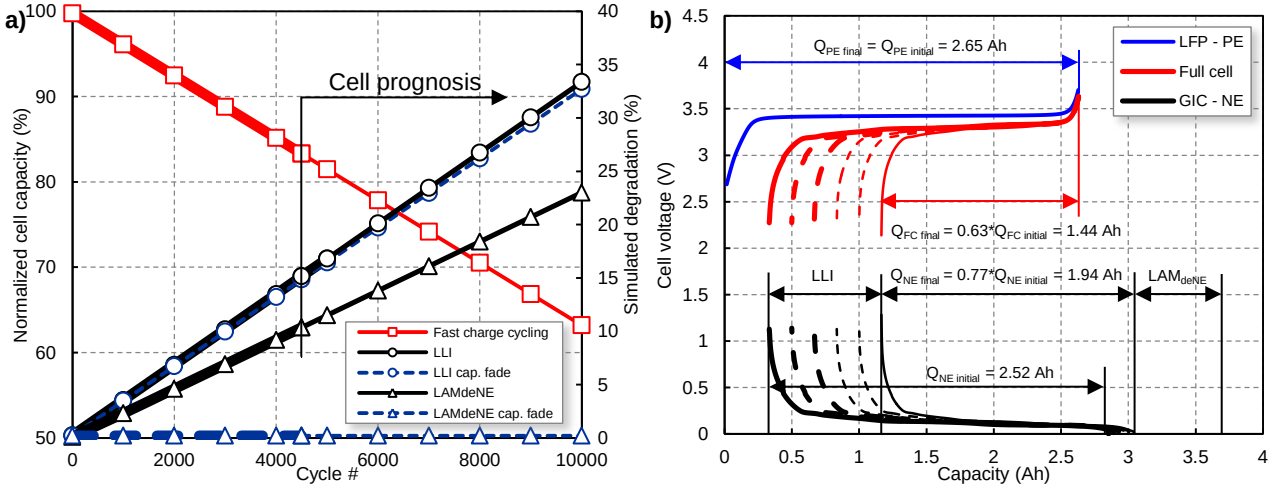

Fig. 7.23. Evolution of the degradation modes under the prognosis analysis at C/25 for scenario 1. In a) the normalized cell capacity evolution (left axis) and the degradation modes with cycle aging (right axis) is shown, whereas b) shows the evolution of the half-cell data from the electrode. Thick lines represent the diagnosis results, whereas thin lines represent the prognosis results.

The simulated cell results show a capacity fade of 37% at cycle 10000. The degradation trend remains linear throughout the entire simulated cycling (see **Fig. 7.23**a). Although the aging process is caused by both the contribution of LLI and LAM_{deNE}, only the effects of LLI directly affects the capacity

fade of the full cell. That is because LAM_{deNE} has a smaller degradation rate than LLI (see slope of LLI and LAM_{deNE} on **Fig. 7.23**a) and its effects remain "silent" causing no direct capacity fade on the full cell. The degradations are depicted in **Fig. 7.23**a, on dashed line $LLI_{cap.fade}$, where it is observed that at cycle 10000 the LLI has caused a degradation of 37%, which matches the final capacity fade of the full cell. On the other hand $LAM_{deNE\ cap.\ fade}$ remains constant at zero, even if there is an actual loss of material of 23% on the NE, caused by LAM_{deNE}. This effect is caused as the PE is the capacity limiting to the full cell, when charge. These facts can be also examined in detail from **Fig. 7.23**b. Since LLI is predominant, the overall effect with cycling on the NE is translated into a slippage over higher relative capacity. Finally, since less active material is taking place in the reactions from the NE ($Q_{NE\ final} = 0.77*Q_{NE\ final}$), and the PE remains intact ($Q_{PE\ final} = Q_{PE\ final}$), the final loading ration (LR_{final}) is therefore reduced to $0.73 = LR_{final} = Q_{NE\ final} / Q_{PE\ final}$.

7.5.2. Scenario 2: Li plating appearance

The results of the simulations up to cycle 10000 are presented in **Fig. 7.24**a-b. **Fig. 7.24**a compares the normalized cell capacity evolution (left axis) and the degradation modes (right axis) with cycling. Thicker lines show the "pre Li plating" stage, whereas thinner lines the "Li plating" stage. The dashed lines show the actual capacity fade that each particular degradation mechanism causes on the full cell. **Fig. 7.24**b shows the evolution of the half-cell data electrodes under scenarios steady degradation. The data evolution of the half cells is shown with the thicker lines for the "pre Li plating", and the thin ones for the "Li plating" part. The initial (cycle 1) and final (cycle 10000) are presented in solid lines, whereas the dashed ones results in 2000 cycle increments.

To simulate scenario (2), we must first explain how, under normal operating conditions and no ORI increases, Li plating can be induced by the studied degradation mechanisms. As commented, from the 4 possible LAM modes, Li plating will appear only when LAM_{deNE} is significant to reach a condition where overcharging the NE occurs [31]. To obtain this aging scenario, we carried out several simulations, and calculated that at least ~0.005% $cycle^{-1}$ of LAM_{deNE} is needed to cause Li plating at cycle 4500 (keeping LLI constant at 0.0033% $cycle^{-1}$).

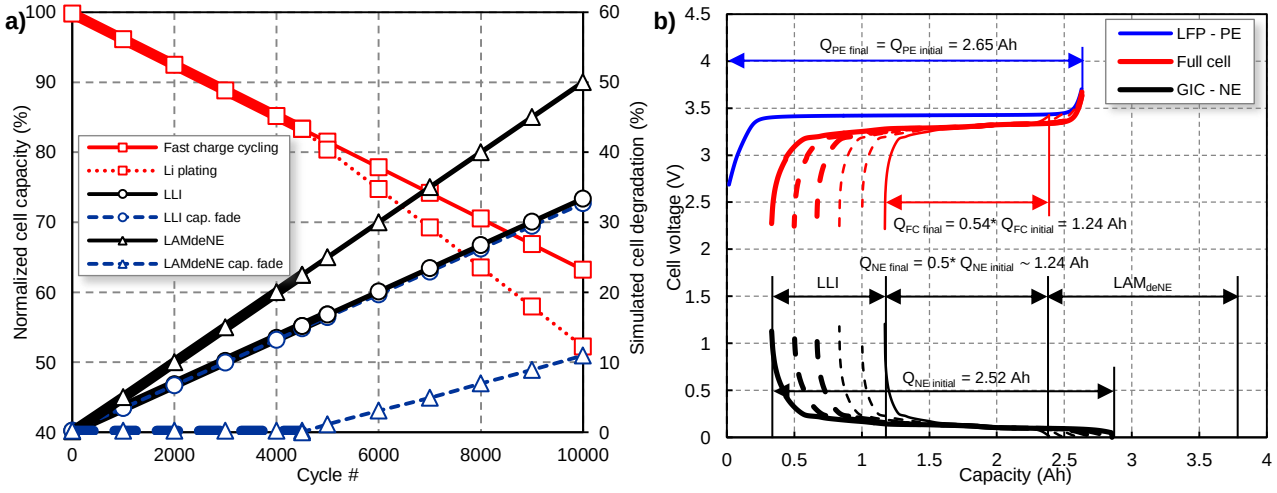

Fig. 7.24. Evolution of the degradation modes under the prognosis analysis at C/25 for scenario 1. In (a) the normalized cell capacity evolution (left axis) and the degradation modes with cycle aging (right axis) is shown, whereas (b) shows the evolution of the half-cell data from the electrode. Thick lines represent the diagnosis results, whereas thin lines represent the prognosis results.

Fig. 7.24a shows the results with the simulated aging modes. As with scenario (1), LLI remains invariant, causing a direct capacity fade on the full cell ($LLI = LLI_{cap.\ fade}$) by 37% at cycle 10000. On the other hand, as LAM_{deNE} is taking place with a pace which almost doubles that of LLI, a capacity fade of

25% at cycle 4500 and 50% at cycle 10000 would be anticipated. Before cycle 4500, LAM_{deNE} should remain silent, not contributing to the capacity loss in the cell. However, at cycle 4500, the NE becomes the capacity-limiting electrode in the charge regime, as a result of the large NE capacity reduction. Hence, Li plating is induced. From cycle 4500 onwards, the capacity fade by LAM_{deNE} may appear in the cell. This effect is depicted by the dotted lines in the simulation results (**Fig. 7.24**a). The resulting capacity loss would depend on how much the plating is reversible [57], [74]. If it is 100% reversible, no additional capacity loss would be expected. If it is 0% reversible, at least an additional 10% capacity fade is expected. The ratio of the reversible Li plating could be assessed from the IC curves (peak ❿), as previously demonstrated in the cell under dynamic stress cycling.

The fading effects could be studied based on the half-cell data from the electrode perspective (see **Fig. 7.24**b). Here, we showed the case of Li plating with 100% irreversibility, as it is more interesting for such study. In the NE, the effect of LLI is translated into a slippage towards a higher relative capacity. On the other hand, due to the high fade rate of LAM_{deNE}, the NE capacity is shrunk abruptly, reducing its active material by 50%. Therefore, the NE becomes the capacity-limiting electrode in the charge regime after cycle 4500 and Li plating would be expected. Finally, since less active material is taking place in the reactions from the NE ($Q_{NE\ final} = 0.5*Q_{NE\ final}$), and the PE remains intact ($Q_{PE\ final} = Q_{PE\ final}$), the final loading ration (LR_{final}) is therefore reduced to 0.47 = $LR_{final} = Q_{NE\ final} / Q_{PE\ final}$.

The simulation results of the IC peak area analysis under scenario 2 are shown in **Fig. 7.25**. The effects of higher LAM_{deNE} than the experimental values (i.e. 0.005% cyc^{-1} vs. 0.0023% cyc^{-1}) affect the evolution of peak ∫❶ and peak ∫❷-❺. In the experimental PA results, up to cycle 4500 both tendencies remained linear (as seen in **Fig. 7.13**), showing a degradation rate of peak ∫❶ larger than peak ∫❷-❺. In contrast, the simulation results show the opposite. Most importantly, peak ∫❶ exhibits a gradual increase until cycle 4500.

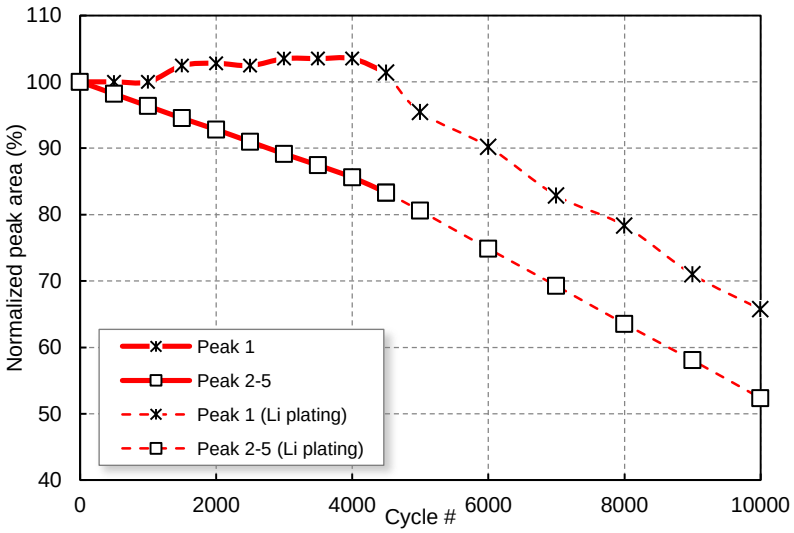

Fig. 7.25. Normalized peak area at C/25 as a function of cycle number for the prognosis analyses under scenario 2.

7.5.3. Aging prognosis: discussion

In this section, a study of the aging prognosis was carried out on the cell tested under fast charge cycling. The aim was to provide a prediction of the aging evolution and life estimation of the tested cell. Based on the *'Alawa* mechanistic model, two "what if" scenarios were proposed. Since Li plating can be caused by fast charging, additional consideration was paid to study the factors that could raise Li plating occurrence on the tested cell.

The simulation results under scenario 1 (i.e. steady degradation) showed a projection of the calculated degradation modes (i.e. LLI = 0.0033% $cycle^{-1}$ and LAM_{deNE} = 0.0023% cyc^{-1}) up to cycle 10000. The analysis showed linear degradation throughout cycling, and little possibility of Li plating on the cell beyond end-of-life. The expected capacity loss at cycle 10000 was 37%.

Scenario 2 (i.e. Li plating occurrence) showed that the cell could encounter Li plating after 4500 cycles only if LAM_{deNE} had increased its fading rate by a factor of 2.3 (i.e. from 0.0023% to 0.005% cyc^{-1}). Under such high loss of active material, the NE would become the limiting electrode on charge at cycle 4500. Hence, Li plating would be expected. Subsequent cycling could lead to a second degradation stage, causing additional capacity loss that depends on the nature of Li plating: if it is 100% reversible, no additional capacity loss would be expected. If it is 0% reversible, at least an additional 10% capacity fade is expected. Hence, the expected capacity loss at cycle 10000 was estimated to be 37% if Li plating is 100% reversible, and 47% under 0% reversible. Still, we should be cautious with this figure, as it may be altered in real life applications: Li plating may trigger other unwanted degradation phenomena [51], [74], [83], [192] which could lead to further degradation [36], [48], [81]. However, from our calculations, we were able to predict which rate of LAM_{deNE} would induce the cell into Li plating at cycle 4500.

Additional analyses of scenario 2 were carried out with the PA evolution to determine the effects that Li plating cause on the evolution of peak ∫❶ and peak ∫❷-❺. The results showed a growth of peak ∫❶, coupled with a gradual decrease of peak ∫❷-❺. This finding has important implications: according to the simulation model, these tendencies show a clear symptom of Li plating incubation. Most importantly, these findings further support previous experimental results carried out on the cell under dynamic stress cycling, which showed Li plating. Indeed, the experimental results showed the same PA evolution pattern as the one described in this prognosis analyses. Hence, a validation of the prognosis model was achieved.

Therefore, it is possible to avoid Li plating by keeping track of the evolution of peak ∫❶ and peak ∫❷-❺. Under normal operation conditions (i.e. avoiding strenuous charges and charging at low temperatures), symptoms of Li plating incubation can be detected if the evolution of peak ∫❶ shows a growing pattern. Under such circumstance, further degradation and Li plating appearance could be avoided by reducing the working operation conditions of the battery system (e.g. reducing power requirements, temperatures, etc.).

7.6. Summary

The purpose of this chapter is to decipher the details of the degradation mechanisms ongoing on the cells tested under standard, fast charge and dynamic stress cycling. This chapter also aims to investigate cell prognosis, projecting the trends of cell degradation under two realistic scenarios. To achieve both diagnosis and prognosis, we conducted a series of mechanistic analysis, based on the simulations obtained from the *'Alawa* toolbox, loaded with harvested half-cell data.

We started by building the simulated cell mechanistic model. An accurate model that behaves as close as possible from the experimental cell is essential to achieve reliable, high quality simulations. For this reason, we propose an innovative strategy, based on feeding the *'Alawa* toolbox with the harvested half-cell data obtained from another, same batch cell as the tested ones. To estimate the cell constructive parameters (i.e. loading ratio and offset) with the best resolution, we developed a strategy based on analyzing the incremental capacity (IC) and peak area (PA) of the harvested graphite electrode. By coupling the cell constructive parameters relations, the experimental IC and PA results, and the mechanistic simulations, we reconstructed the cell mechanistic model. The obtained parameters were a loading ratio (LR) of 0.95% and an offset (OFS) of 12.5%, and were used on the mechanistic simulations. The new approach carried out here provides a level of accuracy and quickness which is unlikely to be achieved under traditional post-mortem analyses.

Once the simulated mechanistic model is completed, we carried out the mechanistic analyses. We started with the cell tested under standard cycling. Here, we show step-by-step the general strategies required to decipher the aging modes, both qualitatively and quantitatively. In addition, the importance of half-cell analysis is shown here. This provides a better understanding on how the aging modes affect the electrodes with cycling: LLI causes a slippage effect on the NE whereas LAM_{deNE} causes a shrinkage effect. Additionally, half-cell analyses enhance the understanding on how Li plating may occur, how a "silent" LAM_{deNE} may cause capacity fade in a later stage of cycle aging, or how the LR and OFS are altered with the predominant degradation modes.

Next, the mechanistic analysis of aging for the cell tested under fast charging was carried out. Here, the suggestions proposed in Chapter **6** are confirmed through mechanistic analysis: the proposed fast charging protocol does not cause additional aging when compared with standard charge, even if recharges are reduced in time by 48 min. In addition, through half-cell analysis, we found that the cell was not at risk of Li plating under the proposed cycling conditions. These findings are significant, since Li plating is often originated during fast charging. Hence, the feasibility of the designed fast charging protocol is also validated through the half-cell mechanistic perspective.

The cell tested under dynamic stress cycling showed the most complicated degradation patterns, including evidences of Li plating. Hence, this analysis was particularly challenging. To overcome such difficulty, we proposed new strategies to decipher the degradation modes by performing simulations from a half-cell perspective. The nature of Li plating was studied first, and we found Li plating was originated due to gradual cell degradation. Then we carried out an estimation of the degradation mechanisms. Next, by analyzing the IC and PA analyses we measured the reversible Li plating capacity associated under peak ❶, which allowed us to set the parameters to run the mechanistic simulations. Additionally, we included the effects of reversible and irreversible Li plating in the half-cell mechanistic simulations. These findings set innovative outcomes, because the aging mechanisms, including the complexity of Li plating analyses, were deciphered through *in situ* techniques.

One key result of this chapter is that battery degradation can be qualified and quantified *in situ*. **Table 7-1** shows the degradation modes calculated in this chapter. Under such different cycling schemes and long-term cycling, with the analyses and techniques carried out in this thesis, we were able to estimate the aging modes, the internal constructive parameters and its evolution with cycling. The

prospects of obtaining these parameters inline during cell monitoring in a battery system operation may improve BMS function for battery performance diagnosis.

Table 7-1. Summary of the degradation calculated on the tested cells. The two terms in the LLI and LAM_{deNE} correspond to stages 1 and 2, respectively.

Cycling scheme	Cycles #	Cap. Fade (%)	LLI (% cyc^{-1})	LAM_{deNE} (% cyc^{-1})	Final OFS (%)	Final LR (%)	Li Plating
Standard	5700	18	0.0033 + 0.0018	0.0023 + 0.0016	27.1	0.84	No
Fast charge	5400	20.2	0.0033 + 0.002	0.0023	30.3	0.83	No
Dynamic stress	1800	31.7	0.0045 + 0.02*	0.017 + 0.025	40.2	0.54	Yes

*0.02% cyc^{-1} corresponds to the effects of LLI + Li plating $_{irrev.}$

From the results described in **Table 7-1**, we observe that LLI + LAM_{deNE} fading mechanism seem to be the common cell degradation for this cell chemistry and architecture. This findings are consistent with those described in [30], and may be probably common in the LFP cell chemistry. Also, under linear degradation we suggest that LLI is the predominant aging mode, accompanied in less degree of LAM_{deNE}. In contrast, we found that under harsh cycling conditions (i.e. dynamic stress cycling), the vast number of intercalation/deintercalation processes (up to 250,000 per cell lifetime in our case) increases abruptly the degradation rate of LAM_{deNE}. This causes accelerated aging that eventually lead to Li plating. This verifies that DST cycling is very detrimental to the cell and causes rapid performance degradation.

To conclude this chapter, a prognosis was performed to show that the tested cell under fast charge was not at risk of Li plating, even beyond end-of-life. The cell could encounter Li plating after 4500 cycles only if LAM_{deNE} had increased its fading rate by a factor of 2.3. In addition, the prognosis analyses carried out here enhance the understanding of Li plating incubation. This is indeed an important achievement, because Li plating is detected and characterized before appearing. Hence, keeping track of the evolution of the NE losses from a quantitative perspective is an exceptional feature for a nondestructive detection and characterization of Li plating. This feature is of crucial interest in BMS, especially in LIB applications where fast charging is required. Deriving such information can be very beneficial for on-board battery diagnosis and prognosis, thus making easier the battery (pack) management, improving its reliability, safety and overall performance.

8. Conclusion

This thesis has investigated battery performance and aging mechanisms, in commercial high power Li-ion battery (LIB) systems. The *in situ*, online techniques used in this work provide a systematic methodology to attain battery diagnosis and prognosis, both qualitatively and quantitatively. The analyses were conducted by a series of non-destructive techniques; including those based on incremental capacity (IC) and peak area (PA) techniques, and the results obtained from mechanistic simulations (using the *'Alawa* toolbox), with an innovative half-cell data approach.

This work reported a study on the performance and the aging mechanisms detected on high power (HP) lithium iron phosphate (LFP) batteries, suitable for electric vehicle (EV) and electrical energy storage (EES) systems. We designed long-term, diverse cycling schemes to decipher the performance and aging modes ongoing in realistic, LIB applications, including driving schedules (i.e. dynamic stress tests, DST). The cycling tests included standard, dynamic stress, and a new fast charging protocol. The latter was designed due to the increasing interest that fast charging is attaining in the LIB industry. The results showed an overall good performance of the tested cells, making them suitable for high power, long-term cycling applications. Safe and efficient (~88%) fast charging was attained within ~22 min. throughout cycling, with a reduction of ~48 min. with respect to the standard charging procedure. Standard and fast charge cycling outperformed the USABC cycle life goals, reaching more than 4500 cycles, whereas dynamic stress cycling reached EOL at cycle 1100.

The degradation in standard and fast charging schemes was caused by a loss of lithium inventory (LLI) and in less degree, loss of active material on the negative delithiatied (LAM_{deNE}). Cell internal resistance did not increase. Most importantly, both cycling schemes caused very close quantitative aging effects on the cells, even under abruptly different cycling schemes. These results have important implications for fast charging of LIBs in real-world applications: as shown, with a proper selection of cell chemistry, cell design and cell manufacturing technology coupled with the use of an efficient fast charging protocol, safe and efficient quick recharges can be attained. In addition, the proposed step-by-step guideline designed to implement fast charging can be used as a valuable tool to develop effective and reliable fast charging protocols.

The degradation during dynamic stress cycling was largely caused by LAM_{deNE} and, in less degree, by LLI. The large amount of LAM_{deNE} originated Li plating, which negatively affected the performance of the cell. The effects of the reversible and irreversible Li plating were identified. The intensification of LAM_{deNE} and subsequent Li plating was identified to be caused by the large number of partial charges/discharges (over 250,000) derived from the DST cycling. This verifies that DST cycling (and therefore driving schemes) is more detrimental to the battery and causes rapid performance degradation, when compared to standard cycling. Even so, we shall point out that the long-term USABC cycle life goal was successfully attained.

To conclude the study, prognosis simulations were performed. We showed that fast charging cycling did not cause risk of Li plating, even beyond end-of-life. In addition, the prognosis analyses enhanced the understanding of Li plating incubation to be detected and characterized before appearing. This feature is of crucial interest in battery management systems (BMS), especially in LIB applications where fast charging is required. Deriving such information can be very beneficial for on-board battery BMS to manage, improve reliability, safety and overall performance of LIB systems.

This work also demonstrates the potential of the proposed methodology to battery diagnosis and prognosis, by using *in situ,* online techniques and its derived analysis strategies. The approaches carried

out in this thesis offer an effective method, with sufficient accuracy yet simplicity in computation to study complex cell behavior. An actual determination of the half-cell data from the harvested electrodes, coupled with the simulation of different and/or combined degradation modes, permit to study the fading effects on tested cells. In this particular LFP cell chemistry, when LLI is the main cause of capacity fade, this results in an overall "slippage" of the negative electrode (NE) correspondence towards a higher relative capacity, reducing the total amount of usable capacity on the full cell. On the other hand, when LAM_{deNE} should become prominent, "shrinkage" of the NE is produced, starting from the lithiated state. These findings enhance the understanding on various key issues: how Li plating may occur from progressive cell degradation, how to detect it and, the most importantly, how to avoid it. Similarly, this work shows in what manner "silent" LAM_{deNE}, after an incubation period can cause capacity fade in a later stage of cycle aging, and how cell constructive parameters (i.e. loading ratio and ofset) are altered with the predominant degradation modes. The prospect of obtaining these parameters online during cell monitoring in a battery system operation provide substantial benefits to improve BMS functions for the diagnosis and prognosis in battery performance.

In conclusion, the research reported in this thesis advances knowledge on LIB performance and degradation mechanisms through *in situ*, online identification techniques. In this work, the characteristics and performance of LFP battery technology have been analyzed, showing good prospects for reliable, long-term high power applications. Moreover, this thesis has demonstrated the potential of carrying out an accurate analysis of the aging modes, both qualitatively and quantitatively. In the same way, the proposed techniques for battery diagnosis and prognosis have proved to be a powerful tool to effectively manage battery systems, predicting battery performance evolution with aging under specific scenarios.

8.1. Summary of contributions

The main contributions of this thesis work toward LIB performance and identification of battery aging mechanism are listed below:

- An updated review that describes and analyzes LIB fundamentals and materials, aging mechanisms, and the main characteristics of commercial LIBs. (Chapter **2**)

- An evaluation of current battery architectures and charging methods for their application in fast charging of LIBs. (Chapter **3**)

- An optimized design strategy to develop safe, efficient, fast charging protocols for LIB applications. (Chapter **3**)
  The strategy is divided into key points, including facts about LIB architecture selection, necessary pre-conditioning and battery evaluation testing, and the design of a multistage charging method.

- A new, efficient and reliable fast charging protocol for the selected high power nanophosphate LIBs. (Chapter **3**)
  The proposed design contemplates avoiding high cell temperatures and reducing the risk of Li plating. The results showed a safe, fast charging within ~22 min., reducing the charging time by $1/3^{rd}$ when compared to standard charge.

- A detailed analysis of the main degradation modes in LIBs is carried out, and a set of tools is provided to facilitate the identification of the aging mechanisms in commercial LIBs, particularized to LFP technology. (Chapter **4**)

The study analyzes the individual aging modes (i.e. LLI, LAM, Li plating and ORI), and their corresponding signatures and effects on IC, PA, capacity fade and half-cell electrode representations.

- Long-term evaluation of high power LFP battery performance under standard, fast charge and dynamic stress cycling. Study of the tested cells performance versus the long-term USABC goals to evaluate the feasibility of this cell technology and architecture for EV applications. (Chapter **6**)

- Validation of the proposed fast charging protocol for the selected cell technology and architecture, by comparing performance and degradation versus standard cycling. (Chapter **6**)
  The analyses of the aging modes, carried out with *in situ* IC and PA techniques showed the same degradation patterns for both cycling procedures.

- Innovative approach to attain accurate simulation results by feeding the *'Alawa* simulation toolbox with harvested half-cell data. (Chapter **7**)
  The materials used in generating the mechanistic model are the same as those used in the tested cells. Therefore, the trends derived from the simulations match to the experimental full cell test results, providing accurate quantification of degradation.

- Innovative approach to calculate internal cell parameters (i.e., LR and OFS) through online techniques. (Chapter **7**)
  A strategy based on analyzing the IC and PA of the harvested graphite electrodes was developed to reconstruct the cell mechanistic model. In this way, the model behaves as the experimental cell with accuracy.

- Quantitative and qualitative analyses of degradation modes in high power LFP batteries tested under standard, fast charge and dynamic stress cycling. (Chapter **7**)
  Degradation parameters can be derived at any given simulation cycle, tracking the degradation modes with cycle aging under complex cell behavior.

- Quantitative and qualitative estimation of Li plating, identifying the reversible and irreversible components. (Chapter **7**)
  Development of innovative strategies based on half-cell analysis, mechanistic simulations and experimental IC and PA to decipher cell degradation and Li plating estimation.

- Prognosis analyses to evaluate cell evolution and prospects of Li plating appearance beyond cycling. (Chapter **7**)
  Prognosis analyses enhance the understanding of Li plating incubation and provide a nondestructive detection and characterization of Li plating appearance.

Finally, this thesis also contributes to establish the necessity to connect both the fundamental science (i.e. material science, electrochemistry, physics and chemistry) with the engineering disciplines (i.e. electrical, power electronics, systems and computer science engineering) to enhance the understanding and capabilities of battery performance and management system's design.

8.2. Future work

While this thesis has demonstrated the potential use of the approaches carried out towards LIBs performance and identification of battery aging mechanisms, opportunities for extending the scope of this thesis remain. This section presents some of these directions:

- The study carried out in this thesis will be complemented through *postmortem* analyses. The tested cells will be disassembled, and postmortem analyses including structural and morphological characterizations will be carried out to further investigate and characterize battery aging from a material science perspective.

- To complement the previously proposed scientific perspective, we also aim to implement, from an electrical engineering approach, a microcontroller-based circuit board that enables automatic cell degradation identification, with the use of IC and PA algorithms implementation and analyses. The synthesis of both disciplines would be embedded in this project.

- The proposed testing schemes carried out in this thesis could be further extended, to carry out tests under several SOC windows, partial charges/discharges, different temperatures or power requirements. Since the techniques used in this work have shown its potential use to identify battery aging, the results of the new proposed testing would be oriented towards the reasoning of how/why different charging schemes may cause different degradation trends.

- The Battery Research Laboratory at the University of Oviedo has recently increased its research scope in the direction of battery modeling, based on a black-box approach. The results obtained in this thesis work will be useful to train and corroborate initial results of the proposed models, to produce reliable estimations on battery aging.

- Since the techniques proposed in this thesis are valid to apply on other LIBs, a complementary study to compare the results obtained in this work versus the results obtained with other commercially available cell technologies (e.g. NMC, LMO, LCO) and architectures would generate new findings on battery performance and degradation on the most commonly used cell technologies. This could be used to settle advantages and drawbacks of batteries, among other interesting conclusions which could be applied to the design of battery systems.

Conclusión

En la presente tesis doctoral se ha analizado el funcionamiento y los mecanismos de envejecimiento en baterías comerciales de litio-ión de alta potencia. Los análisis se llevaron a cabo mediante técnicas no destructivas: capacidad incremental *(incremental capacity, IC)*, área de pico *(peak area, PA)* y simulaciones mecanísticas innovadoras con la *toolbox 'Alawa* alimentada con datos experimentales de semicelda. Se destaca que las técnicas *in situ* empleadas aportan una metodología sistemática para obtener, de manera cualitativa y cuantitativa, el diagnóstico y el pronóstico de la degradación en baterías de litio-ión. El pronóstico de envejecimiento permitirá a los sistemas de gestión de baterías *(battery management systems, BMS)* mejorar el rendimiento, la fiabilidad y la seguridad en las aplicaciones con baterías de litio-ión.

El presente trabajo se ha centrado en el estudio de las prestaciones y del proceso de envejecimiento en baterías de alta potencia de litio hierro fosfato (LFP), una tecnología de amplio uso en vehículos eléctricos *(electric vehicle, EV)* y en sistemas de almacenamiento de energía eléctrica (EES). Para investigar de manera realista el funcionamiento y los fenómenos de degradación en las baterías, se diseñaron test de ensayo extensivo específicos, incluyendo: ciclado estándar, ciclado con un nuevo método de carga rápida y ciclado de estrés dinámico (DST). El protocolo de carga rápida se diseñó dado el interés creciente por disminuir el tiempo necesario para la recarga en las aplicaciones de las baterías de litio-ión, mientras que el ensayo de estrés dinámico deriva de un estándar que emula la conducción en vehículos eléctricos.

Los resultados obtenidos mostraron, de manera general, un buen rendimiento de las baterías ensayadas, lo que valida su empleo en aplicaciones de alta potencia que requieren una larga vida cíclica. Además, con el protocolo de carga rápida diseñado se lograron recargas seguras y eficientes (~88%) en 22 min, lo que supone una reducción del tiempo de carga de 48 min respecto de la carga estándar. Los ensayos de ciclado estándar y de carga rápida superaron con creces los objetivos de largo plazo del USABC *(United States Advanced Battery Consortium)* al alcanzar las baterías una vida útil de más de 4500 ciclos. Por otro lado, el ensayo de estrés dinámico también superó los objetivos del USABC, aunque la vida cíclica en este caso sólo alcanzó los 1100 ciclos.

La degradación observada en los ciclados estándar y de carga rápida se debió principalmente a la pérdida de inventariado de litio *(loss of lithium inventory, LLI)* y, en menor medida, a la pérdida de material activo en el electrodo negativo deslitiado *(loss of active material on the negative electrode delithiated, LAM_{deNE})*. En ambos ciclados la resistencia interna no experimentó cambios notables. Lo más destacado es que ambos ciclados causaron degradaciones muy similares en términos cuantitativos, a pesar de aplicar condiciones de trabajo muy diferentes. Estos resultados conllevan consecuencias importantes: mediante la correcta selección de la tecnología de batería y el empleo de un protocolo eficiente y fiable de carga rápida, se pueden obtener recargas completas y seguras en tiempos reducidos. Además, la metodología propuesta para el diseño de protocolos de carga rápida permite su aplicación a cualquier tecnología de litio-ión.

La degradación observada en el ciclado de estrés dinámico se debió en gran medida al mecanismo LAM_{deNE} y, en menor grado, al mecanismo LLI. La intensa LAM_{deNE} (de un orden de magnitud superior a la medida en ciclados estándar y carga rápida) originó electrodepósito, que afectó de manera negativa al rendimiento de la batería. Asimismo, se identificaron los efectos del electrodepósito reversible y del irreversible. También se concluyó que la intensificación de LAM_{deNE} y la aparición de electrodepósito fueron causados por el excesivo número de cargas y descargas parciales (más de 250.000) asociadas al ciclado de estrés dinámico. Esto demuestra que el ciclado de estrés dinámico que emplea descargas de

simulación de conducción de vehículo eléctrico, es más dañino y causa una mayor y más rápida degradación en el rendimiento de las baterías, en comparación con el ciclado estándar o de carga rápida. Aún así, la batería ensayada bajo estas exigentes condiciones de ciclado logró superar los objetivos a largo plazo de ciclado del USABC.

El trabajo se concluye con un estudio de pronóstico de envejecimiento sobre el ensayo de carga rápida. Se comprueba que, ante las mismas condiciones de ciclado, el protocolo diseñado no origina riesgo de electrodepósito ni siquiera una vez que la capacidad de la batería ha disminuido por debajo del 80% de su capacidad nominal, lo que permitiría una "segunda vida" de la batería. Se desea destacar que los análisis de pronóstico permiten detectar el riesgo de electrodepósito, lo que resulta de gran utilidad en sistemas de gestión de baterías *(battery management systems, BMS)*, en particular en aplicaciones que requieren carga rápida, ya que se podría evitar la aparición del fenómeno.

En la presente tesis también se demuestra la capacidad de las técnicas propuestas para realizar *in situ* diagnósticos y pronósticos fiables. Las estrategias de análisis llevadas a cabo componen un método efectivo, con suficiente precisión y a la vez simplicidad computacional, para estudiar los complejos procesos de degradación asociados generalmente al envejecimiento de las baterías de liti-ión. Por ejemplo, cuando el mecanismo LLI es el principal modo de envejecimiento, se produce un "deslizamiento" del electrodo negativo hacia capacidades relativas mayores, lo que disminuye la capacidad total de la batería. Por el contrario, si LAM_{deNE} es el mecanismo dominante, se produce un "encogimiento" en el electrodo negativo, comenzando desde su estado litiado produciendo pérdida de material activo que últimamente causa electrodepósito. Los detalles de las observaciones realizadas aportan conocimientos importantes; por ejemplo, algunas de las causas que originan el fenómeno de electrodepósito y, lo que es más importante, cómo se puede detectar a tiempo, evitando degradaciones importantes en el futuro. Asimismo, estas técnicas permiten revelar la actividad de determinados mecanismos de degradación "ocultos", como LAM_{deNE}, que tras un periodo de desarrollo interno sin aparente influencia sobre las prestaciones de la batería, ocasiona una repentina y abrupta pérdida de capacidad. En el trabajo realizado también se muestra cómo parámetros constructivos como el *offset (OFS)* y la ratio de carga *(loading ratio, LR)* se ven alterados por los diferentes modos de envejecimiento. La perspectiva de obtener la evolución de estos parámetros a partir de la monitorización en tiempo real de una batería, conlleva por tanto la posibilidad de mejoras sustanciales en los sistemas de gestión BMS con vistas al diagnóstico y pronóstico.

A modo de conclusión, la investigación llevada a cabo en esta tesis doctoral supone un avance en el conocimiento de las prestaciones y de los procesos de degradación ligados al envejecimiento en las baterías de Li-ión. En concreto, los resultados muestran que la tecnología LFP es adecuada en aplicaciones de potencia que requieren sistemas de baterías fiables y duraderos. Además, en este trabajo se ha propuesto una metodología que permite identificar *in situ* los modos de envejecimiento en una batería, desde una perspectiva cualitativa y cuantitativa, lo que posibilita predecir su evolución bajo diferentes escenarios de ciclado. La simplicidad computacional de los análisis abre el camino al empleo de las técnicas propuestas de diagnóstico y pronóstico en sistemas de gestión de baterías (BMS).

Resumen de aportaciones

Las principales aportaciones de la presente tesis doctoral se citan a continuación:

- Revisión actualizada del estado del arte de las baterías de Li-ión. Se presentan los principios y fundamentos de esta tecnología de baterías, los diferentes mecanismos de envejecimiento y las principales características de las baterías comerciales. (Chapter **2**)

- Evaluación de cómo responden los diseños constructivos de las baterías y los métodos de carga actuales ante la aplicación de carga rápida. (Chapter **3**)

- Estrategia de diseño optimizada para el desarrollo de protocolos de carga rápida eficientes y fiables, de aplicación en baterías de Li-ión. (Chapter **3**)
  La estrategia presenta diferentes apartados en los que se selecciona la arquitectura de la batería, se analiza la necesidad de realizar ensayos de pre-acondicionamiento y evaluación de la batería, y se diseña un protocolo multietapa optimizado de carga rápida.

- Protocolo específico de carga rápida, eficiente y fiable, para baterías de alta potencia de tecnología LFP. (Chapter **3**)
  El diseño se ha realizado siguiendo la estrategia propuesta, y tiene en cuenta factores para impedir temperaturas elevadas y reducir el riesgo de electrodepósito. Los resultados obtenidos muestran cargas eficientes, seguras y rápidas (en el entorno de los 20 min) ya que reducen el tiempo total de carga a 1/3 del requerido por el protocolo de carga estándar.

- Análisis detallado de los principales modos de degradación en las baterías de Li-ión, complementado con una guía para facilitar la identificación de los mecanismos de envejecimiento en baterías comerciales de tecnología LFP. (Chapter **4**)
  Este estudio analiza los principales modos de envejecimiento de manera individual y presenta sus principales características y efectos sobre las curvas IC, PA, de evolución de la capacidad, así como la representación individual de la degradación de los electrodos.

- Evaluación de las prestaciones de baterías de alta potencia de tecnología LFP, sometidas a ensayos de ciclado extensivo bajo condiciones estándar, de carga rápida y de estrés dinámico.
  La evaluación se llevó a cabo comparando los resultados experimentales obtenidos con los principales objetivos a largo plazo del USABC, para estudiar la aplicabilidad de las baterías ensayadas en vehículos eléctricos (Chapter **6**)

- Validación del protocolo de carga rápida diseñado, mediante un estudio comparativo de los resultados obtenidos con ciclado estándar y con ciclado de carga rápida. (Chapter **6**)
  El análisis de los mecanismos de envejecimiento mediante técnicas IC y PA muestra idénticos patrones de degradación para ambos tipos de ciclado.

- Desarrollo de una técnica innovadora que asegura que los resultados de las simulaciones son fidedignos, y que consiste en utilizar datos de los materiales electródicos del mismo tipo de la batería ensayada para alimentar la herramienta de simulación. (Chapter **7**)
  Los materiales empleados para generar el modelo mecanístico son los mismos que los empleados en las baterías comerciales ensayadas. Se consigue por tanto que el comportamiento y los patrones derivados de las simulaciones coincidan con aquellos mostrados en los resultados experimentales, lo que conlleva una gran fidelidad en la cuantificación de los fenómenos de degradación.

- Desarrollo de una técnica innovadora para el cálculo de parámetros internos de las baterías de Li-ión (LR y OFS), aplicable en tiempo real. (Chapter **7**)
  La estrategia se basa en el análisis de las curvas IC y PA obtenidas de los electrodos de grafito y LFP extraídos tras la apertura de baterías frescas. Con el uso de la estrategia propuesta se puede emular con exactitud el funcionamiento de las baterías ensayadas.

- Realización de análisis mecanísticos, y posterior identificación cualitativa y cuantitativa de los modos de envejecimiento originados en las baterías ensayadas bajo los test estándar, carga rápida y de estrés dinámico. (Chapter **7**)
  Los parámetros de envejecimiento se pueden obtener en cualquier ciclo de simulación, por lo que se consigue evaluar de forma constante los modos de envejecimiento a lo largo de la vida cíclica de la batería, incluso bajo patrones de degradación complejos.

- Estimación cualitativa y cuantitativa del fenómeno de electrodepósito, identificando sus componentes reversibles e irreversibles. (Chapter **7**)
  Mediante el desarrollo de nuevas técnicas basadas en el análisis de semicelda, de simulaciones mecanísticas y de resultados IC y PA, se logra estimar la degradación de la batería y los efectos del electrodepósito.

- Análisis de pronóstico para evaluar la evolución con el ciclado de la degradación en una batería de tecnología LFP, y analizar la posibilidad de formación de electrodepósito. (Chapter **7**)
  Los análisis de pronóstico permiten una detección anticipada del fenómeno de electrodepósito mediante técnicas no destructivas.

Por último, en esta tesis doctoral se ha demostrado el papel esencial que juega la sinergia entre las disciplinas de ciencias básicas (i.e. ciencia de materiales, electroquímica, físico-química) y las disciplinas aplicadas de la ingeniería (i.e. ingeniería eléctrica, electrónica, de computadores y sistemas) en el campo de las baterías, al haberse logrado una estimulante conexión entre el conocimiento del funcionamiento y degradación de las baterías de Li-ión y su aplicación directa a la optimización de sistemas de gestión de baterías.

Líneas de trabajo futuras

Aunque en esta tesis se ha demostrado la utilidad de varias técnicas y estrategias para el estudio de las prestaciones y el envejecimiento de las baterías de Li-ión, la posibilidad de continuar esta investigación se extiende hacia las siguientes líneas de trabajo futuras:

- El estudio realizado en la presente tesis se va a complementar con análisis *post mortem*. Las baterías ensayadas se desensamblarán en una atmósfera inerte, y se realizarán análisis estructurales y de caracterización morfológica para investigar, desde una perspectiva de ciencia de los materiales, los fenómenos de degradación.

- La línea de trabajo previamente descrita se completaría con un desarrollo tecnológico, que consistiría en diseñar un prototipo de circuito electrónico basado en microcontrolador para la detección automática de los mecanismos de envejecimiento, mediante la implementación de algoritmos IC y PA.

- Los procedimientos de ensayo aplicados en este trabajo se podrían ampliar realizando ensayos con cargas/descargas parciales y a diferentes estados de carga, diferentes temperaturas o requerimientos de potencia. Dado que las técnicas de análisis empleadas han demostrado su fiabilidad para la identificación de los mecanismos de envejecimiento, los nuevos ensayos propuestos estarían enfocados a clarificar cómo diferentes variables de ensayo afectan a las baterías.

- El Laboratorio de Baterías de la Universidad de Oviedo ha incorporado recientemente en sus líneas de investigación el desarrollo de modelos *black-box* de baterías. Los resultados obtenidos en esta tesis serán útiles para el entrenamiento de estos nuevos modelos, lo que permitirá obtener estimaciones fiables sobre el envejecimiento en las baterías de Li-ión.

- Dado que la metodología de estudio propuesta en este trabajo se puede aplicar a otras tecnologías de Li-ión, un análisis complementario basado en el ensayo de otras tecnologías comerciales (e.g., NMC, LMO, LCO) sería de gran utilidad ya que permitiría evaluar de forma comparativa prestaciones y envejecimiento. De este trabajo se obtendrían conclusiones sobre las ventajas e inconvenientes de las diferentes tecnologías ensayadas, dotando al técnico de la información necesaria para seleccionar la tecnología más adecuada para una aplicación, así como para diseñar un sistema optimizado de gestión.

This page intentionally left blank

List of Tables

This page intentionally left blank

List of Figures

This page intentionally left blank

References

[1] M. Yoshio, R. J. Brodd, and A. Kozawa, *Lithium-Ion Batteries*. Springer Verlag, 2009.

[2] B. Scrosati and J. Garche, "Lithium batteries: Status, prospects and future," *J. Power Sources*, vol. 195, no. 9, pp. 2419–2430, May 2010.

[3] R. Mukherjee, R. Krishnan, T.-M. Lu, and N. Koratkar, "Nanostructured electrodes for high-power lithium ion batteries," *Nano Energy*, vol. 1, no. 4, pp. 518–533, Jul. 2012.

[4] T. Reddy, *Linden's Handbook of Batteries*, Fourth. McGraw-Hill Education, 2011.

[5] X. Yuan, H. Liu, and J. Zhang, *Lithium-ion batteries. Advanced Materials and Technologies*, CRC Press. 2011.

[6] G.-A. Nazri and G. Pistoia, *Lithium Batteries*, 1st ed. Springer US, 2003.

[7] M. Dubarry and B. Y. Liaw, "Identify capacity fading mechanism in a commercial LiFePO4 cell," *J. Power Sources*, vol. 194, no. 1, pp. 541–549, Oct. 2009.

[8] I. Bloom, S. A. Jones, E. G. Polzin, V. S. Battaglia, G. L. Henriksen, C. G. Motloch, R. B. Wright, R. G. Jungst, H. L. Case, and D. H. Doughty, "Mechanisms of impedance rise in high-power, lithium-ion cells," *J. Power Sources*, vol. 111, pp. 152–159, 2002.

[9] B. V. Ratnakumar, M. C. Smart, L. D. Whitcanack, and R. C. Ewell, "The impedance characteristics of Mars Exploration Rover Li-ion batteries," *J. Power Sources*, vol. 159, no. 2, pp. 1428–1439, Sep. 2006.

[10] A. J. Bard and L. R. Faulkner, *Electrochemical Methods: Fundamentals and Applications*, vol. 6. Wiley, 2000.

[11] A. Jossen, "Fundamentals of battery dynamics," *J. Power Sources*, vol. 154, no. 2, pp. 530–538, Mar. 2006.

[12] D. Andre, M. Meiler, K. Steiner, H. Walz, T. Soczka-Guth, and D. U. Sauer, "Characterization of high-power lithium-ion batteries by electrochemical impedance spectroscopy. II: Modelling," *J. Power Sources*, vol. 196, no. 12, pp. 5349–5356, Jun. 2011.

[13] J. Newman and K. E. Thomas-Alyea, *Electrochemical Systems*. John Wiley & Sons, 2004.

[14] J. E. B. Randles, "Kinetics of rapid electrode reactions," *Discuss. Faraday Soc.*, vol. 1, p. 11, Jan. 1947.

[15] M. Dubarry, N. Vuillaume, and B. Y. Liaw, "From single cell model to battery pack simulation for Li-ion batteries," *J. Power Sources*, vol. 186, no. 2, pp. 500–507, Jan. 2009.

[16] U. S. A. B. Consortium, "Electric Vehicle Battery Test Procedures Manual," 1996.

[17] J. Tarascon and M. Armand, "Issues and challenges facing rechargeable lithium batteries," *Nature*, vol. 414, no. November, pp. 359–367, 2001.

[18] P. G. Bruce, B. Scrosati, and J.-M. Tarascon, "Nanomaterials for rechargeable lithium batteries.," *Angew. Chem. Int. Ed. Engl.*, vol. 47, no. 16, pp. 2930–46, Jan. 2008.

[19] S. Goriparti, E. Miele, F. De Angelis, E. Di Fabrizio, R. Proietti Zaccaria, and C. Capiglia, "Review on recent progress of nanostructured anode materials for Li-ion batteries," *J. Power Sources*, vol. 257, pp. 421–443, Jul. 2014.

[20] "Altairnano." [Online]. Available: http://www.altairnano.com/. [Accessed: 09-Apr-2015].

[21] D. a. C. Brownson, D. K. Kampouris, and C. E. Banks, "An overview of graphene in energy production and storage applications," *J. Power Sources*, vol. 196, no. 11, pp. 4873–4885, Jun. 2011.

[22] S. Flandrois and B. Simon, "Carbon materials for lithium-ion rechargeable batteries," *Carbon N. Y.*, vol. 37, no. 2, pp. 165–180, Feb. 1999.

[23] D. Aurbach, "A review on new solutions, new measurements procedures and new materials for rechargeable Li batteries," *J. Power Sources*, vol. 146, no. 1–2, pp. 71–78, Aug. 2005.

[24] M. Broussely, P. Biensan, F. Bonhomme, P. Blanchard, S. Herreyre, K. Nechev, and R. J. Staniewicz, "Main aging mechanisms in Li ion batteries," *J. Power Sources*, vol. 146, no. 1–2, pp. 90–96, Aug. 2005.

[25] J. Groot, "State-of-health estimation of li-ion batteries: Cycle life test methods," *Chalmers Univ. Technol. Göteborg*, 2012.

[26] J. R. Dahn, "Phase diagram of LixC6.," *Phys. Rev. B. Condens. Matter*, vol. 44, no. 17, pp. 9170–9177, Nov. 1991.

[27] A. M. Dimiev, G. Ceriotti, N. Behabtu, D. Zakhidov, M. Pasquali, R. Saito, and J. M. Tour, "Direct real-time monitoring of stage transitions in graphite intercalation compounds.," *ACS Nano*, vol. 7, no. 3, pp. 2773–80, Mar. 2013.

[28] V. A. Sethuraman, N. Van Winkle, D. P. Abraham, A. F. Bower, and P. R. Guduru, "Real-time stress measurements in lithium-ion battery negative-electrodes," *J. Power Sources*, vol. 206, pp. 334–342, May 2012.

[29] C. Sole, N. E. Drewett, and L. J. Hardwick, "In situ Raman study of lithium-ion intercalation into microcrystalline graphite.," *Faraday Discuss.*, vol. 172, pp. 223–37, Jan. 2014.

[30] M. Dubarry, C. Truchot, and B. Y. Liaw, "Cell Degradation in Commercial LiFePO4 Cells with High-Power and High-Energy Designs," *J. Power Sources*, vol. 258, pp. 408–419, Feb. 2014.

[31] M. Dubarry, C. Truchot, and B. Y. Liaw, "Synthesize battery degradation modes via a diagnostic and prognostic model," *J. Power Sources*, vol. 219, pp. 204–216, Dec. 2012.

[32] X. Han, M. Ouyang, L. Lu, J. Li, Y. Zheng, and Z. Li, "A comparative study of commercial lithium ion battery cycle life in electrical vehicle: Aging mechanism identification," *J. Power Sources*, vol. 251, pp. 38–54, Apr. 2014.

[33] S. B. Chikkannanavar, D. M. Bernardi, and L. Liu, "A review of blended cathode materials for use in Li-ion batteries," *J. Power Sources*, vol. 248, pp. 91–100, Feb. 2014.

[34] G. Amatucci, "Cobalt dissolution in LiCoO2-based non-aqueous rechargeable batteries," *Solid State Ionics*, vol. 83, no. 1–2, pp. 167–173, Jan. 1996.

[35] C.-H. Doh, D.-H. Kim, H.-S. Kim, H.-M. Shin, Y.-D. Jeong, S.-I. Moon, B.-S. Jin, S. W. Eom, H.-S. Kim, K.-W. Kim, D.-H. Oh, and A. Veluchamy, "Thermal and electrochemical behaviour of C/LixCoO2 cell during safety test," *J. Power Sources*, vol. 175, no. 2, pp. 881–885, Jan. 2008.

[36] J. Vetter, P. Novák, M. R. Wagner, C. Veit, K.-C. Möller, J. O. Besenhard, M. Winter, M. Wohlfahrt-Mehrens, C. Vogler, and A. Hammouche, "Ageing mechanisms in lithium-ion batteries," *J. Power Sources*, vol. 147, no. 1–2, pp. 269–281, Sep. 2005.

[37] Q. Wang, P. Ping, X. Zhao, G. Chu, J. Sun, and C. Chen, "Thermal runaway caused fire and explosion of lithium ion battery," *J. Power Sources*, vol. 208, pp. 210–224, Jun. 2012.

[38] J. W. Fergus, "Recent developments in cathode materials for lithium ion batteries," *J. Power Sources*, vol. 195, no. 4, pp. 939–954, Feb. 2010.

[39] T. Sasaki, T. Nonaka, H. Oka, C. Okuda, Y. Itou, Y. Kondo, Y. Takeuchi, Y. Ukyo, K. Tatsumi, and S. Muto, "Capacity-Fading Mechanisms of LiNiO[sub 2]-Based Lithium-Ion Batteries," *J. Electrochem. Soc.*, vol. 156, no. 4, p. A289, Apr. 2009.

[40] N.-S. Choi, Z. Chen, S. a Freunberger, X. Ji, Y.-K. Sun, K. Amine, G. Yushin, L. F. Nazar, J. Cho, and P. G. Bruce, "Challenges facing lithium batteries and electrical double-layer capacitors.," *Angew. Chem. Int. Ed. Engl.*, vol. 51, no. 40, pp. 9994–10024, Oct. 2012.

[41] A. K. Padhi, K. S. Nanjundaswamy, and J. B. Goodenough, "Phospho-olivines as Positive-Electrode Materials for Rechargeable Lithium Batteries," *J. Electrochem. Soc.*, vol. 144, no. 4, pp. 1188–1194, Apr. 1997.

[42] W. J. Zhang, "Structure and performance of LiFePO4 cathode materials: A review," *J. Power Sources*, vol. 196, no. 6, pp. 2962–2970, Mar. 2011.

[43] S. K. Martha, O. Haik, E. Zinigrad, I. Exnar, T. Drezen, J. H. Miners, and D. Aurbach, "On the Thermal Stability of Olivine Cathode Materials for Lithium-Ion Batteries," *J. Electrochem. Soc.*, vol. 158, no. 10, p. A1115, Oct. 2011.

[44] R. Petibon, N. N. Sinha, J. C. Burns, C. P. Aiken, H. Ye, C. M. VanElzen, G. Jain, S. Trussler, and J. R. Dahn, "Comparative study of electrolyte additives using electrochemical impedance spectroscopy on symmetric cells," *J. Power Sources*, vol. 251, pp. 187–194, Apr. 2014.

[45] L. E. Downie, K. J. Nelson, R. Petibon, V. L. Chevrier, and J. R. Dahn, "The Impact of Electrolyte Additives Determined Using Isothermal Microcalorimetry," *ECS Electrochem. Lett.*, vol. 2, no. 10, pp. A106–A109, Jul. 2013.

[46] S. S. Zhang, "A review on electrolyte additives for lithium-ion batteries," *J. Power Sources*, vol. 162, no. 2, pp. 1379–1394, Nov. 2006.

[47] J. C. Burns, A. Kassam, N. N. Sinha, L. E. Downie, L. Solnickova, B. M. Way, and J. R. Dahn, "Predicting and Extending the Lifetime of Li-Ion Batteries," *J. Electrochem. Soc.*, vol. 160, no. 9, pp. A1451–A1456, Jul. 2013.

[48] V. A. Agubra and J. W. Fergus, "The formation and stability of the solid electrolyte interface on the graphite anode," *J. Power Sources*, vol. 268, pp. 153–162, Dec. 2014.

[49] P. Arora, R. White, and M. Doyle, "Capacity fade mechanisms and side reactions in lithium-ion batteries," *J. Electrochem. Soc.*, vol. 145, no. 10, pp. 3647–3667, 1998.

[50] P. Verma, P. Maire, and P. Novák, "A review of the features and analyses of the solid electrolyte interphase in Li-ion batteries," *Electrochim. Acta*, vol. 55, no. 22, pp. 6332–6341, 2010.

[51] S. J. Harris, A. Timmons, D. R. Baker, and C. Monroe, "Direct in situ measurements of Li transport in Li-ion battery negative electrodes," *Chem. Phys. Lett.*, vol. 485, no. 4–6, pp. 265–274, Jan. 2010.

[52] D. Aurbach, B. Markovsky, G. Salitra, E. Markevich, Y. Talyossef, M. Koltypin, L. Nazar, B. Ellis, and D. Kovacheva, "Review on electrode–electrolyte solution interactions, related to cathode materials for Li-ion batteries," *J. Power Sources*, vol. 165, no. 2, pp. 491–499, Mar. 2007.

[53] E. Peled, D. Golodnistsky, and G. Ardel, "Advanced Model for Solid Electrolyte Interphase Electrodes in Liquid and Polymer Electrolytes," *J. Electrochem. Soc.*, vol. 144, no. 8, p. L208, Aug. 1997.

[54] P. Arora, M. Doyle, and R. E. White, "Mathematical Modeling of the Lithium Deposition Overcharge Reaction in Lithium-Ion Batteries Using Carbon-Based Negative Electrodes," vol. 146, no. 10, pp. 3543–3553, 1999.

[55] J. Christensen and J. Newman, "Cyclable lithium and capacity loss in Li-ion cells," *J. Electrochem. Soc.*, vol. 152, no. 4, p. A818, 2005.

[56] J. Shim and K. A. Striebel, "Cycling performance of low-cost lithium ion batteries with natural graphite and LiFePO4," *J. Power Sources*, vol. 119–121, pp. 955–958, Jun. 2003.

[57] M. C. Smart and B. V. Ratnakumar, "Effects of electrolyte composition on lithium plating in lithium-ion cells," *J. Electrochem. Soc.*, vol. 158, no. 4, p. A379, 2011.

[58] S. S. Zhang, K. Xu, and T. R. Jow, "Study of the charging process of a LiCoO2-based Li-ion battery," *J. Power Sources*, vol. 160, no. 2, pp. 1349–1354, Oct. 2006.

[59] P. Liu, J. Wang, J. Hicks-Garner, E. Sherman, S. Soukiazian, M. Verbrugge, H. Tataria, J. Musser, and P. Finamore, "Aging Mechanisms of LiFePO4 Batteries Deduced by Electrochemical and Structural Analyses," *J. Electrochem. Soc.*, vol. 157, no. 4, p. A499, 2010.

[60] V. Agubra and J. Fergus, "Lithium Ion Battery Anode Aging Mechanisms," *Materials (Basel).*, vol. 6, no. 4, pp. 1310–1325, Mar. 2013.

[61] M. Safari and C. Delacourt, "Aging of a commercial graphite/LiFePO4 cell," *J. Electrochem. Soc.*, vol. 158, no. 10, p. A1123, 2011.

[62] E. Sarasketa-Zabala, I. Gandiaga, E. Martinez-Laserna, L. M. Rodriguez-Martinez, and I. Villarreal, "Cycle ageing analysis of a LiFePO4/graphite cell with dynamic model validations: Towards realistic lifetime predictions," *J. Power Sources*, vol. 275, pp. 573–587, Oct. 2014.

[63] M. Dubarry, B. Y. Liaw, M. S. Chen, S. S. Chyan, K. C. Han, W. T. Sie, and S. H. Wu, "Identifying battery aging mechanisms in large format Li ion cells," *J. Power Sources*, vol. 196, no. 7, pp. 3420–3425, Apr. 2011.

[64] S. C. Nagpure, B. Bhushan, and S. S. Babu, "Multi-Scale Characterization Studies of Aged Li-Ion Large Format Cells for Improved Performance: An Overview," *J. Electrochem. Soc.*, vol. 160, no. 11, pp. A2111–A2154, Oct. 2013.

[65] "USCAR: Energy Storage System Goals." [Online]. Available: http://www.uscar.org/guest/article_view.php?articles_id=85. [Accessed: 10-Apr-2015].

[66] B. Dunn, H. Kamath, and J. M. Tarascon, "Electrical energy storage for the grid: a battery of choices.," *Science*, vol. 334, no. 6058, pp. 928–35, Nov. 2011.

[67] H. Chen, T. N. Cong, W. Yang, C. Tan, Y. Li, and Y. Ding, "Progress in electrical energy storage system: A critical review," *Prog. Nat. Sci.*, vol. 19, no. 3, pp. 291–312, Mar. 2009.

[68] M. Klett, R. Eriksson, J. Groot, P. Svens, K. C. Högström, R. W. Lindström, H. Berg, T. Gustafson, G. Lindbergh, and K. Edström, "Non-uniform aging of cycled commercial LiFePO4//graphite cylindrical cells revealed by post-mortem analysis," *J. Power Sources*, vol. 257, pp. 126–137, Feb. 2014.

[69] M. Kerlau, M. Marcinek, V. Srinivasan, and R. M. Kostecki, "Studies of local degradation phenomena in composite cathodes for lithium-ion batteries," *Electrochim. Acta*, vol. 52, no. 17, pp. 5422–5429, May 2007.

[70] K. Edström, T. Gustafsson, and J. O. Thomas, "The cathode–electrolyte interface in the Li-ion battery," *Electrochim. Acta*, vol. 50, no. 2–3, pp. 397–403, Nov. 2004.

[71] A. Barré, B. Deguilhem, S. Grolleau, M. Gérard, F. Suard, and D. Riu, "A review on lithium-ion battery ageing mechanisms and estimations for automotive applications," *J. Power Sources*, vol. 241, pp. 680–689, Nov. 2013.

[72] K. Striebel, J. Shim, A. Sierra, H. Yang, X. Song, R. Kostecki, and K. McCarthy, "The development of low cost LiFePO4-based high power lithium-ion batteries," *J. Power Sources*, vol. 146, no. 1–2, pp. 33–38, Aug. 2005.

[73] M. Safari and C. Delacourt, "Modeling of a Commercial Graphite/LiFePO[sub 4] Cell," *J. Electrochem. Soc.*, vol. 158, no. 5, pp. A562–A571, 2011.

[74] M. Petzl and M. A. Danzer, "Nondestructive detection, characterization, and quantification of lithium plating in commercial lithium-ion batteries," *J. Power Sources*, vol. 254, pp. 80–87, May 2014.

[75] K. Striebel, A. Guerfi, J. Shim, M. Armand, M. Gauthier, and K. Zaghib, "LiFePO4/gel/natural graphite cells for the BATT program," *J. Power Sources*, vol. 119–121, pp. 951–954, Jun. 2003.

[76] M. Kassem and C. Delacourt, "Postmortem analysis of calendar-aged graphite/LiFePO4 cells," *J. Power Sources*, vol. 235, pp. 159–171, Aug. 2013.

[77] J. Wang, P. Liu, J. Hicks-Garner, E. Sherman, S. Soukiazian, M. Verbrugge, H. Tataria, J. Musser, and P. Finamore, "Cycle-life model for graphite-LiFePO4 cells," *J. Power Sources*, vol. 196, no. 8, pp. 3942–3948, Apr. 2011.

[78] E. Sarasketa-Zabala, F. Aguesse, I. Villarreal, L. M. Rodriguez-Martinez, C. M. López, and P. Kubiak, "Understanding Lithium Inventory Loss and Sudden Performance Fade in Cylindrical Cells during Cycling with Deep-Discharge Steps," *J. Phys. Chem. C*, vol. 119, no. 2, pp. 896–906, 2015.

[79] D. P. Abraham, J. L. Knuth, D. W. Dees, I. Bloom, and J. P. Christophersen, "Performance degradation of high-power lithium-ion cells—Electrochemistry of harvested electrodes," *J. Power Sources*, vol. 170, no. 2, pp. 465–475, Jul. 2007.

[80] M. Winter, J. O. Besenhard, M. E. Spahr, and P. Novμk, "Insertion Electrode Materials for Rechargeable Lithium Batteries," *Adv. Mater.*, no. 10, pp. 725–763, 1998.

[81] Z. Li, J. Huang, B. Y. Liaw, V. Metzler, and J. Zhang, "A review of lithium deposition in lithium-ion and lithium metal secondary batteries," *J. Power Sources*, vol. 254, pp. 168–182, May 2014.

[82] N. Legrand, B. Knosp, P. Desprez, F. Lapicque, and S. Raël, "Physical characterization of the charging process of a Li-ion battery and prediction of Li plating by electrochemical modelling," *J. Power Sources*, vol. 245, pp. 208–216, Jan. 2014.

[83] M. Dollé, L. Sannier, and B. Beaudoin, "Live scanning electron microscope observations of dendritic growth in lithium/polymer cells," *Electrochem. Solid-State Lett.*, vol. 5, no. 12, p. A286, 2002.

[84] R. A. Leising, M. J. Palazzo, E. S. Takeuchi, and K. J. Takeuchi, "Abuse Testing of Lithium-Ion Batteries: Characterization of the Overcharge Reaction of LiCoO[sub 2]/Graphite Cells," *J. Electrochem. Soc.*, vol. 148, no. 8, p. A838, Aug. 2001.

[85] R. Bhattacharyya, B. Key, H. Chen, A. S. Best, A. F. Hollenkamp, and C. P. Grey, "In situ NMR observation of the formation of metallic lithium microstructures in lithium batteries," *Nat. Mater.*, vol. 9, no. 6, pp. 504–510, May 2010.

[86] F. Orsini, A. Du Pasquier, B. Beaudoin, J. . Tarascon, M. Trentin, N. Langenhuizen, E. De Beer, and P. Notten, "In situ Scanning Electron Microscopy (SEM) observation of interfaces within plastic lithium batteries," *J. Power Sources*, vol. 76, no. 1, pp. 19–29, Nov. 1998.

[87] V. Zinth, C. von Lüders, M. Hofmann, J. Hattendorff, I. Buchberger, S. Erhard, J. Rebelo-Kornmeier, A. Jossen, and R. Gilles, "Lithium plating in lithium-ion batteries at sub-ambient temperatures investigated by in situ neutron diffraction," *J. Power Sources*, vol. 271, pp. 152–159, Dec. 2014.

[88] M. W. Verbrugge and B. J. Koch, "The effect of large negative potentials and overcharge on the electrochemical performance of lithiated carbon," *J. Electroanal. Chem.*, vol. 436, no. 1–2, pp. 1–7, Oct. 1997.

[89] S. Tippmann, D. Walper, L. Balboa, B. Spier, and W. G. Bessler, "Low-temperature charging of lithium-ion cells part I: Electrochemical modeling and experimental investigation of degradation behavior," *J. Power Sources*, vol. 252, pp. 305–316, Apr. 2014.

[90] R. Bugga and M. Smart, "Lithium plating behavior in lithium-ion cells," *ECS Trans.*, vol. 25, no. 36, pp. 241–252, 2010.

[91] N. Marx, L. Croguennec, D. Carlier, L. Bourgeois, P. Kubiak, F. Le Cras, and C. Delmas, "Structural and Electrochemical Study of a New Crystalline Hydrated Iron(III) Phosphate FePO 4 ·H 2 O Obtained from LiFePO 4 (OH) by Ion Exchange," *Chem. Mater.*, vol. 22, no. 5, pp. 1854–1861, Mar. 2010.

[92] S. F. Tie and C. W. Tan, "A review of energy sources and energy management system in electric vehicles," *Renew. Sustain. Energy Rev.*, vol. 20, pp. 82–102, Apr. 2013.

[93] L. Tan, L. Zhang, Q. Sun, M. Shen, Q. Qu, and H. Zheng, "Capacity loss induced by lithium deposition at graphite anode for LiFePO4/graphite cell cycling at different temperatures," *Electrochim. Acta*, vol. 111, pp. 802–808, Nov. 2013.

[94] I. Bloom, B. . Cole, J. . Sohn, S. . Jones, E. . Polzin, V. . Battaglia, G. . Henriksen, C. Motloch, R. Richardson, T. Unkelhaeuser, D. Ingersoll, and H. . Case, "An accelerated calendar and cycle life study of Li-ion cells," *J. Power Sources*, vol. 101, no. 2, pp. 238–247, Oct. 2001.

[95] M. Kassem, J. Bernard, R. Revel, S. Pélissier, F. Duclaud, and C. Delacourt, "Calendar aging of a graphite/LiFePO4 cell," *J. Power Sources*, vol. 208, pp. 296–305, Jun. 2012.

[96] E. Sarasketa-Zabala, I. Gandiaga, L. M. Rodriguez-Martinez, and I. Villarreal, "Calendar ageing analysis of a LiFePO4/graphite cell with dynamic model validations: Towards realistic lifetime predictions," *J. Power Sources*, vol. 272, pp. 45–57, Aug. 2014.

[97] R. . Wright, C. . Motloch, J. . Belt, J. . Christophersen, C. . Ho, R. . Richardson, I. Bloom, S. . Jones, V. . Battaglia, G. . Henriksen, T. Unkelhaeuser, D. Ingersoll, H. . Case, S. . Rogers, and R. . Sutula, "Calendar- and cycle-life studies of advanced technology development program generation 1 lithium-ion batteries," *J. Power Sources*, vol. 110, no. 2, pp. 445–470, Aug. 2002.

[98] Q. Zhang and R. E. White, "Calendar life study of Li-ion pouch cells," *J. Power Sources*, vol. 173, no. 2, pp. 990–997, Nov. 2007.

[99] M. Dubarry, A. Devie, and B. Liaw, "The Value of Battery Diagnostics and Prognostics," *J. Energy Power Sources*, vol. 1, no. 5, pp. 242–249, 2014.

[100] P. Braun, J. Cho, J. Pikul, W. King, and H. Zhang, "High power rechargeable batteries," *Curr. Opin. Solid State Mater. Sci.*, vol. 16, pp. 186–198, 2012.

[101] T. B. C. Group, "Batteries for electric cars; challenges, opportunities and the outlook to 2020," Boston, MA, USA, 2011.

[102] T. Ohzuku and R. J. Brodd, "An overview of positive-electrode materials for advanced lithium-ion batteries," *J. Power Sources*, vol. 174, no. 2, pp. 449–456, Dec. 2007.

[103] X. Chen, W. Shen, and T. Vo, "An overview of lithium-ion batteries for electric vehicles," *IPEC, 2012 Conf. …*, pp. 230–235, Nov. 2012.

[104] S. J. Gerssen-Gondelach and A. P. C. Faaij, "Performance of batteries for electric vehicles on short and longer term," *J. Power Sources*, vol. 212, pp. 111–129, Aug. 2012.

[105] R. Faria, P. Marques, R. Garcia, P. Moura, F. Freire, J. Delgado, and A. T. de Almeida, "Primary and secondary use of electric mobility batteries from a life cycle perspective," *J. Power Sources*, vol. 262, pp. 169–177, Sep. 2014.

[106] "DOE Global Energy Storage Database." [Online]. Available: http://www.energystorageexchange.org/. [Accessed: 14-Apr-2015].

[107] A. K. Pahdi, K. S. Nanjundaswamy, and J. B. Goodenough, "Phospho-olivines as Positive-Electrode Materials for Rechargeable Lithium Batteries," *J. Electrochem. Soc.*, vol. 144, no. 4, pp. 3–9, 1997.

[108] M. Park, X. Zhang, M. Chung, G. B. Less, and A. M. Sastry, "A review of conduction phenomena in Li-ion batteries," *J. Power Sources*, vol. 195, no. 24, pp. 7904–7929, Dec. 2010.

[109] J. B. Goodenough and Y. Kim, "Challenges for rechargeable batteries," *J. Power Sources*, vol. 196, no. 16, pp. 6688–6694, Aug. 2011.

[110] E. Prada, D. Di Domenico, Y. Creff, J. Bernard, V. Sauvant-Moynot, and F. Huet, "Simplified Electrochemical and Thermal Model of LiFePO4-Graphite Li-Ion Batteries for Fast Charge Applications," *J. Electrochem. Soc.*, vol. 159, no. 9, pp. A1508–A1519, Aug. 2012.

[111] S. Y. Chung, J. T. Bloking, and Y. M. Chiang, "Electronically conductive phospho-olivines as lithium storage electrodes.," *Nat. Mater.*, vol. 1, no. 2, pp. 123–8, Oct. 2002.

[112] M. Yilmaz and P. T. Krein, "Review of Battery Charger Topologies, Charging Power Levels, and Infrastructure for Plug-In Electric and Hybrid Vehicles," *IEEE Trans. Power Electron.*, vol. 28, no. 5, pp. 2151–2169, May 2013.

[113] "SCiB Rechargeable Battery | Industrial Systems | Toshiba International Corporation." [Online]. Available: https://www.toshiba.com/tic/industrial/rechargable-battery. [Accessed: 22-Jan-2015].

[114] V. Svoboda, *Encyclopedia of Electrochemical Power Sources*. Elsevier, 2009.

[115] S. J. Dillon and K. Sun, "Microstructural design considerations for Li-ion battery systems," *Curr. Opin. Solid State Mater. Sci.*, vol. 16, no. 4, pp. 153–162, Aug. 2012.

[116] "Saft | World leader in high technology batteries." [Online]. Available: http://www.saftbatteries.com/. [Accessed: 30-Apr-2015].

[117] C.-K. Park, Z. Zhang, Z. Xu, A. Kakirde, K. Kang, C. Chai, G. Au, and L. Cristo, "Variables study for the fast charging lithium ion batteries," *J. Power Sources*, vol. 165, no. 2, pp. 892–896, Mar. 2007.

[118] K.-J. Lee, K. Smith, A. Pesaran, and G.-H. Kim, "Three dimensional thermal-, electrical-, and electrochemical-coupled model for cylindrical wound large format lithium-ion batteries," *J. Power Sources*, vol. 241, pp. 20–32, Nov. 2013.

[119] "Chemicals - Environment - European Commission." [Online]. Available: http://ec.europa.eu/environment/chemicals/nanotech/faq/definition_en.htm. [Accessed: 13-Jan-2015].

[120] M. Ender, J. Joos, A. Weber, and E. Ivers-Tiffée, "Anode microstructures from high-energy and high-power lithium-ion cylindrical cells obtained by X-ray nano-tomography," *J. Power Sources*, vol. 269, pp. 912–919, Dec. 2014.

[121] J. R. Dahn, T. Zheng, Y. Liu, and J. Xue, "Mechanisms for lithium insertion in carbonaceous materials," *Science (80-.).*, vol. 270, no. October, 1995.

[122] J. Yang, X. Zhou, J. Li, Y. Zou, and J. Tang, "Study of nano-porous hard carbons as anode materials for lithium ion batteries," *Mater. Chem. Phys.*, vol. 135, no. 2–3, pp. 445–450, Aug. 2012.

[123] A. Burke and M. Miller, "Life cycle testing of lithium batteries for fast charging and second-use applications," in *2013 World Electric Vehicle Symposium and Exhibition (EVS27)*, 2013, pp. 1–10.

[124] A. S. Prakash, P. Manikandan, K. Ramesha, M. Sathiya, J.-M. Tarascon, and A. K. Shukla, "Solution-Combustion Synthesized Nanocrystalline Li 4 Ti 5 O 12 As High-Rate Performance Li-Ion Battery Anode," *Chem. Mater.*, vol. 22, no. 9, pp. 2857–2863, May 2010.

[125] Y. Wang, Y. Wang, E. Hosono, K. Wang, and H. Zhou, "The design of a LiFePO4/carbon nanocomposite with a core-shell structure and its synthesis by an in situ polymerization restriction method.," *Angew. Chem. Int. Ed. Engl.*, vol. 47, no. 39, pp. 7461–5, Jan. 2008.

[126] B. Kang and G. Ceder, "Battery materials for ultrafast charging and discharging.," *Nature*, vol. 458, no. 7235, pp. 190–3, Mar. 2009.

[127] S. Lim, C. S. Yoon, and J. Cho, "Synthesis of Nanowire and Hollow LiFePO 4 Cathodes for High-Performance Lithium Batteries," *Chem. Mater.*, vol. 20, no. 14, pp. 4560–4564, Jul. 2008.

[128] S. S. Zhang, "The effect of the charging protocol on the cycle life of a Li-ion battery," *J. Power Sources*, vol. 161, no. 2, pp. 1385–1391, Oct. 2006.

[129] P. H. L. Notten, J. H. G. O. het Veld, and J. R. G. van Beek, "Boostcharging Li-ion batteries: A challenging new charging concept," *J. Power Sources*, vol. 145, no. 1, pp. 89–94, Jul. 2005.

[130] G. Sikha, P. Ramadass, B. S. Haran, R. E. White, and B. N. Popov, "Comparison of the capacity fade of Sony US 18650 cells charged with different protocols," *J. Power Sources*, vol. 122, no. 1, pp. 67–76, Jul. 2003.

[131] T. Ikeya, N. Sawada, S. Takagi, J. Murakami, K. Kobayashi, T. Sakabe, E. Kousaka, H. Yoshioka, S. Kato, M. Yamashita, H. Narisoko, Y. Mita, K. Nishiyama, K. Adachi, and K. Ishihara, "Multi-step constant-current charging method for electric vehicle, valve-regulated, lead/acid batteries during night time for load-levelling," *J. Power Sources*, vol. 75, no. 1, pp. 101–107, Sep. 1998.

[132] T. Ikeya, N. Sawada, S. Takagi, J. Murakami, K. Kobayashi, T. Sakabe, E. Kousaka, H. Yoshioka, S. Kato, M. Yamashita, H. Narisoko, Y. Mita, K. Nishiyama, K. Adachi, and K. Ishihara, "Charging operation with high energy efficiency for electric vehicle valve-regulated lead–acid battery system," *J. Power Sources*, vol. 91, no. 2, pp. 130–136, Dec. 2000.

[133] Y.-H. Liu, J.-H. Teng, and Y.-C. Lin, "Search for an Optimal Rapid Charging Pattern for Lithium–Ion Batteries Using Ant Colony System Algorithm," *IEEE Trans. Ind. Electron.*, vol. 52, no. 5, pp. 1328–1336, Oct. 2005.

[134] S. Huang, B. Huang, and F. Pai, "Fast Charge Strategy Based on the Characterization and Evaluation of LiFePO Batteries," *IEEE Trans. Power Electron.*, vol. 28, no. 4, pp. 1555–1562, 2013.

[135] T. T. Vo, X. Chen, W. Shen, and A. Kapoor, "New charging strategy for lithium-ion batteries based on the integration of Taguchi method and state of charge estimation," *J. Power Sources*, vol. 273, pp. 413–422, Sep. 2014.

[136] S. K. Chung, A. A. Andriiko, A. P. Mon'ko, and S. H. Lee, "On charge conditions for Li-ion and other secondary lithium batteries with solid intercalation electrodes," *J. Power Sources*, vol. 79, no. 2, pp. 205–211, Jun. 1999.

[137] B. K. Purushothaman and U. Landau, "Rapid Charging of Lithium-Ion Batteries Using Pulsed Currents," *J. Electrochem. Soc.*, vol. 153, no. 3, p. A533, Mar. 2006.

[138] Z. Guo, B. Y. Liaw, X. Qiu, L. Gao, and C. Zhang, "Optimal charging method for lithium ion batteries using a universal voltage protocol accommodating aging," *J. Power Sources*, vol. 274, pp. 957–964, Jan. 2015.

[139] J. Li, E. Murphy, J. Winnick, and P. . Kohl, "The effects of pulse charging on cycling characteristics of commercial lithium-ion batteries," *J. Power Sources*, vol. 102, no. 1–2, pp. 302–309, Dec. 2001.

[140] K. B. Chin, B. V. Ratnakumar, M. C. Smart, K. A. Smith, and S. Narayanan, "Evaluation of Rapid Charge Methodologies for Li-Ion Chemistry," in *ECS Transactions*, 2008, vol. 11, no. 29, pp. 43–53.

[141] F. Savoye, P. Venet, M. Millet, and J. Groot, "Impact of periodic current pulses on Li-Ion battery performance," *IEEE Trans. Ind. Electron.*, vol. 59, no. 9, pp. 3481–3488, Sep. 2012.

[142] T. A. Stuart and A. Hande, "HEV battery heating using AC currents," *J. Power Sources*, vol. 129, no. 2, pp. 368–378, Apr. 2004.

[143] A. Hande and T. Stuart, "AC heating for EV/HEV batteries," *Power Electron. Transp. 2002*, no. 41 9, pp. 119–124, 2002.

[144] A. Pesaran, A. Vlahinos, and T. Stuart, "Cooling and Preheating of Batteries in Hybrid Electric Vehicles," in *6th ASME-JSME Thermal Engineering Joint Conference*, 2003.

[145] X. Zhang, X. Kong, G. Li, and J. Li, "Thermodynamic assessment of active cooling/heating methods for lithium-ion batteries of electric vehicles in extreme conditions," *Energy*, vol. 64, pp. 1092–1101, Jan. 2014.

[146] J. Li, E. Murphy, J. Winnick, and P. A. Kohl, "Studies on the cycle life of commercial lithium ion batteries during rapid charge–discharge cycling," *J. Power Sources*, vol. 102, no. 1–2, pp. 294–301, Dec. 2001.

[147] D. Anseán, M. González, J. C. Viera, V. M. García, C. Blanco, and M. Valledor, "Fast charging technique for high power lithium iron phosphate batteries: A cycle life analysis," *J. Power Sources*, vol. 239, pp. 9–15, 2013.

[148] H.-G. Schweiger, O. Obeidi, O. Komesker, A. Raschke, M. Schiemann, C. Zehner, M. Gehnen, M. Keller, and P. Birke, "Comparison of several methods for determining the internal resistance of lithium ion cells.," *Sensors (Basel).*, vol. 10, no. 6, pp. 5604–25, Jan. 2010.

[149] S. Zhao, F. Wu, L. Yang, L. Gao, and A. F. Burke, "A measurement method for determination of dc internal resistance of batteries and supercapacitors," *Electrochem. commun.*, vol. 12, no. 2, pp. 242–245, Feb. 2010.

[150] M. Dubarry, C. Truchot, M. Cugnet, B. Y. Liaw, K. Gering, S. Sazhin, D. Jamison, and C. Michelbacher, "Evaluation of commercial lithium-ion cells based on composite positive electrode for plug-in hybrid electric vehicle applications. Part I: Initial characterizations," *J. Power Sources*, vol. 196, no. 23, pp. 10328–10335, Dec. 2011.

[151] M. a. Roscher, J. Vetter, and D. U. Sauer, "Characterisation of charge and discharge behaviour of lithium ion batteries with olivine based cathode active material," *J. Power Sources*, vol. 191, no. 2, pp. 582–590, Jun. 2009.

[152] D. Anseán, V. M. García, M. González, J. C. Viera, C. Blanco, and J. L. Antuña, "DC internal resistance during charge : analysis and study on LiFePO 4 batteries," *Electr. Veh. Symp. EVS27. Barcelona, Nov. 2013*, pp. 1–11, 2013.

[153] D. Anseán, J. C. Viera, M. González, V. M. García, C. Blanco, and J. L. Antuña, "Measurement and study of DC internal resistance in LiFePO 4 batteries," *Eur. Electr. Veh. Congr. Brussels, Nov. 2012*, pp. 1–11, 2012.

[154] D. Anseán, V. M. García, M. González, J. C. Viera, J. C. Antón, and C. Blanco, "Evaluation of LiFePO4 batteries for Electric Vehicle applications," *IEEE Trans. Ind. Appl.*, vol. 51, no. 2, pp. 1855–1863, 2015.

[155] C. Vartanian and N. Bentley, "A123 systems' advanced battery energy storage for renewable integration," *2011 IEEE/PES Power Syst. Conf. Expo.*, pp. 1–6, Mar. 2011.

[156] S. H. Jensen, K. Engelbrecht, and C. Bernuy-Lopez, "Measurements of Electric Performance and Impedance of a 75 Ah NMC Lithium Battery Module," *J. Electrochem. Soc.*, vol. 159, no. 6, p. A791, 2012.

[157] A. H. Thompson, "Electrochemical Potential Spectroscopy: A New Electrochemical Measurement," *J. Electrochem. Soc.*, vol. 126, no. 4, p. 608, Apr. 1979.

[158] J. Barker, "Three Electrode Electrochemical Voltage Spectroscopy (TEVS): evaluation of a model lithium ion system," *Electrochim. Acta*, vol. 40, no. 11, pp. 1603–1608, Aug. 1995.

[159] J. Barker, M. Y. Saidi, and R. Koksbang, "Differential capacity as a spectroscopic probe for the investigation of alkali metal insertion reactions," *Electrochim. Acta*, vol. 41, no. 16, pp. 2639–2646, Jan. 1996.

[160] Y. Gao and J. R. Dahn, "Synthesis and Characterization of LiMnO for Li-ion Battery Applications," *J. Electrochem. Soc.*, vol. 143, no. 1, pp. 100–114, 1996.

[161] W. Xing and J. Dahn, "Study of irreversible capacities for Li insertion in hard and graphitic carbons," *J. Electrochem. Soc.*, vol. 144, no. 4, pp. 1195–1201, 1997.

[162] M. Dubarry, V. Svoboda, R. Hwu, and B. Y. Liaw, "Incremental Capacity Analysis and Close-to-Equilibrium OCV Measurements to Quantify Capacity Fade in Commercial Rechargeable Lithium Batteries," *Electrochem. Solid-State Lett.*, vol. 9, no. 10, p. A454, 2006.

[163] M. Dubarry, V. Svoboda, R. Hwu, and B. Y. Liaw, "Capacity and power fading mechanism identification from a commercial cell evaluation," *J. Power Sources*, vol. 165, no. 2, pp. 566–572, Mar. 2007.

[164] M. Dubarry, V. Svoboda, R. Hwu, and B. Y. Liaw, "Capacity loss in rechargeable lithium cells during cycle life testing: The importance of determining state-of-charge," *J. Power Sources*, vol. 174, no. 2, pp. 1121–1125, Dec. 2007.

[165] M. Dubarry, C. Truchot, B. Y. Liaw, K. Gering, S. Sazhin, D. Jamison, and C. Michelbacher, "Evaluation of commercial lithium-ion cells based on composite positive electrode for plug-in hybrid electric vehicle applications. Part II. Degradation mechanism under 2C cycle aging," *J. Power Sources*, vol. 196, no. 23, pp. 10336–10343, Dec. 2011.

[166] a. J. Smith and J. R. Dahn, "Delta Differential Capacity Analysis," *J. Electrochem. Soc.*, vol. 159, no. 3, pp. A290–A293, Jan. 2012.

[167] H. M. Dahn, A. J. Smith, J. C. Burns, D. A. Stevens, and J. R. Dahn, "User-Friendly Differential Voltage Analysis Freeware for the Analysis of Degradation Mechanisms in Li-Ion Batteries," *J. Electrochem. Soc.*, vol. 159, no. 9, pp. A1405–A1409, Aug. 2012.

[168] C. Weng, Y. Cui, J. Sun, and H. Peng, "On-board state of health monitoring of lithium-ion batteries using incremental capacity analysis with support vector regression," *J. Power Sources*, vol. 235, pp. 36–44, Aug. 2013.

[169] B. Y. Liaw and M. Dubarry, *Electric and Hybrid Vehicles, Power Sources, Models, Sustainability, Infrastructure and the Market*. Elsevier, 2010.

[170] M. Dubarry, C. Truchot, B. Y. Liaw, K. Gering, S. Sazhin, D. Jamison, and C. Michelbacher, "Evaluation of commercial lithium-ion cells based on composite positive electrode for plug-in hybrid electric vehicle applications. Part II. Degradation mechanism under 2C cycle aging," *J. Power Sources*, vol. 196, no. 23, pp. 10336–10343, Dec. 2011.

[171] a. Devie, M. Dubarry, and B. Y. Liaw, "Overcharge Study in Li4Ti5O12 Based Lithium-Ion Pouch Cell: I. Quantitative Diagnosis of Degradation Modes," *J. Electrochem. Soc.*, vol. 162, no. 6, pp. A1033–A1040, 2015.

[172] M. Safari and C. Delacourt, "Mathematical Modeling of Lithium Iron Phosphate Electrode: Galvanostatic Charge/Discharge and Path Dependence," *J. Electrochem. Soc.*, vol. 158, no. 2, p. A63, 2011.

[173] V. M. García, D. Anseán, M. González, A. B. Garcia, N. Caméan, and Z. Amghouz, "Morphology analyses of graphite/LFP cells. Internal document. University of Oviedo, National Carbon Institute (INCAR)," 2015.

[174] M. Safari and C. Delacourt, "Simulation-based analysis of aging phenomena in a commercial graphite/LiFePO4 cell," *J. Electrochem. Soc.*, vol. 158, no. 12, p. A1436, 2011.

[175] J. Christensen and J. Newman, "Effect of Anode Film Resistance on the Charge/Discharge Capacity of a Lithium-Ion Battery," *J. Electrochem. Soc.*, vol. 150, no. 11, p. A1416, 2003.

[176] Q. Zhang and R. E. White, "Calendar life study of Li-ion pouch cells," *J. Power Sources*, vol. 179, no. 2, pp. 785–792, May 2008.

[177] Q. Zhang and R. E. White, "Capacity fade analysis of a lithium ion cell," *J. Power Sources*, vol. 179, no. 2, pp. 793–798, May 2008.

[178] A. Devie, M. Dubarry, and B. Y. Liaw, "Investigation of Consistency of Aging Mechanism inside a Batch of Commercial 18650 Cells," in *ECS Meeting Abstracts*, 2014, vol. MA2014–01, no. 1, p. 156.

[179] M. Dubarry, A. Devie, and B. Y. Liaw, "Diagnostics of Li-Ion Commercial Cells – Experimental Case Studies," *Meet. Abstr.*, vol. MA2013–02, no. 6, p. 1217, Oct. 2013.

[180] " 'Alawa Central." [Online]. Available: https://www.soest.hawaii.edu/HNEI/alawa/. [Accessed: 05-Feb-2015].

[181] S. Paul, C. Diegelmann, H. Kabza, and W. Tillmetz, "Analysis of ageing inhomogeneities in lithium-ion battery systems," *J. Power Sources*, vol. 239, pp. 642–650, Oct. 2013.

[182] "A123 Systems. LFP 26650 Lithium Cells." [Online]. Available: http://www.a123systems.com/lithium-ion-cells-26650-cylindrical-cell.htm. [Accessed: 27-Feb-2015].

[183] Y. Zhang, C. Y. Wang, and X. Tang, "Cycling degradation of an automotive LiFePO4 lithium-ion battery," *J. Power Sources*, vol. 196, no. 3, pp. 1513–1520, Feb. 2011.

[184] A. Khandelwal, K. S. Hariharan, P. Gambhire, S. M. Kolake, T. Yeo, and S. Doo, "Thermally coupled moving boundary model for charge–discharge of LiFePO4/C cells," *J. Power Sources*, vol. 279, pp. 180–196, Apr. 2015.

[185] J. Liu, J. Wang, X. Yan, X. Zhang, G. Yang, A. F. Jalbout, and R. Wang, "Long-term cyclability of LiFePO4/carbon composite cathode material for lithium-ion battery applications," *Electrochim. Acta*, vol. 54, no. 24, pp. 5656–5659, Oct. 2009.

[186] B. Nykvist and M. Nilsson, "Rapidly falling costs of battery packs for electric vehicles," *Nat. Clim. Chang.*, vol. 5, no. 4, pp. 329–332, Mar. 2015.

[187] T. Ohzuku, Y. Iwakoshi, and K. Sawai, "Formation of Lithium-Graphite Intercalation Compounds in Nonaqueous Electrolytes and Their Application as a Negative Electrode for a Lithium Ion (Shuttlecock) Cell," *J. Electrochem. Soc.*, vol. 140, no. 9, 1993.

[188] M. Endo, C. Kim, K. Nishimura, T. Fujino, and K. Miyashita, "Recent development of carbon materials for Li ion batteries," *Carbon N. Y.*, vol. 38, no. 2, pp. 183–197, Jan. 2000.

[189] D. Bernardi and J. Go, "Analysis of pulse and relaxation behavior in lithium-ion batteries," *J. Power Sources*, vol. 196, no. 1, pp. 412–427, Jan. 2011.

[190] B. Simon, S. Flandrois, K. Guerin, A. Fevrier-Bouvier, I. Teulat, and P. Biensan, "On the choice of graphite for lithium ion batteries," *J. Power Sources*, vol. 81–82, pp. 312–316, Sep. 1999.

[191] S. M. Rezvanizaniani, Z. Liu, Y. Chen, and J. Lee, "Review and recent advances in battery health monitoring and prognostics technologies for electric vehicle (EV) safety and mobility," *J. Power Sources*, vol. 256, pp. 110–124, Jun. 2014.

[192] C. López, J. Vaughey, and D. Dees, "Morphological transitions on lithium metal anodes," *J. Electrochem. Soc.*, vol. 156, no. 9, p. A726, 2009.